Università degli Studi di Genova

Facoltà di Scienze Matematiche Fisiche Naturali

Tesi di Dottorato di Ricerca in Fisica

3 aprile 2009

Studio dei processi di crescita dalla microfisica delle nuvole alle interfacce critiche

Relatore
Prof. Andrea Mazzino

Relatore esterno
Dott. Antonio Celani

Candidato
Marco Tizzi

Università degli Studi di Genova

Facoltà di Scienze Matematiche Fisiche Naturali

Ph.D. Thesis in Physics

3rd April 2009

Study of growth processes from cloud microphysics to critical interfaces

Supervisor
Prof. Andrea Mazzino

Co-advisor
Dott. Antonio Celani

Candidate
Marco Tizzi

Contents

Introduction

Growth phenomena are ubiquitous in natural systems. They can be encountered in very different disciplines, from mathematics to biology, acting at very separated scales, from the cosmic inflation to molecular clusters. The comprehension of the geometrical and dynamical properties of growth processes is the basis for the description of these systems. To restrict the investigation to physical systems, almost every field needs the study of growth phenomena: black holes in astrophysics, semiconductor deposition on substrata or metal adsorption on surfaces in surface physics, the interfaces between two phases during phase transitions, equilibrium critical clusters in statistical mechanics, droplet condensation or snowflake formation in cloud dynamics, crystal and grain growth, fracture development...

Clearly, such a huge panorama involves very different growth processes, displaying different dynamics and geometries. For instance, the growth of a gravitational system follows a deterministic law, whereas systems growing by collision of external particles are in general subjected to stochastic laws; however, from a macroscopic viewpoint a diffusive growth can be described by deterministic equations as well. Moreover, the shape of the growing object is another distinguishing element, spanning trivially spheroidal and complex fractal structures. It is worth noticing that different physical systems can display similar growth features, whereas in the same system different growing objects can coexist.

An illuminating example is offered by clouds, where, once nucleated, water droplets and ice particles start to grow by vapour diffusion. Here, although the process is stochastic, an effective description is allowed. When particles start to collide one with another, the stochastic description comes again into play. However, while water droplets can be approximated as spherical during almost their whole evolution, ice particles can start to aggregate in a nontrivial way, e.g. leading to the formation of snowflakes with different fractal frames and a two-dimensional development. Analogue structures are shared by other diffusive systems, so that even a mathematical branch, viz. the diffusion-limited aggregation, is devoted to the study of their geometrical properties.

Diffusion-limited aggregation is a typical example of how fruitful the interac-

tion between physicist and mathematicians can be. Indeed, a simple (in definition) class of discrete stochastic growth processes in two dimensions turns out to be a powerful tool in order to describe different physical systems. The search for common symmetries displayed by completely different systems is a recursive feature in physics history, having led to some of the most important scientific revolutions. From this viewpoint, the study of the simplest discrete stochastic growth processes in two dimensions, viz. the exploration processes, and of their continuous limit has quickly resulted in a surprising series of analytical results, allowing the classification of different physical systems in the same universality class.

Let us be more specific. On a planar lattice domain a growing path emerges from the boundary and explores the domain with an assigned stochastic advancing rule. The resulting exploration paths are able to describe the critical interfaces of equilibrium clusters of statistical-mechanics models and can display two properties, Markovianity and conformal invariance, which are revealed to be very fertile if acting together. Recently (in 1999), Oded Schramm defined a family of Markovian and conformally invariant continuous curves stochastically growing on the complex domain, viz. the stochastic Löwner or Schramm–Löwner evolutions (SLE). SLE paths can be classified by one real positive parameter and can be regarded as the continuous limit of particular discrete exploration paths, so describing the interfaces of many different physical systems. Moreover, SLE can also be regarded as the dual theory of the conformal field theory. In other words, SLE provides a geometrical description of two-dimensional dynamical systems. Two relevant remarks are to be considered: thanks to this geometrical approach, a high number of important analytical results has been carried out; most of all, different physical systems have been classified in the same universality class (i.e. are described by the same SLE). To give an idea of the latter statement, consider the class of SLE_4, which is proven to be the limit of the harmonic explorer: it (probably) describes certain level lines of a Gaussian random field and the isolines of the temperature field in a two-dimensional turbulent flow; it is connected to statistical-mechanics models, such as the BCSOS model of roughening transition (which is equivalent to the 4-state Potts model and the double dimer model) and is supposed to give the dual critical interfaces of the Kosterlitz–Thouless transition in the XY model. SLE curves are also able to describe fracture lines.

Our interest in stochastic growth phenomena comes from turbulence and is focused on two very different aspects, the one in atmospheric physics, the other being more mathematical. For the time being, these two directions do not share common points (apart from some investigation means based on the numerical analysis) and in this thesis will be presented in two distinct and independent parts. A deeper introduction to both can be found in the introductions to the

single parts. Here, let us sketch both subjects.

The former problem has been the main topic of the Ph.D. course. We were interested in studying the role played by turbulence for droplet growth in warm clouds. Cloud development can be schematized into three successive stages: first, droplets form around solid particles; then, they grow by condensation; finally, droplets start to collide and coalesce one with another. However, the classical description cannot predict some observed features, such as the transition between the condensation and the collision stages. Our aim was to investigate how turbulent fluctuations in the whole cloud could affect the growth of microscopic droplets. We observed that in turbulent conditions droplets are allowed to nucleate around smaller nuclei and their size distribution broadens in time, so enhancing the collision effectiveness, as registered by experimental measurements in literature.

We dealt with the problem of SLE in the last year of the Ph.D. programme. Since recent studies have showed how some turbulent regimes display SLE features and, thus, can be classified under special universality classes, we were interested in the geometrical description provided by SLE. Although only few cases are proved, SLE curves can be obtained as the limit of discrete exploration processes. However, while SLE curves are a one-parameter family, no equivalent family is present in the discrete case. To solve this problem, in our work we define a new class of discrete explorers by generalizing the harmonic explorer and conjecture a relation between the parameters of the discrete and the continuous case.

This thesis is organized as follows.

Part I is devoted to growth phenomena in warm clouds, i.e. to the formation of a cloud due to water-droplet nucleation and growth. We deal with cloud microphysics, describing the classical approach to droplet evolution. Since such an approach cannot explain some observed features, like the broadening of droplet-size distributions, a complete model is introduced in order to describe droplet nucleation and condensational growth in a turbulent cloud. Numerical results from simulations of this model are presented and discussed with respect to the different considered effects, such as droplet feedback on vapour.

Part II provides a mathematical approach to growth phenomena in two dimensions. Here, the growing object is the simple curve which describes the critical interfaces of statistical-mechanics systems at equilibrium. First, we review the discrete version of these curves, which are explorers on a lattice domain. Then, the continuous case, known as the stochastic Löwner evolution, is presented. An important challenge is the study of the relation between discrete and continuous growth processes. The latter are classified in a one-parameter continuous family. The search for a corresponding family in the former case is the topic of the rest of part II. We define a new class of discrete explorers and conjecture

their convergence to specific continuous curves. Finally, this conjecture is tested numerically.

List of publications

International journals

- "Droplet feedback on vapor in a warm cloud"
  Antonio Celani, Andrea Mazzino, Marco Tizzi
  submitted to *International Journal of Modern Physics B*, pp. 1-10

- "The equivalent size of cloud condensation nuclei"
  Antonio Celani, Andrea Mazzino, Marco Tizzi
  New Journal of Physics **10**, 075021, pp. 1-16 (2008)

- "Route to non-Gaussian statistics in convective turbulence"
  Roberto Festa, Andrea Mazzino, Marco Tizzi
  Physical Review E **75**, 035301(R), pp. 1-4 (2007)

- "Droplet condensation in two-dimensional Bolgiano turbulence"
  Antonio Celani, Andrea Mazzino, Agnese Seminara, Marco Tizzi
  Journal of Turbulence **8**, no. 17, pp. 1-9 (2007)

In preparation

- "Overruled harmonic explorers and SLE"
  Antonio Celani, Andrea Mazzino, Marco Tizzi

Conference proceedings

- "Role of Turbulence for Droplet Condensation"
  Antonio Celani, Andrea Mazzino, Agnese Seminara, Marco Tizzi
  In *Advances in Turbulence XI, Proceedings of the 11th EUROMECH European Turbulence Conference, Porto (Portugal), June 25-28, 2007* (eds. J. M. L. M. Palma and A. Silva Lopes), Springer Proceedings in Physics, vol. 117, pp. 465-7, Springer, Heidelberg. ISBN 978-3-540-72603-6

Part I

Droplet growth and turbulence

Introduction

Clouds are one of the most complex and fascinating natural laboratories. They are aerosols consisting of gases (above all, air and water vapour), liquids (water droplets) and solids (ice particles, dusts, salts...).

Their dynamics usually couple a dozen (and sometimes even more) of orders of magnitudes of dynamical scales. Concerning only their liquid water content, diffusing water molecules can form clusters of nanoscopic sizes, the radius of the smallest water droplets is submicrometric, cloud droplets reach tens of micrometres in size and raindrops few millimetres. At the same time, moist air is subjected to turbulent motions, which are characterized by a broad inertial range of nonlinearly coupled scales, up to the few kilometres of cloud height. In addition clouds can form systems with a horizontal development of hundreds of kilometres. The extreme case is an extratropical disturbance.

Moreover, the study of cloud development requires to deal with many different scientific disciplines. The global atmospheric dynamics involves climatology, whereas local instabilities generate turbulent and convective motions. Thermodynamic transformations, such as adiabatic cooling of air and phase transitions, continuously take place. Atmospheric gases and aerosol particles are subjected to chemical reactions. Electromagnetic phenomena span from the electrostatic attraction between water droplets to the impressive fury of lightnings.

Furthermore, clouds display very different features and properties. They can have a vertical or a horizontal structure and contain only liquid water or ice particles or both together. Some clouds can persist for days, whereas some others can appear and precipitate in half an hour.

Perhaps because of this complex scenario, clouds did not enter scientific studies until the nineteenth century and are still one of the few classical physical systems far from a complete interpretation, although they play a crucial role in the equilibrium of the Earth and human activities have a relevant impact on them. The beginning of cloud physics is associated to the classification of clouds proposed for the first time by Luke Howard in 1803. Howard distinguished clouds in stratiform (*strati*) and convective (*cumuli*) and according to the altitude of their basis and their height. Clouds at the highest altitudes, only composed by

ice, were called *cirri*. Such a classification has the merit of identifying different physical mechanisms on the basis of cloud formation and development.

Many atmospheric situations can lead to the formation of a cloud. For instance, the topography forces warmer air to ascend and thus to expand, cooling down. Similar updrafts are also generated by the convergence of air in a low-pressure region or due to lifting along weather fronts. Moreover, thermal instability drives convective flows. In all these cases, warmer moist air ascends and, if the transformation can be considered adiabatic, cools down by adiabatic expansion. The lower the temperature, the larger the saturation vapour pressure. Metre by metre, the air becomes more and more saturated, until water starts to condense or depose, forming cloud droplets and ice particles, respectively. Then, the activated particles can grow by vapour diffusion. Visually, a cloud is formed when these particles are large and numerous enough to filter and reflect light.

Although very different kinds of cloud exist, the macroscopic cloud dynamics can be described by the evolution of the microscopic water particles in a simple general scheme. Such an approach leads to cloud microphysics. Three successive stages can be identified during cloud formation and development. Chance collisions of water molecules diffusing in moist air can generate water clusters which could become droplets or crystals if the environmental conditions were favourable. Since this is not the case in real clouds, water droplets and ice crystals can only form around solid particles, called *cloud condensation nuclei* (CCN) and *ice nuclei* (IN), respectively, which provide a larger size to win the curvature effect. This process is named *heterogeneous nucleation*. Then, if the environment is supersaturated enough, vapour flows through particle surfaces and particles can grow by diffusion (*growth by condensation* and *by deposition*). However, this is a slowing process; if only diffusive growth is involved a precipitating cloud would be formed after weeks, whereas it is well known that less than one hour could be a sufficient time. In fact, a third process comes into play: once droplets are large enough to feel gravitation, they quickly reach their terminal velocity; thus, collisions with faster and slower droplets can occur; the result of the collision could be the coalescence of the colliding droplets. This stage is called *collection*, because it can be regarded from the viewpoint of a faster droplet which collects smaller droplets along its path. The growth rate in this case is increasing in time in an explosive way, so that raindrop sizes are reached in tens of minutes. For ice particles different mechanisms act (e.g. the aggregation of ice crystals in a snowflake).

Although this simple approach is able to capture the main physical mechanism behind droplet growth, some features are still unexplained and some problems arise. In particular, the classical model leads to an inconsistency in the transition between the condensation and the collection stages. Let us consider a warm cumulus, where no ice is present, and the evolution of the droplet-size distribution

(often referred to as the *size spectrum*). The spectrum of the nucleated particles clearly recovers that of the CCN. During the condensation stage smaller droplets grow faster than larger ones. Thus, the population of cloud droplets becomes more and more homogeneous, narrowing the spectrum. But close sizes means close terminal velocities, i.e. low probability of collision; no precipitation can occur in this way. On the contrary, experimental measurements attest a *spectrum broadening* during the condensation stage. The problem in the classical model is that all droplets are supposed to live inside a small portion of the cloud, viz. the *air parcel*, where they feel the same environment conditions, i.e. the same supersaturation.

Several explanations have been proposed to solve this *bottleneck of condensation*, but only a part of them is able to provide partial justifications for the observed spectra. The entrainment of dry air from above into the cloud causes the evaporation of a part of droplet population and, thus, is responsible for a spectrum broadening in the peripheral regions of the cloud; such a mechanism does not appear to play a significant role in the inner core. It is observed that the presence of giant CCN can turn a non-precipitating cloud in a precipitating one; in this case a broader spectrum is supposed from the very beginning. Moreover, preferential concentration of particles in regions of lower and higher vorticity in a turbulent flow has been revealed as a relevant mechanism. Nevertheless, a univocal explanation is still vacant.

Recently, the effect of turbulent fluctuations up to the largest scales of the cloud has been observed to provide an important spreading mechanism, essentially based on the strong correlation between droplet trajectories and cloud regions rich in vapour. We embraced such an approach in order to study the role played by turbulence for atmospheric growth phenomena and in particular for droplet growth in warm cumuli. Our models are based on the removal of the air parcel as an investigation tool, focusing the analysis on the whole cloud. Indeed, in the typical times for the condensation to occur, initially close particles are able to span very far regions in the whole cloud, so experiencing very different environmental conditions. Thus, fluctuations on the largest turbulent scales are a crucial source for spectrum broadening.

We studied turbulence role in two main directions. The first question was on whether turbulence could serve as an effective CCN, providing large fluctuations and so allowing droplets to cross the curvature barrier in apparently unfavourable environments. In this case, smaller CCN would be sufficient for nucleation. Moreover, if turbulent fluctuations are able to sustain a spectrum broad enough to start up collection, one can avoid invoking the presence of giant and ultragiant CCN.

We tested our models in different settings (e.g. in homogeneous isotropic and in convective turbulence) and considering different effects (e.g. the feedback of

growing droplets on the surrounding vapour) by means of direct numerical simulations. The identified spreading mechanism seems to be robust. In the presence of turbulence a smaller CCN results sufficient to lead to a mean growth, which would be classically forbidden. Turbulence allows droplet to grow even in an unsaturated (on average) environment. Most of all, a strong spectrum broadening is observed also when droplet feedback on vapour is taken into account.

This part is organized as follows.

In chapter 1 the classical description of droplet growth is presented. Before dealing with it, some notions of the thermodynamics of moist air are recalled. Then, the nucleation of droplets in a saturated environment is discussed. It is observed that droplets cannot nucleate on their own in standard conditions, but need the aid of solid particles. The diffusive processes responsible for the condensational growth of droplets are described, together with the resulting evolution law for droplet radii. Finally, the stage when droplets start to collide and coalesce is mentioned.

Open problems in the classical description of droplet growth are reported in chapter 2. In particular, the focus is on the evolution of the droplet-size distribution, which broadens in time in contradiction with the classical prediction. Previous studies which tried to explain this broadening are briefly reviewed. Then, our turbulent model is presented as a generalization of the classical air-parcel model under turbulent conditions in the whole cloud. The complete model takes into account droplet nucleation, both curvature and solute effects, droplet feedback on vapour and thermal convection. The resulting model equations are strongly coupled and a study trying to isolate the main effects is required. The last part of the chapter presents our first works, where droplet nucleation, curvature effect and solute effect were not considered.

Chapter 3 reports the results of the direct numerical simulations of the model where droplet nucleation is included. Two cases are analysed, both with homogeneous isotropic two-dimensional turbulence. First, the back-reaction of droplets on turbulent fields is neglected. The results on droplet growth, unobtainable with a classical approach, allow us to measure turbulence effects in an equivalent effective classical framework. In the second case, droplet feedback on vapour is considered. The broadening of droplet-size distribution is discussed in both cases.

Finally, a summary of this part is provided (page 77). There, some conclusions are drawn and some perspectives proposed.

Chapter 1

Cloud microphysics

As anticipated in the introduction, clouds are one of the most complex and fascinating physical systems in nature. Indeed, they embrace a huge amount of coupled dynamical scales, from the submicrometric sizes of the smallest droplets to the continental scale of the largest extratropical disturbances. Many different scientific disciplines are involved in the study of cloud dynamics. Contributions to cloud development come from turbulent motions, thermodynamic transformations, phase transitions, electromagnetic phenomena, chemical reactions... Moreover, clouds can display very different features, such as size, shape, composition, behaviour...

Nevertheless, some common elements are on the basis of cloud formation and allow a schematic description of the earliest dynamics. Clouds are essentially composed by air, aerosol particles and water and start to form when water droplets and ice particles emerge from the water vapour present in the atmosphere. Thus, understanding these phase transitions and the successive evolution of the nucleated particles is a crucial challenge, which requires the study of particle properties. Such an approach leads to the so-called *cloud microphysics*, where the focus is on the physical mechanisms ruling the formation and growth of a single particle. The idea is to describe what happens at the microscopic level in order to understand the macroscopic phenomena. From this point of view, cloud development can be schematized as the succession of three different stages: *nucleation*, when water droplets and ice particles start to form; *condensation* and *deposition*, when particles grow by subtracting vapour from the surrounding environment; *collection* and *aggregation*, when particle growth is led by the collision and merging of different particles. If the last stage results in an explosive growth, a further stage can occur, i.e. a *precipitation*.

Our work is aimed at understanding the role played by turbulent motions in particle growth. In some sense, it corresponds to the opposite path with respect to the microphysics approach: we want to investigate how macroscopic features

affect the microscopic dynamics. In particular, our study is addressed to droplet growth. Although the physics behind this process is simple thermodynamics, this is a topic where some key elements are not yet well understood. An example is the evolution of the droplet-size distribution during the condensation stage. Thanks to a thermodynamic effect known as *supercooling*, water droplets are able to populate also very cold clouds (more precisely, as far as the temperature is larger than $-41\ ^\circ\mathrm{C}$). Below $-12\ ^\circ\mathrm{C}$ finding ice particles becomes a likely event. Since we are interested in water droplets, we will limit our analysis to a special kind of cloud, *warm cumuli*, i.e. convective clouds with vertical development where water is only present in the liquid and in the vapour phases.

The classical approach to droplet growth assumes that droplets are contained in a fictional small portion of the cloud, the so-called *air parcel*, corresponding to a volume of few litres of moist air. Air parcels follow vertical motions in the cloud: upwards in *updrafts* and downwards in *downdrafts*. An ascending air parcel is subjected to an adiabatic expansion and, hence, cools down, resulting in more and more saturated environment. Then, droplets start to nucleate and grow by condensation. In this classical description, which is able to capture the basic elements of cloud formation, droplets are subjected to the same environmental conditions inside the air parcel.

The present chapter provides a review of cloud microphysics (a deep detailed study can be found in [PK97]). Before dealing with it, in section 1.1 we recall some thermodynamics of moist air and we give the equations of cumulus dynamics (which we will generalize in our turbulent models). Then, droplet growth is described. In section 1.2 it is shown that droplets cannot nucleate without any external aid in standard environmental conditions, but need the availability of solid particles to start the growing process. Growth by condensation is described in section 1.3. Here, the classical Twomey model for droplet growth is presented.

1.1 Evolution of warm clouds

Although the scheme of the cloud formation in three successive stages is valid in many kinds of cloud, different environment conditions lead to different laws ruling droplet growth and evolution. Thus, we need to set the problem more precisely in the proper atmospheric contest. Warm cumuli are the subject of our studies. In this kind of cloud no ice particles are present; cumuli form under the driving effect of convection (e.g. activated by atmospheric stratification) and air motions are vertically structured in updrafts and downdrafts. In particular, our analysis will focus on the so-called cloud *quasiadiabatic core*, where boundary effects are negligible and thermodynamic transformations can be approximated as adiabatic. Air in updrafts adiabatically expands, thus cooling

down (section 1.1.2). The effect of this process onto the vapour content and the temperature of the ascending air parcel is described in section 1.1.3.

1.1.1 Thermodynamics of moist air

Neglecting the presence of microscopic solid particles, the environment where the cloud forms is initially composed by moist air, i.e. by a homogeneous system of dry air and a small amount of water vapour (the mass of the latter being usually about $1\ \%$ of that of the former). Both fractions behave as an ideal gas in an excellent approximation (the error being smaller than $1\ \permil$). Thus, the corresponding state equations read

$$p_{\mathrm{a}} = \rho_{\mathrm{a}} R_{\mathrm{a}} T \tag{1.1a}$$

$$e = \rho_{\mathrm{v}} R_{\mathrm{v}} T \tag{1.1b}$$

where T is the temperature, p_{a} and e are the partial pressures of dry air and water vapour, respectively, ρ_{a} and ρ_{v} their corresponding mass densities and R_{a} and R_{v} the *specific gas constants*. The specific gas constant of the species X with molar weight M_{X} is defined as $R_{\mathrm{X}} = \mathcal{R}/M_{\mathrm{X}}$, where $\mathcal{R} \simeq 8.31\ \mathrm{J/(mol\,K)}$ is the universal gas constant. Here as in the following we label dry air with subscript 'a' and water vapour with subscript 'v'. From the Dalton law for the total pressure ($p = p_{\mathrm{a}} + e$), we conclude that also the system behaves as an ideal gas with state equation

$$p = \rho R T \tag{1.1c}$$

Since the density of dry air can be considered as constant, $(1.1\mathrm{a})$ shows the air *stratification*: the air pressure decreases with the height and the same trend is thus followed by the temperature. In other words, a mean vertical negative gradient of temperature is present.

Once first droplets have nucleated, water is present in the system in the gas phase and in the condensed liquid phase. The system is at *saturation* if the two phases are at equilibrium. The *saturation vapour pressure* e_{sat}, i.e. the partial vapour pressure at saturation, follows the Clausius–Clapeyron equation, which for the condensation-evaporation process can be approximatively expressed as

$$\frac{\mathrm{d}}{\mathrm{d}T} \log e_{\mathrm{sat}} \simeq \frac{L_{\mathrm{w}}}{R_{\mathrm{v}} T^2} \tag{1.2}$$

where L_{w} is the evaporation latent heat of pure water. From (1.2) we get

$$e_{\mathrm{sat}}(T) \propto \mathrm{e}^{-\frac{L_{\mathrm{w}}}{R_{\mathrm{v}} T}} \tag{1.3}$$

showing the strong dependency of e_{sat} on T: the saturation vapour pressure strongly decreases by decreasing the temperature. This is just what happens in an ascending air parcel.

The ratio between the vapour pressure and the saturation vapour pressure gives the relative humidity of the environment, saturation being described by a humidity of $100\ \%$. A more useful indicator for the departure from the saturation is the *supersaturation*

$$s = \frac{e}{e_{\mathrm{sat}}} - 1 \begin{cases} < 0 & \text{undersaturated environment} \\ = 0 & \text{saturated environment} \\ > 0 & \text{supersaturated environment} \end{cases}$$

Typical values of s in the atmosphere rarely exceed the order of $1\ \%$.

Moreover, the amount of water vapour present in the composed system can be controlled by the *water vapour mixing ratio*

$$r_{\mathrm{v}} = \frac{\rho_{\mathrm{v}}}{\rho_{\mathrm{a}}}$$

Once droplets start to nucleate, liquid water is also present. Analogously, the *liquid water mixing ratio* is defined as

$$r_{\mathrm{l}} = \frac{\rho_{\mathrm{l}}}{\rho_{\mathrm{a}}}$$

In absence of both ice particles and entrainment of new air from the outside, the mass conservation during the phase transition simply ensures that

$$r_{\mathrm{l}} = -r_{\mathrm{v}} \tag{1.4}$$

1.1.2 Adiabatic cooling

Moist air is initially undersaturated. How can it become saturated and then more and more supersaturated, starting up droplet nucleation, if no further vapour is provided from the exterior? Schematically, warm air present at a low altitude (e.g. as a result of stratification) is less dense and, hence, is forced by buoyancy to move upwards; the ascending air adiabatically expands, thus cooling down; as a consequence of (1.3), the saturation vapour pressure strongly decreases, so that e gets closer and closer to e_{sat}; finally, the former exceeds the latter and the environment becomes supersaturated, allowing droplets to nucleate.

Now, let us give a more quantitative description of this phenomenon by considering the energy balance for an air parcel. The air parcel is defined as a small

portion of air thermally insulated from its environment (i.e. its temperature varies only adiabatically), in *hydrostatic equilibrium* with the surrounding environment (i.e. sharing the same pressure) and subjected to slow motions (i.e. its kinetic energy is much smaller than its internal energy). Thus, two constraints rule the evolution of an air parcel: the first law of thermodynamics

$$c_p \,\mathrm{d}T - \frac{1}{\rho}\,\mathrm{d}p = \delta q \tag{1.5}$$

where c_p is the specific heat capacity of air and δq is the heat variation per unit of mass, and the balance at the hydrostatic equilibrium

$$\mathrm{d}p = -\rho g \,\mathrm{d}z \tag{1.6}$$

which is valid for parcel velocities up to $10\ \mathrm{m/s}$.

If only dry air is present, no phase transitions are possible and the adiabatic expansion can be approximated as reversible, so resulting in an isentropic process where $\delta q = 0$:

$$c_{p_\mathrm{a}} \,\mathrm{d}T = \frac{1}{\rho_\mathrm{a}}\,\mathrm{d}p_\mathrm{a} \tag{1.7}$$

Combining (1.7) with (1.6) for dry air leads to

$$c_{p_\mathrm{a}} \,\mathrm{d}T = -g \,\mathrm{d}z \tag{1.8}$$

As a results, we find that dry air decreases its temperature with the height at the rate

$$\Gamma_\mathrm{a} = -\left(\frac{\mathrm{d}}{\mathrm{d}z}T\right)_\mathrm{a} = \frac{g}{c_{p_\mathrm{a}}} \simeq 9.8\ \frac{\mathrm{K}}{\mathrm{km}} \tag{1.9}$$

which is called *dry adiabatic lapse rate*. In moist conditions, as far as the air is undersaturated and no phase transition is acting, the air parcel still follows an isentropic process. A similar computation shows that moist air cools down according to a *moist adiabatic lapse rate*

$$\Gamma_\mathrm{m} = -\left(\frac{\mathrm{d}}{\mathrm{d}z}T\right)_\mathrm{m} = \frac{g}{c_p} \approx \Gamma_\mathrm{a} \tag{1.10}$$

Thanks to the last relation, which holds in standard atmospheric conditions, in the following we will use the dry value in place of the moist one.

Once the ascending air parcel is cooled enough to be saturated, a condensation process can take place, releasing latent heat. Now, the transformation is no more isentropic. In this case, the heat variation is given by the mass transfer from water vapour to the condensed phase and the energy balance is

$$c_p \,\mathrm{d}T - \frac{1}{\rho}\,\mathrm{d}p = -L_\mathrm{w} \,\mathrm{d}r_\mathrm{vsat} \tag{1.11}$$

Again, plugging the hydrostatic-equilibrium condition (1.6) into (1.11) returns

$$c_p \,\mathrm{d}T - g \,\mathrm{d}z = -L_\mathrm{w} \,\mathrm{d}r_\mathrm{vsat} \approx \left(\frac{\mathrm{d}}{\mathrm{d}T} r_\mathrm{l}\right) \mathrm{d}T \tag{1.12}$$

the last relation being due to the fact that the saturation vapour mixing ratio slightly depends on the pressure (as a consequence of the exponential dependency of the saturation pressure on the temperature). Recasting (1.12) as

$$\left(1 + \frac{L_\mathrm{w}}{c_p} \frac{\mathrm{d}}{\mathrm{d}T} r_\mathrm{vsat}\right) \mathrm{d}T + \Gamma_\mathrm{m} \,\mathrm{d}z = 0$$

we find that the air cooling is now described by the *saturation adiabatic lapse rate*

$$\Gamma_\mathrm{sat} = -\left(\frac{\mathrm{d}}{\mathrm{d}z} T\right)_\mathrm{sat} = \frac{\Gamma_\mathrm{a}}{1 + \frac{L_\mathrm{w}}{c_p} \frac{\mathrm{d}}{\mathrm{d}T} r_\mathrm{vsat}} \tag{1.13}$$

which varies with elevation (through r_vsat). As an order of magnitude, $\Gamma_\mathrm{sat} \sim 6.5 \ \mathrm{K/km}$. In fact, this is a *pseudoadiabatic* description, but the result would be almost the same, if we considered an isentropic process where the air parcel is a closed system and the condensed water cannot leave it. Thus, the name of adiabatic lapse rate still makes sense. Besides, the inclusion of the entrainment of new air from the outside causes the addition of a new term to the numerator of (1.13). However, since we set our investigation inside the cloud core, in the following we will neglect the entrainment contribution.

If we consider the *environmental lapse rate* $\Gamma = -\frac{\mathrm{d}}{\mathrm{d}z} T$, three possible situations can occur.

- $\Gamma < \Gamma_\mathrm{sat} < \Gamma_\mathrm{a}$: *absolute stability*
  An air parcel displaced upward by an adiabatic process would then be more dense than its environment and would tend to sink back to its level of origin with harmonic oscillations.

- $\Gamma_\mathrm{sat} < \Gamma < \Gamma_\mathrm{a}$: *conditional instability*
  Under such conditions an air parcel at the environmental temperature is unstable to upward vertical displacements if it is saturated, unstable to downward displacements if it is saturated and contains cloud water, but stable to all small vertical displacements if it is undersaturated.

- $\Gamma_\mathrm{sat} < \Gamma_\mathrm{a} < \Gamma$: *absolute instability*
  The column of air has a *superadiabatic* lapse rate. An air parcel displaced vertically would be accelerated in the direction of the displacement and its kinetic energy would consequently increase with increasing distance from its level of origin.

1.1.3 Cumulus dynamics

The effect of the adiabatic cooling is a cloud organized in a vertical structure, where air parcels move upwards and downwards with a vertical velocity $w = \boldsymbol{u}\cdot\hat{\boldsymbol{z}}$. Now, the static picture presented in section 1.1.2 can be rephrased in a dynamical way by substituting the derivative with respect to z with a time derivative.

Therefore, the evolution of the temperature is obtained by taking the time derivative of (1.12):

$$\frac{\mathrm{d}}{\mathrm{d}t}T = -\frac{g}{c_p}w - \frac{L_\mathrm{w}}{c_p}\frac{1}{1+r_\mathrm{v}}\frac{\mathrm{d}}{\mathrm{d}t}r_\mathrm{v} \tag{1.14}$$

where the saturation mixing ratio has been substituted by the vapour mixing ratio in order to consider the more general case where a slight supersaturation is present. It is useful to express the mixing ratio in terms of the supersaturation by exploiting the ideal-gas law:

$$r_\mathrm{v} = \frac{e}{p_\mathrm{a}}\frac{R_\mathrm{a}}{R_\mathrm{v}} = \frac{e}{e_\mathrm{sat}}\frac{e_\mathrm{sat}}{p_\mathrm{a}}\frac{R_\mathrm{a}}{R_\mathrm{v}} = (1+s)\frac{e_\mathrm{sat}R_\mathrm{a}}{p_\mathrm{a}R_\mathrm{v}} \tag{1.15}$$

Plugging (1.15) in (1.14) leads to

$$\frac{\mathrm{d}}{\mathrm{d}t}T = -\frac{g}{c_p}w - \frac{L_\mathrm{w}}{c_\mathrm{p}}\frac{1}{1+(1+s)\frac{e_\mathrm{sat}R_\mathrm{a}}{p_\mathrm{a}R_\mathrm{v}}}\frac{\mathrm{d}}{\mathrm{d}t}r_\mathrm{v} \tag{1.16}$$

If we define the two dimensionless coefficients

$$a_T = \frac{L_\mathrm{w}}{c_pT_\mathrm{ref}}\frac{p_\mathrm{a}R_\mathrm{v}}{e_\mathrm{sat}R_\mathrm{a}}$$
$$b_T = 1 + \frac{p_\mathrm{a}R_\mathrm{v}}{e_\mathrm{sat}R_\mathrm{a}}$$

T_ref being a reference temperature (e.g. the mean temperature at cloud middle height), and we exploit (1.4) and (1.10), (1.16) is finally simplified in

$$\frac{\mathrm{d}}{\mathrm{d}t}T = -\Gamma_\mathrm{a}w + \frac{a_TT_\mathrm{ref}}{b_T+s}\frac{\mathrm{d}}{\mathrm{d}t}r_\mathrm{l} \tag{1.17}$$

Here, on the r.h.s. the first term represents the *adiabatic cooling*, the second term the *latent heat release* by condensation.

The evolution law for the supersaturation can be extracted by differentiat-

ing (1.15) with respect to time:

$$\begin{aligned}\frac{\mathrm{d}}{\mathrm{d}t}r_\mathrm{v} &= \frac{e_\mathrm{sat}R_\mathrm{a}}{p_\mathrm{a}R_\mathrm{v}}\frac{\mathrm{d}}{\mathrm{d}t}s + (1+s)\frac{R_\mathrm{a}}{p_\mathrm{a}R_\mathrm{v}}\frac{\mathrm{d}}{\mathrm{d}t}e_\mathrm{sat} - (1+s)\frac{e_\mathrm{sat}R_\mathrm{a}}{p_\mathrm{a}^2R_\mathrm{v}}\frac{\mathrm{d}}{\mathrm{d}t}p_\mathrm{a} = \\ &= \frac{e_\mathrm{sat}R_\mathrm{a}}{p_\mathrm{a}R_\mathrm{v}}\frac{\mathrm{d}}{\mathrm{d}t}s + (1+s)\frac{R_\mathrm{a}}{p_\mathrm{a}R_\mathrm{v}}\frac{e_\mathrm{sat}L_\mathrm{w}}{R_\mathrm{v}T^2}\frac{\mathrm{d}}{\mathrm{d}t}T - (1+s)\frac{e_\mathrm{sat}R_\mathrm{a}}{p_\mathrm{a}^2R_\mathrm{v}}\left(-\frac{gp_\mathrm{a}w}{R_\mathrm{a}T}\right) = \\ &= \frac{e_\mathrm{sat}R_\mathrm{a}}{p_\mathrm{a}R_\mathrm{v}}\left(\frac{\mathrm{d}}{\mathrm{d}t}s + (1+s)\frac{L_\mathrm{w}}{R_\mathrm{v}T^2}\frac{\mathrm{d}}{\mathrm{d}t}T + (1+s)\frac{gw}{R_\mathrm{a}T}\right) \quad (1.18)\end{aligned}$$

where we have explicitly used the Clausius–Clapeyron equation (1.2) and the hydrostatic approximation (1.6) in order to compute the derivatives of the saturation vapour pressure and the air pressure, respectively. Now, (1.18) can be recast in terms of time derivative of the supersaturation:

$$\begin{aligned}\frac{\mathrm{d}}{\mathrm{d}t}s &= \frac{p_\mathrm{a}R_\mathrm{v}}{e_\mathrm{sat}R_\mathrm{a}}\frac{\mathrm{d}}{\mathrm{d}t}r_\mathrm{v} - (1+s)\left(\frac{L_\mathrm{w}}{R_\mathrm{v}T^2}\frac{\mathrm{d}}{\mathrm{d}t}T + \frac{gw}{R_\mathrm{a}T}\right) = \\ &= \frac{p_\mathrm{a}R_\mathrm{v}}{e_\mathrm{sat}R_\mathrm{a}}\frac{\mathrm{d}}{\mathrm{d}t}r_\mathrm{v} - (1+s)\left(-\frac{L_\mathrm{w}}{R_\mathrm{v}T^2}\frac{gw}{c_p} - \frac{L_\mathrm{w}}{R_\mathrm{v}T^2}\frac{L_\mathrm{w}}{c_p}\frac{\mathrm{d}}{\mathrm{d}t}r_\mathrm{v} + \frac{gw}{R_\mathrm{a}T}\right) = \\ &= (1+s)\left(\frac{L_\mathrm{w}}{R_\mathrm{v}T^2}\frac{g}{c_p} - \frac{g}{R_\mathrm{a}T}\right)w + \left(\frac{p_\mathrm{a}R_\mathrm{v}}{e_\mathrm{sat}R_\mathrm{a}} + (1+s)\frac{L_\mathrm{w}^2}{c_pR_\mathrm{v}T^2}\right)\frac{\mathrm{d}}{\mathrm{d}t}r_\mathrm{v} \quad (1.19)\end{aligned}$$

where we have substituted the time derivative of the temperature directly with (1.14) (with the approximation $\frac{1}{1+r_\mathrm{v}} \simeq 1$). Let us define

$$\begin{aligned}G_s &= \frac{gL_\mathrm{w}}{c_{p_\mathrm{a}}R_\mathrm{v}T^2} - \frac{g}{R_\mathrm{a}T} \\ a_s &= \frac{L_\mathrm{w}^2}{c_{p_\mathrm{a}}R_\mathrm{v}T^2} \\ b_s &= 1 + \frac{c_{p_\mathrm{a}}R_\mathrm{v}T^2}{L_\mathrm{w}^2}\frac{p_\mathrm{a}R_\mathrm{v}}{e_\mathrm{sat}R_\mathrm{a}}\end{aligned}$$

which can be all regarded as constants. Here G_s is the *adiabatic saturation rate* and a_s and b_s are two dimensionless coefficients. Finally, exploiting the mass conservation (1.4) in the absence of both ice and entrainment, (1.19) is simplified in

$$\frac{\mathrm{d}}{\mathrm{d}t}s = G_s w(1+s) - a_s(b_s+s)\frac{\mathrm{d}}{\mathrm{d}t}r_\mathrm{l} \quad (1.20)$$

On the rhs of (1.20) the first term represents the progressive saturation of the expanding ascending parcel by adiabatic cooling, the second one is the *vapour absorption* due to condensation.

Both (1.17) and (1.20) are not closed, because the derivative of the liquid mixing ratio is still in an implicit form. Thus, we have to describe droplet growth in order to both close the equations and, above all, understand how droplets evolve in the cloud.

1.2 Droplet nucleation

A warm cloud forms when, under some environmental conditions, droplets start to emerge from moist air. This process is called *nucleation*. From a macroscopic viewpoint, one can be induced to think that, once the air has reached its saturation point, droplets start to appear spontaneously in the system. However, as we will see, this is not the case. Indeed, the saturation pressure over the curved surface of a droplet is larger than the environmental value (which is referred to a flat surface). In other words, if we consider a small droplet in a saturated environment over a flat surface of water, the droplet would evaporate immediately, whereas the water is in equilibrium with the air. Thus, only supersaturated air allows droplets to reach an equilibrium state. In this case they can form by themselves, without any external aid; only water is involved and the process is called *homogeneous nucleation* (section 1.2.1). However, if wettable solid particles are present, it could be easier for a droplet to condense on them, because larger radii are allowed. Not surprisingly, the latter process is called *heterogeneous nucleation* (section 1.2.2). As we will see, in real clouds no homogeneous nucleation is possible.

Now, the focus has to be moved to the microscopic scale in order to investigate the equilibrium properties of a single droplet. This is the field of cloud microphysics. For nucleation, this amounts to studying under what conditions a chance collision between water molecules has the possibility to generate a surviving droplet.

1.2.1 Homogeneous nucleation

Let us first begin from the case where no solid particles are involved, but only moist air, where water molecules are free to move. At molecule scales (which are nanoscales) the motions are purely diffusive and collisions continually occur. Clearly, a more dense vapour enhances collisions between water molecules. Now, the question is on when a cluster formed by a chance collision of a few water molecules can survive. If such a process is convenient, from the cluster an embryonal droplet emerges; otherwise, the cluster breaks up. The convenience of the liquid phase with respect to the vapour one is controlled by the variation of the Gibbs free energy ΔG, which results from the contrast between a surface

and a volume term: the former is the work needed to create the interface of the *embryo*, the latter is the free energy released by the phase transition.

More quantitatively, if an embryo of N water molecules is bounded by an interface of area A enclosing a volume V, the variation of the Gibbs free energy is

$$\Delta G = A\sigma + N(\mu_\mathrm{l} - \mu_\mathrm{v}) \tag{1.21}$$

where the surface tension σ is the work needed to create a surface unit of interface between water and air and the chemical potentials μ_l and μ_v are the molecular Gibbs free energies of the vapour and the liquid phases, respectively. To compute this difference, let us consider the variation of the Gibbs free energy for a single molecule

$$\mathrm{d}\mu = \mathrm{d}g = -s\,\mathrm{d}T + v\,\mathrm{d}p = v\,\mathrm{d}p \tag{1.22}$$

s and v being the entropy and the volume of the molecule. The last equality is due to the constant temperature. Rewriting (1.22) for each phase

$$\begin{cases} \mathrm{d}\mu_\mathrm{l} = v_\mathrm{l}\,\mathrm{d}e & \text{(1.23a)} \\ \mathrm{d}\mu_\mathrm{v} = v_\mathrm{v}\,\mathrm{d}e & \text{(1.23b)} \end{cases}$$

and subtracting $(1.23\mathrm{b})$ from $(1.23\mathrm{a})$ returns

$$\mathrm{d}(\mu_\mathrm{l} - \mu_\mathrm{v}) = (v_\mathrm{l} - v_\mathrm{v})\,\mathrm{d}e \approx -v_\mathrm{v}\,\mathrm{d}e = -k_\mathrm{B}T\frac{\mathrm{d}e}{e} \tag{1.24}$$

where we have neglected the liquid volume ($v_\mathrm{l} \ll v_\mathrm{l}$) and used the ideal-gas law for a single molecule ($ev_\mathrm{v} = k_\mathrm{B}T$, with k_B the Boltzmann constant). Integrating (1.24) between e and e_sat leads to

$$\mu_\mathrm{l} - \mu_\mathrm{v} = -k_\mathrm{B}T\log\frac{e}{e_\mathrm{sat}} \tag{1.25}$$

If the embryo has a spherical shape with radius R and $n = N/V$ is the molecule-number density, plugging (1.25) into (1.21) finally gives

$$\Delta G = 4\pi R^2\sigma - \frac{4}{3}\pi R^3 n k_\mathrm{B}T\log\frac{e}{e_\mathrm{sat}} \tag{1.26}$$

At equilibrium G is minimum, i.e. $\Delta G = 0$. The surface contribution in (1.26) is always positive, whereas the sign of volume term depends on whether $e < e_\mathrm{sat}$ or $e > e_\mathrm{sat}$. The trend of ΔG in both cases in sketched in figure 1.1a

If $e < e_\mathrm{sat}$, $\Delta G > 0$ for any radius and the only minimum is at $R = 0$. Thus, in an undersaturated environment embryo formation is not favoured: if a cluster of molecules is formed by chance collision, it breaks up soon. No homogeneous nucleation is possible.

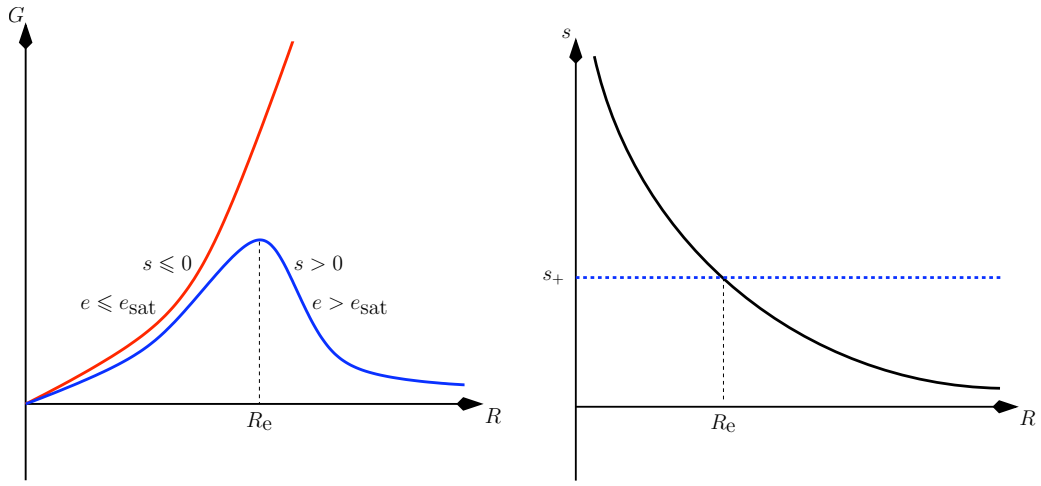

(a) Gibbs free energy of a droplet **(b)** Kelvin curve

Figure 1.1: For the homogeneous nucleation of a droplet a supersaturated environment is needed. Indeed, as shown in figure (a), if the vapour pressure is smaller than the saturation value, the Gibbs free energy for the condensation process is minimized only at $R = 0$, so that an embryo emerging from a chance collision of water molecules evaporates immediately. If the vapour pressure exceeds the saturation value, an unstable-equilibrium radius R_{e} is present: below it, the embryo still evaporates; above it, the embryo can grow by condensation. The equilibrium radius is a function of the supersaturation, as described by the Kelvin curve in figure (b). If the environmental supersaturation is smaller than the equilibrium supersaturation over the water surface, the embryo evaporates following the Kelvin curve upwards; otherwise, it can grow indefinitely following the curve downwards.

If $e > e_{\mathrm{sat}}$, the volume energy is negative and the Gibbs free energy has a minimum at an *equilibrium radius* R_{e}. When $R > R_{\mathrm{e}}$, ΔG reduces for increasing R and condensation is favoured; when $R < R_{\mathrm{e}}$, ΔG reduces for decreasing R and evaporation is favoured. From a molecular viewpoint, if a chance collision generates an embryo with a size larger than the equilibrium value, then it survives and continues to grow by condensation: in this case a droplet has been *activated*. Otherwise, it breaks up. The equilibrium radius can be easily derived from $\partial_R \Delta G = 0$

$$R_{\mathrm{e}} = \frac{2\sigma}{n k_{\mathrm{B}} T \log \frac{e}{e_{\mathrm{sat}}}} = \frac{c}{\log \frac{e}{e_{\mathrm{sat}}}} \tag{1.27}$$

which is known as the Kelvin equation and shows that the saturation vapour pressure over a curved surface is larger than on a flat surface. Here, c is the

curvature coefficient defined as

$$c = \frac{2\sigma}{nk_{\mathrm{B}}T} = \frac{2\sigma}{\rho_{\mathrm{w}}R_{\mathrm{v}}T} \simeq 1.2 \text{ nm}$$

where ρ_{w} is the water density. In terms of the supersaturation, the Kelvin equation can be rewritten as

$$s_{\mathrm{e}} = s(R_{\mathrm{e}}) = \mathrm{e}^{\frac{c}{R_{\mathrm{e}}}} - 1 \tag{1.28}$$

where s_{e} is the *equilibrium supersaturation*. The equilibrium curve in the R-s plane described by (1.28) is called *Kelvin curve* and is schematically plotted in figure 1.1b.

Let us now give a brute estimation of a homogeneous-nucleation process. Suppose the extreme case of 100 simultaneous collisions. Since a water molecule has a radius of about 0.1 nm, the resulting embryo would have a radius larger than 10 nm. Thus, its equilibrium supersaturation would be larger than 12 %, whereas in the atmosphere values in the range $s \sim 0.1 \div 1$ % are observed. This would correspond to the very unlikely concomitant collision of thousands and thousands of water molecules! As a consequence, homogeneous nucleation cannot occur in real atmospheric conditions.

1.2.2 Heterogeneous nucleation

Although homogeneous nucleation is not possible in the atmosphere, we known that clouds and rain do exist — besides, they are the subject of our study! Thus, nature must provide a more efficient mechanism to form water droplets. Indeed, in moist air a huge amount of *aerosol particles* is present. These solid particles come from very different phenomena (both natural and anthropogenic) and display very different sizes (embracing nanometric and micrometric scales) and properties. In particular, there are wettable and even soluble particles. A wettable aerosol particle can serve as a nucleus for water condensation. Indeed, water molecules can be captured on its surface after a collision with it. Molecule by molecule, the entire surface of the particle can be covered by a thin water film. Then, the interface becomes an interface between pure water and moist air and the wet particle behaves as a pure-water droplet. For this reason wettable aerosol particles are named *cloud condensation nuclei* or CCN. A CCN is a catalyst for condensation, providing a larger size from which it is easier to win the curvature effect. Indeed, if the same number of molecules is involved, in the homogeneous case a much smaller droplet is built, with less chance of surviving. Such a process is called *heterogeneous nucleation*.

If the CCN is not soluble in water, once the droplet is nucleated, it still follows the equilibrium Kelvin curve (1.28) as in the homogeneous case. Its initial radius

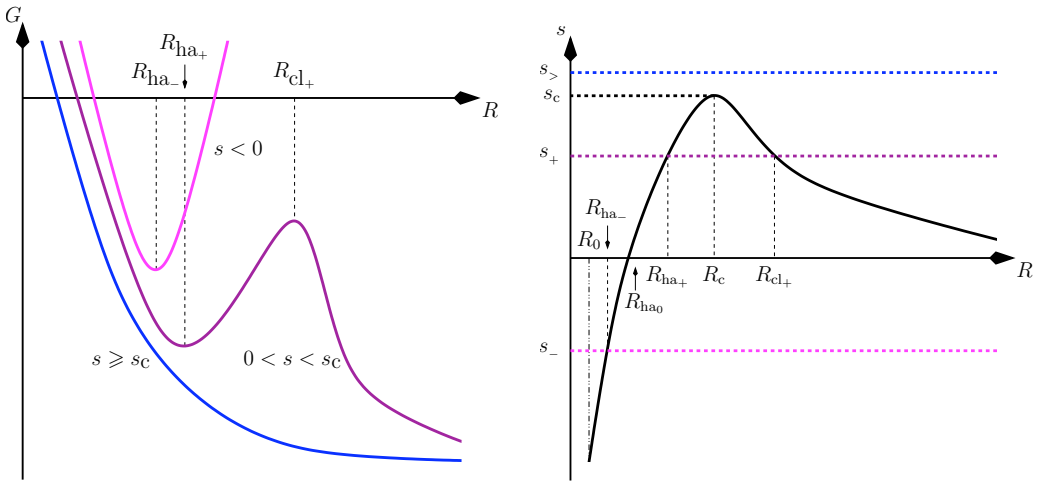

(a) Gibbs free energy of a droplet **(b)** Köhler curve

Figure 1.2: The heterogeneous nucleation around a hygroscopic CCN is able to generate droplets in conditions unfavourable for pure water (even in undersaturated environments). Figure 1.2a shows three possible situations for the Gibbs free energy at increasing values of the environmental supersaturation: a stable, a stable plus an unstable or an unstable radius are present, respectively. In the stable case a haze droplet with radius R_{ha} is nucleated, whereas in the unstable case, if the embryo radius is larger than R_{cl}, a growing cloud droplet is generated. This picture is more clear if we plot the equilibrium Köhler curve, as in figure 1.2b. If the environmental supersaturation intersects it at the point R_{ha}, only a stable population of haze droplets is possible. If the intersection points are two, also an unstable population of cloud droplets can be present; in this case, if a cloud droplet is slightly smaller than the unstable-equilibrium size, it evaporates to the stable size following the Köhler curve; if it is slightly larger, it can grow indefinitely as a cloud droplet. Finally, if the environmental supersaturation is larger than the critical equilibrium value s_{c}, all the nucleated droplets are allowed to cross the curvature barrier following the equilibrium curve and, then, growing indefinitely.

will be the CCN radius R_0. Again, if $R_0 < R_{\mathrm{e}}$, the droplet evaporates releasing its CCN in the environment. On the contrary, if $R_0 > R_{\mathrm{e}}$, the droplet is allowed to grow by condensation. For an environmental supersaturation of about $0.1\ \%$, a CCN radius of $0.5\ \mu\mathrm{m}$, which is common in the atmosphere, is sufficient to activate the droplet.

If the CCN is hygroscopic, a stronger mechanism comes into play, i.e. the *solute effect*. Water molecules are absorbed by the CCN one by one, until it, partially or wholly, dissolves in a solution droplet. This is a powerful effect, because the saturation vapour pressure over a water-solution surface is less than over pure water, decreasing as the CCN mass increases.

1.2.3 Cloud condensation nuclei

Solid particles play a key role for the formation of clouds. Indeed, without them droplets cannot nucleate in the environmental conditions provided by the atmosphere. Among the huge and varied amount of aerosol particles, only a small subset can serve as a nucleus upon which water vapour condenses to form a droplet. The size of these cloud condensation nuclei is also important: the larger the size, the more readily it is wetted by water; moreover, the greater its solubility, the lower the supersaturation needed to serve as a CCN. As an example, if the environmental supersaturation is of the order of $1\ \%$, a non-soluble CCN needs to be at least $\sim 0.1\ \mu\mathrm{m}$ in radius, whereas a hygroscopic particle can serve as a CCN even if small as $\sim 0.01\ \mu\mathrm{m}$. Usually, CCN are a mixture of soluble and insoluble components.

Worldwide measurements of CCN concentrations have not revealed any systematic latitudinal or seasonal variations. However, near the Earth's surface, continental air masses generally contain larger concentrations than marine air masses. Generally, the concentration decreases at higher altitudes and a daily variation is also registered.

CCN origin from several natural and anthropogenic phenomena. First, it appears that the land acts as a source for CCN. Some of the soil particles and dusts that enter the atmosphere probably serve as CCN, but they do not seem to be a dominant source. On the contrary, forest fires are an important source. CCN may come from marine salts, although their role does not result significant. There appears to be a widespread and probably a fairly uniform source of CCN over both the oceans and the land, whose nature has not been definitely established. A likely candidate is a gas-to-particle conversion triggered by solar radiation, which can produce CCN up to $\sim 10\ \mu\mathrm{m}$ in radius; typical particles of this kind are sulfates from organic sulfures from the ocean. Finally, it is worth noticing that pollutants, e.g. coming from oil combustion or engine emissions, are an increasing source of CCN.

1.3 Droplet growth by condensation

Once droplets are nucleated, the surrounding environment can either sustain droplet growth providing further vapour or force them to decrease their size. In the latter case, a complete evaporation is not the only possibility; indeed, droplets can reach a small stable size, forming atmospheric haze. Here, we are not interested in this situation, but in the development of a precipitating cloud. Thus, we want to understand how nucleated droplets can reach the raindrop size in the short time of half an hour. Droplets are allowed to grow by condensation if

a flux of water molecules coming from the infinity (i.e. the environment) is able to flow through droplet surface. This diffusive process takes place as a vapour gradient is present between the infinity and the external neighbourhood of the surface. Both thermal and vapour diffusion are to be considered at a molecular level. Then, the law of droplet growth by condensation is computed, as presented in section 1.3.1. Here, it is noticed that, if the supersaturation is large enough, after a transient cloud droplets grow at a rate given by the supersaturation. This allows some simplifications leading to the well-known classical Twomey model (section 1.3.2).

1.3.1 Radius evolution

Once formed, droplets begin their path to become raindrops. As already observed, this typically takes less than half an hour in real clouds. The remarkable efficiency of precipitation formation is poorly understood at now. Indeed, since the typical size of a CCN is less than $1\ \mu\mathrm{m}$, droplet radius evolution must cover more than 3 orders of magnitude in order to produce $2\ \mathrm{mm}$-sized raindrops. To tackle this problem, let us continue by following the single-droplet evolution as for nucleation.

After the CCN has been completely covered by water, the vapour molecules keep diffusing on droplet surface and grow the droplet by condensation. The typical time of diffusion over droplet surface is much less than the typical time of condensation and of the smallest turbulent scale in the atmosphere (see [VYG01]). Hence, the detailed characterization of the vapour-field variation over droplet surface is generally avoided, in favour of a mean-field type description. A detailed comparison of the temporal scales (associated with the diffusion of water vapour molecules on droplet surface and with the changes in the ambient conditions related to turbulence) reveals that this approximation is valid for droplets smaller than $20\ \mu\mathrm{m}$ in radius for typical cloud conditions [VYG01]. Mass and energy conservations coupled with the steady diffusion equation over a spherical droplet with radius R give the equation of radius evolution

$$\frac{\mathrm{d}}{\mathrm{d}t}R^2 = 2C_R\left(1 + s - \mathrm{e}^{\frac{c}{R} - \frac{h}{R^3}}\right) = 2C_R\big(s - s_\mathrm{e}(R_0, R)\big) \tag{1.29}$$

where s_e is the equilibrium supersaturation describing the Köhler curve of figure 1.2b, C_R is a function of thermodynamic variables and parameters (see e.g. [PK97]) and h the *hygroscopicity coefficient* (see [CMT08]). When droplets are large enough, the Kelvin term (i.e. the term in c) and the Raoult term (i.e. the term in h) become negligible, and (1.29) is simplified in the more famous radius evolution

$$\frac{\mathrm{d}}{\mathrm{d}t}R^2 = 2C_R s \tag{1.30}$$

Here the growth rate is proportional to the environmental supersaturation.

1.3.2 Twomey model

Supersaturation computation requires the knowledge of the thermodynamic environment surrounding the droplet. This is a very hard information to obtain by *in situ* measurements. On the other hand, a model for the supersaturation evolution requires a characterization of transport and thermodynamics in the atmosphere.

The most simple model for supersaturation evolution in an air parcel rising with velocity w is the well-known *Twomey model* [Two59], which is obtained by explicating the derivative of the mixing ratio in (1.20) and exploiting (1.30). Indeed, if δQ indicates an extensive quantity of the air parcel whose volume and droplet number are δV and δN, respectively, the liquid mixing ratio evolves as

$$\frac{\mathrm{d}}{\mathrm{d}t}r_\mathrm{l} = \frac{\mathrm{d}}{\mathrm{d}t}\left(\frac{\rho_\mathrm{l}}{\rho_\mathrm{a}}\right) = \frac{\mathrm{d}}{\mathrm{d}t}\left(\frac{\delta M_\mathrm{l}}{\delta M_\mathrm{a}}\right) \simeq \frac{1}{\delta M_\mathrm{a}}\frac{\mathrm{d}}{\mathrm{d}t}\delta M_\mathrm{l} = \frac{1}{\rho_\mathrm{a}\delta V}\frac{\mathrm{d}}{\mathrm{d}t}\left(\sum_{i=1}^{\delta N}\rho_\mathrm{w}\frac{4}{3}\pi R_i^3\right) =$$

$$= \frac{4}{3}\pi\frac{\rho_\mathrm{w}}{\rho_\mathrm{a}}\frac{1}{\delta V}\sum_{i=1}^{\delta N}\left(\frac{3}{2}R_i\frac{\mathrm{d}}{\mathrm{d}t}R_i^2\right) = \frac{4}{3}\pi\frac{\rho_\mathrm{w}}{\rho_\mathrm{a}}\frac{1}{\delta V}\sum_{i=1}^{\delta N}\left(\frac{3}{2}R_i\ 2C_R s\right) =$$

$$= 4\pi\frac{\rho_\mathrm{w}}{\rho_\mathrm{a}}C_R s\frac{1}{\delta V}\sum_{i=1}^{\delta N}R_i = 4\pi\frac{\rho_\mathrm{w}}{\rho_\mathrm{a}}C_R s\frac{\delta N}{\delta V}\frac{1}{\delta N}\sum_{i=1}^{\delta N}R_i = 4\pi\frac{\rho_\mathrm{w}}{\rho_\mathrm{a}}C_R n\left\langle R\right\rangle s \quad (1.31)$$

where n is droplet-number density.

The Twomey equation is the linear version of (1.20)

$$\frac{\mathrm{d}}{\mathrm{d}t}s = G_s w s - a_s b_s\frac{\mathrm{d}}{\mathrm{d}t}r_\mathrm{l} \quad (1.32)$$

where the derivative of the mixing ratio is substituted by (1.31) and the *absorption time* $\tau_s = \rho_\mathrm{a}/(4\pi a_s b_s C_R \rho_\mathrm{w} n\left\langle R\right\rangle)$ is considered:

$$\frac{\mathrm{d}}{\mathrm{d}t}s = G_s w s - \frac{s}{\tau_s} \quad (1.33)$$

The term of adiabatic cooling, $G_s w$, describes the decrease in temperature and pressure due to vertical ascent. The combination of these two effects results in a net increase of s with the height. The term $-s/\tau_s$ is due to the phase change of water and vapour onto droplet surface. This directly modifies the vapour content inside the volume and also exchange latent heat thus modifying the temperature. The absorption time gives an idea on how much supersaturation dynamics is affected by droplets evolution: the larger τ_s, the more time is necessary to the environment to feel droplet growth.

Chapter 2

Turbulent model for droplet growth

The formation of a warm vertical cloud is classically described by the evolution of microscopic droplets, as presented in chapter 1. Droplets start to nucleate around solid particles in a favourable environment (i.e. for positive supersaturation in the absence of solute effect). Then, if the available vapour is sufficient, they grow by condensation. Once their size is large enough, their terminal velocity is no more negligible and they start to collide with both slower and faster droplets. The resulting growth by coalescence is explosive and eventually a precipitation can occur. This simple description is able to capture the basic mechanisms behind the first development of the cloud.

Nevertheless, the classical description leaves some problems open and also leads to a serious inconsistency. Indeed, the prediction for the condensational growth states that smaller droplets grow faster than larger droplets. As a result, during the condensation stage the droplet population becomes more and more homogeneous, while the growth slows down. On the one hand, this slowing process cannot lead to a precipitation in reasonable times; on the other hand, the explosive process ensured by collisions cannot occur, if all the droplets share the same size (i.e. the same terminal velocity). Therefore, the size distribution (known as *size spectrum*) during the condensation stage must broaden in some way. Such a contradiction with the classical prediction is confirmed by experimental observations in clouds, where a broader size spectrum is detected.

To solve this problem, sometimes referred to as the *bottleneck of condensation*, many different models have been proposed, either improving the classical model with the inclusion of neglected effects or rephrasing it with a different approach. For the time being, no univocal explanation has been provided. Partial justifications are based on entrainment with dry air, on the role of giant condensation nuclei or on the local effects of turbulence.

A different approach is adopted in a series of recent works [CFMS05; CMT08; CMT09; CMTS07; LSTep], where a basic ingredient, previously not taken into account, is added, i.e. turbulence in the whole cloud. Rather than following the evolution of a small air parcel and the fluctuations inside it, the focus is on a large part of the cloud. The effects of global turbulent motions are considered. The idea is that droplets get to know very different environmental conditions in short times, so that very different sizes are present in droplet population.

Moreover, the aim of this model is also to investigate the role of turbulence for droplet nucleation. Here, the question is on whether it is really necessary to invoke the presence of giant nuclei or, on the contrary, the effect of large fluctuations acts in their place. In the latter case turbulence reshapes the distribution of condensation nuclei.

This chapter is devoted to the formulation of the complete version of the global turbulent model. Before dealing with it, open problems in cloud formation and proposed explanations are briefly reviewed in section 2.1. In section 2.2 the model is presented as a generalization of the Twomey model, where both curvature and solute effects are included and the surrounding environment is described by turbulent fields. Some results from the first applications of this model (without considering the nucleation stage) are given in section 2.3. The results of the numerical analysis of the (almost) complete model are the subject of chapter 3.

2.1 Open problems

As anticipated, although the basic mechanisms of droplet growth are described by the the classical approach, some phenomena remain not completely understood.

Concerning nucleation, in section 1.2.3 we reported that recently much attention has been devoted to CCN. In particular, the attention is addressed to their interaction with human activities. From a global viewpoint, the impact of anthropogenic CCN on climate could be relevant. Locally, there is a great interest in inducing artificial precipitations. The composition of CCN populations is the subject of a large number of studies and observations. However, despite the elementary physics behind the nucleation process, CCN effectiveness for droplet formation can depend on the properties of the environment in a not-trivial way. E.g. the role of turbulence is not yet investigated enough. Indeed, a classical approach requires the availability of CCN larger than a particular size (the one at which the corresponding Köhler curve lies below the environmental supersaturation), but turbulent fluctuations locally provide large amounts of vapour, allowing nucleation on smaller particles. The quantification of this effect is one

of the aims of the present work.

As discussed above, during the condensation stage the *size spectrum* (i.e. the probability distribution of the square radii) must encounter some spreading mechanisms not considered in the classical picture. Since our model was initially motivated by this specific problem, we deal with it in more details in section 2.1.1.

The successive collection stage is still a field to be deeply explored. It is also the most difficult to handle, because it involves many different mechanisms. In fact, the description of collection uses an effective approach, rather than trying to explain how each mechanism enters the collection kernel and the collection efficiency. In a first approximation, the probability of collision is a function of the cross section and the relative velocity, but can be enhanced by wake and electricity effects. In the former case, the wake of a large droplet attracts smaller droplets, so that back-collisions are possible. In the latter case, the electrostatic charge present on the polarized droplets favours collisions. Moreover, turbulence motions can strongly affect the collision efficiency. It is worth noticing that the terminal velocity is different in turbulent conditions, in a non-trivial way [MA08; MAMOep]. Finally, inelastic collisions occur. Then, the coalescence efficiency is even more delicate to compute. The model presented here does not treat this stage. The study of collisions will be the natural successive step.

2.1.1 Spectrum broadening

Let us come back to droplet growth by condensation. Droplets have been activated from a CCN population whose size spectrum is given by a distribution $P_0(R_0^2)$. Then, they start to grow according to the evolution law (1.29), i.e.

$$\frac{\mathrm{d}}{\mathrm{d}t}R^2 = 2C_R\big(s - s_{\mathrm{e}}(R_0, R)\big)$$

As droplets becomes large enough (say, $R \gtrsim 1\ \mu\mathrm{m}$), the effects of curvature and hygroscopicity become negligible and their growth depends only on the environmental supersaturation. Thus, the radius grows according to

$$\frac{\mathrm{d}}{\mathrm{d}t}R = C_R\frac{s}{R}$$

from which it is evident that, for a given positive constant value of s, smaller droplets grow faster than larger ones. Quickly, if the supersaturation they experience is the same, the droplets converge to the same size and their radius continues to grows as $\sqrt{t}$. In this way, the raindrop size would be reached after some weeks, while in real clouds the complete process takes some hours.

Actually, after some minutes condensation becomes a subleading effect, overtaken by collection. Indeed, a falling droplet which intercepts smaller droplets on

its path grows faster than t, because the growth rate linearly depends on its terminal velocity and on its cross section, both proportional to R^2. However, since the collection efficiency is proportional to the relative velocity between droplets, only a broad size spectrum is able to start up an efficient collection.

On the contrary, the droplet population inherited from the condensation stage is homogeneous, so that no gravitational collisions are possible. This follows from the classical prediction for the evolution of the size spectrum during the condensation stage. Integrating (1.30) leads to

$$R^2(t) = R_0^2 + 2C_R \int_0^t s\big(\boldsymbol{X}(t')\big)\,\mathrm{d}t' \tag{2.1}$$

where the integral on the r.h.s. is meant along droplet trajectory. However, in the classical approach droplets are assumed to grow in a closed air parcel where the supersaturation field is uniform. Thus, the integral in (2.1) is the same for each droplet and reduced to an integral along the air-parcel trajectory. Therefore, the initial square radius of each droplet undergoes the same growth and the initial distribution translates in time:

$$P_t\big(R^2(t)\big) = P_t\left(R_0^2 + 2C_R \int_0^t s(t')\,\mathrm{d}t'\right) = P_0\left(R^2(t) - 2C_R \int_0^t s(t')\,\mathrm{d}t'\right)$$

The standard deviation does not evolve in time and the size spectrum becomes sharper and sharper as the square radius grows.

The incompatibility of this prediction with the successive formation of rain drops has been a focal point of cloud physics research for several decades, as discussed in [CA89; PK97; Rog89]. Several series of measurements in real clouds have been carried out in the last 40 years, confirming that the classic prediction is in contrast with the experimental observations, where a relevant *spectrum broadening* is detected. Broad spectra have been observed both near the cloud boundaries and in the inner cloud core, in warm clouds as well as in cold clouds (see [BC01; LTC00] for recent experimental campaigns). As a result, the collection stage can take place and the spectrum becomes bimodal, with the transfer of almost the whole water mass from the large number of smaller droplets to a small number of larger collector droplets (as showed in figure 2.1b).

2.1.2 Relevant results in literature

The failure of the classical model is essentially due to the mean-field type description: if droplets feel the same environmental conditions, there is no way for them to know different growths. However, a theoretical understanding of how broad spectra can be obtained by condensation is still lacking. This striking

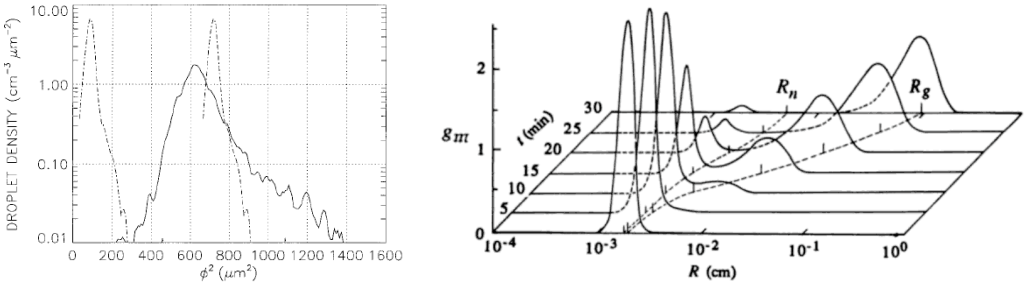

(a) Observed spectrum broadening **(b)** Schematic spectrum evolution

Figure 2.1: Droplet-size spectrum broadens in time (or, with the height, if an updraft is followed), as observed by measurements in warm cumuli. First results in this direction can be found in [LP77]. Figure (a) shows more recent results from [BC01] in the adiabatic cloud core. The dot-dashed line on the left refers to the initial spectrum at $z_0 = 715$ m, the one on the right to the classical spectrum at $z = 2188$ m; the solid line represents the observed spectrum at the latter height. Figure (b), from [BR74], shows the spectrum evolution as a result of stochastic collection. R_n and R_g are the mean radius of the number distribution and the mass distribution, respectively. The distribution becomes bimodal and almost the whole water mass is captured by larger droplets, although smaller droplets outnumber them.

feature of real clouds, that allows for the fast initiation of gravitational collisions, droplet coalescence and therefore rain formation, has not been univocally explained. Partial justifications are based on different mechanisms, acting in different regions of the cloud.

The entrainment of dry air from the outside of the cloud (in particular from above) causes evaporation, spreading droplet spectra, especially in the peripheral regions of the cloud [Tel96].

The role of the shape of the initial distribution has also been investigated: exceptionally broad initial CCN spectra are able to activate collisions, in particular if giant ($1\ \mu\mathrm{m} < R_0 < 10\ \mu\mathrm{m}$) and ultra-giant ($R_0 > 10\ \mu\mathrm{m}$) condensation nuclei are present citesegal04,johnson82,blyth03. For example, the addition of a small amount of giant CCN (e.g. 1 particle in 10^6) can transform a nonprecipitating stratocumulus cloud into a precipitating one [WH06].

The presence of the droplets themselves has been proposed to be source for local fluctuations of the turbulent kinetic energy [JM05] and of the vapour field [SRCV98], thus providing fluctuations in the environmental conditions.

Moreover, since a droplet growing by condensation is warmer than the environment, it loses heat by radiation and the saturation vapour pressure above its surface is lower. Thus, it grows faster. This effect is greater for larger droplets

and radiative broadening of spectra occurs.

Of course, in a turbulent medium, gravitation is not the only source of collisions. The collision kernel receives substantial contributions coming from turbulence [FFS02; GDHSFJ05]. The effect of turbulence can enhance droplet density by means of the well-known preferential concentration of inertial particles [LSWS07; SC97]. Caustic events are another mechanism of enhancement of collision efficiency [WMB06].

Hence, turbulence results as a key aspect for the explanation of the condensation-collection gap. Surprisingly, the first direct numerical simulations of a turbulent flow in an ascending air parcel [VYBG02; VYG01] have shown that droplet spectra are more narrow than without turbulence. Our idea is that the air parcel is not a proper tool and turbulent fluctuations at larger scales cannot be neglected.

2.2 Generalization of the Twomey model

In section 2.1.2 several effects involved in the transition from condensation to collection are presented. However, a complete explanation is still missing. Two crucial points have been highlighted: the mean-field type description does not provide any fluctuation of supersaturation; the focus on an ascending small air parcel does not provide enough fluctuations either. The starting point of our approach is the remark that droplets are able to span the whole cloud in some minutes thanks to turbulent motions (e.g. less than 10 minutes are needed to cover $500\ \mathrm{m}$ in an updraft of $1\ \mathrm{m/s}$). Moreover, turbulence causes fast separations between droplets. Thus, in the same time spent during their condensational growth, two initially close droplets reach very different regions of the clouds, experiencing very different environmental conditions, both along their own paths and one with respect to the other. As a consequence, we cannot neglect turbulence and we cannot limit the investigation to a small part of the cloud where droplets are supposed to be confined. For these reasons, we name our model as a *global turbulent model*.

Clearly, our model has not the aim of giving a complete explanation of spectrum broadening. Indeed, it does not include many of the effects presented in 2.1.2, which partially contribute to this phenomenon. The idea is to define a simple model in order to identify other possible mechanisms. Then, the model can be complicated *ad libitum* by considering previously neglected effects one by one. As a first stage only condensation was considered and different kinds of turbulent statistics analysed: isotropic 2D turbulence in [CFMS05] (section 2.3.1), Bolgiano convective 2D turbulence in [CMTS07] (section 2.3.2) and isotropic 3D turbulence in [LSTep] (section 2.3.3). Then, in [CMT08; CMT09] also the

nucleation stage has been included (chapter 3). The latter case is the subject of this Ph.D. thesis. Moreover, we studied the role of droplet feedback on vapour.

For the sake of simplicity, although the model was improved step by step, we prefer to present the complete, latest version before the results of the simple special cases. We generalize the Twomey model in two directions: we include both the curvature and the solute effects in the Twomey equation for the supersaturation (section 2.2.1) and we consider the supersaturation as a turbulent field ruled by a turbulent version of the Twomey equation (section 2.2.2).

2.2.1 Curvature and solute effects

Let us follow the same procedure as that presented in 1.3.2 for the derivation of the Twomey model, now without neglecting nonlinear terms in (1.20) and the equilibrium supersaturation in (1.29).

The former equation reads

$$\frac{\mathrm{d}}{\mathrm{d}t}s = G_s w(1+s) - a_s(b_s+s)\frac{\mathrm{d}}{\mathrm{d}t}r_\mathrm{l} \tag{2.2}$$

Again, the time derivative of the mixing ratio has to be made explicit in order to close the model. Writing the mixing ratio in terms of the mass δM_l of liquid water contained in the air parcel, $\frac{\mathrm{d}}{\mathrm{d}t}r_\mathrm{l}$ can be expressed as the time derivative of droplet radii. Standard models for condensation stage do not take into account either curvature or solute effects, so that droplets grow at a rate proportional to s. Thus, the absorption term becomes proportional to $n\left\langle R\right\rangle s = s/\tau_s$, where n and $\left\langle R\right\rangle$ are the number density and the mean radius of droplets in the air parcel. This was essentially the Twomey framework.

Since the model presented here also include nucleation, allowing droplets to nucleate from a hygroscopic CCN and to release it again in case of complete evaporation, the variation of the liquid mass in the air parcel does not depend on the sole supersaturation, but also on droplet curvature and CCN sizes. The size evolution of the i-th droplet, which is subject to a supersaturation $S_i(t)$, is given by

$$\frac{\mathrm{d}}{\mathrm{d}t}R_i^2 = 2C_R\left(1 + S_i - \mathrm{e}^{\frac{c}{R_i} - \frac{h_i}{R_i^3}}\right) \tag{2.3}$$

where $h_i = h(R_{0i})$ is the hygroscopicity coefficient of the CCN of radius R_{0i} around which the i-th droplet nucleates. The factor between brackets is a dimensionless Lagrangian term, only depending on the trajectory of the i-th droplet. We can recast it in the form $L_i(t)/R_i(t)$, where

$$L_i(t) = \frac{R_i^2}{C_R}\frac{\mathrm{d}}{\mathrm{d}t}R_i \tag{2.4}$$

is the *condensation length* of the i-th droplet. The droplet grows by condensation or slims down by evaporation depending on whether L_i is positive or negative, respectively. Then, (2.3) becomes

$$\frac{\mathrm{d}}{\mathrm{d}t}R_i^2 = 2C_R\frac{L_i}{R_i}$$

Now we are ready to compute the derivative of the liquid mixing ratio of the air parcel. Indicating with δQ the value of an extensive quantity Q computed for the whole air parcel (e.g. the total number δN of droplets in an air parcel with volume δV), we obtain

$$\begin{aligned}\frac{\mathrm{d}}{\mathrm{d}t}r_\mathrm{l} = \frac{\mathrm{d}}{\mathrm{d}t}\left(\frac{\rho_\mathrm{l}}{\rho_\mathrm{a}}\right) = \frac{\mathrm{d}}{\mathrm{d}t}\left(\frac{\delta M_\mathrm{l}}{\delta M_\mathrm{a}}\right) \simeq \frac{1}{\delta M_\mathrm{a}}\frac{\mathrm{d}}{\mathrm{d}t}\delta M_\mathrm{l} = \\ = \frac{1}{\rho_\mathrm{a}\delta V}\frac{\mathrm{d}}{\mathrm{d}t}\left(\sum_{i=1}^{\delta N}\rho_\mathrm{w}\frac{4}{3}\pi R_i^3\right) = \frac{4}{3}\pi\frac{\rho_\mathrm{w}}{\rho_\mathrm{a}}\frac{1}{\delta V}\sum_{i=1}^{\delta N}\left(\frac{3}{2}R_i\frac{\mathrm{d}}{\mathrm{d}t}R_i^2\right) = \\ = \frac{4}{3}\pi\frac{\rho_\mathrm{w}}{\rho_\mathrm{a}}\frac{1}{\delta V}\sum_{i=1}^{\delta N}\left(\frac{3}{2}R_i\ 2C_R\frac{L_i}{R_i}\right) = 4\pi\frac{\rho_\mathrm{w}}{\rho_\mathrm{a}}C_R\frac{1}{\delta V}\sum_{i=1}^{\delta N}L_i = \\ = 4\pi\frac{\rho_\mathrm{w}}{\rho_\mathrm{a}}C_R\frac{\delta L}{\delta V} = 4\pi\frac{\rho_\mathrm{w}}{\rho_\mathrm{a}}C_R\lambda \quad (2.5)\end{aligned}$$

Here

$$\lambda(t) = \frac{\delta L}{\delta V}$$

is the *condensation density* of the air parcel: when on average condensation exceeds evaporation inside the parcel, λ results positive. The Twomey model is recovered if both c and h_i vanish and $S_i = s$ is the same for each droplet. In this case, $L_i = R_i s$ and $\lambda = n\langle R\rangle s$, as reported above.

Finally, let us define the *vapour absorption rate*

$$C_s = 4\pi\frac{\rho_\mathrm{w}}{\rho_\mathrm{a}}a_s C_R$$

and plug (2.5) in (2.2):

$$\frac{\mathrm{d}}{\mathrm{d}t}s = G_s w(1+s) - C_s\lambda(b_s + s) \quad (2.6)$$

The same computation can be carried out for the temperature of the air parcel. In this case, we define the *latent-heat release rate*

$$C_T = 4\pi\frac{\rho_\mathrm{w}}{\rho_\mathrm{a}}a_T C_R = \frac{e_\mathrm{sat}C_s}{\rho_\mathrm{a}L_\mathrm{w}}$$

and plug (2.5) in (1.17):

$$\frac{\mathrm{d}}{\mathrm{d}t}T = -\Gamma_{\mathrm{a}} w + \frac{C_T T_{\mathrm{ref}} \lambda}{b_T + s} \tag{2.7}$$

C_s and C_T account for the rates of vapour absorption and latent-heat release through droplet surfaces, respectively. Indeed, they have the dimensions of a diffusivity.

Notice that no turbulent field is considered until this point: (2.6) and (2.7) refer to the time evolution of the mean supersaturation and the mean temperature of an air parcel, which is moving with velocity w vertically. In updrafts s increases by adiabatic expansion and cooling, but could decrease as soon as droplets inside start to grow feeding on surrounding vapour (and vice versa in downdrafts). A similar behaviour holds for by the temperature, which decreases by adiabatic cooling in updrafts, but could increase as soon as droplets grow by condensation, so releasing latent heat (and vice versa in downdrafts).

To describe the balance between these two effects, it is useful to introduce the dimensionless numbers

$$F_s = -\frac{\text{vapour absorption}}{\text{adiabatic cooling}} = \frac{C_s \lambda (b_s + s)}{G_s w (1 + s)} \tag{2.8}$$

and

$$F_T = -\frac{\text{latent-heat release}}{\text{adiabatic cooling}} = \frac{C_T T_{\mathrm{ref}} \lambda}{G_T w (b_T + s)}$$

When F_s tends to zero, the droplet feedback on vapour is negligible. This occurs for low droplet densities or very small droplets or not enough supersaturated environments. In the Twomey description

$$F_s = \frac{s}{G_s w \tau_s} \sim 1$$

with $s \sim 1\ \%$, $w = 1\ \mathrm{m/s}$ and the absorption time $\tau_s \sim 15\ \mathrm{s}$. Thus, in standard conditions this feedback plays an important role.

2.2.2 Turbulence in a warm cloud

The approach given in section 2.2.1 is still classical. Indeed, the focus is on the evolution of an air parcel of given vertical velocity. Moreover, although both the supersaturation and the mixing ratio evolve in time, they are considered as mean fields. We know from literature that this mean-field type approach is in contrast with the observed broadening of droplet spectra. As reviewed in section 2.1.2, to solve this problem several effects have been included into condensation models. In

particular, it is necessary to consider local fluctuations of vapour density, because droplets need to experience different values of supersaturation in order to allow a non trivial spectrum evolution. [VYBG02; VYG01] showed that considering turbulent fields inside a small portion of the cloud, such as an air parcel, does not result in an appreciable spectrum broadening. As anticipated, the key to explain this failure is to consider turbulent fluctuations in a large part of the cloud. Indeed, particles starting close to each other from an air parcel can span very different regions of the cloud in times of the order of one turnover time.

From a classical point of view the cloud is formed by a high number of air parcels moving inside it, some in updrafts, other in downdrafts. Every parcel has a supersaturation and a temperature which evolve according to (2.6) and (2.7), respectively, where w can be either positive or negative. The basic idea is to consider w as the vertical component of the turbulent velocity field $\boldsymbol{u} = (u, v, w)$ and to leave the Lagrangian approach given by parcel evolution, following the Eulerian behaviour of turbulent fields (here the velocity, the supersaturation and the temperature) in the whole cloud. Thus, the variation of s and T have to be computed with a material derivative along parcel trajectories:

$$\frac{\mathrm{d}}{\mathrm{d}t}s(t) = \partial_t s(\boldsymbol{x}, t) + \boldsymbol{u} \cdot \boldsymbol{\partial} s(\boldsymbol{x}, t)$$
$$\frac{\mathrm{d}}{\mathrm{d}t}T(t) = \partial_t T(\boldsymbol{x}, t) + \boldsymbol{u} \cdot \boldsymbol{\partial} T(\boldsymbol{x}, t)$$

The incompressible ($\boldsymbol{\partial} \cdot \boldsymbol{u} = 0$) velocity field $\boldsymbol{u}(\boldsymbol{x}, t)$ is ruled by the Navier–Stokes equation, where, as customary, the buoyancy term is expressed in terms of the temperature, according to the Boussinesq approximation [KC01]. Adding the diffusion term to the equation for both the supersaturation and the temperature, the complete set of equations reads

$$\begin{cases} \partial_t \boldsymbol{u} + \boldsymbol{u} \cdot \boldsymbol{\partial} \boldsymbol{u} = -\dfrac{1}{\rho_\mathrm{a}} \boldsymbol{\partial} p + \big(1 - \beta(T - T_\mathrm{ref})\big)\boldsymbol{g} + \nu \partial^2 \boldsymbol{u} & (2.9\mathrm{a}) \\ \partial_t s + \boldsymbol{u} \cdot \boldsymbol{\partial} s = G_s w (1 + s) - C_s \lambda (b_s + s) + D \partial^2 s & (2.9\mathrm{b}) \\ \partial_t T + \boldsymbol{u} \cdot \boldsymbol{\partial} T = -\Gamma_\mathrm{a} w + \dfrac{C_T T_\mathrm{ref} \lambda}{b_T + s} + \varkappa \partial^2 T & (2.9\mathrm{c}) \end{cases}$$

where β is the thermal-expansion coefficient of air, $\boldsymbol{g} = (0, 0, -g)$ the gravitational acceleration, ν the kinematic viscosity of air, D the vapour diffusivity and $\varkappa$ the thermal diffusivity.

In equations $(2.9\mathrm{b})$ and $(2.9\mathrm{c})$ λ is now a condensation density field coupling

droplet evolution with the vapour and the temperature fields. Its equation is

$$\lambda(\boldsymbol{x},t) = \frac{1}{\delta V}\sum_{i=1}^{\delta N(\boldsymbol{x},t)} L_i\big(\boldsymbol{X}_i(t),t\big) = \\ = \frac{1}{\delta V}\sum_{i=1}^{\delta N(\boldsymbol{x},t)} R_i(t)\left(1+s\big(\boldsymbol{X}_i(t),t\big) - \mathrm{e}^{\frac{c}{R_i(t)}-\frac{h_i}{R_i^3(t)}}\right) \quad (2.10)$$

where $\delta N(\boldsymbol{x},t)$ is the total number of droplets present at time t inside a small volume δV centred in $\boldsymbol{x}$ and $L_i\big(\boldsymbol{X}_i(t),t\big)$ is the same given by (2.4) provided that it is computed along particle trajectories $\boldsymbol{X}_i(t)$. Hence, in the absorption term C_s gives the absorption rate, whereas λ localizes where either condensation or evaporation occurs.

Clearly, the system is not yet closed, because the condensation density λ depends on droplet evolution, which has to be specified. In the general case we present here, droplets are treated as independent, passive, inertial particles. Since the water density is much larger than the air density, their trajectories can be described by Stokes drag, resulting in the following system

$$\begin{cases} \dfrac{\mathrm{d}}{\mathrm{d}t}\boldsymbol{X}_i(t) = \boldsymbol{U}_i(t) + \sqrt{2D}\boldsymbol{\eta}_i(t) & (2.11\mathrm{a}) \\ \dfrac{\mathrm{d}}{\mathrm{d}t}\boldsymbol{U}_i(t) = \dfrac{\boldsymbol{u}\big(\boldsymbol{X}_i(t),t\big) - \boldsymbol{U}_i(t)}{\tau_i(t)} + \boldsymbol{g} & (2.11\mathrm{b}) \end{cases}$$

where $\boldsymbol{\eta}_i$ are independent three-dimensional white noises and

$$\tau_i(t) = \frac{R_i^2(t)}{3\nu}\frac{\rho_\mathrm{a}+2\rho_\mathrm{w}}{3\rho_\mathrm{a}} \quad (2.12)$$

is the *Stokes time* of the i-th particle. The radius is given by (2.3).

2.2.3 Complete model

The model system is now closed. Let us express it in a more compact form. Indeed, if a thermal vertical gradient G_T is present, we can split the temperature field into three contributions:

$$T(\boldsymbol{x},t) = T_\mathrm{ref}\big(1+\vartheta(\boldsymbol{x},t)\big) - G_T(z-z_\mathrm{ref}) \quad (2.13)$$

where the *thermal fluctuation* field $\vartheta(\boldsymbol{x},t)$ is a dimensionless and zero-mean field. Substituting (2.13) in $(2.9\mathrm{c})$ and dividing by T_ref leads to

$$\partial_t\vartheta + \boldsymbol{u}\cdot\boldsymbol{\partial}\vartheta = -\frac{1}{T_\mathrm{ref}}(\Gamma_\mathrm{a}-G_T)w + \frac{C_T\lambda}{b_T+s} + \varkappa\partial^2\vartheta \quad (2.14)$$

To simplify the notation we rename $C_T = C_\vartheta$ and $b_T = b_\vartheta$ and define the *cooling lapse rate*

$$G_\vartheta = \frac{1}{T_{\mathrm{ref}}}(\Gamma_{\mathrm{a}} - G_T)$$

which is positive if the dry adiabatic cooling prevails against the environmental stratification (as in real clouds).

Finally, it is useful to take the curl of the Navier–Stokes equation and express it in terms of the *vorticity* field $\boldsymbol{\omega} = \boldsymbol{\partial} \times \boldsymbol{u}$. The buoyancy term can be recast as

$$\begin{aligned}\boldsymbol{\partial} \times \big(1 - \beta(T - T_{\mathrm{ref}})\big)\boldsymbol{g} &= \beta \boldsymbol{g} \times \boldsymbol{\partial} T = \\ &= \beta \boldsymbol{g} \times \boldsymbol{\partial}\big(T_{\mathrm{ref}}(1+\vartheta) - G_T(z - z_{\mathrm{ref}})\big) = \beta \boldsymbol{g} \times \boldsymbol{\partial}(\vartheta T_{\mathrm{ref}}) = \boldsymbol{g} \times \boldsymbol{\partial}\vartheta\end{aligned}$$

if the thermal-expansion coefficient can be regarded as a constant and expressed in the usual form $\beta = 1/T_{\mathrm{ref}}$ for an ideal gas such as air. Incompressibility is guaranteed by the continuity equation

$$\boldsymbol{\partial} \cdot \boldsymbol{\omega} = 0$$

Then, the complete closed version of our model is given by the following system

$$\begin{cases} \partial_t \boldsymbol{\omega} + \boldsymbol{u} \cdot \boldsymbol{\partial}\boldsymbol{\omega} = \boldsymbol{\omega} \cdot \boldsymbol{\partial}\boldsymbol{u} + \boldsymbol{g} \times \boldsymbol{\partial}\vartheta + \nu \partial^2 \boldsymbol{\omega} & \text{(2.15a)} \\ \partial_t s + \boldsymbol{u} \cdot \boldsymbol{\partial} s = G_s w(1+s) - C_s \lambda (b_s + s) + D\partial^2 s & \text{(2.15b)} \\ \partial_t \vartheta + \boldsymbol{u} \cdot \boldsymbol{\partial}\vartheta = -G_\vartheta w + \dfrac{C_\vartheta \lambda}{b_\vartheta + s} + \varkappa \partial^2 \vartheta & \text{(2.15c)} \\ \dfrac{\mathrm{d}}{\mathrm{d}t}\boldsymbol{X}_i(t) = \boldsymbol{U}_i(t) + \sqrt{2D}\boldsymbol{\eta}_i(t) \qquad i = 1, N & \text{(2.15d)} \\ \dfrac{\mathrm{d}}{\mathrm{d}t}\boldsymbol{U}_i(t) = \dfrac{\boldsymbol{u}\big(\boldsymbol{X}_i(t), t\big) - \boldsymbol{U}_i(t)}{\tau_i(t)} + \boldsymbol{g} & \text{(2.15e)} \\ \dfrac{\mathrm{d}}{\mathrm{d}t}R_i^2(t) = 2C_R \left(1 + s\big(\boldsymbol{X}_i(t), t\big) - \mathrm{e}^{\frac{c}{R_i(t)} - \frac{h_i}{R_i^3(t)}}\right) \qquad R_i(t) \geqslant R_{0i} & \text{(2.15f)} \end{cases}$$

where $\lambda(\boldsymbol{x}, t)$ is given by (2.10) and $\tau_i(t)$ by (2.12), both depending on particle evolution.

The field λ represents the coupling between the Lagrangian and the Eulerian dynamics; it is the *droplet feedback* on the environment due to condensation/evaporation process. While C_ϑ and C_s account for the time rate of this process and can be regarded as constants, λ is a condensation density, i.e. an

intensive quantity telling us where condensation occurs: positive λ signal the regions where a mean droplet growth is registered, whereas regions at $\lambda = 0$ are at equilibrium on average.

An important remark about model (2.15) concerns the evolution of the N particles. The initial size is the size of the CCN around which each droplet can nucleate. Once the i-th particle is activated, the radius follows $(2.15\mathrm{f})$ as long as it does not reach the CCN radius R_{0i} again. In the latter case, R_i remains fixed to R_{0i} until a new nucleation occurs. This means that a totally evaporated droplet does not disappear from the cloud, but releases its own CCN, which is free to continue its evolution and eventually to start up a new nucleation process.

Obviously, model (2.15) is not able to include all the effects characterizing a warm cumulus. In particular, in moist conditions the buoyancy term does not depend only on the temperature gradients, but also on the vapour field, as reported in [Ste05]. Moreover, it is important to remember that collisions between droplets are not allowed by the model. Thus, the description is valid as far as droplets do not reach the size above which collection is the leading mechanism.

2.2.4 Numerical constraints

System (2.15) is strongly coupled and nonlinear. If we want to investigate turbulent conditions, a numerical integration is needed and some limitations cannot be avoided.

In particular, the discretization of the volume and computational constraints limit the number of available scales. To give an order of magnitude, with 1024 nodes per side, the integration on a two-dimensional domain is accessible with multiprocessor clusters, whereas on a three-dimensional domain a supercomputer is required. Now, a choice is needed concerning the largest (or, which is the same, the smallest) scale we would describe. If we want to study the microscales, the integration box should be smaller than a air parcel. Since our model wants to investigate the whole cloud (or a large part of it), the largest scale L should be of the order of $1\ \mathrm{km}$. As a consequence, the smallest scale we describe is of the order of $1\ \mathrm{m}$. The focus on global turbulence implies the loss of the details of the smaller scales. Below $1\ \mathrm{m}$ a classical description is assumed.

A further constraint is on the total number of droplets. Droplet number density $n \sim 10^7 \div 10^8\ \mathrm{m}^{-3}$ in real clouds is clearly far from any computational capacity if the focus is moved to large scales. Indeed, it would require the seeding of each grid cell with 10^8 CCN! On the other hand, this number is already larger than the maximum allowed in our computer facilities (for human integration time, of course). However, inside the grid cell the fields are smooth and there is no reason to improve the statistics here. Therefore, each cell is seeded with only few CCN, at least one on average. Thus, each droplet is representative of a larger

number of particles.

It is worth noticing that we did not integrate the complete model (2.15), but only some simplified versions. The idea is to consider different effects one by one in order to identify their contributions.

2.3 Turbulent models for condensation

The guiding idea of our work is that the dramatic fluctuations experienced by droplets inside cloud turbulence may justify the significant broadening of size distributions described in section 2.1.1. In order to verify this general idea we performed direct numerical simulations (DNS) in different settings and highlighted the presence of a robust mechanism for the formation of broad size spectra, i.e. the correlation between droplet trajectories and the fluctuating vapour field.

Before dealing with a deeper numerical analysis of our most recent results, where nucleation is considered, let us review the first works where simplified versions of model (2.15) were proposed and integrated. The common feature of the models reported in [CFMS05; CMTS07; LSTep] is that only condensation is considered. This is a remarkable difference with respect to our recent improvements. Indeed, if a droplet is subjected to a total evaporation, in the latter case it releases its own CCN, which remains free to move in the cloud until a new nucleation occurs. In the first model presented below, a complete evaporation causes the disappearance of the particle from the cloud. This unphysical feature was justified by the focus turned to the condensation range of sizes. As a consequence, the equilibrium supersaturation given by the Kelvin and the Raoult terms is neglected.

The main differences between the three models presented in the following are in the dimensionality (two dimensions in [CFMS05; CMTS07] and three dimensions in [LSTep]) and in the kind of turbulence considered (homogeneous isotropic turbulence in [CFMS05; LSTep] and thermal-convective turbulence in [CMTS07]). However, also other details are different and in the last case a different approach is provided. In all these three cases nonlinear terms in s are neglected, because $s \sim 1\ \%$.

2.3.1 Homogeneous isotropic 2D turbulence

The first model embracing the global turbulent approach was proposed by [CFMS05] in two dimensions, neglecting buoyancy and droplet back reaction on

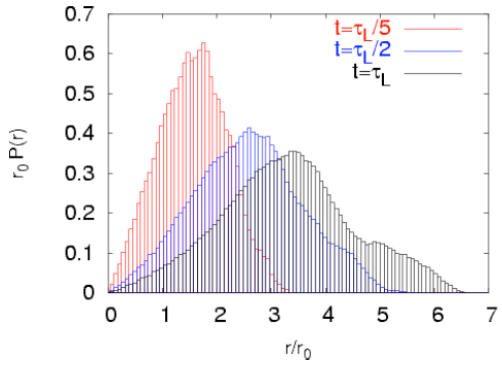

Figure 2.2: Droplet-size spectrum broadens in time. This spectrum evolution was obtained in [CFMS05] by pseudo-spectral DNS of model equations (2.16). No buoyancy and no droplet-vapour interaction are taken into account. The particles are initially monodispersed with radius $R_0 = 5\ \mu\mathrm{m}$ and positioned at random. After one large-eddy turnover time, about $40\ \%$ of droplets reach a size of $20\ \mu\mathrm{m}$.

the vapour field. The model system is reduced to

$$\begin{cases} \partial_t \omega + \boldsymbol{u} \cdot \boldsymbol{\partial} \omega = f_\omega + \nu \partial^2 \omega & (2.16a) \\ \partial_t s + \boldsymbol{u} \cdot \boldsymbol{\partial} s = G_s w + D \partial^2 s & (2.16b) \\ \dfrac{\mathrm{d}}{\mathrm{d}t} \boldsymbol{X}_i(t) = \boldsymbol{U}_i(t) + \sqrt{2D}\boldsymbol{\eta}_i(t) & (2.16c) \\ \dfrac{\mathrm{d}}{\mathrm{d}t} \boldsymbol{U}_i(t) = \dfrac{\boldsymbol{u}\big(\boldsymbol{X}_i(t), t\big) - \boldsymbol{U}_i(t)}{\tau_i(t)} + \boldsymbol{g} & (2.16d) \\ \dfrac{\mathrm{d}}{\mathrm{d}t} R_i^2(t) = 2C_R s\big(\boldsymbol{X}_i(t), t\big) & (2.16e) \end{cases}$$

where f_ω is random forcing. This framework finally results in a homogeneous isotropic scheme that holds for adiabatic cloud cores at spatial scales up to around $100\ \mathrm{m}$, where turbulent mixing is more important than stratification. As mentioned above, the focus is on the large scales of the problem. The spatial scales from $100\ \mathrm{m}$ down to roughly $10\ \mathrm{cm}$ are resolved on a two-dimensional 1024×1024 grid. For smaller scales the turbulent fields were basically smooth.

In this large volume, the study follows the trajectories and radii of thousands of droplets, initially put at random with uniform probability in the volume. Here, the droplet density is small and the sink of water vapour onto droplet surface is basically negligible (and this is the reason why the term in λ is removed).

The main result of this set of simulations is that a remarkable broadening of size distribution is found, as shown in figure 2.2. After one *large-eddy turnover time* τ_L (the typical time spent by a fluid particle to span the largest eddy), about

$40\ \%$ of the total population has reached the threshold size for the beginning of collisions.

Besides, it is observed that, after a small fraction of the turnover time, droplets segregate in moist regions. Indeed, droplets dwelling for long enough in a dry region evaporate completely, leaving dry regions void of particles. The persistence of droplets in regions with the same vapour content is due to correlations coming from turbulence, as both are advected by the same velocity field. Of course, segregation can be observed only in the case where correlations of droplet trajectories with the (negative) value of supersaturation last longer than the time needed for droplets to evaporate. Therefore, when droplets become large enough, they need such a long time to completely evaporate that they manage to escape from the dry region and segregation disappears. This happens at about one turnover time.

This effect suggested the presence of long-lasting correlations between droplet trajectories and supersaturation values. A detailed analysis of the statistics reveals that correlations are actually active, thus explaining the observed remarkable broadening of size spectrum. Indeed, droplet population can be roughly divided in two parts. Some droplets are initially placed at random in a moist region and remain correlated to high values of supersaturation, thus growing fast. Other droplets, correlated to less moist regions, grow slower. At the very bottom we find droplets correlated to very dry regions that, as already discussed above, disappear. This intuitively justifies the observed spreading of size distributions.

Correlations are also responsible for a mean growth of droplet even in the presence of a zero-mean supersaturation. Indeed, surviving droplets do not sample the volume at random, but are more probably located in the moist regions. In other words the Lagrangian average of the supersaturation is higher than the Eulerian one. It is worth noticing that broad size distributions are observed also at local level, so that large and small droplets turn out to be close together.

2.3.2 Convective 2D turbulence

The real dynamics of cloud formation is of course more complex than what described above. In particular, convection is a key point of the large-scale atmospheric circulation. The general picture of cloud formation is that cloud condensation nuclei are introduced inside the cloud from below. After being activated, they grow as cloud droplets while rising toward the top of the cloud. In the case of appropriate conditions, droplets might grow enough during the updraft condensation and, once arrived around the top, might begin their fall. In this case, the successive collection stage takes place during the fall and the cloud might precipitate.

In order to check the robustness of the qualitative mechanism described

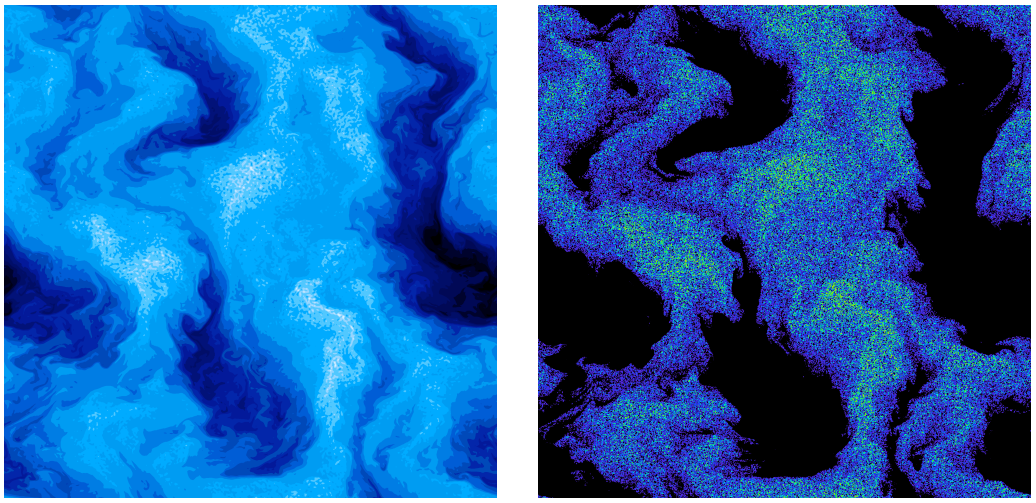

(a) Supersaturation **(b)** Absorption frequency

Figure 2.3: A strong correlation between vapour field (left) and droplet trajectories (right) is present. Figures (a) and (b) show the snapshots of the supersaturation and the absorption frequency fields, respectively. The latter field, $1/\tau_s(\boldsymbol{x},t) \propto \sum_i^{\delta N(\boldsymbol{x},t)} R_i(t)$, signals where and how large droplets are. The two snapshots from [CMTS07] are taken at the same time.

in [CFMS05], in [CMTS07] we consider a more detailed version of the model, restoring the buoyancy term and and allowing droplet feedback on vapour (but neglecting droplet feedback on temperature fluctuations). Since in [CFMS05] it was found that differences between spectra of inertial and tracer droplets are not appreciable, we consider them as tracers. Now, model system reads

$$\begin{cases} \partial_t \omega + \boldsymbol{u}\cdot\boldsymbol{\partial}\omega = -g\partial_x \vartheta + \nu\partial^2\omega & \text{(2.17a)} \\ \partial_t s + \boldsymbol{u}\cdot\boldsymbol{\partial} s = G_s w - \dfrac{s}{\tau_s} + D\partial^2 s & \text{(2.17b)} \\ \partial_t \vartheta + \boldsymbol{u}\cdot\boldsymbol{\partial}\vartheta = -G_\vartheta w + \varkappa\partial^2\vartheta & \text{(2.17c)} \\ \dfrac{\mathrm{d}}{\mathrm{d}t}\boldsymbol{X}_i(t) = \boldsymbol{u}\big(\boldsymbol{X}_i(t),t\big) + \sqrt{2D}\boldsymbol{\eta}_i(t) & \text{(2.17d)} \\ \dfrac{\mathrm{d}}{\mathrm{d}t}R_i^2(t) = 2C_R s\big(\boldsymbol{X}_i(t),t\big) & \text{(2.17e)} \end{cases}$$

where $s/\tau_s(\boldsymbol{x},t)$ is the simplified version of absorption term when neither the Kelvin nor the Raoult contributions are taken into account. Despite the same form as in the Twomey equation, here the *absorption frequency* $1/\tau_s$ is a field coupling Lagrangian droplet evolution with Eulerian vapour field. While s is a

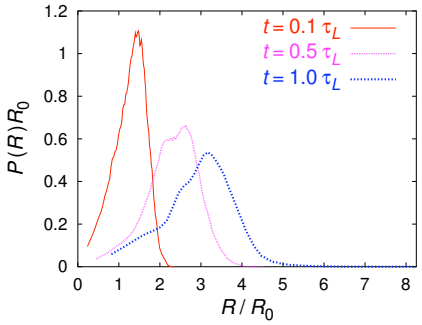

(a) Spectra with droplet feedback

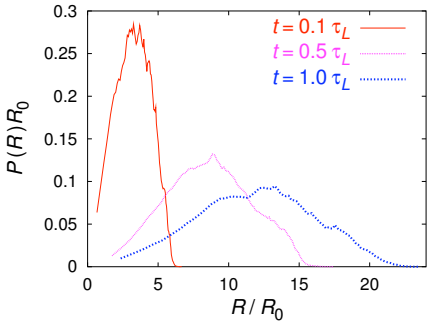

(b) Spectra without droplet feedback

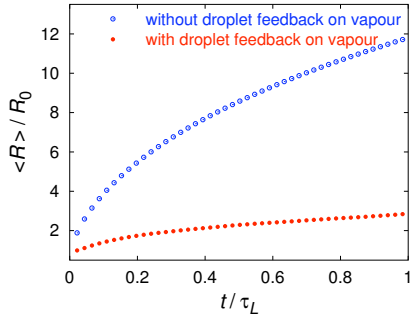

(c) Square radius growth

Figure 2.4: Droplet-size spectra broaden in time (top) and the mean square radius grows despite the undersaturated environment (bottom). Both behaviours are still present, though reduced, also when droplet feedback is taken into account and convective turbulence is considered. Droplet-spectrum evolutions are obtained in [CMTS07] by DNS of condensation stage in the Bolgiano convective 2D regime for the cases of accounted (figure 2.4a) and neglected (figure 2.4b) feedback of droplets on vapour. In figure 2.4c the time evolution of the mean value of the droplet size is represented by filled red and open blue circles for the cases where droplet-vapour interaction is considered or neglected, respectively. The population of droplets is initially monodispersed with radius $R_0 = 4$ µm. The feedback of droplets on vapour slows down the broadening and the mean growth of the size distribution. The result without droplet feedback on vapour gives maximum radii of $85 \div 90$ µm with average 50 µm, while the result accounting for the feedback gives a more reasonable maximum size of $20 \div 22$ µm and average size of 12 µm.

passive scalar, temperature fluctuations are active on the velocity: the resulting convective regime is the two-dimensional *Bolgiano regime* [Bol59].

The main conclusion of this work is that, despite the completely different statistical regime, the qualitative mechanism of correlation and segregation holds

also in this case, as showed in figure 2.3. This is a remarkable feature of the result, showing that, though with different quantitative settings, the identified spreading mechanism could hold in general conditions.

By accounting for the loss of water vapour onto droplet surface, we obtain an expected slowing down of condensational growth and spectrum broadening (see figure 2.4). Indeed, we consider here the fact that droplets grow absorbing vapour from the surrounding, thus providing a drier and drier environment for their own growth. The final expectation on spectrum broadening results less optimistic and more reasonable for typical cloud conditions.

In this framework, the initial condition for the vapour field is obtained as the stationary state achieved by equations $(2.17\mathrm{a})$, $(2.17\mathrm{b})$ and $(2.17\mathrm{c})$. However, with the initial activation of droplets the stationary state is lost, in favour of a decaying dynamics. Roughly speaking, droplets in moist regions absorb vapour whose loss is not compensated by droplet evaporation, because after a while droplets in dry regions evaporate completely and disappear (giving the same segregation phenomenology observed for the non-convective case). The net effect is that the environment becomes on average undersaturated. The mean radius growth shown in figure 2.4c is thus even more remarkable, because it lasts despite the mean undersaturation.

2.3.3 Homogeneous isotropic 3D turbulence

Recently, [LSTep] approached the global turbulent model with a slightly different viewpoint. There, the idea is to describe the effects of the strong turbulent fluctuations on condensation by focusing on small clouds and increasing their height. In this framework, a series of three-dimensional DNS was performed. No buoyancy is considered. Model equations are:

$$\begin{cases} \partial_t \boldsymbol{\omega} + \boldsymbol{u} \cdot \boldsymbol{\partial} \boldsymbol{\omega} = \boldsymbol{\omega} \cdot \boldsymbol{\partial} \boldsymbol{u} + \boldsymbol{f}_{\boldsymbol{\omega}} + \nu \partial^2 \boldsymbol{\omega} & (2.18\mathrm{a}) \\ \partial_t s + \boldsymbol{u} \cdot \boldsymbol{\partial} s = G_s w - \dfrac{s}{\tau_s} + D \partial^2 s & (2.18\mathrm{b}) \\ \dfrac{\mathrm{d}}{\mathrm{d}t} \boldsymbol{X}_i(t) = \boldsymbol{U}_i(t) + \sqrt{2D} \boldsymbol{\eta}_i(t) & (2.18\mathrm{c}) \\ \dfrac{\mathrm{d}}{\mathrm{d}t} \boldsymbol{U}_i(t) = \dfrac{\boldsymbol{u}\big(\boldsymbol{X}_i(t), t\big) - \boldsymbol{U}_i(t)}{\tau_i(t)} + \boldsymbol{g} & (2.18\mathrm{d}) \\ \dfrac{\mathrm{d}}{\mathrm{d}t} R_i^2(t) = 2 C_R s\big(\boldsymbol{X}_i(t), t\big) & (2.18\mathrm{e}) \end{cases}$$

Different cloud heights are considered, thus allowing to draw a trend of the size-distribution behaviour with the size of the cloud or equivalently with the

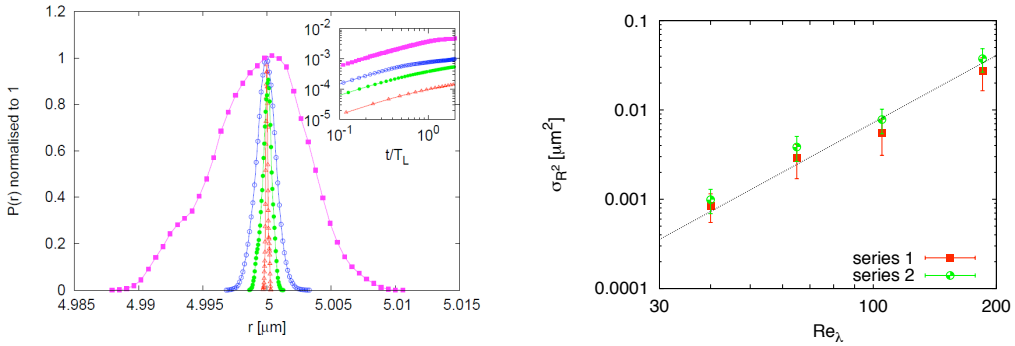

(a) Size spectra **(b)** Spectrum standard deviations

Figure 2.5: In figure (a), droplet-size distribution after $1\ \tau_L$ displays a limited broadening. Results have been obtained by [LSTep] through three-dimensional DNS of condensation in homogeneous isotropic turbulence. Red, green, blue and magenta lines correspond respectively to simulations where cloud height is $L = 9$, 18, 38 and $70\ \mathrm{cm}$. Droplets were initially put randomly with homogeneous distribution in space and monodispersed radius $R_0 = 5\ \mu\mathrm{m}$. In the inset the evolutions of the droplet-size variance with time are plotted for the four simulations. The colours are organized as in the main frame. In figure (b), droplet-spectrum standard deviation achieved after $1\ \tau_L$ increases with a power law of the Reynolds number of cloud turbulence. The dashed line is the dimensional prediction $\sigma(R^2) \sim \mathcal{R}e_\lambda^{5/2}$. The trend of this curve points to a broadening of $(25 \pm 3)\ \mu\mathrm{m}^2$ after $1\ \tau_L \approx 150\ \mathrm{s}$ for a cloud core of size $L \approx 100\ \mathrm{m}$ with initial supersaturation fluctuations $s_{\mathrm{rms}} \approx 2\ \%$.

Reynolds number of cloud turbulence. While the results for each single simulation give a limited degree of broadening (see figure 2.5a), as already pointed out in [VYBG02; VYG01], the trend of the latter with Reynolds number is a power law with positive exponent, pointing to a relevant spreading achieved for sufficiently large clouds. This is due to the fact that droplet radius grows according to the local supersaturation fluctuation experienced on the trajectory. In larger clouds the fluctuations in the vapour field are stronger. Therefore, the radius growth varies more and more from a droplet to another and the size distribution broadens faster and faster.

The broadening of the size distribution after one turnover time τ_L is considered as a function of the microscale Reynolds number $\mathcal{R}e_\lambda \sim \mathcal{R}e^{1/2}$ (a definition of Taylor microscale λ can be found in [Fri95]). On the basis of equation $(2.18\mathrm{e})$, one can roughly estimate the square size broadening as

$$\sigma(R^2) \sim 2C_R s_{\mathrm{rms}} \tau_L \tag{2.19}$$

The supersaturation field s is initially in a stationary state, whose fluctuations

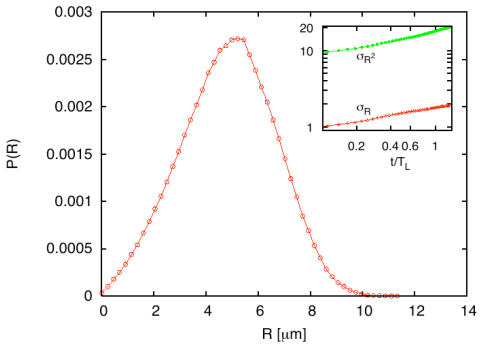

Figure 2.6: Spectrum broadening after $1\ \tau_L \approx 150s$ is slightly smaller than that extrapolated by data for smaller clouds. This spectrum from [LSTep] refers to the simulation matched to the large scales of the cloud. In the inset, the time evolutions of the standard deviation of radius and square radius are reported.

can be simply estimated by a dimensional relation on the basis of $(2.18\mathrm{b})$:

$$s_{\mathrm{rms}} \sim G_s L \sim \mathcal{R}e_\lambda^{3/2} \tag{2.20}$$

By substituting (2.20) in (2.19) and remembering that τ_L scales as $\tau_L \sim \mathcal{R}e_\lambda$, we easily end up with

$$\sigma(R^2) \sim \mathcal{R}e_\lambda^{5/2}$$

shown for comparison in figure 2.5b. We expect this behaviour to be modified when vapour fluctuations start to appreciably decay after the introduction of droplets, which grow absorbing water vapour from the surrounding. The extrapolation of the power law $\mathcal{R}e_\lambda^{5/2}$ to the Reynolds number of real cloud turbulence gives a spreading of around $(25 \pm 3)\ \mu\mathrm{m}^2$ after $1\ \tau_L \approx 150\ \mathrm{s}$.

Finally, let us consider the following point. The broadening mechanism is essentially based on the fact that droplets experience different ambient conditions. While it is impossible to simulate a flow with the huge inertial range of real cloud turbulence, one can obtain appropriate supersaturation fluctuations by simply tuning the coefficient G_s. This essentially corresponds to simulate the large scales of the problem and is equivalent to what already discussed in section 2.3.1, here applied in a three dimensional contest and accounting for droplet feedback on vapour. Is this enough to obtain the broadening expected on the basis of the small-scale trend? Large-scale simulations are provided in [LSTep], where the parameters are tuned on a cloud core of size $L = 100\ \mathrm{m}$. With 256^3 grid points spatial scales down to $\eta \approx 30\ \mathrm{cm}$ are resolved. Other typical values are: $u_{\mathrm{rms}} \approx 0.6\ \mathrm{m/s}$, $s_{\mathrm{rms}} \approx 2\%$, $N = 7\ 10^6$, $\tau_L \approx 150\ \mathrm{s}$. For large enough supersaturation fluctuations, the segregation mechanism already observed in the two-dimensional case appears. In figure 2.6 the droplet-size spectrum after $1\ \tau_L$ is

shown. With the same initially monodispersed spectrum, a spectrum broadening of $\sigma(R^2) = (18 \pm 5)\ \mu\mathrm{m}^2$ is observed, slightly smaller than expected on the basis of the extrapolation described above. This points to the fact that the substantial contribution to the fast spectrum broadening is given by the strong fluctuations of the vapour field, whence the great importance of large scales. A correction might arise for real cloud turbulence due to the much stronger intermittency with respect to the simulated turbulence.

Chapter 3

Two-dimensional numerical analysis

The role of turbulence for droplet condensation has been revealed as crucial, if turbulent fluctuations are considered in the whole cloud rather than in a small air parcel. As presented in [CFMS05; CMTS07; LSTep] and reviewed in section 2.3, turbulence provides both sustenance for droplet growth even in an undersaturated environment and a spreading mechanism for the droplet-size distribution.

Essentially, droplets are separated very fast by the turbulent flow and experience very different environmental conditions, thanks to the large fluctuations available in a turbulent medium. Two extreme events can occur during their wanders: droplets could run up against a dry region, where they are forced to evaporate; a very supersaturated region could be reached, where a fast growth by condensation takes place. Although these two kinds of region are equally distributed in a saturated cloud, there is no symmetry in droplet evolution. Indeed, in the former case droplets could disappear, whereas in the latter case they could become so large to be able to span even undersaturated regions without disappearing. This basic effect is responsible for both a mean growth in classically-forbidden conditions and a huge spectrum broadening.

The robustness of this description has been tested in different system settings. The specific statistics of the turbulent flow (such as isotropic or convective) does not seem to affect results (section 2.3.2). No remarkable difference has been found between the cases where droplets are regarded as either tracers or inertial particles [CFMS05]. On the one hand, taking into account droplet feedback on vapour reduces the observed effects; on the other hand, the same qualitative effects are still present even in very unfavourable conditions (section 2.3.2). Finally, the extrapolation of the droplet evolution in clouds with increasing sizes to larger clouds confirms that broader spectra are expected as larger fluctuations are allowed (section 2.3.3). However, all these studies only refer to the condensation

stage: droplets are supposed to have nucleated before and are put in the cloud with a large size ($\sim 5\ \mu\mathrm{m}$); if a complete evaporation occurs, the particle disappears from the cloud. Moreover, as droplets reach too large sizes ($\sim 25\ \mu\mathrm{m}$), the simulations are stopped, because collection cannot be neglected.

With respect to the models reviewed in section 2.3, the numerical analysis presented in this chapter aims at answering a different question and is set in a different scenario, though in a similar framework. Indeed, since turbulence has been revealed as a crucial element during the condensation stage, the question on its role during heterogeneous nucleation naturally arises. In particular, we are interested in the relation between turbulence and CCN spectra, in two directions. First, it is well known that the larger the CCN, the easier and more likely the nucleation process; if the environmental conditions are not favourable, a larger CCN is required to activate a droplet. The first question is on whether large CCN are really necessary or, rather, large turbulent fluctuations could act in CCN place. Does turbulence act as an effective CCN? How can we measure its effect on nucleation? Moreover, the introduction of giant CCN in a non-precipitating cloud can induce a precipitation [WH06]. The second idea on the basis of the present work is to estimate how much turbulence can trim giant-CCN role in order to start up the collection stage.

We consider two cases, depending on whether droplet feedback on vapour is taken into account or not. The latter case corresponds to the limit of low droplet density and allows us to define an equivalent CCN size depending on turbulence intensity (section 3.1). In the former case droplet number densities are fixed to standard atmospheric values (section 3.2). Both cases are published in papers: in [CMT08] vapour absorption is neglected, whereas in [CMT09] is taken into account.

3.1 Growth at low droplet densities

As a first step let us consider the simplest version of model (2.15) where nucleation is allowed. Thus, our cloud is seeded by cloud condensation nuclei instead of nucleated droplets; hence, curvature and solute effects are included (section 3.1.1). The model presents some free parameters, such as turbulence intensity and CCN sizes; section 3.1.2 provides a complete discussion on the choice of model parameters. Some details on the numerical procedure are given in section 3.1.3. Then, the numerical analysis is presented. First, we investigate usual growth features (section 3.1.4). Finally, we propose a measure of turbulence effects via a redefinition of droplet initial size (section 3.1.5).

3.1.1 Model equations

In the same way as for turbulent models focused only on the condensation stage, we start from the simplest model which includes nucleation without losing the basic ingredients of our global turbulent approach. Besides, as reported in section 2.3 and observed above, different settings and effects do not change the general scenario drawn for the condensation stage. Therefore, neither thermal convection nor particle inertia are considered here. Furthermore, as a first step we focus on the situation where the number of droplets is small enough not to affect the vapour field. Model system (2.15) is thus reduced to

$$\begin{cases} \partial_t \omega + \boldsymbol{u} \cdot \boldsymbol{\partial} \omega = f_\omega + \nu \partial^2 \omega & (3.1a) \\ \partial_t s + \boldsymbol{u} \cdot \boldsymbol{\partial} s = G_s w + D \partial^2 s & (3.1b) \\ \dfrac{\mathrm{d}}{\mathrm{d}t} \boldsymbol{X}_i(t) = \boldsymbol{u}\big(\boldsymbol{X}_i(t), t\big) + \sqrt{2D}\boldsymbol{\eta}_i(t) \qquad i = 1, N & (3.1c) \\ \dfrac{\mathrm{d}}{\mathrm{d}t} R_i^2(t) = 2C_R \left(s\big(\boldsymbol{X}_i(t), t\big) - \dfrac{c}{R_i(t)} + \dfrac{h}{R_i^3(t)} \right) \qquad R_i(t) \geqslant R_0 & (3.1d) \end{cases}$$

where f_ω is a random forcing. As in the previous models, the nonlinear term ws is neglected in $(3.1\mathrm{b})$. In $(3.1\mathrm{d})$ the equilibrium supersaturation $s_\mathrm{e} = \mathrm{e}^{c/R_i - h/R_i^3}$ is approximated to the first order. Finally, we seed the cloud with N equal CCN ($h_i = h \ \forall i$). It is worth noticing that, if a nucleated droplet experiences a complete evaporation, it releases its own CCN, which continues its previous trajectory.

3.1.2 Choice of parameters

Let us now focus our attention on the model parameters to mimic a realistic cloud system. Here, we are interested in warm cumuli, i.e. vertical clouds without ice particles, during their first development stage. To start our study, many cloud features — such as height, dissipation rate and mean supersaturation — need to be fixed. As it will be shown, this choice needs some care because of its dependence on the particular features one would like to study. In other words, we have to decide which parameters are to be left free in order to test how the system depends on them.

As already anticipated, our aim is now to understand the possible role of turbulence in aiding cloud droplets to eventually cross the barrier in the Köhler curve (even in an undersaturated environment) and thus to grow in time until the coalescence phase will take place. It is thus customary to study the system response as the turbulent dissipation rate ε increases. The system we are going to

	$\tau_L = 160$ s		S1	S2	S3	S4
ε ($\mathrm{m^2/s^3}$)	L (m)	u_{rms} (m/s)	$\overline{s}_{\mathrm{rms}}$ (%)	$\overline{s}_{\mathrm{rms}}$ (%)	$\overline{s}_{\mathrm{rms}}$ (%)	$\overline{s}_{\mathrm{rms}}$ (%)
$3.0\ 10^{-3}$	110	0.69	0.59	0.73	0.84	0.90
$1.2\ 10^{-2}$	220	1.4	1.2	1.5	1.7	1.8
$2.7\ 10^{-2}$	330	2.1	1.8	2.2	2.5	2.7
$4.7\ 10^{-2}$	440	2.7	2.4	2.9	3.4	3.6
$7.4\ 10^{-2}$	550	3.4	3.0	3.6	4.2	4.5
$1.1\ 10^{-1}$	660	4.1	3.5	4.4	5.0	5.4
$1.5\ 10^{-1}$	770	4.8	4.1	5.1	5.9	6.3
$1.9\ 10^{-1}$	880	5.5	4.7	5.8	6.7	7.2
$2.4\ 10^{-1}$	990	6.2	5.3	6.6	7.6	8.1
$3.0\ 10^{-1}$	1100	6.9	5.9	7.3	8.4	9.0

Table 3.1: The height of the cloud core L and the typical velocity u_{rms} are functions of the dissipation rate ε once the large-eddy turnover time is kept fixed. We considered ten values of ε in the range $3\ 10^{-3} \div 3\ 10^{-1}\ \mathrm{m^2/s^3}$. Time-averaged root mean square supersaturation $\overline{s}_{\mathrm{rms}}$ is also reported for each different initial configuration of our simulations labelled with $\mathrm{S1}$, $\mathrm{S2}$, $\mathrm{S3}$ and $\mathrm{S4}$. Note that all these quantities are proportional to $\sqrt{\varepsilon}$.

investigate being two-dimensional, other parameters, as for instance the Reynolds number, are not particularly meaningful. We thus selected ten values of ε ranging from $3\ 10^{-3}$ to $3\ 10^{-1}\ \mathrm{m^2/s^3}$, an interval representative of what happens in clouds [SRCV98; VYG01]. Lower values were also considered, but our results showed that turbulence plays a negligible role in those cases. In order to facilitate the comparison with the available literature, from now on ε will be expressed in SI units.

The comparison of these different situations (characterized by different ε) suggests the use of a common observation period of the order of a large-eddy turnover time τ_L, which will be kept fixed in our studies. This also permits to carry out the Lagrangian simulations within the same Eulerian fields. Clearly, a fixed τ_L implies that the larger the value of ε, the higher the typical size, L, of the considered cloud core (and the higher the root mean square velocity u_{rms}). This immediately follows from the fact that

$$\varepsilon \sim \frac{u_{\mathrm{rms}}^3}{L} \sim \frac{L^2}{\tau_L^3}$$

once $\tau_L = L/u_{\mathrm{rms}}$ is kept fixed. For a given value of ε, we have to fix τ_L in a way that the resulting cloud size is of the order of hundreds of meters, as in realistic clouds. We are indeed interested in describing the whole cloud and not a small portion of it, as in the air-parcel approach. The choice we did for ε and L leads to values of τ_L of the order of 3 minutes, compatible with the typical time for the condensation phase to occur [Sha03]. Table 3.1 gives the values of L and u_{rms} (corresponding to $\tau_L = 160$ s) for three values of ε among the ten considered. Table 3.2 shows some other model constants and fixed parameters.

$\langle \boldsymbol{u} \rangle$	$\langle s \rangle$	G_s (m^{-1})	b_s	C_s (m^2/s)	D (m^2/s)	C_R ($\mu\mathrm{m}^2/\mathrm{s}$)	c (nm)	n_s	M_s (g/mol)
$\mathbf{0}$	0	$5.7\ 10^{-4}$	2.0	$1.6\ 10^{-4}$	$2.7\ 10^{-5}$	73	1.2	3	132.14

Table 3.2: Some useful constants and fixed parameters are listed. M_s and n_s refer to $(\mathrm{NH_4})_2\mathrm{SO_4}$.

Let us now deal with environmental conditions. Since at this level the model (3.1) does not involve quantities such as temperature or pressure, we do not mention them here, keeping them fixed to standard atmospheric values. The sole mean supersaturation $\langle s \rangle$ thus remains to be discussed. Literature reports that it can rarely exceed the order of per cent. It is important to notice that a classical-model approach needs a positive $\langle s \rangle$ in order to observe a mean droplet growth, although the solute effect might ensure droplet nucleation even in an undersaturated environment. However, here no positive mean supersaturation is assumed, because we want to assess whether turbulent fluctuations alone are (or not) able to win the curvature effect and to carry droplets until the coalescence stage. Accordingly, a saturated environment corresponding to $\langle s \rangle = 0$ is assumed.

Although we set $\langle s \rangle$ to zero, the supersaturation field has strong temporal fluctuations (whereas spatial fluctuations are controlled by ε) and its root mean square s_rms experiences strong fluctuations of about $25\ \%$ of its average value during a time period of $10\ \tau_L$. This is due to the structure of $(3.1\mathrm{b})$ itself, where the passive field s is forced by the anisotropic $G_s w$ term, which is strongly fluctuating. For this reason we have selected four initial conditions, labelled by $\mathrm{S1}$, $\mathrm{S2}$, $\mathrm{S3}$ and $\mathrm{S4}$, characterized not only by different values of s_rms, but also by different temporal trends of it (see again table 3.1).

Finally, we have to specify which salt is responsible for the solute effect. Both sodium chloride and ammonium sulphate, two of the most common cloud salts, have been considered, giving similar results. However, for the sake of conciseness, the latter has been chosen for a deeper analysis and the results presented here refer to the sole $(\mathrm{NH_4})_2\mathrm{SO_4}$. The latter solute dissolves in water in two ammonium ions and one sulphate ion. Since its molar mass is more than twice the NaCl one (see table 3.2), CCN mass m_s being equal in both cases, h is lower for $(\mathrm{NH_4})_2\mathrm{SO_4}$ and therefore the curvature barrier is a little higher, while the critical radius occurs before [PK97].

The last parameter to be discussed is the CCN mass, i.e. the initial radius R_0. Again, as stated from the beginning, one of the aims of this work is the definition of the required sizes for efficient condensation nuclei once turbulence is included. So, not surprisingly, m_s will be left free, in order to test the contribution of the starting CCN size on droplet growth. The main question addressed here is on how relevant the presence of large CCN is to activate a cloud droplet and on whether

m_{s} (fg)	h ($\mu\mathrm{m}^3$)	R_0 (μm)	R_{ha_0} (μm)	R_{c} (μm)	s_{c} (%)
10^2	$9.8\ 10^{-3}$	0.24	2.9	4.9	$1.6\ 10^{-2}$
10^3	$9.8\ 10^{-2}$	0.51	9.0	16	$5.1\ 10^{-3}$
m_*	$9.8\ 10^{-5}\ m_*$	$0.051\ m_*^{1/3}$	$0.29\ m_*^{1/2}$	$0.49\ m_*^{1/2}$	$0.16\ m_*^{-1/2}$

Table 3.3: Some model quantities are functions of the CCN mass m_{s}. Here, the $(\mathrm{NH_4})_2\mathrm{SO_4}$ water solution is considered. In our DNS two different values are tested for m_{s}. In the last row the explicit dependence on the mass is presented for a generic value m_* expressed in femtograms.

or not turbulence can reduce their role with respect to the classical picture where turbulence is not accounted for. Two situations are compared here, both in a high region of the mass range $10^{-1} \div 10^3$ fg reported by [PK97]: we consider hygroscopic nuclei with masses of 10^2 and 10^3 fg and corresponding radii of 0.24 and 0.51 μm, respectively. In the first case, only a series of S1 simulations was performed, while in the second case all (four) initial conditions were used. Table 3.3 summarizes the principal model parameters having a dependence on the mass m_{s}.

3.1.3 Numerical procedure

We performed a series of two-dimensional direct numerical simulations (DNS) of resolution 1024^2 of model system (3.1). First, we integrated the equations for vorticity and supersaturation by a standard pseudospectral method on a doubly-periodic square domain of length 2π. As usual, in $(3.1\mathrm{a})$ the viscous term is substituted by a hyperviscous one, here of order 8, and a linear friction is added in order to prevent energy accumulation at the lowest modes; furthermore the fields s has been $2/3$-dealiased. Details on the pseudospectral method can be found in [For96].

After more than about $10\ \tau_L$ a K41 stationary state (see [Fri95; Kol41a; Kol41b]) is reached for both fields and four different frames, separated from each other by a time interval of the order of τ_L, are selected from it and used as initial fields for simulations S1-S4. In these sets of simulations 10^5 hygroscopic nuclei are put randomly in the domain with the same initial radius at $t = 0$ and particle evolution is followed for a time $\Delta t = 1\ \tau_L$. Tests with a larger number of nuclei, up to $5\ 10^6$, showed that our results do not depend on the number of CCN. Equations $(3.1\mathrm{a})$ and $(3.1\mathrm{b})$ are advanced in time via a standard second-order Runge–Kutta scheme, while equations $(3.1\mathrm{c})$ and $(3.1\mathrm{d})$ via a first-order Euler one (see [KP92] for details on both schemes). The time step δt has to be smaller than the smallest time-scale τ_{min}, which is connected here to the Raoult

term in $(3.1\mathrm{d})$ and, thus, of the order of

$$\tau_{\min} \sim \frac{R_0^5}{2C_R h} \propto m_{\mathrm{s}}^{2/3}$$

The time step should thus decrease as smaller and smaller masses are considered. We used $\delta t = 8.6\ 10^{-6}\ \tau_L \simeq 7\ 10^{-4}\ \tau_\eta$ when $m_{\mathrm{s}} = 10^2$ fg and $\delta t = 7.1\ 10^{-5}\ \tau_L \simeq 6\ 10^{-3}\ \tau_\eta$ when $m_{\mathrm{s}} = 10^3$ fg. Below the Kolmogorov time τ_η, dissipation is the leading effect. For what concerns the spatial resolution, δx, it is fixed at $L/1024$ once the largest scale L is chosen; therefore it depends on ε, running from 0.1 to 1 m: the focus on larger scales clearly implies that details of smaller ones are necessarily lost.

3.1.4 Spectrum broadening without feedback

Let us first consider the situation where turbulent fluctuations of the field s are not taken into consideration. This amounts to considering the classical view with s replaced by $\langle s \rangle$ in $(3.1\mathrm{d})$. Figure 1.2b helps us to understand the basic mechanism which influences droplet growth when $s = \langle s \rangle$. Focusing, as already stated before, on the case $\langle s \rangle = 0$, CCN of radius R_0 are subjected to the same environmental supersaturation. Once nucleation has occurred, droplets start to evolve along the Köhler curve from the point $\big(R_0, s_{\mathrm{e}}(R_0)\big)$, which lies below the environmental supersaturation $\big(s_{\mathrm{e}}(R_0) < 0\big)$. There droplet surroundings are poor in vapour with respect to the environment, so that vapour diffusion manages to bring droplets to the stable-equilibrium size, set at $R_{\mathrm{ha_0}}$, where the Köhler curve intersects the environmental condition (here, the R-axis). The growth process is due to the solute effect and produces an equilibrium state consisting of a population of haze droplets having the same size $R_{\mathrm{ha_0}}$. Nothing else can classically happen and evolution stops. It is worth noticing that droplet square radius takes more than $3\ \tau_L$ (for $m_{\mathrm{s}} = 10^2$) and $15\ \tau_L$ (for $m_{\mathrm{s}} = 10^3$ fg) to reach $R_{\mathrm{ha_0}}$. In a word, an indefinite growth is classically possible only if either the solute effect is so strong that the Köhler curve lies below the R axis (and no critical point is present) or $\langle s \rangle > s_{\mathrm{c}}$.

Let us now present our main results where turbulent fluctuations are explicitly considered. The results discussed in the classical picture will serve as a reference framework to better understand the role of turbulence. The first question we address is on the characterization of growing droplets. At $t = 0$ we put N CCN randomly in the cloud. We observe that around all these nuclei a droplet is nucleated, such that N becomes the total number of droplets. This behaviour is not realistic and is due to the fact that $(3.1\mathrm{d})$ is not accurate for the smallest radii, as discussed in section 1.3.1. However, we are not interested in the exact description of the nucleation process, but we want to take it into account in the

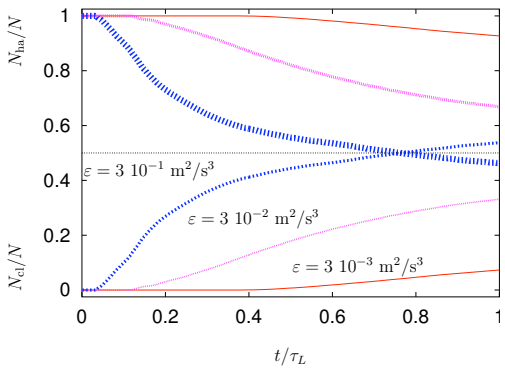

Figure 3.1: The total number of cloud droplets ($N_{\rm cl}$) increases in time at the expense of the total number of haze droplets ($N_{\rm ha} = N - N_{\rm cl}$). Three different dissipation rates are reported (critical radii are listed in table 3.3). Here we considered the initial conditions S4 and $m_{\rm s} = 10^3$ fg.

simplest way. In particular, like in real clouds, particles cannot disappear from the cloud once a complete evaporation occurs, but serve as condensation nuclei for new droplets.

We can split the N droplets in two groups: the $N_{\rm cl}$ cloud droplets with radius larger than the Köhler critical radius $R_{\rm c}$ and the $N_{\rm ha} = N - N_{\rm cl}$ haze droplets with radius below the critical one. Figure 3.1 shows the temporal evolution of both $N_{\rm cl}$ and $N_{\rm ha}$. $N_{\rm cl}$ increases monotonically in time (being already comparable with $N_{\rm ha}$ after less than $1\ \tau_L$), a clear clue of a continuous droplet growth by condensation. This monotonic trend is found in all simulations and seems to be approximately independent of $m_{\rm s}$. On the contrary, the growth rate strongly depends on spatial turbulent fluctuations, i.e. on ε, as showed in figure 3.1.

In figures from 3.2 to 3.4 droplet-size spectra (i.e. distributions of droplet square radii) are shown. The initial distribution of the CCN sizes is a Dirac delta and it is not reported. A feature common to all these plots is the presence of very spread spectra characterized by a peak in the haze-droplet range and a very long right tail in the cloud-droplet range. Two regions are thus associated to different dynamical conditions experienced by droplets.

Figure 3.2 shows the spectrum time evolution, which is clearly characterized by a fast broadening: after $0.5\ \tau_L$ the distribution embraces a scale interval of more than two decades even in the less turbulent simulation (figure 3.2(a)). Such behaviour is totally absent in the aforementioned classical picture. It is worth noticing how the "haze peak" slowly evolves in time remaining almost frozen for a time of the order of $0.5\ \tau_L$. On the other hand a continuous flux of droplets from the haze-peak region toward the far "cloud-droplet tail" is also evident from the spectra, an effect clearly due to turbulence.

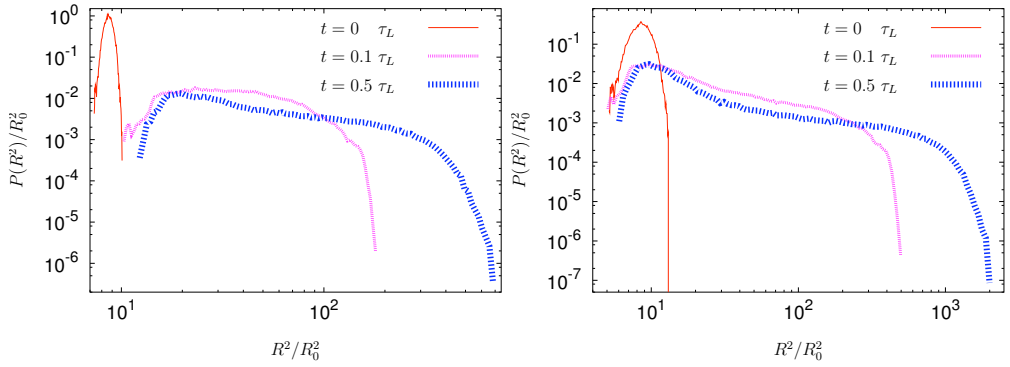

(a) $\varepsilon = 3\ 10^{-3}\ \mathrm{m}^2/\mathrm{s}^3$ **(b)** $\varepsilon = 3\ 10^{-2}\ \mathrm{m}^2/\mathrm{s}^3$

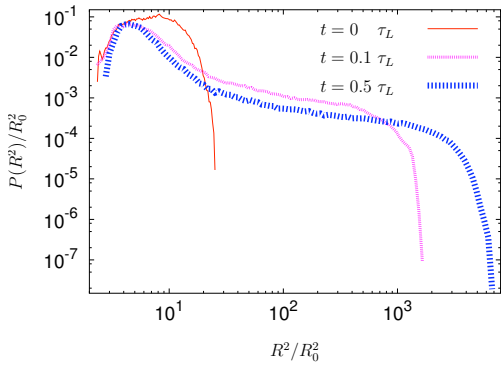

(c) $\varepsilon = 3\ 10^{-1}\ \mathrm{m}^2/\mathrm{s}^3$

Figure 3.2: Droplet size spectra broaden in time. As ε increases, a larger broadening is observed (notice that radius ranges are different in the three figures). Spectra at $t = 0$ are actually taken some time steps after 0, whereas the initial spectrum is a Dirac distribution $\delta(R_0^2)$. Note that the branch to the left of the peak is almost frozen with the right branch tending to erode it as time runs. Here we considered the initial conditions S1 and $m_\mathrm{s} = 10^3$ fg, i.e. $R_0 \simeq 0.5$ µm.

Let us now compare spectra in the two cases having different CCN masses. We can plot either the size distributions normalized with the initial radius, $R_0^2 P(R^2/R_0^2)$, as reported in figure 3.3, or the bare distribution $P(R^2)$. In the first case we observe spectra collapsing in the haze-peak region, in the second case spectrum collapsing occurs in the region corresponding to the cloud-droplet tail. To understand the meaning of this behaviour, we have to come back to the Köhler curve plotted in figure 1.2b and remember that s is a field having zero mean. Thus, statistically, there will be half cloud undersaturated and half supersaturated. Roughly speaking, we can imagine that in positive regions we have $s \sim +s_\mathrm{rms}$, while in negative ones $s \sim -s_\mathrm{rms}$. If $s_\mathrm{rms} > s_\mathrm{c}$, as in all our simulations (compare tables 3.1 and 3.3), droplets hosted by positive regions should

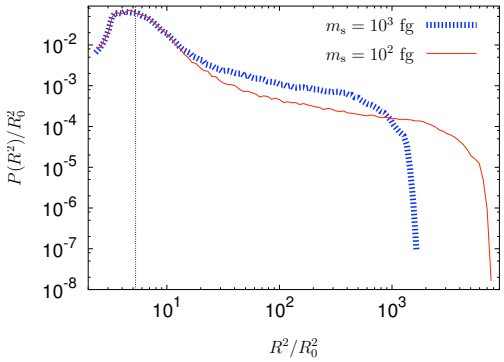

Figure 3.3: Size spectra for two different hygroscopic nuclei are compared. As reported in table 3.3, $m_s = 10^2$ fg corresponds to the CCN size $R_0 \simeq 0.2$ µm, while the other case to $R_0 \simeq 0.5$ µm. The vertical dotted line, set at the size R_{ha-}/R_0 which is the same in both cases, is very close to the spectrum peak and the two spectra overlap in the range around it: droplets in this size range behave dynamically as haze droplets with $s \sim -s_{rms}$. If we plotted $P(R^2)$ instead of $R_0^2 P(R^2/R_0^2)$, right tails would overlap, because the evolution of larger droplets only depends on the turbulent supersaturation field. Here we have $t = 0.1\ \tau_L$, $\varepsilon = 10^{-1}$ m^2/s^3 and initial conditions S1.

grow indefinitely, whereas droplets in the negative regions should only reach their haze radius $R_{ha-} := R_{ha}(-s_{rms})$. This schematic interpretation agrees with the situation in figure 3.3, where the vertical line shows that the peak is just at R_{ha-}/R_0. Note that the two distributions overlap around R_{ha-}/R_0 because both R_{ha-} and R_0 are proportional to $m_s^{1/3}$. The physical meaning associated to the tail overlapping in the spectra of $P(R^2)$ lies in the fact that for particles belonging to these tails no solute effect enters into play and droplets grow thanks to $+s_{rms}$ only, i.e. thanks to turbulent fluctuations which are the same for both $m_s = 10^2$ and $m_s = 10^3$ fg.

Particles initially distributed inside the two previously identified regions tend to mix from one region to the other with the final result that the growth process appears strongly fluctuating in time. We indeed observe that droplets experience very different values of s during their evolution, crossing positive and negative regions, growing and evaporating. This evolution is however not symmetric: when droplet size becomes too small the solute effect takes place to prevent their evaporation, but no limit is present for the growth of large radii. This explains why the distribution around R_{ha-} is eroded in time and the number of haze droplets decreases monotonically in favour of cloud droplets.

To conclude this part devoted to the size spectra, in figure 3.4 we compare the width of two distributions with two different ε. It is evident that increasing the dissipation rate, i.e. turbulent fluctuations, implies a further broadening of

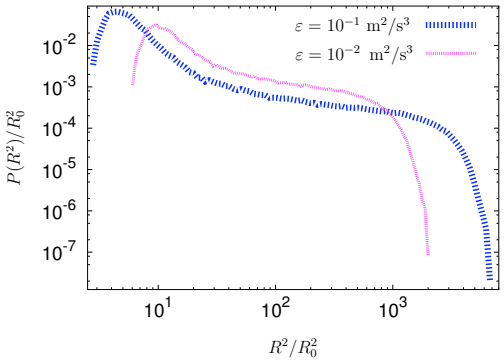

Figure 3.4: Size spectra for two different dissipation rates are compared. We can clearly see that the larger ε the broader the radius distribution. Here we have $t = 0.5\ \tau_L$, $m_s = 10^3$ fg and initial conditions S1.

the spectrum. This is the fingerprint of the role of turbulence in producing a broad distribution in the size of cloud droplets.

3.1.5 Equivalent CCN radius

In section 3.1.4 the basic role of turbulence for droplet condensation has been explained in a qualitative way. Turbulent fluctuations allow droplets to cross the curvature barrier, continuing to grow even in a saturated environment (i.e. having $\langle s \rangle = 0$) and causing a strong spreading of the initial radius distribution. Our aim now is to find an equivalent classical description which incorporates the dynamical role of turbulence into some effective parameters. In other word, we assume the description where turbulence is explicitly taken into account as our "real world" and we search for an "equivalent" classical model sharing one (or more) relevant features with the "real" situation. The concept of renormalized CCN radius will naturally appear.

The observable we impose to remain unchanged passing from the real situation to the equivalent (classical) one is the growth rate of R^2. In other words, we have $\langle R^2 \rangle \sim 2C_R s_{\rm eq} t$ in the presence of turbulence, with some $s_{\rm eq}$ depending, e.g., on ε and the initial conditions S1-S4, and we define a classical model in a way that $R^2 \sim 2C_R \langle s \rangle t$ with $\langle s \rangle = s_{\rm eq}$. The fact that $\langle R^2 \rangle \propto s_{\rm eq} t$ in the turbulent situation can be clearly seen in figure 3.5. There we observe that, after a brief transient where both solute and curvature effects give a contribution, the mean square radius grows linearly in time, the growth rate depending on ε but not on m_s. This clearly means that fluctuation intensity alone, rather than the initial size, is important for the mean growth.

Figure 3.6 shows that the *equivalent supersaturation* $s_{\rm eq}$ follows a power law in ε, the initial conditions giving the slope only. More precisely, the equivalent

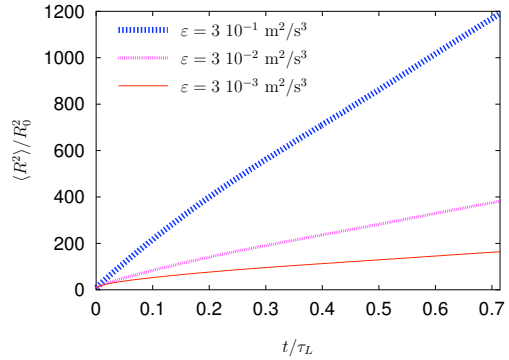

Figure 3.5: The mean square radius grows in time at a rate increasing with ε. Here we have initial conditions S1 and $m_\mathrm{s} = 10^3$ fg. Since $R_0 \simeq 0.5$ µm, in the most turbulent case the mean radius reaches values close to 20 µm. Same results also occur for the lighter nucleus; this is an important clue on how droplet growth depends on turbulent fluctuations rather than on CCN peculiarities. This behaviour allows the identification of an equivalent supersaturation s_eq via the linear fit $\langle R^2 \rangle \sim 2 C_R s_\mathrm{eq} t$.

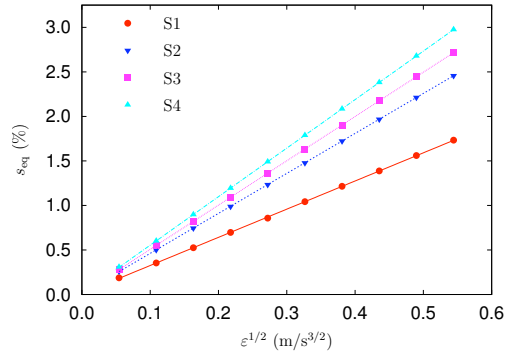

Figure 3.6: The equivalent supersaturation is a function of the dissipation rate. All the four different initial conditions S1-S4 are reported. A linear fit in $\varepsilon^{1/2}$ (lines) shows that initial conditions do not affect the dependency on the dissipation rate. The two cases with $m_\mathrm{s} = 10^2$ and 10^3 fg (both with initial conditions S1) coincide, showing that s_eq depends on the fluctuations alone, rather than the initial distribution of CCN sizes.

supersaturation increases linearly in the square root of the dissipation rate.

The equivalent supersaturation gives a direct classical reading of our turbulent model: although the cloud is saturated on the average, droplets feel an effective supersaturated environment with $\langle s \rangle = s_\mathrm{eq}$ thanks to fluctuations. However, for the moment this picture tells us nothing about the CCN sizes involved in nucleation in our equivalent standard model. We need a further step. From figure 1.2b we know that a classical (linear in time) growth can occur only if

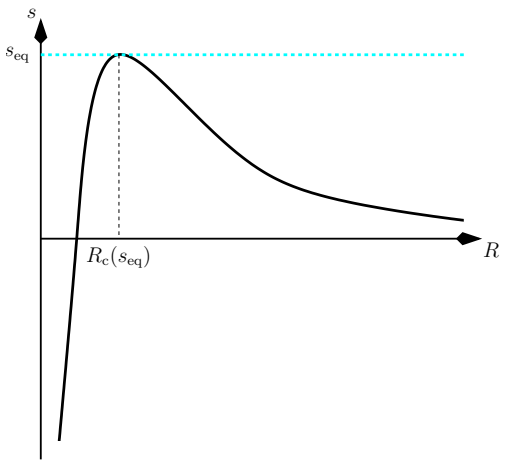

Figure 3.7: How can turbulent growth be interpreted in a classical framework? If we look at figure 1.2b, we realize that a classical growth can occur only when the mean supersaturation is at least s_{c}. There, the curvature and the solute effects become negligible and every droplet grows linearly in time according to $R^2 \sim 2C_R s_{\mathrm{c}} t$. From figure 3.5 we know that in the presence of turbulence also $\langle R^2 \rangle$ increases linearly in time and we can define an equivalent supersaturation such that $\langle R^2 \rangle \sim 2C_R s_{\mathrm{eq}} t$. Now the basic idea consists in reading turbulent results as classical ones with $s_{\mathrm{c}} = s_{\mathrm{eq}}$. One can thus calculate $R_{\mathrm{c}}(s_{\mathrm{eq}})$ and $h(s_{\mathrm{eq}})$ to obtain a renormalized Köhler curve with a higher curvature barrier. Finally, the renormalized CCN radius R_{eq} can be easily extracted from $h(s_{\mathrm{eq}})$.

the constant mean supersaturation exceeds the critical value; thus, at least, at s_{c} itself. The basic idea now is to associate the observed s_{eq} to the minimal required supersaturation s_{c}, as sketched in figure 3.7. Fluctuations induce a linear growth with rate s_{eq} and classically this can happen only if $s_{\mathrm{eq}} = s_{\mathrm{c}}$, at least. Since s_{eq} is a function of ε, with that identification we can plot a different Köhler curve for every ε, such that the critical point corresponds to s_{eq}. The crucial point now is that the Köhler curve and its critical point depend on the specific CCN properties, i.e. on the parameter $h = 4c^3/(27s_{\mathrm{c}}^2)$ or the particle mass, once the other parameters are kept fixed. Thus, we have a procedure to associate an equivalent CCN mass to every dissipation rate via the definition of the *equivalent hygroscopicity coefficient*

$$h_{\mathrm{eq}}(\varepsilon) = \frac{4c^3}{27 s_{\mathrm{eq}}^2(\varepsilon)}$$

and finally, using the definition of h in terms of $m_{\mathrm{s}} = 4\pi\rho_{\mathrm{s}} R_0^3/3$, we can define

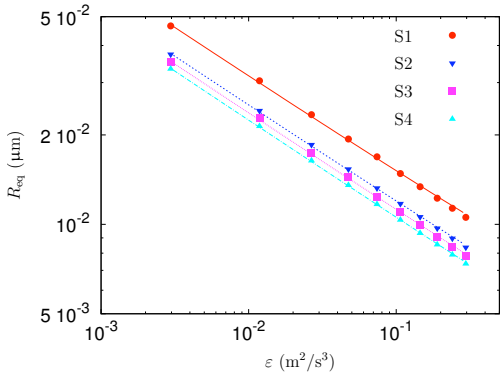

Figure 3.8: For the four initial conditions S1-S4 the behaviour of the renormalized (equivalent) CCN radius is shown as a function of the dissipation rate. The lines correspond to a fit with respect to $\varepsilon^{-1/3}$. Note that the effect of turbulence is so strong that the initial CCN radii (0.24 and 0.51 µm in the 10^2 and 10^3 fg case, respectively) are not reported, lying more than one order of magnitude above the equivalent radii.

the *equivalent CCN radius* R_{eq} as

$$R_{\mathrm{eq}}(\varepsilon) = \left(\frac{h_{\mathrm{eq}}(\varepsilon)\rho_{\mathrm{w}}M_{\mathrm{s}}}{n_{\mathrm{s}}\rho_{\mathrm{s}}M_{\mathrm{w}}}\right)^{1/3} = \left(\frac{4c^3\rho_{\mathrm{w}}M_{\mathrm{s}}}{27s_{\mathrm{eq}}^2(\varepsilon)n_{\mathrm{s}}\rho_{\mathrm{s}}M_{\mathrm{w}}}\right)^{1/3} \propto s_{\mathrm{eq}}^{-2/3}(\varepsilon) \propto \varepsilon^{-1/3}\,.$$

The last equality comes from results presented in figure 3.6, i.e. from the observed relation $s_{\mathrm{eq}} \propto \varepsilon^{1/2}$. Figure 3.8 confirms that the equivalent CCN radius decreases as turbulent fluctuations increase, with the power law $R_{\mathrm{eq}} \propto \varepsilon^{-1/3}$, initial conditions not affecting this slope. It is worth noticing that this result is totally independent of the initial CCN size R_0. Turbulence appears as a strong effect, reducing the CCN radii by more than one order of magnitude even in the situation with the smallest fluctuations.

3.2 Growth at standard droplet densities

As far as the amount of droplets in the cloud is small, like in the earliest stage of cloud formation, the vapour subtracted by them to the environment is negligible. In those conditions, the large positive fluctuations of the supersaturation field provided by the turbulent motions allow droplet growth from CCN, although such a growth would be classically forbidden. In section 3.1 we showed that the growth rate does not depend on the initial CCN size, but on the turbulent dissipation rate.

However, nucleation is a continuous process. Thus, after a short time the number density of activated droplets become high enough to make the vapour-

	$\tau_L = 220$ s		S5
ε ($\mathrm{m^2/s^3}$)	L (m)	u_{rms} (m/s)	$\overline{s}_{\mathrm{rms}}$ (%)
$1.1\ 10^{-3}$	110	0.49	0.72
$1.1\ 10^{-2}$	330	1.5	2.2
$1.1\ 10^{-1}$	1100	4.9	7.2

Table 3.4: The height of the cloud core L and the typical velocity u_{rms} are functions of the dissipation rate ε once the large-eddy turnover time is kept fixed. We considered three values of ε in the range $10^{-3} \div 10^{-1}\ \mathrm{m^2/s^3}$. Time-averaged root mean square supersaturation $\overline{s}_{\mathrm{rms}}$ of the stationary state is also reported; however, once CCN are put, s and s_{rms} are strongly affected by droplet evolution.

ε ($\mathrm{m^2/s^3}$)	10^{-1}	10^7	$3\ 10^7$	10^8	n ($\mathrm{m^{-3}}$)
$1.1\ 10^{-3}$	$10^2, 10^3$	10^3	$10^2, 10^3$	-	
$1.1\ 10^{-2}$	$10^2, 10^3$	10^3	$10^2, 10^3$	-	m_{s} (fg)
$1.1\ 10^{-1}$	$10^2, 10^3$	$10^2, 10^3$	$10^2, 10^3$	10^3	

Table 3.5: Model system 3.2 involves three free parameters: the turbulence dissipation rate ε, the CCN mass m_{s} and the droplet-number density n. Here we list all the simulated values.

absorption term no more negligible. In the present section we analyse the evolution of droplets interacting with the surrounding environment.

3.2.1 Model settings

As already discussed in section 3.1.1, we analyse a simplified version of model system (2.15), where neither buoyancy nor inertial particles are considered. Now, we improve model system (3.1) by including droplet feedback on supersaturation and using a more accurate equation for radius evolution:

$$\begin{cases} \partial_t \omega + \boldsymbol{u} \cdot \boldsymbol{\partial} \omega = f_\omega + \nu \partial^2 \omega & \text{(3.2a)} \\ \partial_t s + \boldsymbol{u} \cdot \boldsymbol{\partial} s = G_s w - b_s C_s \lambda + D \partial^2 s & \text{(3.2b)} \\ \dfrac{\mathrm{d}}{\mathrm{d}t} \boldsymbol{X}_i(t) = \boldsymbol{u}\big(\boldsymbol{X}_i(t), t\big) + \sqrt{2D}\boldsymbol{\eta}_i(t) \qquad i = 1, N & \text{(3.2c)} \\ \dfrac{\mathrm{d}}{\mathrm{d}t} R_i^2(t) = 2C_R \left(1 + s\big(\boldsymbol{X}_i(t), t\big) - \mathrm{e}^{\frac{c}{R_i(t)} - \frac{h}{R_i^3(t)}} \right) \qquad R_i(t) \geqslant R_0 & \text{(3.2d)} \end{cases}$$

As customary, we neglect the nonlinear terms on the r.h.s. of $(3.2\mathrm{b})$, so that now $G_s w$ represents the adiabatic cooling and $-b_s C_s \lambda$ the vapour absorption. We remember that λ is the condensation density field coupling droplet Lagrangian evolution and supersaturation Eulerian evolution.

To mimic several cloud situations and conditions, here we can vary three main free parameters of the model: the turbulence intensity given by the dissipation

rate ε, the CCN size R_0 (or equivalently their mass m_s) and the number density of droplets n (which is proportional to λ). All these quantities can experience very different values in different clouds, e.g. $\varepsilon \sim 10^{-3} \div 10^{-1}\ \mathrm{m}^2/\mathrm{s}^3$, $m_\mathrm{s} \sim 10^{-1} \div 10^{3}\ \mathrm{fg}$ and $n \sim 10^{7} \div 10^{8}\ \mathrm{m}^{-3}$ (see [SRCV98; Sha03; VYG01]). We tested three values of ε in the reported range (as reported in table 3.4) and we chose a population of $(\mathrm{NH_4})_2\mathrm{SO_4}$ CCN of the same size, considering two cases at $m_\mathrm{s} = 10^2\ \mathrm{fg}$ and $10^3\ \mathrm{fg}$ (see again table 3.3). The novelty with respect to section 3.1 is represented by droplet density, which is fixed at zero when droplet feedback on vapour is neglected. Also for n we tested different values in the reported range and we focused on the comparison between the cases with and without feedback. As discussed in section 3.1.2, we keep the large-eddy turnover time fixed (here $\tau_L = 220\ \mathrm{s}$), varying cloud height in order to get different turbulence intensities. Finally, here we only tested one initial condition of the supersaturation field (labelled as $\mathrm{S5}$). A complete list of simulated parameters is provided in table 3.5.

We performed a series of two-dimensional DNS of resolution 1024^2 of model system (3.2). As in the case without feedback, $(3.2\mathrm{a})$ and $(3.2\mathrm{b})$ are integrated by a standard pseudospectral method on a doubly-periodic square domain of length 2π and advanced in time with a standard second-order Runge–Kutta scheme with time step δt. As usual, in $(3.2\mathrm{a})$ the viscous term is substituted by a hyperviscous one, again of order 8, and a linear friction is added in order to prevent energy accumulation at the lowest modes; furthermore, the supersaturation field has been $2/3$-dealiased. After more than about $10\ \tau_L$ a K41 stationary state is reached for both ω and s and $5\ 10^6$ hygroscopic nuclei are put randomly in the domain with the same initial radius at $t = 0$. Then, $(3.2\mathrm{c})$ and $(3.2\mathrm{d})$ are advanced in time for a period of $1.6\ \tau_L$ via a first-order Euler scheme with time step $\delta t/2$. The time step depends on the CCN size: $\delta t = 2.9\ 10^{-6}\ \tau_L \approx 2\ 10^{-4}\ \tau_\eta$ for $m_\mathrm{s} = 10^2\ \mathrm{fg}$ and $\delta t = 1.2\ 10^{-5}\ \tau_L \approx 8\ 10^{-4}\ \tau_\eta$ for $m_\mathrm{s} = 10^3\ \mathrm{fg}$. Since τ_L is kept fixed, the spatial resolution depends on ε: $\delta x = 0.1 \div 1\ \mathrm{m}$ as $\varepsilon = 10^{-3} \div 10^{-1}\ \mathrm{m}^2/\mathrm{s}^3$.

3.2.2 Droplet feedback on vapour

As in the case where droplet feedback on vapour is not considered, we want to investigate whether and how much turbulent fluctuations can allow droplets to cross the curvature barrier and grow up to a size comparable with the one at which collection begins to play a decisive role. A mark of the importance of turbulence in winning the curvature effect is given by the time trend of the number N_cl of cloud droplets present in the cloud, plotted at different dissipation rate, as shown in figure 3.9. We observe that, independently of ε, a large percentage $(15 \div 35\ \%)$ of droplets are able to cross the critical radius very fast. Then, a

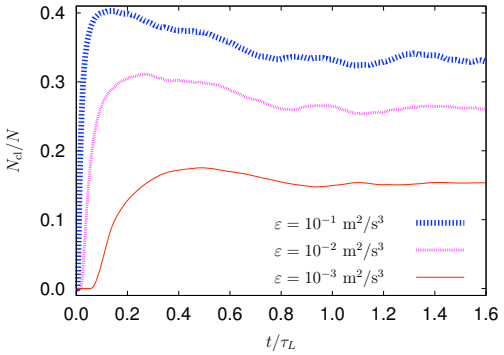

Figure 3.9: First, the number of cloud droplets $N_{\rm cl}$ grows quickly at a rate increasing with the turbulent dissipation rate ε. Then, $N_{\rm cl}$ reaches a stationary level, which still depends on ε. This stationarity is a fingerprint of the separation between the populations of haze and cloud droplets and is due to the progressive erosion of large positive fluctuations of s. Here we have $m_{\rm s} = 10^2$ fg and $n = 3\ 10^7 {\rm m}^{-3}$.

stationary number is reached, telling us that there is no mean flux of droplets between the two populations. This stationary separation is explainable as a reminiscence of the observed bimodality of droplet spectra.

It remains to understand why no more droplets become cloud droplets, whereas in the case without feedback reported in section 3.1 a continuous growth of $N_{\rm cl}$ was observed. Clearly the role of the feedback is crucial here. Until no vapour absorption is taken into account, the fluctuations of s are not affected by droplet growth, continuing to feed it, and the mean supersaturation is fixed at zero. In figure 3.10 we can see what happens once the supersaturation field is able to feel droplet growth. On the left the trends of both $\langle s \rangle$ and $\langle s \rangle_{\rm cl}$ (i.e., averaged on the trajectories of the $N_{\rm cl}$ cloud droplets) are shown. In the first stage $\langle s \rangle$ decreases to more and more negative values, whereas $\langle s \rangle_{\rm cl}$ is positive. We can explain that with the fact that large positive fluctuations of s allow droplets to cross the critical radius; at the same time this condensation subtracts vapour to the environment, eroding those fluctuations. When no large positive fluctuations are any longer available, in supersaturated regions cloud droplets have no further sustenance to grow, while in undersaturated regions haze droplets have reached their stable radius, so that the system settles in a stationary state. On the right of figure 3.10 we observe that the mean square radius of cloud droplets does not grow indefinitely as in the case without feedback, but reaches a stable value. It is worth noticing that this mean value (here about $10\ \mu{\rm m}$) is of the same order of the size at which collection starts to occur. Moreover, cloud droplets are big enough to be able to span the whole cloud without dramatically evaporating (as attested by $\langle s \rangle_{\rm cl}$, which oscillates around zero).

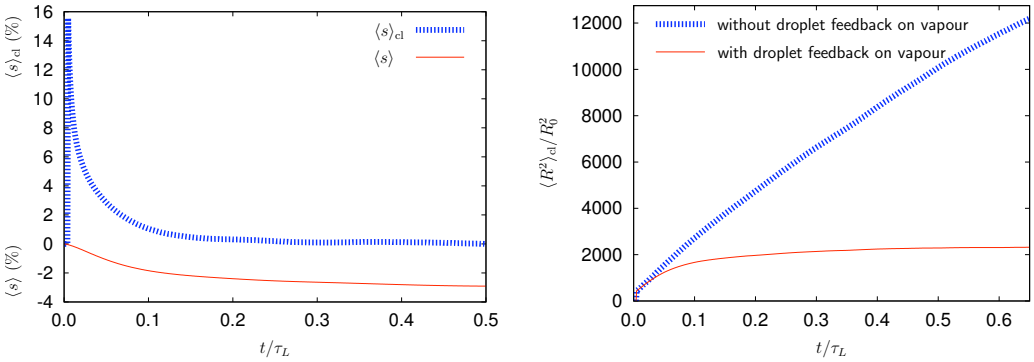

(a) Mean supersaturation **(b)** Mean square radius

Figure 3.10: Initially the environment where CCN are put is saturated on average ($\langle s \rangle = 0$), as shown in figure (a). When droplets start to nucleate and grow by condensation, they subtract vapour to the cloud and $\langle s \rangle$ becomes more and more negative. On the other hand, the mean supersaturation $\langle s \rangle_{\rm cl}$ experienced by cloud droplets is strongly positive, as a consequence of the fact that only large positive fluctuations of s enable droplets to cross the critical radius. After half a turnover time, no large fluctuations are any longer available, cloud droplets decorrelate from positive regions and, on average, stop to grow. As expected, the resulting cloud-droplet growth is slower when the feedback term is taken into account (figure (b)). Clearly, in this case cloud droplets absorb the surrounding vapour, so eroding their sustenance and slowing down their growth. Here we have $\varepsilon = 10^{-1}$ m^2/s^3, $s_{\rm rms}(0) = 5.4$ %, $m_{\rm s} = 10^2$ fg, $n = 3\ 10^7$ m^{-3} (red full line in figure (b)) and $n = 10^{-1}$ m^{-3} (blue dashed line in figure (b)).

The system seems to be ready for the third stage of cloud development, i.e. collisions and coalescence: one turnover time after CCN insertion, two populations of droplets are present in the cloud, one with small droplet sizes, the other composed of large droplets which can wander also undersaturated regions. Now we want to verify in a qualitative way whether droplet spectra are spread enough in order to start up collection. Figure 3.11a shows the time evolution of the spectra, whereas figure 3.11b a comparison between the case with and without feedback. We can observe that, although taking into account vapour absorption results in a lower effect, a strong spectrum broadening is still evident. Notice that the separation between the two populations is clear there: the spectrum peak corresponds to haze-droplet radii, whereas the long right tail to cloud ones.

Finally it is interesting to follow the feedback trend in time, as measured by the feedback factor

$$F_s = \frac{b_s C_s \langle \lambda \rangle}{G_s w_{\rm rms}}$$

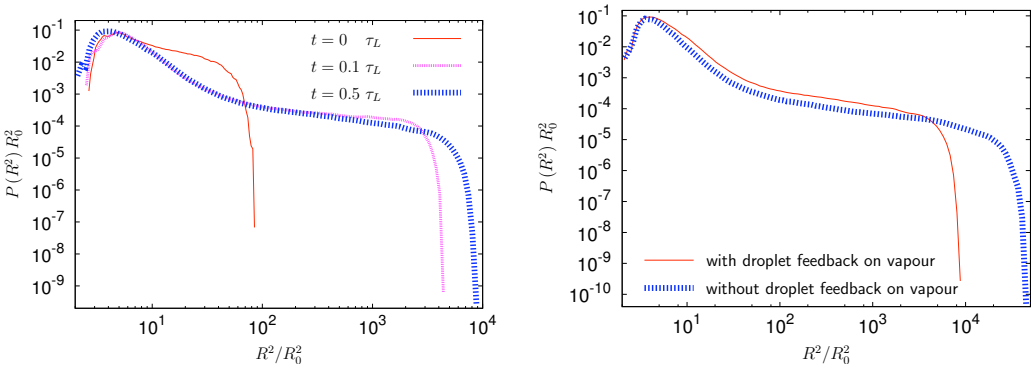

(a) $P(R^2;t)$ **(b)** $P(R^2;n)$

Figure 3.11: Droplet size spectra strongly broaden in time, as shown in figure (a). Time $t = 0$ corresponds actually to some time steps after 0, whereas the initial spectrum is a Dirac distribution. Figure (a) refers to the case with feedback. A comparison between the cases with and without feedback is presented in figure (b). Although vapour absorption slows down droplet growth by condensation, a strong spectrum broadening is still evident. At lower dissipation rates spectra broaden less. In both figures we have $\varepsilon = 10^{-1}\ \mathrm{m}^2/\mathrm{s}^3$, $m_\mathrm{s} = 10^2\ \mathrm{fg}$ and $n = 3\ 10^7\ \mathrm{m}^{-3}$ (red full line in figure (b)); blue dashed line in figure (b) refers to $n = 10^{-1}\ \mathrm{m}^{-3}$.

where λ and w of (2.8) are substituted by $\langle\lambda\rangle$ and w_rms here, respectively. Figure 3.12 shows that vapour absorption plays a decisive role only in the first phase. Then, when large positive fluctuations of s are eroded and the system has reached a stationary state, the feedback tends to zero on average.

3.3 Results summary

We have investigated the role of turbulence in the early stage of the droplets growth process dominated by condensation. Inspired by [CFMS05; CMTS07], turbulence effects are incorporated in our model by a simple generalization of the Twomey model. Accordingly, the concept of ambient humidity is replaced by a (turbulent) field transported by a Navier–Stokes (turbulent) velocity field. In addition the curvature effect and the solute effect have been described in the present model. The latter effect can now be considered owing to the explicit treatment of CCN dynamics. In other words, unlike what happens in [CFMS05; CMTS07], the growth process now starts from an initial population of CCN and, more importantly, a complete evaporation of a cloud droplet does not imply its disappearance as in [CFMS05; CMTS07] but simply that it leaves a bare CCN

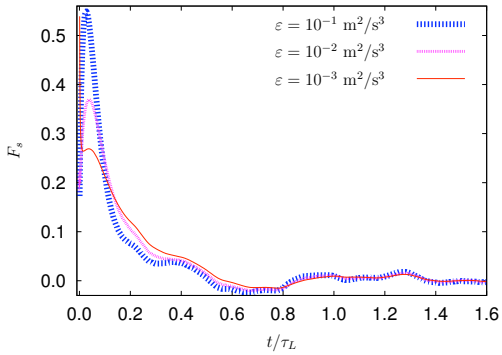

Figure 3.12: Droplet feedback on vapour plays an important role at the beginning, as measured by the feedback factor F_s, which is the ratio between the two effects of vapour absorption and adiabatic cooling. Then, the system settles in a stationary state around $F_s = 0$. Indeed, in the first phase droplet growth has a relevant impact on the supersaturation field, eroding large positive fluctuations. Thus, in the second phase there is not enough vapour available in order to sustain further droplet growth and vapour absorption is strongly reduced. Here we have $m_{\rm s} = 10^2$ fg and $n = 3\ 10^7$ m^{-3}.

from which a new growth process can be activated under favourable ambient conditions.

For the same physical mechanisms discussed in section 2.3, also in the present study turbulence causes a broad distribution of the cloud-droplet sizes, in qualitative agreement with experimental results. With the present model formulation we are not in the position to perform a quantitative comparison with experiments. However, we try to isolate some basic mechanisms and try to contribute to the understanding of nontrivial observations as the broadening of droplet spectrum. From our studies it emerges that turbulence is an essential ingredient that acts to enlarge the droplet size spectrum. Of course, the expectation to be able to capture the details of this phenomenon with a model which is two-dimensional and has periodic boundary conditions appears strongly unrealistic.

The explicit incorporation of CCN in our dynamical description allowed us to propose a criterion to provide a quantitative measure of the turbulence effect on the growth process as far as droplet density is low enough to weakly affect the vapour field. In section 3.1 we observed that turbulence acts as an effective CCN: droplet growth does not depend on the initial CCN size, but on turbulence intensity. This idea leads to the concept of the equivalent CCN radius, i.e. an effective parameter to be inserted into the classical theory of the droplet-growth process with the goal of parametrizing dynamical effects played by turbulence. In other words the equivalent radius is the CCN radius in an equivalent classical scenario where droplet grows with the same rate as in turbulent conditions. The

equivalent radius results much smaller than the actual CCN radius.

This picture is valid when few small droplets are present in the cloud. As their number increases, the effect of their interaction with the environment cannot be neglected. Although vapour absorption by droplets reduces both the condensational growth and spectrum broadening, both behaviours are still present, even when the cloud becomes undersaturated on average. Indeed, growing droplets erode the large positive fluctuations of s initially available. After few minutes the system has reached a stationary state, where no mean growth is observed and droplets are divided in two populations. Such a time and a size distribution are compatible with those required for the collection to start.

Conclusions

The knowledge of the growth processes occurring in the atmosphere is a crucial topic in order to understand how clouds form and develop. In particular, the capacity of being a precipitating cloud depends on the kind of population emerging from the nucleation and the successive growth of water droplets and ice particles. For instance, in a warm cloud precipitations can only be generated by an effective droplet growth by collisions and collisions are strongly enhanced by broad droplet-size distributions. The observed broadening in time of the size distribution is still an open problem in cloud dynamics and only partial explanations have been proposed. In the present work we have investigated the role played by turbulence for droplet growth in warm cumuli.

The classical picture is focused on the evolution of a small portion of moist air, known as air parcel. In an unstable environment, the warmer air parcels present at lower altitudes are induced by buoyancy to move upwards, thus experiencing an adiabatic expansion and cooling down. As a result, the air humidity increases and, finally, parcels become supersaturated. In these favourable conditions, droplets are allowed to form around wettable solid particles, called cloud condensation nuclei (CCN). Then, the vapour diffuses through droplet surfaces and droplets grow by condensation. The latter is a slowing process where larger droplets grow slower than smaller ones. Thus, during the condensation stage droplet population becomes more and more homogeneous. Moreover, weeks are needed in order to observe a precipitation from such a population. In fact, a third phenomenon takes place once droplets are large enough to feel the gravity: droplets with different terminal velocities (i.e. with different sizes) can collide and, in case, coalesce, resulting in an explosive growth process which can lead to a precipitation in half an hour. This simple scheme is able to highlight the main problems arising in the classical description. In particular, how can collection start from a homogeneous population? The action of several effects, such as the entrainment of dry air from above, the presence of giant CCN or the preferential concentration, has been proposed in order to justify the observed size-spectrum broadening. Nevertheless, a univocal explanation is still vacant.

The failure of the classical model for condensation is due to its mean-field

type description: droplets experience the same supersaturation and grow according to the same law, thus preventing a spectrum broadening. However, even taking into account turbulent fluctuations inside the air parcel results in a negligible broadening. The key point is that the air parcel is not able to provide enough fluctuations. On the contrary, droplets do experience very different environmental conditions, because initially close particles are quickly separated and can span very far regions of the cloud in a time compatible with the one for condensation to occur. Thus, the air parcel is not a proper tool in order to investigate condensation. The starting idea for our work is the removal of the air parcel as a laboratory for droplet evolution, turning the focus to the turbulent motions of the whole cloud.

The first studies [CFMS05; CMTS07; LSTep] embracing such an approach for the description of the condensational growth identified a strong spreading mechanism in the correlation between droplet trajectories and the turbulent vapour field. Indeed, on a macroscopic scale turbulence provides large field fluctuations; droplets initially correlated with undersaturated cloud regions quickly evaporate, whereas droplets emerging from very supersaturated regions are able to grow enough to survive even if a dry region is crossed. As a result of the numerical analysis, a mean growth is observed, though classically forbidden, and size spectra remarkably broaden in time.

In these works the first step was the definition of the simplest turbulent model containing the basic elements needed to describe the condensation stage. Once a spreading mechanism has been identified, other mechanisms have been included and different settings have been analysed in order to test the robustness of the description. In particular, [CFMS05] compares the behaviours of droplets treated as tracers or inertial particles, finding that no appreciable difference is present; this is probably due to the small Stokes numbers involved during the condensational growth. In [CMTS07] a different turbulent framework is analysed: a two-dimensional convective regime is considered instead of a homogeneous isotropic one, but the completely different field statistics does not affect the results drawn in [CFMS05] in any way. Moreover, in [CMTS07] we added a further ingredient to the model, i.e. the droplet feedback on the vapour field; indeed, growing droplets feed on the surrounding vapour, subtracting it from the environment and thus slowing down their growth; as expected, both the mean growth and the spectrum broadening are reduced, but the important result is that they are still present, although now the environment becomes more and more undersaturated. Finally, in [LSTep] a different approach is provided in a three-dimensional isotropic framework: small clouds with increasing heights are considered and the evolution of the spectrum variances is extrapolated for larger clouds, resulting in a spectrum broadening comparable with the observed ones. Again, results are not sensitive to the different statistics. As a final remark, we

can state that the identified spreading mechanism seems to be robust.

In [CFMS05; CMTS07; LSTep] only the condensation stage is analysed. Droplets are supposed to have nucleated before and their initial size is large enough to neglect the curvature effect (and thus the solute effect too). However, a problem arises as droplets in dry regions head for a complete evaporation, so disappearing from the cloud. Indeed, since in real clouds only heterogeneous nucleation occurs, such an event should imply the release of the original CCN, which could bring to the nucleation of a new droplet. Thus, the description of the nucleation process is necessary in order to avoid the aforementioned unphysical mechanism. The turbulent model presented in this work is devoted to the study of both the nucleation and the condensation stage.

Here, our interest was different. The starting question was on whether turbulence can act as an effective CCN. Indeed, CCN provide a larger size and, in case, a powerful mechanism (the solute effect) for water vapour to condense. On the other hand, the large fluctuations of supersaturation provided by turbulence could allow vapour to condense on much smaller particles. Moreover, if the hygroscopic CCN is small, the nucleated droplet can only reach a stable small radius remaining a haze droplet; then, we wondered whether turbulent fluctuations can allow haze droplets to cross the curvature barrier and grow indefinitely as cloud droplets. Besides, the comprehension of the role played by turbulence in the earliest stages of cloud development also has important consequences for the problem of the transition from condensation to collection. Indeed, the immission of giant CCN in a non-precipitating cloud can change it in a precipitating one, but the presence of turbulence could avoid invoking their presence.

A quantitative measure of turbulence effects has been proposed in the first part of our work, where we considered the case of low droplet densities. In our numerical analysis we observed that a mean size growth is again present, although the environment is saturated on average. Such a growth is linear in time as in a classical framework where a positive mean supersaturation is present. Then, we rephrased our turbulent model with the equivalent classical model where the same results on droplet growth occur. This allowed us to define an equivalent CCN size induced by turbulence. Such a radius resulted as a decreasing function of turbulence intensity according to the power law $\varepsilon^{1/3}$ and one order of magnitude smaller than the smallest CCN put in the cloud, even in the least turbulent case and independently on the actual initial size. Therefore, turbulence allows droplets to nucleate around smaller particles and to cross the curvature barrier toward sizes compatible with the typical size where collection is the leading effect.

Moreover, we observed a strong spectrum broadening and the separation of droplet population into two families, the small stable haze droplets and the growing cloud droplets. Both results are in qualitative agreement with the experimental observations, where broad bimodal spectra emerge from the condensation

stage, thus providing a proper droplet distribution in order to trigger particle collisions effectively.

In this model the low number of droplets allowed us to neglect their feedback on the vapour field. In the second part of our work we took this effect into account by considering standard atmospheric values for the droplet-number density and we compared the results with the case where no feedback is involved. As expected and already observed for [CMTS07], the subtraction of vapour from the environment slows down the growth of the largest droplets and after one turnover time a stationary state is reached. All the observed effects are reduced by the inclusion of vapour absorption by droplets. Nevertheless, spectra still broaden in time remarkably. As in the low-density case, the more intensive the turbulence, the broader the spectrum. Furthermore, turbulence sustains a broad distribution in a stationary state, whereas in the classical picture droplet population tends to homogeneity. The stationary state is reached in a time compatible to the typical condensation times and can be replaced by the collection stage triggered by such a broad droplet distribution.

Our studies [CMT08; CMT09; CMTS07] concerning droplet growth in warm cumuli have been published in (or, the last, submitted to) international journals. In the future, two directions could be explored: an improvement of the present model with the inclusion of neglected mechanisms and, above all, the investigation of the role of turbulence in the collection stage.

In the former case, a better description of the nucleation stage is needed. Indeed, in our model the droplet-evolution law is not accurate enough for the smallest radii and the solute effect results stronger than in real clouds. Moreover, moist buoyancy would be considered, with the direct feedback of the droplets on the velocity field. Finally, a better numerical resolution (with a grid refinement in three dimensions and a higher number of particles) would help us to test the robustness of the results.

The study of the collection stage is still an open and challenging field. Here, several different effects are involved and many features are already not understood. In particular, turbulence could play a crucial role. On the one hand, it could enhance collisions by turbulent mixing; on the other hand, it could reduce droplet terminal velocities and thus the collision probability. A turbulent model for collection could also include electrostatic effects. Another interesting mechanism to be considered is the wake effect, which could enhance collisions by dragging smaller droplets into the wake of a larger one.

Bibliography

[BC01] J. L. Brenguier and L. Chaumat. "Droplet spectra broadening in cumulus clouds. Part I: broadening in adiabatic cores". In: *J. Atmos. Sci.* 58 (2001), pp. 628–641. See pp. 36, 37.

[BR74] Edwin X Berry and Richard L. Reinhardt. "An analysis of cloud drop growth by collection: part I. Double distributions". In: *J. Atmos. Sci.* 31.7 (1974), pp. 1814–1824. DOI: 10.1175/1520-0469(1974)031<1814:AAOCDG>2.0.CO;2. See p. 37.

[Bol59] R. Bolgiano. "Turbulent spectra in a stably stratified atmosphere". In: *J. Geophys. Res.* 64 (1959), pp. 2226–2228. See p. 50.

[CA89] William R. Cotton and Richard A. Anthes. *Storm and cloud dynamics*. San Diego: Academic Press, 1989. See p. 36.

[CFMS05] Antonio Celani, Gregory Falkovich, Andrea Mazzino, and Agnese Seminara. "Droplet condensation in turbulent flows". In: *Europhysics Letters* 70.6 (June 2005), pp. 775–781. DOI: 10.1209/epl/i2005-10040-4. See pp. 34, 38, 46, 47, 49, 55, 73, 78, 79.

[CMT08] Antonio Celani, Andrea Mazzino, and Marco Tizzi. "Droplet condensation in two-dimensional Bolgiano turbulence". In: *New J. Phys.* 10 (2008), 075021(1–16). See pp. 31, 34, 38, 56, 80.

[CMT09] Antonio Celani, Andrea Mazzino, and Marco Tizzi. "Droplet feedback on vapor in a warm cloud". submitted to *International Journal of Modern Physics B*. 2009. See pp. 34, 38, 56, 80.

[CMTS07] Antonio Celani, Andrea Mazzino, Marco Tizzi, and Agnese Seminara. "Droplet condensation in two-dimensional Bolgiano turbulence". In: *J. Turbul.* 8.17 (2007), pp. 1–9. See pp. 34, 38, 46, 49, 50, 55, 73, 78–80.

[FFS02] Gregory Falkovich, A. Fouxon, and G. Stepanov. "Acceleration of rain initiation by cloud turbulence". In: *Nature* 419 (2002), pp. 151–154. See p. 38.

[For96] Bengt Fornberg. *A practical guide to pseudospectral methods*. Vol. 1. Cambridge Monographs on Applied and Computational Mathematics. Cambridge: Cambridge University Press, 1996, pp. x+231. ISBN: 0-521-49582-2. See p. 60.

[Fri95] Uriel Frisch. *Turbulence*. The legacy of A. N. Kolmogorov. Cambridge: Cambridge University Press, 1995, pp. xiv+296. ISBN: 0-521-45103-5. See pp. 52, 60.

[GDHSFJ05] S. Ghosh, J. Davila, J. C. R. Hunt, A. Srdic, H. J. S. Fernando, and P. R. Jonas. "How turbulence enhances coalescence of settling particles with applications to rain in clouds". In: *Proc. Royal Soc.* 461 (2005), pp. 3059–3088. See p. 38.

[JM05] A. Jaczewski and S. P. Malinowski. "Spatial distribution of cloud droplets in a turbulent cloud chamber flow". In: *Quart. Journ. Roy. Met. Soc.* 131 (2005), pp. 2047–2062. See p. 37.

[KC01] P.K. Kundu and I.M. Cohen. *Fluids Mechanics*. 2nd. Elsevier Academic Press, 2001. See p. 42.

[KP92] Peter E. Kloeden and Eckhard Platen. *Numerical solution of stochastic differential equations*. Vol. 23. Applications of Mathematics (New York). Berlin: Springer-Verlag, 1992, pp. xxxvi+632. ISBN: 3-540-54062-8. See p. 60.

[Kol41a] A. N. Kolmogorov. "Local structure of turbulence in an incompressible fluid for very large Reynolds numbers". In: *Dokl. Akad. Nauk. SSSR* 30 (1941), pp. 299–303. See p. 60.

[Kol41b] A. N. Kolmogorov. "Energy dissipation in locally isotropic turbulence". In: *Dokl. Akad. Nauk. SSSR* 32 (1941), pp. 19–21. See p. 60.

[LP77] I. J. Lee and H. R. Pruppacher. "A comparative study on the growth of cloud drops by condensation using an air parcel model with and without entrainment". In: *Pure Appl. Geophys.* 115 (1977), pp. 523–545. See p. 37.

[LSTep] Alessandra S. Lanotte, Agnese Seminara, and Federico Toschi. "Cloud droplet growth by condensation in homogeneous isotropic turbulence". In: *J. Atmos. Sci.* (preprint). DOI: 10.1175/2F2008JAS2864.1. See pp. 34, 38, 46, 51–53, 55, 78, 79.

[LSWS07] K. Lehmann, H. Siebert, M. Wendish, and R. A. Shaw. "Evidence for inertial droplet clustering in weakly turbulent clouds". In: *Tellus B* 59.1 (2007), pp. 57–65. See p. 38.

[LTC00] S. Lasher-Trapp and W. A. Cooper. "Comparison of theory and observations of broadening of cloud droplet size distributions in warm cumuli". In: *Proceeding 13th Int. Conf. on Clouds and Precipitation*. 2000, pp. 90–93. See p. 36.

[MA08] Marco Martins Afonso. "The terminal velocity of sedimenting particles in a flowing fluid". In: *J. Phys. A: Math. Theor.* 41.38 (2008), 385501(1–15). DOI: 10.1088/1751-8113/41/38/385501. See p. 35.

[MAMOep] Marco Martins Afonso, Andrea Mazzino, and Piero Olla. "Renormalized transport of inertial particles in surface flows". In: (preprint). URL: http://arxiv.org/abs/0810.4949v1. See p. 35.

[PK97] H. R. Pruppacher and J. D. Klett. *Microphysics of Clouds and Precipitation*. Boston: Kluwer Academic Publishers, 1997. See pp. 18, 31, 36, 59, 60.

[Rog89] R. R. Rogers. "Raindrop collision rates". In: *J. Atmos. Sci.* 46 (1989), pp. 2469–2472. See p. 36.

[SC97] S. Sundaram and L. R. Collins. "Collision statistics in an isotropic particle-laden turbulent suspension. Part I: direct numerical simulations". In: *J. Fluid Mech.* 335 (1997), pp. 75–109. See p. 38.

[SRCV98] R. A. Shaw, W. C. Reade, L. R. Collins, and J. Verlinde. "Preferential concentration of Cloud Droplets by turbulence: effects in the early evolution of cumulus cloud droplet spectra". In: *Journ. Atmos. Sci.* 55 (1998), pp. 1965–1976. See pp. 37, 58, 70.

[Sha03] Raymond A. Shaw. "Particle-turbulence interactions in atmospheric clouds". In: *Annual Review of Fluid Mechanics* 35.1 (2003), pp. 183–227. DOI: 10.1146/annurev.fluid.35.101101.161125. See pp. 58, 70.

[Ste05] B. Stevens. "Atmospheric moist convection". In: *Ann. Re. Earth Planet. Sci.* 33 (2005), pp. 605–643. See p. 45.

[Tel96] J. W. Telford. "Clouds with turbulence; the role of entrainment". In: *Atmos. Res.* 40 (1996), pp. 261–282. See p. 37.

[Two59] S. Twomey. "The nuclei of natural cloud formation, Part II: The supersaturation in natural clouds and the variation of cloud droplet concentrations". In: *Geofis. Pura. Appl.* 43 (1959), pp. 243–249. See p. 32.

[VYBG02] P. A. Vaillancourt, M. K. Yau, P. Bartello, and W. W. Grabowski. "Microscopic approach to cloud droplet growth by condensation. Part II: turbulence, clustering and condensational growth". In: *J. Atmos. Sci.* 59 (2002), pp. 3421–3435. See pp. 38, 42, 52.

[VYG01] P. A. Vaillancourt, M. K. Yau, and W. W. Grabowski. "Microscopic approach to cloud droplet growth by condensation. Part I: model description and results without turbulence". In: *J. Atmos. Sci.* 58 (2001), pp. 1945–1964. See pp. 31, 38, 42, 52, 58, 70.

[WH06] John M. Wallace and Peter V. Hobbs. *Atmospheric Science: An introductory survey.* 2nd. U.S.A.: Acadamic Press, 2006. See pp. 37, 56.

[WMB06] M. Wilkinson, B. Mehlig, and V. Bezuglyy. "Caustic activation of rain showers". In: *Phys. Rev. Lett.* 97 (2006), p. 048501. See p. 38.

Part II

Exploration processes and stochastic Löwner evolution

Introduction

One of the most fascinating aspects of physics emerges when different systems of difficult comprehension display common fundamental symmetries which allow a simpler and more general description. A typical example is quantum mechanics, where the identification of invariances under some group transformations implies the conservation of particular charge currents. Very complex classical systems, such as the turbulent flows, where an infinite number of strongly interacting degrees of freedom is present, also display useful symmetries (on a statistical level). A special kind of symmetry, viz. *scale invariance*, is peculiar to a high number of phenomena of different disciplines, from critical to nonlinear systems: scale-invariant systems appear statistically identical when blown up.

In two dimensions locality often extends scale invariance to a wider class of conformal transformations that allow non-uniform rescaling. In this case conformal invariance holds: the system is invariant under local dilations and rotations. While in three (or more) dimensions conformal invariance turns out to be a too tight property and in one dimension a too loose one, in two dimensions the group is infinite dimensional and conformally invariant objects embrace a rich symmetry degree, revealing conformal invariance as a powerful tool in order to carry out analytical results for systems sharing the same symmetry.

Two-dimensional systems play an important role in physics. On the one hand they offer a useful and convenient laboratory for the study of systems with more dimensions. E.g. some properties of two-dimensional turbulence are also present in three dimensions and analogous tools can also be used. Moreover, the numerical analysis of two-dimensional systems is now affordable for small research groups with limited computational facilities. On the other hand, many physical systems, from the atmospheric perturbations to soap films, actually display a two-dimensional structure.

For a long time, physicists of different fields had been using different approaches to phenomena only apparently different. While critical phenomena were investigated by means of mean-field theories and Kolmogorov formulated the phenomenological theory of turbulence on the basis of dimensional arguments, in the same period the field theory was developed in quantum mechanics.

(a) Karel Löwner

(b) Oded Schramm

Figure 3.13: Löwner was born in Bohemia in 1893, but after the Nazi invasion he took refuge to the USA, where he was naturalized as Charles Loewner. In 1926 he derived the equation ruling conformal-map evolution. Oded Schramm (born in 1961) is the Israeli mathematician who invented SLE in 1999, by considering stochastic Löwner evolutions.

However, thanks to a process of cross-fertilization between distinct disciplines, tools developed in one field resulted very fruitful in the other, often revealing common symmetries between very far systems. An impressive example is offered by conformal invariance, which allows the classification of a huge amount of two-dimensional systems in universality classes labelled by one real parameter.

This is possible thanks to the *stochastic Löwner evolution* (SLE), which can be regarded as the dual theory of the conformal field theory, the latter giving a dynamical description of the system, the former a geometrical one. The idea for the definition of SLE comes from growth process on planar lattice domains. The simplest stochastic growth processes are *explorers*, i.e. a growing path on lattice edges emerging from a boundary point and wandering in the domain according to a given stochastic advancing rule, in general depending on the boundary conditions. A surprising property of the exploration paths is that they describe the critical interfaces of equilibrium clusters in statistical-mechanics models. Indeed, the measures of an exploration path and a critical interface coincide (when a correspondence exists). Thus, the physical content of a statistical-mechanics model can be described by the geometrical properties of a growing path.

Among the various properties displayed by exploration paths, two are very powerful when acting together, viz. Markovianity and conformal invariance. The former holds if the probability of a completed path, given its first n steps, is the same as the probability of starting a new exploration from the tip after n steps in the domain restricted by the first part of the curve. Markovianity is usually imposed by construction. On the contrary, the conformal invariance in

the continuous limit has to be proved for each explorer in every kind of lattice. If both properties hold, the scaling limit of the path describes an SLE curve.

SLE was defined by Oded Schramm in 1999 by considering stochastically growing curves in a complex domain (for this reason SLE is often referred to as Schramm–Löwner evolution). Instead of describing their differential evolution, Schramm exploited a Löwner approach giving the evolution law of the conformal mapping removing the curve from the domain. SLE curves constitute a family in the diffusive parameter $\varkappa$, which labels the universality classes of two-dimensional conformally-invariant systems. However, a corresponding family of discrete explorers does not exist, for the time being. Some families arise from some classes of spin models, but the definition of an exploration path by means of a statistical-mechanics model is an involute and fruitless way.

Our work on discrete growth process aimed at defining such a family by generalizing the well-known harmonic explorer. Indeed, its simple exploration rule based on the launch of a random walk at each step can be slightly modified by upholding the random-walk outcome with a probability p. Such a definition guarantees Markovianity and, likely, conformal invariance. Moreover, the parameter p can be related to $\varkappa$. The relation between them is conjectured and numerically tested in our work.

This part is organized as follows.

In chapter 4 we deal with discrete growth processes on a planar lattice. In particular, our focus is on the simplest class of growth process, i.e. the exploration processes, which describe the growth of a curve emerging from a boundary point. Many classical examples (such as percolation and the Ising model) are reviewed and compared with a corresponding statistical-mechanics description, noticing that the measure of the exploration paths is the same as that of the cluster interfaces in the corresponding statistical-mechanics model. Two important properties of the exploration paths, Markovianity and conformal invariance, are highlighted and the search for a continuous family of explorers with both properties is discussed.

Chapter 5 is devoted to the definition of the stochastic Löwner evolution as a continuous growing curve displaying both Markovianity and conformal invariance. The curve is described by the evolution law of the conformal map which removes it from the complex domain. Therefore, details about particular conformal mappings, such as Löwner chains and Schwarz–Christoffel mappings, are provided. Then, the main properties of $\mathrm{SLE}_\varkappa$ curves are investigated with respect to the real positive parameter $\varkappa$. In particular, the fractal dimensions of their traces are computed, together with those of some subsets of the trace. Finally, the famous crossing formula is derived.

In chapter 6 a new class of discrete explorers is defined. First, the well-known

case of the harmonic explorer is analysed in order to extract what features can ensure the scaling limit for a discrete process. The exploration rule based on random walks, which are conformally invariant (apart from a time dilation), is identified as the key ingredient. Then, the same rule is slightly modified via a real function f in order to define the new class of stretched harmonic explorers. The case where f is linear leads to the definition of the subclass of overruled harmonic explorers, which are parametrized by the uphold probability p. Such explorers are the subject of our work. Their convergence to $\mathrm{SLE}_\varkappa$ is conjectured together with a guessed relation between the two parameters p and $\varkappa$. The last part of the chapter is devoted to the search for a proof of the conjecture.

Chapter 7 presents the numerical analysis on our realizations of the overruled harmonic explorers. Before dealing with it, some technical details are given on how the exploration process is actually implemented on the honeycomb lattice. In particular, some problems arising in a non-compact domain are fixed. Then, an atlas of explorer samples in different domains is provided. The conformal invariance of the new class of explorers is tested via the crossing probabilities. In the rest of the chapter the relation between p and $\varkappa$ is tested via different means, with a final comparison between conjectures and numerical results.

Finally, a summary of this part is provided (page 191). There, some conclusions are drawn and some perspectives proposed.

Chapter 4

Discrete growth processes

The name of discrete growth processes embraces a huge amount of stochastic processes on lattice domains. As a common feature, they can be dynamically described by the progressive invasion which takes place when an object lying on the domain starts to expand according to some stochastic law. The simplest example is a polygonal chain emerging from a lattice node: step by step, its tip occupies one of the adjacent vertices following some stochastic rule, so describing a growing path on the edges of lattice faces (or an *exploration process*). Another simple process is the growth of clusters, occurring when adjacent lattice faces are, say, coloured red with some assigned probability (or associated to a fixed value of a physical observable, such as the spin). In several cases, only changing little details in the definition of the growth process leads to a system with very different features.

The interest in discrete growth processes comes from many fields of both mathematics and physics and the study of their properties has become a common goal, reaching a fast development in the last few years. The crucial aspect is that growth processes are closely related to the critical systems of statistical mechanics. In particular, random curves and random clusters on a lattice can describe interfaces and clusters, respectively, of critical systems, such as an Ising model at the critical point (which is the simplest model for the phase transition between paramagnetism and ferromagnetism). The idea is to investigate the geometrical properties of growing objects in order to extract, say, the critical exponents, rather than to compute them from the a cumbersome partition function.

Moreover, taking the continuous limit of some special classes of two-dimensional discrete growth processes allows a geometrical study of many physical systems. The most remarkable continuous limit is the stochastic Löwner evolution or Schramm–Löwner Evolution (SLE, presented in chapter 5), which can be viewed as the dual mathematical theory of the conformal-field theory (CFT).

Giving only some examples, SLE curves are involved in the study of quantum gravity, turbulence, diffusion, fractures.... Another notable continuous limit is the diffusion-limited aggregation (DLA), where a diffusive growth takes place. A nice example of DLA is the growth of a snowflake.

The richness and fertility of discrete growth processes is due to the symmetries systems can share. Indeed, physical systems from different fields and with different definitions are discovered to belong to the same class of universality according to some symmetry group. Two powerful properties are displayed by many two-dimensional growth processes, viz. Markovianity and conformal invariance. The former holds when the probability of a specific growth from each step on is the same as the same growth imagined as starting in the cut domain at that step. The latter is present if the continuous limit of the system is invariant under local rotations and scale transformations. The presence of both properties is the essential element for the convergence of the process to an SLE.

This chapter provides a brief review of some famous growth processes. Our aim is not to offer a deep description of this systems, but to give a qualitative idea of their construction and main properties. In particular, we will show the parallelism between exploration processes of the domain and statistical-mechanics realizations. More details about growth processes and their relation with SLE and CFT can be found in [BB06; Car05] (to which this chapter is inspired) and references therein. In sections 4.1 and 4.3 some geometrical examples are considered, viz. the critical percolation, the harmonic explorer and the self-avoiding walk. Section 4.2 presents two examples from statistical mechanics, viz. the Ising model and the $\mathrm{O}(n)$ model. Finally, in section 4.4 processes other than growing curves are mentioned.

4.1 Percolation

Percolation processes are surely the simplest examples among both discrete growth processes and statistical-mechanics systems. Besides, they contain all the essential features we are interested in and are excellent examples in order to understand the parallelism between geometry and statistical mechanics. Therefore, we will deal with both approaches. From now on we will only consider two-dimensional processes.

First, we have to define the domain where the stochastic processes take place. A planar lattice domain $\mathcal{D}^\#$ is composed by N faces (or rather, their centres, which constitutes the *main lattice*) and their vertices (the *dual lattice*). For our purposes, the domain can be non-compact, but must have a boundary $\mathcal{B}^\#$ and be simply connected. Then, defining $\mathcal{D}^\#$ means assigning the shape and the size of both the faces and the domain together with some boundary conditions.

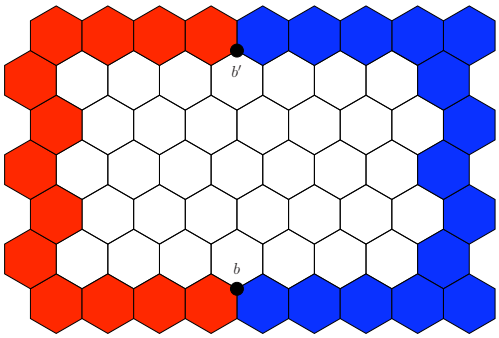

Figure 4.1: A lattice domain $\mathcal{D}^{\#}$, here a honeycomb rectangle, has admissible boundary conditions if they change only in two points, say b and b'. In this way, the domain boundary is split in two parts, a left boundary with red (e.g. negative-spin) condition and a right boundary with blue (e.g. positive-spin) condition.

A common and convenient choice is the *honeycomb lattice*, where the faces are regular hexagons, whose sides have length l_6. The main lattice is the hexagonal lattice formed by hexagon centres, whereas the dual lattice is the triangular lattice formed by hexagon vertices. In this chapter we will only consider compact domains, such as the rectangular domain shown in figure 4.1. Boundary conditions are given by fixing the configuration of boundary faces. A configuration can be regarded as a choice of colour (e.g. blue or red) or the value of a physical observable (such as the spin $s = \pm 1$). Standard boundary conditions, often called *admissible boundary conditions*, provide for a red boundary of connected red faces (*left boundary*) separated by vertices b and b' from a blue boundary of connected blue faces (*right boundary*). This is the common set-up of both the geometrical system and the statistical-mechanics one.

4.1.1 Critical percolator

Let us start a growth process on lattice edges from one of the two point where boundary conditions change, say point $r_0 \equiv b$ on the lower boundary (see figure 4.2a). The first step is the choice of the colour of face v_1 in front of r_0. We colour it red with probability

$$P_- = p_c = \tfrac{1}{2}$$

If the outcome is red, the explorer turns right to the adjacent vertex to the right of r_0; if the outcome is blue, the explorer turns left. Then, the new tip is located in r_1 and a new face (v_2) has to be coloured following the same rule. If the explorer encounters a face which has been already coloured either red or blue, it turns either right or left, respectively. As the explorer advances, an exploration

path is drawn with red faces lying on its left and blue faces on its right, as sketched in figure 4.2b. It is worth to notice that, by construction, such an exploration path can neither intersect itself (it is *self-avoiding*) nor escape from the domain (unless the explorer has reached the other boundary point $r_* \equiv b'$ where boundary conditions change). Indeed, there is no way for the explorer to go through two faces of the same colour, because it is forced to turn in the opposite direction. Therefore, after a certain number N_{st} of steps the explorer must have reached the exit point r_* (see figure 4.2c). Indeed, there is always at least one path joining r_0 with r_* and leaving only red faces on the left and only blue faces on the right. For reasons we will explain soon, this stochastic process is called *critical percolator*.

The assigned rules define a probability distribution, i.e. a measure, over the ensemble of all the possible paths (which are finite in a compact domain). More precisely, the probability of a path $\gamma_* = \gamma_{N_{\mathrm{st}}}$ from r_0 to $r_* = r_{N_{\mathrm{st}}}$ is

$$\mu(\gamma_{N_{\mathrm{st}}}, \mathcal{D}^{\#}) \coloneqq \mathscr{P}[\gamma_{N_{\mathrm{st}}} \in \mathcal{D}^{\#}] = \tfrac{1}{2}^{N_{\mathrm{st}}} = p_{\mathrm{c}}^{N_{\mathrm{st}}}$$

Therefore, it only depends on path length. The growth process is completely characterized by its specific measure, which highlights symmetries and properties of the system.

The critical percolator displays three remarkable properties. The most direct is *locality*: if we modify the domain (e.g. by moving the boundary or removing a part of the domain) in a region not yet reached by the explorer, the measure is not affected. Indeed, the advancing rule is local, not depending on boundary conditions (unless a boundary is reached). Alternatively, locality can be explained by the measure itself, which only depends on the number of steps, not on what happens far from the path:

The second fundamental property is the *domain Markov property*: if we split the completed path in two parts, the probability of the latter conditioned to the former in the initial domain is the same as the probability of the latter in a *cut domain*, where the former is removed. This kind of Markovianity is slightly different from the one of stochastic processes. Indeed, a Markovian process X_t is a memoryless stochastic process, where the previous story does not affect the actual probability:

$$\forall s \leqslant t \quad \mathscr{P}[X_t | X_r, r \leqslant s] = \mathscr{P}[X_t | X_s]$$

Domain Markovianity expresses the memorylessness of the growth process. During the exploration process the available domain is progressively reduced. The configuration of the domain after n steps can also be viewed as the starting configuration for a new explorer emerging from point r_n. Under this interpretation,

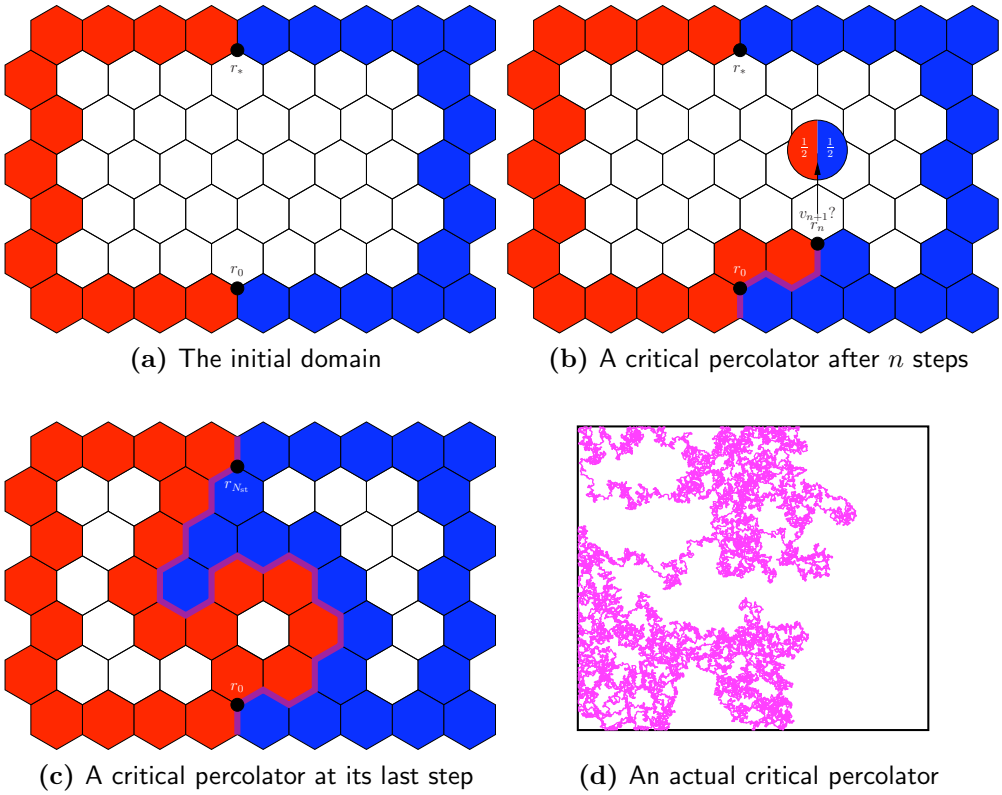

(a) The initial domain (b) A critical percolator after n steps

(c) A critical percolator at its last step (d) An actual critical percolator

Figure 4.2: A critical percolator (magenta) emerges from vertex r_0 on the boundary (figure (a)). At each step a coin is flipped in order to determine the colour of the face in front of the percolator tip and, consequently, the turn direction (figure (b)). Sooner or later, the critical percolator reaches the other vertex (r_*) separating red and blue boundaries; the resulting exploration path leaves red faces on its left and blue faces on its right (figure (c)). In figure (d) an actual sample of critical percolator is shown; it corresponds to a completed exploration in a rectangle with 500×500 hexagons.

path boundaries at step n become part of the boundaries of the cut domain. Domain Markovianity states that continuing the exploration in the initial domain is the same as starting a new exploration in the domain inherited from the previous exploration. The critical percolator gets this property by construction. For the sake of simplicity, in the following the domain Markov property will simply be called Markovianity.

Finally, in the continuous limit the critical percolator displays *conformal invariance*, i.e. its measure is invariant under local scale transformations and rotations. This property is the most delicate, because it involves a limit operation (for an infinite number of faces with a side converging to 0). Therefore, proving its pres-

ence can be very difficult and in many cases it is only conjectured on the basis of numerical analyses. The critical percolator is one of the few cases where this challenge was completed (thanks to Stanislav Smirnov's work [Smi01; Smi05]). Intuitively, if the measure only depends on path lengths, it is preserved in the limit of $N \to \infty$ and $l_6 \to 0$ with $Nl_6 \sim 1$. The great interest in conformal invariance follows from the very powerful symmetry it allows in two dimensions.

Other properties are displayed by the critical percolator, such as the invariance under reflections. However, the three considered above are the most interesting in order to compare discrete and continuous growth processes. Let us summarize them with a formal notation.

Property 4.1 (Domain Markovianity)**.**

$$\mu\left(\gamma_n|\gamma_m, \mathcal{D}^\#\right) = \mu\left(\gamma_n \setminus \gamma_m, \mathcal{D}^\# \setminus \gamma_m\right)$$

where $\mathcal{D}^\# \setminus \gamma_m$ is the cut domain where the boundary of γ_m becomes part of the domain boundary.

Property 4.2 (Conformal invariance)**.**

$$\mu\left(\gamma_n, \mathcal{D}^\#\right) = \mu\big(g(\gamma_n), g(\mathcal{D}^\#)\big)$$

where $g : \mathcal{D}^\# \to g(\mathcal{D}^\#)$ is a conformal map. Here, the domains are considered as embedded in the complex plane ($\mathcal{D}^\# \subset \mathbb{C}$) and the equality is intended in the continuous limit of infinite faces and zero lattice-spacing ($N \to \infty$, $l_6 \to 0$ with $Nl_6 \sim 1$)

Property 4.3 (Locality)**.**

$$\mu\left(\gamma_n, \mathcal{D}^\#\right) = \mu\left(\gamma_n, D'^\#\right)$$

where $\mathcal{D}^\#$ and $\mathcal{D}'^\#$ are two admissible domains sharing at least the same exploration path γ_n ($\gamma_n \subset \mathcal{D}^\# \cap \mathcal{D}'^\#$).

4.1.2 Critical percolation

Starting from the same initial domain $\mathcal{D}^\#$ shown in figure 4.1 we can define a different stochastic system, without any growth or exploration concept. Suppose to colour all the internal faces either blue or red (or to mark them with spin ± 1) independently with the same probability $p_c = \frac{1}{2}$ (as sketched in figure 4.3). The final configuration is a realization of *critical percolation on independent sites*. Such a system can be useful in the study of the infiltration of fluids through granular materials, whence the name of percolation.

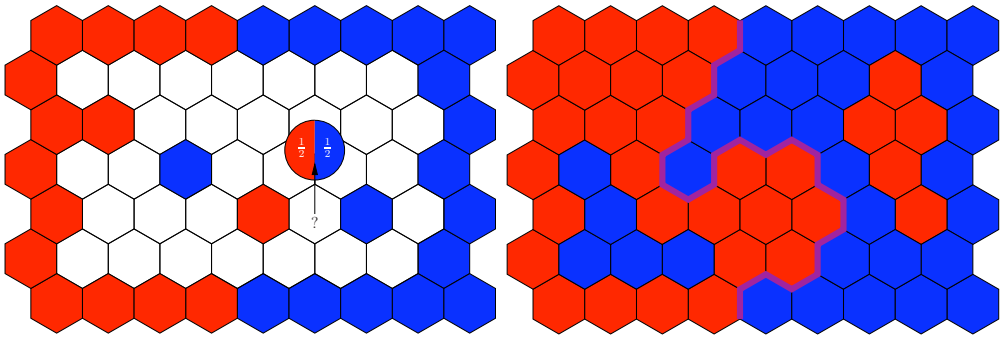

(a) Critical percolation in progress (b) A realization of critical percolation

Figure 4.3: A realization of critical percolation is simply obtained by flipping a coin for each internal face independently (figure (a)). In the final configuration the whole domain is coloured and the faces form clusters of the same colour (2 red and 2 blue in figure (b)). With admissible boundary conditions, among all the cluster interfaces there is only one interface connecting boundaries (magenta): its measure is the same as that of a completed critical-percolation exploration.

Every realization presents a certain number of *clusters*, which are the connected regions of the domain formed by faces of the same colour. E.g. in figure 4.3b 4 clusters (2 red and 2 blue) can be easily detected. Clusters are the main subject of study, not only for critical percolation. Indeed, they contain the whole statistical information of the system. One of the most famous formulae in lattice stochastic processes, the *Cardy crossing formula*, concerns the probability that a critical-percolation cluster connects two disjointed part of the boundary. We will deal with its generalized continuous version in section 5.2.5; in section 7.3 our numerical analysis of crossing probabilities will be presented.

The clusters of faces are separated by polygonal chains on lattice edges. Studying cluster properties is the same as studying the statistics of these curves. In particular, from figure 4.3b it is clear that there is always only one path connecting the two boundary points where boundary conditions change. Which is the probability of this path? Not surprisingly, it is the same as the probability that a critical percolator had covered the same path. From a statistical point of view, there is no difference in generating a path by either an exploration process or a realization of an equilibrium model from statistical mechanics. This crucial statement is basic in our work. Owing to this equivalence, in the following we will indifferently refer to either critical percolator or critical percolation.

4.1.3 Unfair percolation

If we slightly modify the advancing rule of the exploration process, we can test how sensitive the above properties are with respect to the definition of the process. The simplest generalization can be obtained by colouring face v_{n+1} red with a different probability

$$P_- = p \neq \tfrac{1}{2}$$

At each step, this corresponds to flipping an unfair coin, whose red side has weight p. Alternatively, the same rule can be exploited in order to mark independently all the internal faces; the final configuration is a realization of *unfair-coin percolation* (or unfair percolation). The resulting measure is

$$\mu(\gamma_{N_{\rm st}}, \mathcal{D}^{\#}) = p^{N_-}(1-p)^{N_{\rm st}-N_-}$$

where N_- is the total number of red outcomes (i.e. of right turns).

As p spans the range $[0,1]$, a one-parameter family of explorers is covered. In the two extreme cases at $p = 0$ and $p = 1$ the exploration path is forced to follow the left or the right boundary, respectively. Indeed, in the former case, at the first step the face in front of the tip is coloured blue and the explorer turns left. Then, it faces a red boundary and turns right. This two steps are repeated up to the exit point. Therefore, reflection symmetry is broken. This is true for each unfair-percolation system, where a drift proportional to $p - p_{\rm c}$ is present. There is only the exception at the critical value $p = p_{\rm c} = \frac{1}{2}$. This explains why at this value percolation is critical: if we consider an infinite domain, at $p < p_{\rm c}$ the existence of infinite red clusters has zero probability, whereas at $p \geqslant p_{\rm c}$ they surely exists.

Concerning the properties of unfair percolation, locality and Markovianity still hold. Indeed, the advancing rule is still local and independent of boundary conditions. On the contrary, the conformal invariance is broken, essentially as a consequence of reflection-symmetry breakdown.

4.2 Spin models

Exploiting statistical-mechanics systems, it is possibile to assign less trivial probabilities of colouring a face red. In spin models this probability is linked to the mean magnetisation of the face with respect to the global spin configuration. Therefore, the knowledge of the partition function of the system is required.

4.2.1 Ising model

Let us consider the two-dimensional version of the celebrated Ising model, which is the prototype of any statistical-mechanics system. In this model each

lattice face z is a spin site with available values $s(z) = \pm 1$. Each pair of adjacent faces is coupled via the factor βJ, i.e. the interaction is between nearest neighbours. Then, $\beta J \sum_{<zz'>} s(z)s(z')$ is the usual Ising energy function ($\sum_{<zz'>}$ is intended over adjacent sites). Expressing the sum over all the possible configurations via the trace operator $\mathrm{Tr} = \prod_z \big(\frac{1}{2} \sum_{s(z)}\big)$, the resulting partition function is

$$Z_{\mathrm{Is}} = \mathrm{Tr}\, \mathrm{e}^{\beta J \sum_{<zz'>} s(z)s(z')}$$

or, after some algebra and a renormalization,

$$Z_{\mathrm{Is}} = \mathrm{Tr} \prod_{<zz'>} \big(1 + ts(z)s(z')\big) \tag{4.1}$$

where $t = \tanh \beta J$ is a temperature-like parameter. At infinite temperature, i.e. at $t = 0$, the interaction vanishes and the system is completely disordered. Indeed, the spin on each site is independent of the neighbouring spins and is positive with the same probability as it is negative. In other words, in the high-temperature limit the critical percolation is restored. The opposite case at zero temperature, i.e. at $t = 1$, presents a long-range order. The system knows a phase transition at a critical value t_{c}.

Then, we can define a new exploration process, the *Ising explorer*, by colouring the face in front of the tip red (or by marking it with -1) with probability

$$P_{-}(v_{n+1}) = \tfrac{1}{2}\big(1 + m(v_{n+1})\big)$$

Here, v_{n+1} is the face to be coloured after n steps and $m(v_{n+1})$ is the mean magnetisation of its Ising spin, in an Ising model defined in the whole of the cut domain, with the specified boundary conditions (such as those illustrated in figure 4.2b):

$$m(v_{n+1}) = \frac{\mathrm{Tr}\Big(s(v_{n+1}) \prod_{<zz'>} \big(1 + ts(z)s(z')\big)\Big)}{\mathrm{Tr} \prod_{<zz'>} \big(1 + ts(z)s(z')\big)} \tag{4.2}$$

Again, if v_{n+1} is coloured red, the explorer turns right. The critical percolator is recovered at $t = 0$.

Once the explorer has reached the exit point r_*, the completed exploration path has the same measure as the interface between the red and the blue clusters connected with the boundary in a realization of an equilibrium Ising model in the initial domain. The parallelism between exploration processes and statistical-mechanics model is confirmed. However, this case shows that the computational cost of the algorithm is not the same. Indeed, when $t > 0$ actually carrying out the algorithm would be much harder, because simulating the equilibrium

Ising model is required at every step, although the domain narrows step by step. Clearly, it would be easier to simulate an equilibrium Ising model in the initial domain once and for all, sample one configuration and draw the only path connecting r_0 with r_*. Nevertheless, if the domain is not compact, one would prefer to carry on an exploration path instead of simulating the equilibrium system in the whole infinite domain. This is a crucial motivation for our work, as we will see.

Let us try to explain why the equality between the two measures holds. The initial configuration space has 2^N points, corresponding to all possible values of the N free spins in the lattice. The Ising weights define a measure on this space. As the path grows, a *filtration* process occurs: the configuration space is narrowed down by fixing the spin in front of the tip. At the same time, the measure is conditioned in such a way that the spins either side of the exploration path become fixed. The expectation value of the spin at v_{n+1} can be evaluated either in terms of this conditioned measure in the cut domain or in terms of original measure in the whole domain. Thus, the Ising explorer is Markovian. Moreover, its conformal invariance is also observed (but not yet proved).

The computation of $m(v_{n+1})$ highlights the sensitivity of this model with respect to what happens in the whole domain. Since all the sites are involved in (4.2), even modifying a faraway region of the domain affects the mean magnetisation in front of the tip. Therefore, the Ising explorer is not local. Actually, locality is a special property, displayed only by percolation (only by critical percolation among the Markovian and conformally invariant explorers).

4.2.2 $\mathrm{O}(n)$ model

Ising partition function (4.1) can be thought of in an alternative way by associating each coupling $ts(z)s(z')$ to the edge between faces z and z'. Expanding the product in (4.1) results in a sum where each term involves a certain number of edges. Thus, each term selects a subset of lattice edges, the graph $\mathcal{G}^{\#}$, composed by all the edges (zz') with corresponding factor $ts(z)s(z')$ contained in that term. After the computation of the trace only the factors associated to not-intersecting loops survive in each term, together with the factors associated to open paths beginning and ending at a boundary (with our boundary conditions there is only one open path of this kind). If each graph $\mathcal{G}^{\#}$ contains $n_{\mathrm{lo}}(\mathcal{G}^{\#})$ loops (including the open path connecting boundaries) involving $N_{\mathrm{lo}}(\mathcal{G}^{\#})$ edges altogether (the total length), the Ising partition function is simplified in

$$Z_{\mathrm{Is}} = \sum_{\mathcal{G}^{\#}} t^{N_{\mathrm{lo}}(\mathcal{G}^{\#})}$$

When t is small, the mean length of a single loop is small. Thus, the cluster enclosed by it is small and the system has a disordered configuration. Above a critical value t_c, the mean length diverges, huge clusters are present and the system has a long-range order.

This approach describing a *loop gas* system is useful in order to generalize the Ising model by weighting each loop with a *fugacity* n:

$$Z_{\mathrm{O}(n)} = \sum_{\mathcal{G}^\#} n^{n_{\mathrm{lo}}(\mathcal{G}^\#)} t^{N_{\mathrm{lo}}(\mathcal{G}^\#)} \tag{4.3}$$

This partition function can be regarded as coming from that of an Ising-like model where the spins $\boldsymbol{s}(z) = (s_1(z), \ldots, s_n(z))$ are n-component vectors:

$$Z_{\mathrm{O}(n)} = \mathrm{Tr} \prod_{<zz'>} \left(1 + t\boldsymbol{s}(z) \cdot \boldsymbol{s}(z')\right) \tag{4.4}$$

where $\mathrm{Tr}\, s_i(z) s_j(z) = \delta_{ij}$. Indeed, following the same procedure as before, the same set of closed loops (and open paths connecting boundaries) is obtained. The only difference is that the sum over the last spin involves a factor n. This model is called the $\mathrm{O}(n)$ *model* because it is symmetric under spin rotations. Clearly, partition function (4.4) makes sense only if n is a positive integer, whereas the loop-gas version in (4.3) is valid for real values of the fugacity. In the latter case a one-parameter family of statistical-mechanics models is generated. For some special values of n well-known models are restored:

- $n = -2$: loop-erased random walk or LERW ([LSW04a; Sch00])
- $n = 0$: self-avoiding walk or SAW (section 4.3.3)
- $n = 1$: Ising model (section 4.2.1)
- $n = 2$: XY model ([Ber70; KT73])
- $n = 3$: Heisenberg model ([SK66; Tri79])

For $n \in [0, 2]$ it is known [Nie82] that the critical point is at $t_c = \left(2 + (2 - n)^{1/2}\right)^{1/2}$; at larger t, the system is in its dense phase, still showing a critical behaviour.

In the same way as for the Ising model, an exploration path can be defined, provided that the Boltzmann weights of the Ising model are substituted by those of the $\mathrm{O}(n)$ model. Again, the completed exploration process from r_0 to r_* describes the only boundary-connecting interface of an $\mathrm{O}(n)$ realization in the whole domain (the only with our boundary conditions, which change sign only

in r_0 and r_*). Thus, the path shares the same measure and properties of the corresponding statistical-mechanics model.

Once more, also the $\mathrm{O}(n)$ model is Markovian, but not local. This follows from reasons analogous to those given in the Ising case. Concerning the difficult challenge of proving conformal invariance, the scaling limit of the $\mathrm{O}(n)$ model is conjectured to display it at $n \in [-2, 2]$ (but is proved only in few cases). Therefore, in this range a one-parameter family of Markovian and conformally invariant paths is defined.

However, the $\mathrm{O}(n)$ model is not the only family with this features. Another important continuous family of Markovian and conformally invariant paths can be defined in a similar way from the famous *q-state Potts model* [BKW76]. In this model, each lattice site is associated to a one-dimensional spin which can take values in $\{1, 2, \ldots, q\}$, where q is a positive integer. In the resulting partition function q plays a role similar to that of n in the $\mathrm{O}(n)$ model. As in the latter case, the partition function is still valid for real values of q. Under some conditions, the two models can be considered as dual: in the scaling limit (if it exists), the critical interfaces between the so-called *Fortuin–Kastelyn clusters* [FK72] in the Potts model at its critical point are the same as the closed loops of the dense phase of the $\mathrm{O}(n)$ model with $n = \sqrt{q}$.

The great interest in continuous families of discrete paths is motivated by their possible scaling limit. Indeed, some discrete interfaces are proved to converge to SLE curves, as we will see. Since SLE is a one-parameter family in the diffusivity $\varkappa$, the question on whether it exists a discrete corresponding family naturally arises. The $\mathrm{O}(n)$ model and the Potts model are good candidates, but defining an exploration path based on them is a bit cumbersome and requires a high computational cost. The aim of our work is just to introduce a new class of more agile explorers as a discrete counterpart of SLE.

4.3 More exploration processes

In section 4.1 we introduced the concept of exploration processes by presenting the simplest available example, the critical percolation, which is Markovian, conformally invariant and local. Then, we tried to generalize it in order to get a class of more general explorers. Unfortunately, conformal invariance is lost when the fair-coin toss needed to determine the new explorer direction is substituted by an unfair-coin toss, as in the unfair percolation. An alternative way of generalizing the critical percolator comes from statistical mechanics (section 4.2). The exploration rule can be linked to a realization of a statistical-mechanics equilibrium model in the cut domain. Locality is lost, but Markovianity and conformal invariance are preserved, although the latter is only conjectured in the majority

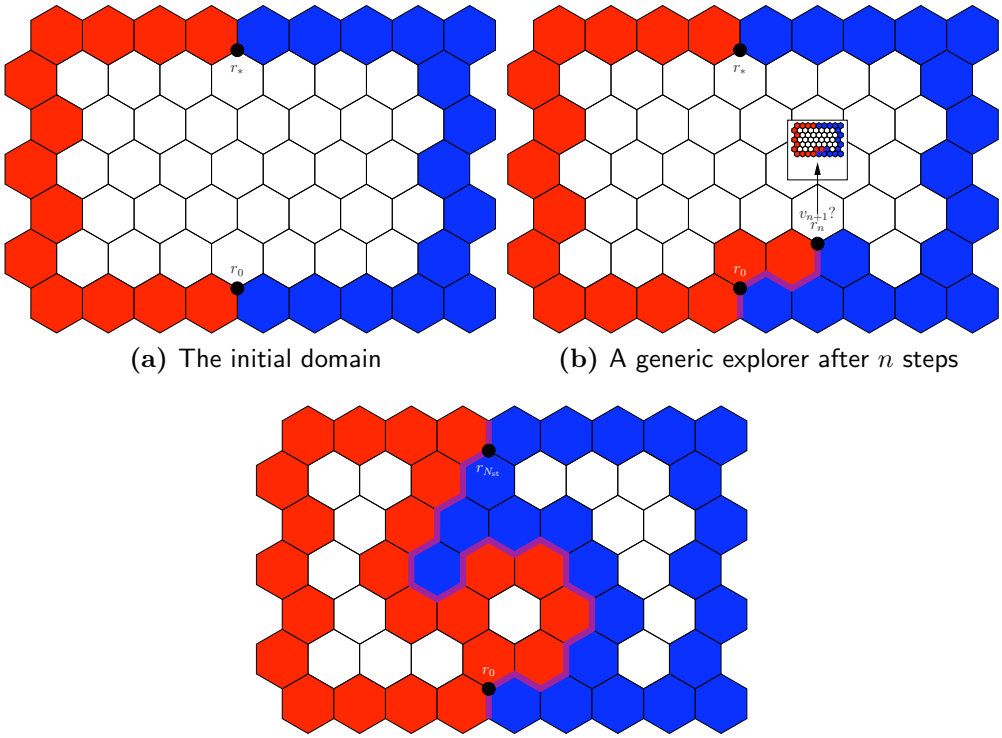

(a) The initial domain

(b) A generic explorer after n steps

(c) A generic explorer at its last step

Figure 4.4: A discrete exploration process is defined in a lattice domain, here a honeycomb rectangle with the boundary conditions shown in figure (a) (left red, right blue). The explorer (magenta) advances turning right with a probability depending on boundaries, where both sides of the path are included (figure (b)). Finally, in figure (c) the exploration path is completed, leaving red and blue faces on its left and right, respectively.

of cases. Moreover, sharing the same measure, exploration paths describe the critical interfaces of the clusters of the statistical-mechanics model.

However, exploration rules coming from these models are not very easy to implement. Then, it could be more convenient to define simple geometrical rules, without involving statistical mechanics. The scheme is the same: in a honeycomb lattice two boundary points r_0 and r_* are selected; the boundary conditions are chosen red on their left and blue on their right (figure 4.4a); the explorer emerges from r_0 and lies on lattice vertices (following edges); the explorer advances in the domain by turning either left or right depending on whether the tip faces a blue or a red hexagon; at step $n > 0$, the hexagon in front of the explorer tip is coloured red (if it has not been yet coloured) with probability $P_-(v_{n+1})$; $P_-(v_{n+1})$ defines the exploration rule and, hence, the kind of explorer and generally can depend on

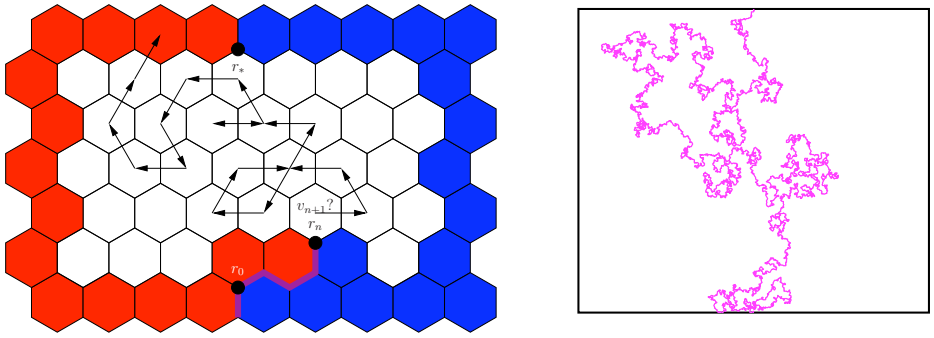

(a) A harmonic explorer after n steps **(b)** An actual harmonic explorer

Figure 4.5: At each step the harmonic explorer (magenta) determines its new direction according to the outcome of a random walk emerging from the face in front of its tip (figure (a)). If the random walker hit a red boundary first, face v_{n+1} is coloured red and the explorer turns right, otherwise left. The random walk is intended in the cut domain where both sides of the exploration path are part of the boundary. In figure (b) an actual sample of harmonic explorer is shown; it corresponds to a completed exploration in a rectangle with 500×500 hexagons.

the boundary conditions of the cut domain (figure 4.4b); the cut domain is the domain where the boundary is composed by the initial boundary and the path boundaries, i.e. by all the coloured faces; sooner or later, r_* is finally reached (figure 4.4c). Colours can be viewed as representative of spins, but also of other quantities, as we will see soon.

This procedure ensures Markovianity. On the other hand, conformal invariance has to be verified case by case. In addition, each explorer displays a specific property which singles out it, such as locality for the critical percolation. It is worth noticing that this is not the only way of defining an exploration process: different lattices, boundary conditions, starting and exit points can be chosen. The scaling limit of the latter explorers can display different properties, although in some ways connected to those of the former explorers.

4.3.1 Harmonic explorer

Let us define a new explorer, the so-called *harmonic explorer*, which will be the basis for our work. The exploration rule is assigned as follows: at each step, a random walker on faces is started from the face to be coloured; by definition, step by step the random walker moves to one of the adjacent faces with equal probability; eventually it will hit the boundary, either that of the initial domain or the left and right sides of the existing path; if it hit the red boundary first,

the face is coloured red, otherwise blue. Thus, at step n the harmonic explorer turns right with the same probability of a random walker from v_{n+1} to the red boundary, as schematized in figure 4.5a. Alternatively, the probability $P_-(v_{n+1})$ of colouring v_{n+1} red can be viewed as the solution $H_n(v_{n+1})$ of the discrete Laplace equation $\triangle H_n(z) = 0$ with the specified boundary conditions (1 on red, 0 on blue). Indeed, in section 6.1.1 it is proved that the probability of a random walk between v_{n+1} and the red boundary satisfies the Laplace equation. This explains the name of harmonic explorer.

The space of all the possible paths is composed by 2^N points and, hence, is the same as in percolation and Ising model, but the weights are different. Now, the question is whether these weights correspond to those of the interfaces in some equilibrium process. The harmonic probability of a random walk between face z and the red boundary can be rearranged in an Ising-like form as

$$P_-(v_{n+1}) = H_n(v_{n+1}) = \tfrac{1}{2}\big(1 + m(v_{n+1})\big)$$

with again $\triangle m(z) = 0$ (but boundary conditions $m = \pm 1$). If we define a continuous variable $\varphi(z)$ on faces, $m(v_{n+1})$ will be the expectation value of $\varphi(v_{n+1})$ with respect to the Gibbs measure $\mathrm{e}^{-\beta\sum_{z,z'}(\varphi(z)-\varphi(z'))^2}$:

$$m(v_{n+1}) = \frac{\mathrm{Tr}\Big(\varphi(v_{n+1})\mathrm{e}^{-\beta\sum_{z,z'}(\varphi(z)-\varphi(z'))^2}\Big)}{\mathrm{Tr}\,\mathrm{e}^{-\beta\sum_{z,z'}(\varphi(z)-\varphi(z'))^2}}$$

which returns a Gaussian model. Therefore, the exploration process can be carried on by simulating an equilibrium configuration at each step and turning either left or right according to the sign of the mean magnetisation. The resulting measure is the same as that of the harmonic explorer. Moreover, one path separating negative and positive regions can be identified in each realization of the Gaussian model in the whole domain. Unfortunately, this does not mean that φ takes values ± 1 on the two sides of the path. The conditional rule does not work in the simple way of the Ising model. However, Oded Schramm and Scott Sheffield [SS05] proved that, for a particular value of β and in the scaling limit, the two measures are equal.

In [SS05] the conformal invariance of the harmonic explorer is proved. As we will see in 6.1.2, the reason is that the random walk is conformally invariant (apart from a time dilation). Markovianity is ensured by construction. Furthermore, property 6.1 is the peculiar property of the harmonic explorer: it states that the harmonic function H_n is a martingale, i.e. its mean value conditioned to a path up to step $m < n$ is H_m. In section 6.2 a schematic proof is provided.

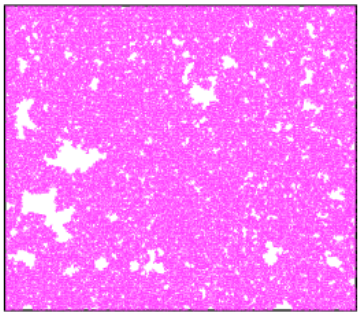

Figure 4.6: An actual sample of antiharmonic explorer (magenta) ends its exploration in a honeycomb rectangle with 500×500 hexagons. Its space-filling tendency is evident, especially if compared to the opposite case of the harmonic explorer shown in figure 4.5b.

4.3.2 Variations on the harmonic explorer

The exploration rule based on random walks allows interesting variations on the harmonic explorer. First of all, let us consider the case where the outcome of the random walk is always overturned, i.e. the face in front of the tip is coloured blue if the random walker hits a red boundary first (and vice versa). Thus, now the probability of turning right is the complementary probability of the harmonic one:

$$P_{-}(v_{n+1}) = 1 - H_n(v_{n+1})$$

Since this can be regarded as the opposite case of the harmonic explorer, such an explorer is called the *antiharmonic explorer* (or the harmonic antinavigator, as you can find in [BB06]). A sample of it is provided in figure 4.6. From the comparison between figure 4.5b and 4.6 it is evident that the two explorers behave in completely different ways. In particular, the antiharmonic explorer reveals a space-filling tendency. This can be understood as follows: suppose that the neighbourhood of the face to be coloured contains much more faces of one colour than of the other one; then, there is a high probability that the outcome of the random walk is the predominant colour; for the harmonic explorer the face is coloured with this colour, whereas for the antiharmonic explorer it is coloured with the other one; in the former case the explorer is subjected to a repulsive force, which prevents the path from coming too close to another piece of itself; on the contrary, in the latter case the explorer is attracted by its boundaries. The antiharmonic explorer is still Markovian and its conformal invariance is guessed.

Overturning in some way (with some probability) the outcome of the random walk will allow us to introduce a generalized class of explorers. The idea is the same as that behind the antiharmonic explorer: at each step a random walker is

still launched from the face in front of the tip, but now the colour of the boundary it hits first is accepted under some conditions. This corresponds to turning right with probability

$$P_{-}(v_{n+1}) = f\big(H_n(v_{n+1})\big)$$

where f is a real function with some constraints. We call this class of explorers *stretched harmonic explorers*. We will deal with them in more details in section 6.3.1. Furthermore, if f is a linear function a subclass of explorers is identified: we call them *overruled harmonic explorers*. The study of their properties and their possibile scaling limit is the aim of this work and is presented from section 6.3.2 on. The critical percolation, the harmonic explorer and the antiharmonic explorer can be regarded as special cases among this class.

Another deformation of the harmonic explorer would be to keep only the initial boundary conditions to compute the measure, i.e. let path boundaries be transparent to the random walker. In that case the face from where the random walker emerges is coloured red with a probability which depends only on the position of that face, but not on the existing path. In other words, this probability is the harmonic function in the whole domain:

$$P_{-}(v_{n+1}) = H_0(v_{n+1})$$

This exploration rule defines the *boundary harmonic explorer*. In [BB06] some details about this growth process are provided. Here, it is worth noticing that the domain Markov property does not hold: indeed, since the exploration rule depends on the initial boundary conditions rather than on those of the cut domain, removing the beginning of the path from the domain and starting the process for the cut domain at the tip is not the same as continuing the process in the initial domain. Besides, neither conformal invariance is supposed to be present.

4.3.3 Self-avoiding walk

In the present chapter we showed how some equilibrium systems from statistical mechanics can be interpreted as Markovian exploration processes. However, this parallelism does not always hold. A simple example of an equilibrium model whose critical interfaces cannot be read as growing paths are the *self-avoiding walks* (SAW), which can be obtained from the $\mathrm{O}(n)$ model at $n = 0$. Despite this name, also all the other example we considered are self-avoiding, but the weights of the present case single it out from the others.

Plugging $n = 0$ in (4.3) suppresses all the closed loops, so that a single non-self-intersecting path survives. It connects the two boundary points r_0 and r_* and is weighted by its length N_{st}. In this picture, all the paths of the same length are counted with the same weight. Such a weight arises by considering

the walks of m steps emerging from, say, boundary point r_0 in a certain lattice domain. Their total number grows as θ^n, where θ depends on the lattice. Thus, it is natural to weight all the paths of length m with the inverse of this number, i.e. $\theta^{-m} = t^m$.

However, given the first m steps of a path, there is no simple algorithm to determine the probability of a left turn. Indeed, since the measure depends on the total number of paths of the same length, it is necessary to sample the entire population of walks at each step. For the time being, no exploration process is associated to the self-avoiding walk.

Nevertheless, self-avoiding walks are Markovian: given the first part of the path, the measure on the remaining part weights all walks by the correct factor $t^{N_{\mathrm{st}}-m}$. Besides, although the conformal invariance is not yet proven, it is observed [Car03; DS88; LSW04b]. Finally, the characterizing property of the self-avoiding walk is the *restriction*: if the domain is restricted (as for the critical-percolation case), then the measure on self-avoiding walks in the whole domain, restricted to stay in the new domain, is the same as the measure on self-avoiding walks in the restricted domain.

Although in the following we will not deal with this kind of stochastic processes, we presented them here because they are a paradigmatic example of how a simple equilibrium model can lead to very complicated systems with powerful symmetries. Moreover, self-avoiding walks are supposed to describe the behaviour of long flexible polymer chains. In particular, above the critical value t_{c} there is a dense phase where the mean length diverges and the polymers spread in the whole domain.

4.4 Other growth processes

The exploration processes described in the previous section are the simplest example of discrete growth processes. They can be extended and generalized in many ways.

First, one can allow the presence of more than one explorer starting from different boundary points. An important question is whether the final joint measure is the same as that obtained by growing paths one by one. If the single explorer has a statistical-mechanics equivalent, this is true, because the *multiple explorers* still describe the equilibrium interfaces. Their scaling limit (when it exists) leads to the study of multiple SLE, which is a field of interest for many applications.

Another possibility is allowing a single explorer (or even multiple explorers) to branch at its tip with some stochastic rule. Branching at some other points can also be considered. In neither case Markovianity has a simple generalization.

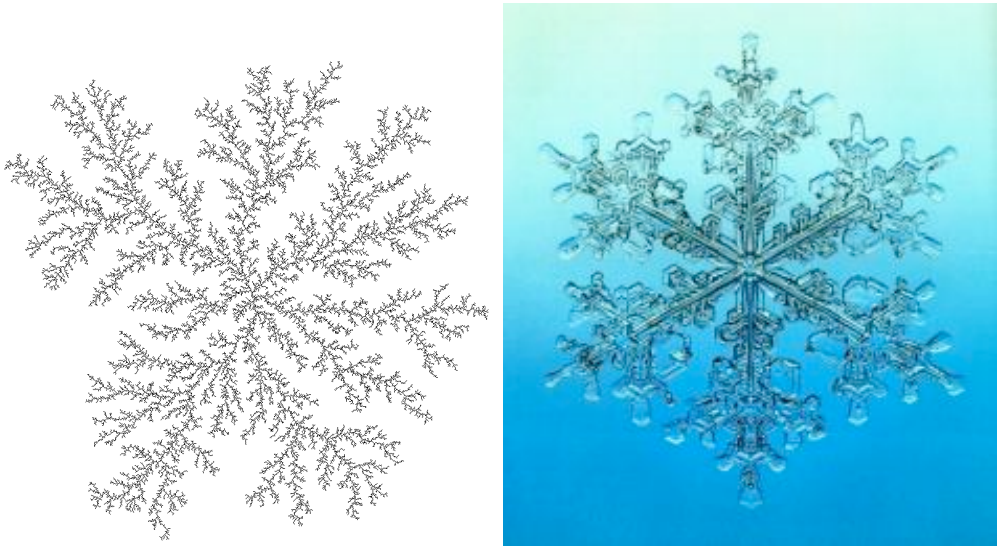

(a) A DLA cluster (b) A snowflake

Figure 4.7: A cluster of diffusion-limited aggregation is showed in figure (a). Particles diffusing from infinite cluster around the attracting set, here the central point. Figure (b) provides a real example of DLA-like cluster: a snowflake.

4.4.1 Diffusion-limited aggregation

Generalising an exploration process is not the only way to build a growth process. Let us present a simple powerful model which exploits a different strategy. Given the existing set $\mathcal{K}^{\#} \subset \mathcal{D}^{\#}$ (which can be a generic set of, say, faces of $\mathcal{D}^{\#}$, not necessarily a simple path), we reverse the harmonic explorer by allowing a random walker to approach from infinity. At the point of $\mathcal{K}^{\#}$ which the random walker hits first a new face is added. Since the random walk defines a harmonic probability (see section 6.1.1), this operative definition can be converted in a more formal version solving the discrete Laplace equation $\triangle\varphi$ with boundary conditions $\varphi \sim \log|z|$ as $|z| \to\infty$ and $\varphi = 0$ on $\mathcal{K}^{\#}$. The value of φ on a face neighbouring to $\mathcal{K}^{\#}$ gives the probability that it is added to $\mathcal{K}^{\#}$.

This process describes the diffusive growth of a domain which aggregates diffusing particles coming from infinity. Therefore it is called discrete *diffusion-limited aggregation* (discrete DLA). The actual DLA is obtained in the continuous limit [WS81; WS83]. Since Laplace equation is involved in many different physical problems, this model can be applied to fields such as fluid dynamics and electrostatics.

DLA clusters can be very different depending on the geometry of the attracting set. Surely, the most common (and beautiful) example of DLA cluster is the

snowflake, where the diffusing particles are ice particles (figure 4.7). This example shows how growth processes from atmospheric physics can result in a very broad class of different phenomena: the three-dimensional diffusive growth of a cloud droplet (seen in part I) displays a simple spherical geometry, whereas the two-dimensional diffusive growth of a snowflake a complicated fractal structure.

It is worth noticing that all the considered growth processes can display conformal invariance. Unfortunately, the conformal-maps method we will see in chapter 5 allows a huge amount of analytic computations only for the continuous limit of simple exploration paths. The other cases do not seem to be analytically tractable.

Chapter 5

Stochastic Löwner evolutions

If discrete exploration processes display both Markovianity and conformal invariance, they can converge to a continuous limit, known as stochastic Löwner evolution (SLE). As an exploration path, an SLE is a stochastically-growing curve, now in a simply-connected bounded complex domain. However, they are described in a different way with respect to the discrete processes. Here, rather then describing the evolution of the curve in the domain, the focus is on the evolution of the conformal map which remove the curve from the domain. Such an approach, proposed in the 1920s by Karel Löwner, is well known in the theory of the conformal transformation. The very powerful novelty, introduced by Oded Schramm in 1999, is the stochastic law ruling the evolution. The study of the growing curve is thus reduced to the dynamics of one point on the real axis, i.e. the conformal image of the curve tip which follows a one-dimensional diffusive process, labelled by one real parameter. Such a parameter is able to classify very different system in universality classes.

This chapter provides a brief review of SLE foundation (section 5.1) and fundamentals properties (section 5.2). Some computations with SLE, useful for the following scopes, are also presented. Finally, some discrete processes proved or conjectured to converge to SLE curves are listed.

5.1 Stochastic Löwner evolution

5.1.1 Postulates

SLE gives a description of the continuum limit of the lattice curves connecting two points on the boundary of a domain $\mathcal{D}$ which were introduced in chapter 4. The idea is to define a *measure* $\mu(\gamma; \mathcal{D}, r_0, r_*)$ on these continuous curves. (Note that the notion of a probability density of such objects does not make sense, but

the more general concept of a measure does.)

There are two basic properties of this continuum limit which must either be assumed, or, better, proven to hold for a particular lattice model. The former is the continuum version of property 4.1.

Property 5.1 (Domain Markovianity, continuum version)**.** *Denote the curve by γ, and divide it into two disjoint parts: γ_1 from r_0 to r_t, and γ_2 from r_t to r_*. Then the conditional measure $\mu(\gamma_2|\gamma_1; \mathcal{D}, r_0, r_*)$ is the same as $\mu(\gamma_2; \mathcal{D} \setminus \gamma_1, r_t, r_*)$.*

This property we expect to be true for the scaling limit of all such curves in the $\mathrm{O}(n)$ model (at least for $n \geqslant 0$), even away from the critical point. However the second property encodes the notion of conformal invariance, and it should be valid, if at all, only at $t = t_c$ and, separately, for $t > t_c$.

Property 5.2 (Conformal invariance)**.** *Let g be a conformal mapping of the interior of the domain $\mathcal{D}$ onto the interior of $\mathcal{D}'$, so that the points (r_0, r_*) on the boundary of $\mathcal{D}$ are mapped to points (r'_0, r'_*) on the boundary of $\mathcal{D}'$. The measure μ on curves in $\mathcal{D}$ induces a measure $g*\mu$ on the image curves in $\mathcal{D}'$. The conformal invariance property states that this is the same as the measure which would be obtained as the continuum limit of lattice curves from r'_0 to r'_* in $\mathcal{D}'$. That is*

$$(g * \mu)(\gamma; \mathcal{D}, r_0, r_*) = \mu(g(\gamma); \mathcal{D}', r'_0, r'_*) \tag{5.1}$$

5.1.2 Löwner equation

We have seen that, on the lattice, the curves γ may be 'grown' through a discrete exploration process. The Löwner process is the continuum version of this. Because of property 5.2 it suffices to describe this in a standard domain $\mathcal{D}$, which is taken to be the upper half plane $\mathbb{H}$, with the points r_0 and r_* being the origin and infinity respectively.

The first thing to notice is that, although on the honeycomb lattice the growing path does not intersect itself, in the continuum limit it might (although it still should not cross itself.) This means that there may be regions enclosed by the path which are not on the path but nevertheless are not reachable from infinity without crossing it. We call the union of the set of such points, together with the curve itself, up to time t, the *hull* $\mathcal{K}_t$. (This is a slightly different usage of this term from that in the physics percolation literature.) It is the complement of the connected component of the half plane which includes ∞, itself denoted by $\mathbb{H} \setminus \mathcal{K}_t$. See figure 5.1.

Another property which often holds in the half-plane is that of *reflection invariance*: the distribution of lattice paths starting from the origin and ending at

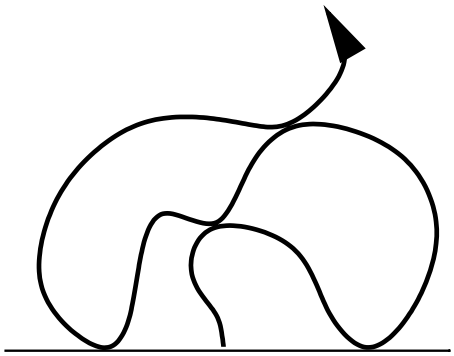

Figure 5.1: Schematic view of a trace and its hull.

∞ is invariant under $x \to -x$. For the lattice paths in the $\mathrm{O}(n)$ model discussed in section 4.2.2 this follows from the symmetry of the underlying weights, but for the boundaries of the FK clusters in the Potts model it is a consequence of duality. Not all simple curves in lattice models have this property. For example if we consider the 3-state Potts model in which the spins on the negative and positive real axes are fixed to different values, there is a simple lattice curve which forms the outer boundary of the spin cluster containing the positive real axis. This is not the same as the boundary of the spin cluster containing the negative real axis, and it is not in general symmetric under reflections.

Since $\mathbb{H} \setminus \mathcal{K}_t$ is simply connected, by the Riemann mapping theorem it can be mapped into the standard domain $\mathbb{H}$ by an analytic function $g_t(z)$. Because this preserves the real axis outside $\mathcal{K}_t$ it is in fact real analytic. It is not unique, but can be made so by imposing the behaviour as $z \to \infty$

$$g_t(z) \sim z + O(1/z) \tag{5.2}$$

It can be shown that, as the path grows, the coefficient of $1/z$ is monotonic increasing (essentially it is the electric dipole moment of $\mathcal{K}_t$ and its mirror image in the real axis.) Therefore we may reparametrise time so that this coefficient is $2t$ (the factor 2 being historical). Note that the length of the curve is not be a useful parametrisation in the continuum limit, since the curve is a fractal.

The function $g_t(z)$ maps the whole boundary of $\mathcal{K}_t$ onto part of the real axis. In particular, it maps the growing tip r_t to a real point u_t. Any point on the real axis outside $\mathcal{K}_t$ remains on the real axis. As the path grows, the point u_t moves on the real axis. For the path to describe a curve, it must always grow only at its tip, and this means that the function u_t must be continuous, but not necessarily differentiable.

A simple but instructive example is when γ is a straight line growing vertically

upwards from the starting point r_0. In this case

$$g_t(z) = r_0 + \left((z - r_0)^2 + 4t\right)^{1/2} \tag{5.3}$$

This satisfies (5.2), and $r_t = 2\mathrm{i}\sqrt{t}$. More complicated deterministic examples can be found [KNK04]. In particular, $u_t \propto t^{1/2}$ describes a straight line growing at a fixed angle to the real axis.

Löwner's idea [Löw23] was to describe the path γ and the evolution of the tip r_t in terms of the evolution of the conformal mapping $g_t(z)$. It turns out that the equation of motion for $g_t(z)$ is simple:

$$\frac{\mathrm{d}}{\mathrm{d}t} g_t(z) = \frac{2}{g_t(z) - u_t} \tag{5.4}$$

This is the Löwner equation. The idea of the proof is straightforward. Imagine evolving the path for a time t, and then for a further short time δt. The image of $\mathcal{K}_{t+\delta t}$ under g_t is a short vertical line above the point u_t on the real axis. Thus we can write, using (5.3)

$$g_{t+\delta t}(z) \approx u_t + \left((g_t(z) - u_t)^2 + 4\delta t\right)^{1/2} \tag{5.5}$$

Differentiating with respect to δt and then letting $\delta t \to 0$, we obtain (5.4).

Note that, even if u_t is not differentiable (as is the case for SLE), (5.4) gives for each point z_0 a solution $g_t(z_0)$ which is differentiable with respect to t, up to the time when $g_t(z_0) = u_t$. This is the time when z_0 is first included in $\mathcal{K}_t$. However, it is sometimes useful to normalise the Löwner mapping differently, defining $h_t(z) = g_t(z) - u_t$, which always maps the growing tip r_t to the origin. If u_t is not differentiable, neither is h_t, and the Löwner equation should be written in differential form as $\mathrm{d}h_t = (2\,\mathrm{d}t/h_t) - \mathrm{d}u_t$.

Given a growing path, we can determine the hull $\mathcal{K}_t$ and hence, in principle, the function $g_t(z)$ and thereby $u_t = g_t(r_t)$. Conversely, given u_t we can integrate (5.4) to find $g_t(z)$ and hence in determine the curve (although proving that this inverse problem gives a curve is not easy.)

5.1.3 Stochastic evolution

In the case that we are interested in, γ is a random curve, so that u_t is a random continuous function. What is the measure on u_t? This is answered by the following remarkable result, due to Schramm [Sch00]:

Theorem 5.1 (Schramm)**.** *If properties 5.1 and 5.2 hold, together with reflection symmetry, then u_t is proportional to a standard Brownian motion.*

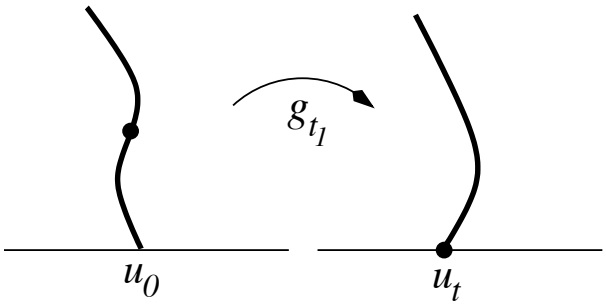

Figure 5.2: A hull evolved from u_0 for time t_1, then to infinity. The measure on the image of the rest of the curve under g_{t_1} is the same, according to the postulates of SLE, as a hull evolved from u_{t_1} to ∞.

That is

$$u_t = \sqrt{\varkappa} B_t \tag{5.6}$$

so that $\langle u_t \rangle = 0$, $\langle \left(u_{t_1} - u_{t_2}\right)^2 \rangle = \varkappa |t_1 - t_2|$. The only undetermined parameter is $\varkappa$, the diffusion constant. It will turn out that different values of $\varkappa$ correspond to different universality classes of critical behaviour.

The idea behind the proof is once again simple. As before, consider growing the curve for a time t_1, giving γ_1, and denote the remainder $\gamma \setminus \gamma_1 = \gamma_2$. Property 5.1 tells us that the conditional measure on γ_2 given γ_1 is the same as the measure on γ_2 in the domain $\mathbb{H} \setminus \mathcal{K}_{t_1}$, which, by property 5.2, induces the same measure on $g_{t_1}(\gamma_2)$ in the domain $\mathbb{H}$, shifted by u_{t_1} (see figure 5.2). In terms of the function u_t this means that the probability law of $u_t - u_{t_1}$, for $t > t_1$, is the same as the law of u_{t-t_1}. This implies that all the increments $\Delta_n \equiv u_{(n+1)\delta t} - u_{n\delta t}$ are independent identically distributed random variables, for all $\delta t > 0$. The only process that satisfies this is Brownian motion with a possible drift term: $u_t = \sqrt{\varkappa} B_t + \alpha t$. Reflection symmetry then implies that $\alpha = 0$.

5.1.4 Radial SLE

So far we have discussed a version of SLE that gives a conformally invariant measure on curves which connect two distinct boundary points of a simply connected domain $\mathcal{D}$. For this reason it is called *chordal* SLE. There are variants which describe other situations. For example, one could consider curves γ which connect a given point r_0 on the boundary to an interior point r_*. The Riemann mapping theorem allows us to map conformally onto another simple connected domain, with r_* being mapped to any preassigned interior point. It is simplest to choose for the standard domain the unit disc $\mathbb{D}$, with r_* being mapped to the

origin. So we are considering curves γ which connect a given point $\mathrm{e}^{\mathrm{i}\vartheta_0}$ on the boundary with the origin. As before, we may consider growing the curve dynamically. Let $\mathcal{K}_t$ be the hull of that portion which exists up to time t. Then there exists a conformal mapping g_t which takes $\mathbb{D} \setminus \mathcal{K}_t$ to $\mathbb{D}$, such that $g_t(0) = 0$. There is one more free parameter, which corresponds to a global rotation: we use this to impose the condition that $g_t'(0)$ is real and positive. One can then show that, as the curve grows, this quantity is monotonically increasing, and we can use this to reparametrise time so that $g_t'(0) = \mathrm{e}^t$. This normalised mapping then takes the growing tip r_t to a point $\mathrm{e}^{\mathrm{i}\vartheta_t}$ on the boundary.

The Löwner theorem tells us that $\frac{\mathrm{d}}{\mathrm{d}t} g_t(z)/g_t(z)$, when expressed as a function of $g_t(z)$, should be holomorphic in $\overline{\mathbb{D}}$ apart from a simple pole at $\mathrm{e}^{\mathrm{i}\vartheta_t}$. Since g_t preserves the unit circle outside $\mathcal{K}_t$, $\frac{\mathrm{d}}{\mathrm{d}t} g_t(z)/g_t(z)$ should be pure imaginary when $|g_t(z)| = 1$, and in order that $g_t'(0) = \mathrm{e}^t$, it should approach 1 as $g_t(z) \to 0$. The only possibility is

$$\frac{\mathrm{d}}{\mathrm{d}t} g_t(z) = -g_t(z) \, \frac{g_t(z) + \mathrm{e}^{\mathrm{i}\vartheta_t}}{g_t(z) - \mathrm{e}^{\mathrm{i}\vartheta_t}} \tag{5.7}$$

This is the radial Löwner equation. In fact this is the version considered by Löwner [Löw23].

It can now be argued, as before, that given properties 5.1 and 5.2 (suitably reworded to cover the case when r_* is an interior point) together with reflection, ϑ_t must be proportional to a standard Brownian motion. This defines radial SLE. It is not immediately obvious how the radial and chordal versions are related. However, it can be shown that, if the trace of radial SLE hits the boundary of the unit disc at $\mathrm{e}^{\mathrm{i}\vartheta_{t_1}}$ at time t_1, then the law of $\mathcal{K}_t$ in radial SLE, for $t < t_1$, is the same chordal SLE conditioned to begin at $\mathrm{e}^{\mathrm{i}\vartheta(0)}$ and end at $\mathrm{e}^{\mathrm{i}\vartheta_{t_1}}$, up to a reparametrisation of time. This assures us that, in using the chordal and radial versions with the same $\varkappa$, we are describing the same physical problem.

However, one feature that the trace of radial SLE possesses which chordal SLE does not is the property that it can wind around the origin. The winding angle at time t is simply $\vartheta_t - \vartheta_0$. Therefore it is normally distributed with variance $\varkappa t$.

A third alias of SLE is called *dipolar*. Here, the starting point r_0 is still on the boundary, whereas the end point is not fixed, but can lies in the boundary interval between the two boundaries point r_- and r_+ (with $r_0 \notin [r_-, r_+]$). A canonic domain for dipolar SLE his the strip $\mathbb{S} = (-\infty, +\infty) \times \mathrm{i}\pi$. In this case there are two infinite points.

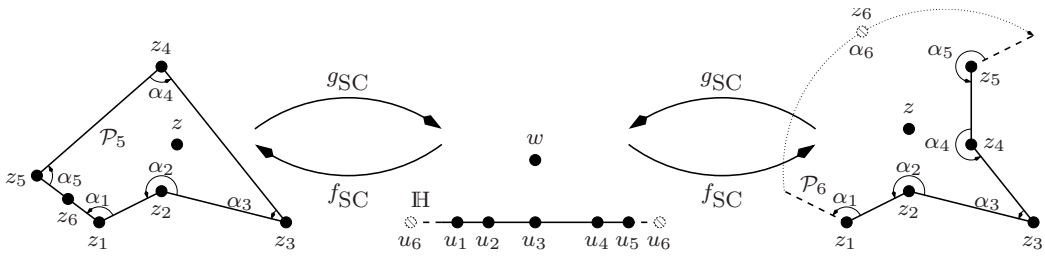

Figure 5.3: Schwarz–Christoffel mappings are conformal transformations mapping the interior of an l-sided polygonal domain $\mathcal{P}_l$ into a canonic domain, usually the upper half-plane $\mathbb{H}$. A classical example with a pentagonal domain $\mathcal{P}_5$ is presented on the left. On the right, a common generalization where the vertex z_6 of a hexagonal domain $\mathcal{P}_6$ is pushed to infinity. In both cases, all the images $u_i = g_{\mathrm{SC}}(z_i)$ of the vertices z_i lie on the real axis, because boundary points are mapped into boundary points. If $z_i \neq \infty$, all the angles are in the range $0 < \alpha_i \leqslant 2\pi$. Angles at infinity, like α_6 here on the right, have negative values ($-2\pi \leqslant \alpha_i \leqslant 0$ if $z_i = \infty$); indeed, the closure at infinity of two sides requires a clockwise turn.

5.1.5 Schwarz–Christoffel mapping

In the previous sections we have considered three SLE aliases, differentiated by the localization of the final point r_*. One canonic domain $\mathcal{D}_{\mathrm{c}}$, where the mapping function $g_t : \mathcal{D}_{\mathrm{c}} \setminus \mathcal{K}_t \mapsto \mathcal{D}_{\mathrm{c}}$ acts, has been associated to each alias. However, SLE can develop in every complex domain $\mathcal{D} \subset \mathbb{C}$ but $\mathbb{C}$ itself. Since normally properties and probabilities are computed in the canonic domains resorting to a lot of ingenuity, it is easier to transform these results in the generic domain $\mathcal{D}$ instead of computing them again in this more complicated domain. Indeed, SLE properties being conformally invariant, it is sufficient to find a conformal map $g_{\mathrm{c}} : \mathcal{D} \mapsto \mathcal{D}_{\mathrm{c}}$, or its inverse $f_{\mathrm{c}} = g_{\mathrm{c}}^{-1}$. In other words, a probability $P(\varkappa; w_1, \ldots, w_l)$, where $w_i \in \mathcal{D}_{\mathrm{c}}$ and $1 \leqslant i \leqslant l$, is equal to $P\big(\varkappa; f_{\mathrm{c}}(w_1), \ldots, f_{\mathrm{c}}(w_l)\big)$.

For some reasons, it is often useful to work in an l-sided polygonal domain $\mathcal{P}_l$, e.g. when an exploration process in a finite lattice is involved. The *Schwarz–Christoffel mappings* $f_{\mathrm{SC}} : \mathcal{D}_{\mathrm{c}} \mapsto \mathcal{P}_l$ map the canonic domain into the polygonal one conformally. The general formula for the upper half-plane reads ([DT02])

$$f_{\mathrm{SC}}(w) = C \int^{w} \prod_{i=1}^{l} (\omega - u_i)^{\alpha_i/\pi - 1} \, \mathrm{d}\omega + c \tag{5.8}$$

where C and $c = f_{\mathrm{SC}}(w_0)$ are complex constants, $w_0, w \in \mathbb{H}$ are the extreme points of the integration path $\gamma(w_0, w)$ and $\alpha_i \in (0, 2\pi]$ are the angles between the i-th and $i+1$-th sides with vertex in $z_i = f_{\mathrm{SC}}(u_i)$ (in counter-clockwise order, the polygon interior lying on the left as i increases). The points $u_i \in \mathbb{R}$

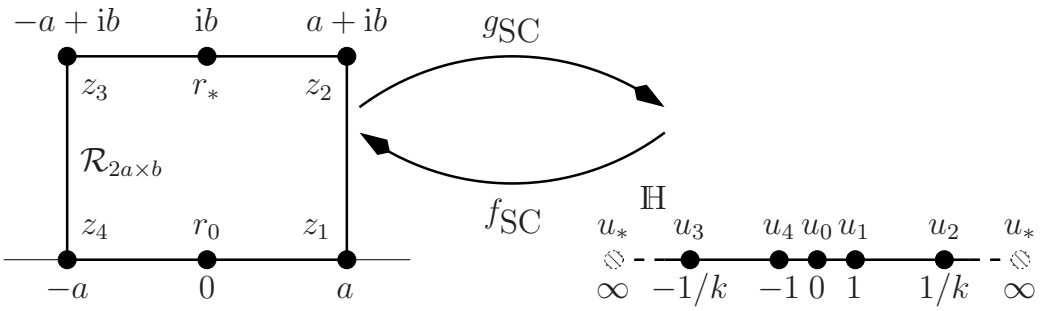

Figure 5.4: The conformal transformation g_{SC} which maps the rectangular domain $\mathcal{R}_{2a\times b}$ (with lower side lying on the real axis) to the upper half-plane $\mathbb{H}$. Here $\alpha_i = \pi/2$ for $1 \leqslant i \leqslant 4$. It is customary to require that the origin is mapped into itself and the lower vertices into ± 1. As a consequence, the point r_* is mapped to infinity and the upper vertices into $\pm 1/k$, k being determined by the integral equation $(5.12\mathrm{b})$.

are the preimages on the real axis of the vertices of the polygon according to the inverse mapping and, therefore, are called *prevertices*. It is worth noticing that such a map can be generalized by an open polygon which can be imagined closed at infinity; this amounts to pushing some of the vertices z_i to infinity and to consider their corresponding angles in the range $[-2\pi, 0]$. Figure 5.3 provides a complete explanation of the symbols.

The Schwarz–Christoffel mapping can be given in a simplified way, where the product in (5.8) has $l-1$ factors. Indeed, once $l-1$ preimages are kept fixed to finite values on the real axis, the last one is pushed to infinity with an arbitrary scaling factor and its contribution is absorbed by C, leading to

$$f_{\mathrm{SC}}(w) = C \int^{w} \prod_{i=1}^{l-1} (\omega - u_i)^{\alpha_i/\pi - 1} \, \mathrm{d}\omega + c \tag{5.9}$$

for $f_{\mathrm{SC}} : \mathcal{D}_{\mathrm{c}} = \mathbb{H} \mapsto \mathcal{P}_l$.

Now, let us deal with the particular case of a rectangle $\mathcal{P}_4 = \mathcal{R}_{2a\times b}$, which will be useful in the following, more specifically when exploration processes in rectangular domains will be considered and their conformal invariance tested. As sketched in figure 5.4, the lower side has length $2a$ and lies on the real axis with its middle point on the origin. The aspect ratio is $R = 2a/b$, b being the height of the rectangle. Thus, the four vertices are located in $z_1 = a$, $z_2 = a + \mathrm{i}b$, $z_3 = -a + \mathrm{i}b$, $z_4 = -a$, respectively, and, obviously, every angle $\alpha_i = \pi/2$ is a right angle. The three mapping parameters c, u_1 and u_4 are fixed by requiring that the origin is mapped into itself and the lower vertices into ± 1, respectively (more precisely, $c = f_{\mathrm{SC}}(w_0 = 0) = 0$, $u_1 = g_{\mathrm{SC}}(z_1 = a) = 1$ and $u_4 = g_{\mathrm{SC}}(z_4 = -a) = -1$). Since the images of three boundary points are given,

general theorems ensure that the map is completely determined. By symmetry considerations, one can easily be convinced that the point $r_* = \mathrm{i}b$ is mapped to the infinity and the images of the upper vertices are also opposite. Denoting them with $u_2 = 1/k$ and $u_3 = -1/k$, where $0 < k < 1$, (5.8) returns

$$z = f_{\mathrm{SC}}(w) = C \int_0^w \frac{\mathrm{d}\omega}{\sqrt{\omega^2 - 1}\sqrt{k^2\omega^2 - 1}} \tag{5.10}$$

C absorbing a factor k. To determine the two last mapping parameters C and k we need to evaluate (5.10) in two points, e.g. the right vertices, and, then, to solve the system

$$\begin{cases} a = C \displaystyle\int_0^1 \frac{\mathrm{d}u}{\sqrt{1 - u^2}\sqrt{1 - k^2u^2}} = CK(k) & (5.11a) \\ b = C \displaystyle\int_1^{1/k} \frac{\mathrm{d}u}{\sqrt{u^2 - 1}\sqrt{k^2u^2 - 1}} = CK\left(\sqrt{1 - k^2}\right) & (5.11b) \end{cases}$$

where $K(k)$ indicates the *complete elliptic integral of the first kind* and k is called *elliptic modulus*. Finally, exploiting the *elliptic function* $\mathrm{sn}(z; k)$, the inverse mapping $w = g_{\mathrm{SC}}(z) : \mathcal{R}_{2a\times b} \mapsto \mathbb{H}$ can be expressed in the compact form

$$\begin{cases} w = \mathrm{sn}\left(K(k)\dfrac{z}{a}; k\right) & (5.12a) \\ k \quad \text{such that} \quad \dfrac{K(k)}{K\left(\sqrt{1 - k^2}\right)} = \dfrac{a}{b} = \dfrac{R}{2} & (5.12b) \end{cases}$$

In [Akh90] a detailed derivation of (5.12) can be found, together with a complete presentation of the theory of elliptic functions.

5.2 Properties of SLE

5.2.1 Renyi dimensions

Before getting to the heart of this analysis, let us recall some background information concerning fractal dimensions (more details can be found in [ER85; PV87]). Indeed, a continuous spectrum of fractal dimensions can be defined, viz. the *Renyi dimensions* d_α of order $\alpha \geqslant 0$:

$$d_\alpha = \lim_{\varepsilon \to 0} \frac{\frac{1}{1-\alpha} \log\left(\sum_{i=1}^{n_{\mathrm{fs}}(\varepsilon)} p_{\mathrm{fs}_i}^\alpha(\varepsilon)\right)}{\log \frac{1}{\varepsilon}} \tag{5.13}$$

where p_{fs_i} is the *natural measure*, i.e. the probability that element i of the fractal set is occupied (normalized such that $\sum_{i=1}^N p_{\mathrm{fs}_i} = 1$), and n_{fs} is the number

of elements of linear size ε forming a finite cover of the fractal set. The first three integer values of α return well-known fractal dimensions, viz. the *capacity dimension* d_0, the *information dimension* d_1 and the *correlation dimension* d_2. After some algebra, they take the form

$$d_0 = -\lim_{\varepsilon\to 0}\frac{\log n_{\mathrm{fs}}(\varepsilon)}{\log\varepsilon} \tag{5.14a}$$

$$d_1 = \lim_{\varepsilon\to 0}\frac{\langle\log p_{\mathrm{fs}}(\varepsilon)\rangle}{\log\varepsilon} = \lim_{\varepsilon\to 0}\frac{\sum_{i=1}^{N(\varepsilon)} p_{\mathrm{fs}_i}(\varepsilon)\log p_{\mathrm{fs}_i}(\varepsilon)}{\log\varepsilon} \tag{5.14b}$$

$$d_2 = \lim_{\varepsilon\to 0}\frac{\log C_{\mathrm{fs}}(\varepsilon)}{\log\varepsilon} = \lim_{\varepsilon\to 0}\lim_{n_{\mathrm{fs}}\to\infty}\frac{\log\frac{m_{\mathrm{fs}}(\varepsilon)}{n_{\mathrm{fs}}^2}}{\log\varepsilon} \tag{5.14c}$$

where the *correlation integral* C_{fs} is defined in terms of the number m_{fs} of pairs of points closer than ε and in terms of the number n_{fs} of points describing the fractal set.

In plain words, d_0 is simply a box-counting dimension and tells us how the number of boxes scales with the box size. Furthermore, d_1 considers how the average information needed to identify an occupied box scales, as the box scale gets smaller. Finally, d_2 gives an idea on how close the set points are; it is the easiest to determine. It can be proved that $d_2 \leqslant d_1 \leqslant d_0$. If Renyi dimensions are not all equal, the fractal object has a *multifractal* structure.

As we will see in next sections, SLE$_\varkappa$ traces are fractals. The computation of their dimensions is the first step in order to describe their geometrical properties. An important result is that SLE$_\varkappa$ traces are *unifractal* objects, i.e. d_α is the same for every α. Thanks to this feature, the most convenient definition can be exploited in order to either analytically compute or numerically determine the single fractal dimensions of both traces and special subsets of them.

5.2.2 Phases of SLE

Before computing the fractal dimensions of SLE curves, we address the qualitative question of how the trace (the trajectory of r_t) looks for different values of $\varkappa$. For $\varkappa = 0$, it is a vertical straight line. As $\varkappa$ increases, the trace should randomly turn to the left or right more frequently. However, it turns out that there are qualitative differences at critical values of $\varkappa$. To see this, let us first study the process on the real axis. Let $x_t = g_t(x_0) - u_t$ be the distance between the image at time t of a point which starts at x_0 and the image u_t of the tip. It obeys the stochastic equation

$$\mathrm{d}x_t = \frac{2\,\mathrm{d}t}{x_t} - \sqrt{\varkappa}\,\mathrm{d}B_t \tag{5.15}$$

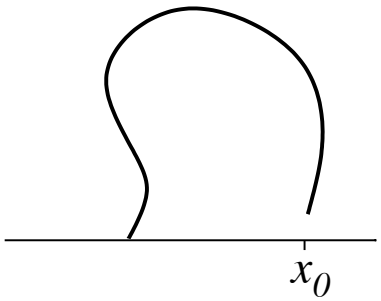

Figure 5.5: The trace is about to hit the axis at x_0 and enclose a region. At the time this happens, the whole region including the point x_0 is mapped by g_t to the same point u_t.

Physicists often write such an equation as $\frac{\mathrm{d}}{\mathrm{d}t}x = (2/x) - \eta_t$ where η_t is 'white noise' of strength $\varkappa$. Of course this does not make sense since x_t is not differentiable. Such equations are always to be interpreted in the 'Itô sense', that is, as the limit as $\delta t \to 0$ of the forward difference equation $x_{t+\delta t} \approx x_t + (2\delta t/x_t) + \int_t^{t+\delta t} \eta_{t'} dt'$.

(5.15) is known as the Bessel process. If we set $R_t = (d-1)^{1/2} x_t/2$ and $\varkappa^2 = 4/(d-1)$ it describes the distance R_t from the origin of a Brownian particle in d dimensions. The point x_t is repelled from the origin but it is also subject to a random force. Its ultimate fate can be inferred from the following crude argument: if we ignore the random force, $x_t^2 \sim 4t$, while, in the absence of the repulsive term, $\langle x_t^2 \rangle \sim \varkappa t$. Thus for $\varkappa < 4$ the repulsive force wins and the particle escapes to infinity, while for $\varkappa > 4$ the noise dominates and the particle collides with the origin in finite time (at which point the equation breaks down.) A more careful analysis confirms this. What does this collision signify in terms of the behaviour of the trace? In figure 5.5 we show a trace which is about to hit the real axis at the point x_0, thus engulfing a whole region. This is visible from infinity only through a very small opening, which means that, under g_t, it gets mapped to a very small region. In fact, as the tip r_t approaches x_0, the size of the image of this region shrinks to zero. When the gap closes, the whole region enclosed by the trace, as well as r_t and x_0, are mapped in to the single point u_t, which means, in particular, that $x_t \to 0$. The above argument shows that for $\varkappa < 4$ this never happens: the trace never hits the real axis (with probability 1.) For the same reason, it neither hits itself. Thus for $\varkappa < 4$ the trace γ is a *simple curve*.

The opposite is true for $\varkappa > 4$: points on the real axis are continually colliding with the image u_t of the tip. This means that the trace is continually touching both itself and the real axis, at the same time engulfing whole regions. Moreover, since it is self-similar object, it does this on all scales, an infinite number of times

within any finite neighbourhood! Eventually the trace swallows the whole half plane: every point is ultimately mapped into u_t. For $\varkappa < 4$ only the points on the trace itself suffer this fate. The case $\varkappa = 4$ is more tricky: in fact the trace is then also a simple curve.

When $\varkappa$ is just above 4, the images of points on the real axis under g_t collide with u_t only when there happen to be rare events when the random force is strong enough to overcome the repulsion. When this happens, whole segments of the real axis are swallowed at one time, corresponding to the picture described above. Conversely, for large $\varkappa$, the repulsive force is negligible except for very small x_t. In that case, two different starting points move with synchronised Brownian motions until the one which started off closer to the origin is swallowed. Thus the real line is eaten up in a continuous fashion rather than piecemeal. There are no finite regions swallowed by the trace which are not on the trace itself. This means that the trace is *space-filling*: γ intersects every neighbourhood of every point in the upper half plane. We shall argue later (section 5.2.3) that the fractal dimension of the trace is $d_\gamma = 1 + \varkappa/8$ for $\varkappa \leqslant 8$ and 2 for $\varkappa \geqslant 8$. Thus it becomes space-filling for all $\varkappa \geqslant 8$.

5.2.3 Trace fractal dimensions

The fractal dimension of any geometrical object embedded in the plane can be defined roughly as follows: let $N(\varepsilon)$ be the minimum number of small discs of radius ε required to cover the object. Then if $N(\varepsilon) \sim \varepsilon^{-d_0}$ as $\varepsilon \to 0$, d_0 is the fractal dimension, rather the capacity dimension.

One way of computing d_0 for a random curve γ in the plane is to ask for the probability $P(x, y, \varepsilon)$ that a given point $\zeta = x + iy$ lies within a distance ε of γ. A simple scaling argument shows that if P behaves like $\varepsilon^\delta f(x, y)$ as $\varepsilon \to 0$, then $\delta = 2 - d_0$. We can derive a differential equation for P along the lines of the previous calculation. The only difference is that under the conformal mapping $g_{\mathrm{d}t}$, $\varepsilon \to |g'_{\mathrm{d}t}(\zeta)|\varepsilon \sim \big(1 - 2\,\mathrm{d}t\,\mathrm{Re}(1/\zeta^2)\big)\varepsilon$. The differential equation (written for convenience in cartesian coordinates) is

$$\left(\frac{2x}{x^2+y^2}\frac{\partial}{\partial x} - \frac{2y}{x^2+y^2}\frac{\partial}{\partial y} + \frac{\varkappa}{2}\frac{\partial^2}{\partial x^2} - \frac{2(x^2-y^2)}{(x^2+y^2)^2}\varepsilon\frac{\partial}{\partial \varepsilon}\right) P = 0 \qquad (5.16)$$

Now P is dimensionless and therefore should have the form $(\varepsilon/r)^{2-d_\gamma}$ times a function of the polar angle ϑ. In fact, the simple ansatz $P = \varepsilon^{2-d_gamma}y^\alpha(x^2 + y^2)^\beta$, with $\alpha + 2\beta = d_\gamma - 2$ satisfies the equation. This gives $\alpha = (\varkappa - 8)^2/8\varkappa$, $\beta = (\varkappa - 8)/2\varkappa$ and

$$d_\gamma = 1 + \varkappa/8 \qquad (5.17)$$

This is correct for $\varkappa \leqslant 8$: otherwise there is another solution with $\alpha = \beta = 0$ and $d_f = 2$.

We see that the fractal dimension increases steadily from the value 1 when $\varkappa = 0$ (corresponding to a straight line) to a maximum value of 2 when $\varkappa = 8$. Beyond this value γ becomes space-filling: every point in the upper half plane lies on the curve.

Summarizing, a SLE curve has fractal dimension

$$d_\gamma = \begin{cases} 1 + \dfrac{\varkappa}{8} & \varkappa \leqslant 8 \\ 2 & \varkappa \geqslant 8 \end{cases} \tag{5.18}$$

Moreover, different subsets of special points of the curve can be considered. A remarkable example is given by the point of the SLE path lying on the real axis, i.e. the points where the curve hits the real axis. Their fractal dimension can be extracted by the *hitting probability*, leading to

$$d_{\mathrm{rp}} = \begin{cases} 0 & \varkappa \leqslant 4 \\ 2 - \dfrac{8}{\varkappa} & 4 \leqslant \varkappa \leqslant 8 \\ 1 & \varkappa \geqslant 8 \end{cases} \tag{5.19}$$

When the curve hits itself rather than the real axis, it displays a double point, i.e. a point labelled by two different times. Their density in the complex plain is given by the fractal dimensions

$$d_{\mathrm{dp}} = \begin{cases} 0 & \varkappa \leqslant 4 \\ \dfrac{(\varkappa - 4)(\varkappa + 12)}{8\varkappa} & 4 \leqslant \varkappa \leqslant 12 \\ 2 & \varkappa \geqslant 12 \end{cases} \tag{5.20}$$

5.2.4 SLE duality

For $\varkappa > 4$ the curve continually touches itself and therefore its hull $\mathcal{K}_t$ contains earlier portions of the trace (see figure 5.1). However, the *frontier* of $\mathcal{K}_t$ (i.e. the boundary of $\mathbb{H} \setminus \mathcal{K}_t$, minus any portions of the real axis), is by definition a simple curve. A beautiful result, first suggested by Duplantier and proved by Beffarafor the case $\varkappa = 6$, is that locally this curve is an $\mathrm{SLE}_{\tilde{\varkappa}}$, with

$$\tilde{\varkappa} = 16/\varkappa \tag{5.21}$$

For example, the exterior of a percolation cluster contains many 'fjords' which, on the lattice, are connected to the main ocean by a neck of water which is only a finite number of lattice spacings wide. These are sufficiently frequent and the fjords macroscopically large that they survive in the continuum limit. SLE_6

describes the boundaries of the clusters, including the coastline of all the fjords. However, the coastline as seen from the ocean is a simple curve, which is locally $\mathrm{SLE}_{8/3}$, the same as that conjectured for a self-avoiding walk. This suggests, for example, that locally the frontier of a percolation cluster and a self-avoiding walk are the same in the scaling limit. It has be proven that $\mathrm{SLE}_\varkappa$ and $\mathrm{SLE}_{\tilde{\varkappa}}$ correspond to conformal field theories with the same value of the central charge c.

5.2.5 Crossing probability

Given a critical percolation problem inside a simply connected domain $\mathcal{D}$, what is the probability that a cluster connects two disjoint segments AB and CD of the boundary? This problem was conjectured to be conformally invariant A formula based on conformal field theory as well as a certain amount of guesswork was conjectured in [Car92]. It was proved, for the continuum limit of site percolation on the triangular lattice, by Smirnov [Smi01].

Within SLE, it takes a certain amount of ingenuity [Sch00] to relate this problem to a question about a single curve. As usual, let $\mathcal{D}$ be the upper half plane. It is always possible to make a fractional linear conformal mapping which takes AB into $(-\infty, x_1)$ and CD into $(0, x_2)$, where $x_1 < 0$ and $x_2 > 0$. Now go back to the lattice picture and consider critical site percolation on the triangular lattice in the upper half plane, so that each site is independently coloured black or white with equal probabilities $\frac{1}{2}$. Choose all the boundary sites on the positive real axis to be white, all those on the negative real axis to be black (see figure 5.6). There is a cluster boundary starting at the origin, which, in the continuum limit, will be described by SLE_6. Since $\varkappa > 4$, it repeatedly hits the real axis, both to the L and R of the origin. Eventually every point on the real axis is swallowed. Either x_1 is swallowed before x_2, or vice versa.

Note that every site on the L of the curve is black, and every site on its R is white. Suppose that x_1 is swallowed before x_2. Then, at the moment it is swallowed, there exists a continuous path on the white sites, just to the R of the curve, which connects $(0, x_2)$ to the row just above $(-\infty, x_1)$. On the other hand, if x_2 is swallowed before x_1, there exists a continuous path on the black sites, just to the L of the curve, connecting $0-$ to a point on the real axis to the R of x_2. This path forms a barrier (as in the game of Hex) to the possibility of a white crossing from $(0, x_2)$ to $(-\infty, x_1)$. Hence there is such a crossing if and only if x_1 is swallowed before x_2 by the SLE curve.

Recall that in section 5.2.2 we related the swallowing of a point x_0 on the real axis to the vanishing of $x_t = g_t(x_t) - u_t$, which undergoes a Bessel process

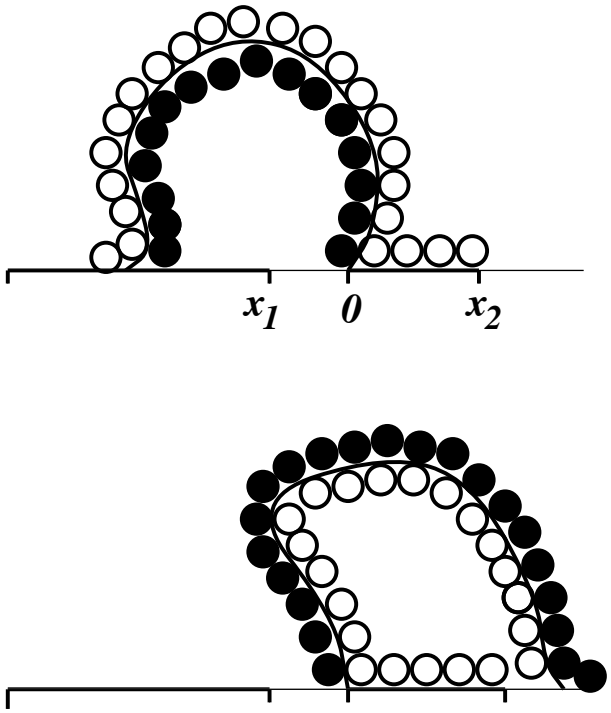

Figure 5.6: Is there a crossing on the white discs from $(0, x_2)$ to $(-\infty, x_1)$? This happens if and only if x_1 gets swallowed by the SLE before x_2.

on the real line. Therefore

$$\mathscr{P}\big[\text{crossing from } (0,x_2) \text{ to } (-\infty,x_1)\big] = \mathscr{P}\big[x_{1t} \text{ vanishes before } x_{2t}\big] \quad (5.22)$$

Denote this by $P\big(x_1,x_2\big)$. By generalising the SLE to start at u_0 rather than 0, we can write the differential equation:

$$\left(\frac{2}{x_1-u_0}\frac{\partial}{\partial x_1}+\frac{2}{x_2-u_0}\frac{\partial}{\partial x_2}+\frac{\varkappa}{2}\frac{\partial^2}{\partial u_0^2}\right)\ P\big(x_1,x_2;u_0\big)=0 \qquad (5.23)$$

Translational invariance implies that we can replace ∂_{u_0} by $-(\partial_{x_1}+\partial_{x_2})$. Finally, P can in fact depend only on the ratio $\eta=(x_2-u_0)/(u_0-x_1)$, which again reduces the equation to hypergeometric form. The solution is (specialising to $\varkappa=6$ for percolation)

$$P=\frac{\Gamma(\frac{2}{3})}{\Gamma(\frac{4}{3})\Gamma(\frac{1}{3})}\eta^{1/3}{}_2F_1(\tfrac{1}{3},\tfrac{2}{3},\tfrac{4}{3};\eta) \qquad (5.24)$$

It should be mentioned that this is but one of a number of percolation crossing formulae. Another, conjectured by Watts,for the probability that there is cluster which simultaneously connects AB to CD and BC to DA, has since been proved by Dubédat.However, other formulae, for example for the mean number of distinct clusters connecting AB and CD, and for the probability that exactly N distinct clusters cross an annulus, are as yet unproven using SLE methods.

For a generic $\varkappa$ the crossing formula reads

$$P_{\rm cr}(\varkappa;r)=1-\frac{r^{1-\frac{4}{\varkappa}}}{1-\frac{4}{\varkappa}}\,\frac{\Gamma\left(2-\frac{8}{\varkappa}\right)}{\Gamma\left(1-\frac{4}{\varkappa}\right)}\,{}_2F_1\left(1-\frac{4}{\varkappa},2-\frac{8}{\varkappa},2-\frac{4}{\varkappa};-r\right) \qquad (5.25)$$

5.3 Convergence of discrete models to SLE

This result allows use to make a tentative identification with the various realisations of the $\mathrm{O}(n)$ model described in section 4.2.2. It can be computed that $n=-2\cos(4\pi/\varkappa)$ with $2\leqslant\varkappa\leqslant4$ describing the critical point at t_c, and $4<\varkappa\leqslant8$ corresponding to the dense phase. Some important special cases are therefore:

- $\varkappa=-2$: loop-erased random walks (proven in [LSW04a]);
- $\varkappa=\frac{8}{3}$: self-avoiding walks, as already suggested by the restriction property; unproven, but see [LSW04b] for many consequences;
- $\varkappa=3$: cluster boundaries in the Ising model, however as yet unproven;

- $\varkappa = 4$: BCSOS model of roughening transition (equivalent to the 4-state Potts model and the double dimer model), as yet unproven; also certain level lines of a Gaussian random field and the harmonic explorer (proven in [SS05]); also believed to be dual to the Kosterlitz–Thouless transition in the XY model;
- $\varkappa = 6$: cluster boundaries in percolation (proven in [Smi01]);
- $\varkappa = 8$: dense phase of self-avoiding walks; boundaries of uniform spanning trees (proven in [LSW04a]).

It should be noted that no lattice candidates for $\varkappa > 8$, or for the dual values $\varkappa < 2$, have been proposed. This possibly has to do with the fact that, for $\varkappa > 8$, the SLE trace is not reversible: the law on curves from r_1 to r_2 is not the same as the law obtained by interchanging the points. Evidently, curves in equilibrium lattice models should satisfy reversibility.

Chapter 6

Overruled harmonic explorers

In section 5.3 one of the main problems concerning the relation between exploration processes on a lattice and on a complex domain were discussed. Indeed, in the scaling limit a large number of two-dimensional discrete stochastic models, some examples of which were presented in chapter 4, are supposed to share conformal invariance and Markovianity, hence being fully described by a stochastic Löwner evolution. Despite experimental and numerical evidence of convergence to SLE, proving it rigorously remains a great challenge and until now only for two cases has the demonstration been completed: the critical percolation converges to SLE_6, the harmonic explorer to SLE_4. Moreover, while the $\mathrm{SLE}_\varkappa$ are a one-parameter family of continuous growth processes, in the discrete case only statistical-mechanics models can offer one-parameter families of (likely) conformally invariant patterns. However, building an exploration process from a statistical-mechanics model is a very cumbersome and involute way. On the other hand, only few and isolated examples of discrete exploration processes are observed to converge to an $\mathrm{SLE}_\varkappa$. In this chapter I will show how from the remarkable example of the harmonic explorer it is possible to define a general class of explorers and a one-parameter subfamily, whose one-to-one convergence to $\mathrm{SLE}_\varkappa$ is guessed.

From the construction itself the harmonic explorer inherits some features which ensure its convergence to SLE_4 in the scaling limit. In particular, its exploration rule is based on the random walk, whose conformal invariance (with different times) is presented in section 6.1. In section 6.2 the property shared by the harmonic exploration process and SLE_4, i.e. the martingale property of the harmonic function, is explained. In section 6.3 a generalized class of explorers based on the random walk is defined. In section 6.4 some special cases of generalized harmonic explorers are discussed and their possible scaling limit is guessed.

6.1 The harmonic-exploration process

Among several discrete exploration processes, the harmonic explorer, described in section 4.3.1, is the most interesting case. First, because it is one of the only two models which are proved to converge to SLE. However, the other case, the critical percolation, does not offer the same richness of the harmonic explorer. The key is its exploration rule based on the random walk, which is Markovian by definition and conformally invariant, apart from a time dilation. The latter feature is crucial in order to ensure the scaling limit at $\varkappa = 4$. In this section we will see that a probability based on the random walk is described by the harmonic function (section 6.1.1) and how the random walk transforms under conformal maps (section 6.1.2).

6.1.1 Random walk and harmonicity

As discussed in chapter 4, an exploration process on lattice edges — say, in a hexagonal lattice — is defined by some boundary conditions plus a stochastic exploration rule, which is needed in order to determine the colour of the face — the hexagon — v_{n+1} located in front of the explorer tip after n steps and, consequently, the new explorer direction. In the case of the harmonic explorer a random walker on lattice faces is launched from v_{n+1} and stopped once it hits the boundary for the first time, as sketched in figure 6.1. Then, the boundary condition of the hit boundary face is assigned to v_{n+1}. Thus, the probability P_- that v_{n+1} is coloured red is given evaluating (in v_{n+1}) the probability $H_n(z)$ that a random walker on faces, starting from a generic face z, hits a red boundary before a blue one. Notice that the subscript n cannot be omitted, because after each step domain boundary changes with the addition of the face v_n, so that the value of H_{n-1} and H_n are different in a bulk face.

From a mathematical viewpoint we are interested in finding what kind of function is involved in this probability, i.e. what properties characterize $H_n(z)$. First, boundary conditions are needed and straightforward assigned: since we are yet on the boundary, no random walker has to run and $H_n(z) = 1$ if z is red, $H_n(z) = 0$ if z is blue. Now, let us consider a generic bulk face centred in z on a complex domain and surrounded by m not-yet-coloured faces centred in z_j ($j = 1, m$; $m = 6$ in honeycomb lattice):

$$\begin{aligned} H_n(z) &= \mathscr{P}[\text{random walk from } z \text{ hits red boundary first}] = \\ &= \sum_{j=1}^{m} \mathscr{P}[z \to z_j] H_n(z_j) = \sum_{j=1}^{m} \frac{1}{m} H_n(z_j) = \sum_{j=1}^{m} \frac{1}{m} H_n\left(z + a\mathrm{e}^{\mathrm{i}j\frac{2\pi}{m}}\right) \end{aligned} \quad (6.1)$$

where a is the lattice spacing. If we put the Taylor expansion of $H_n(z_j)$ up to

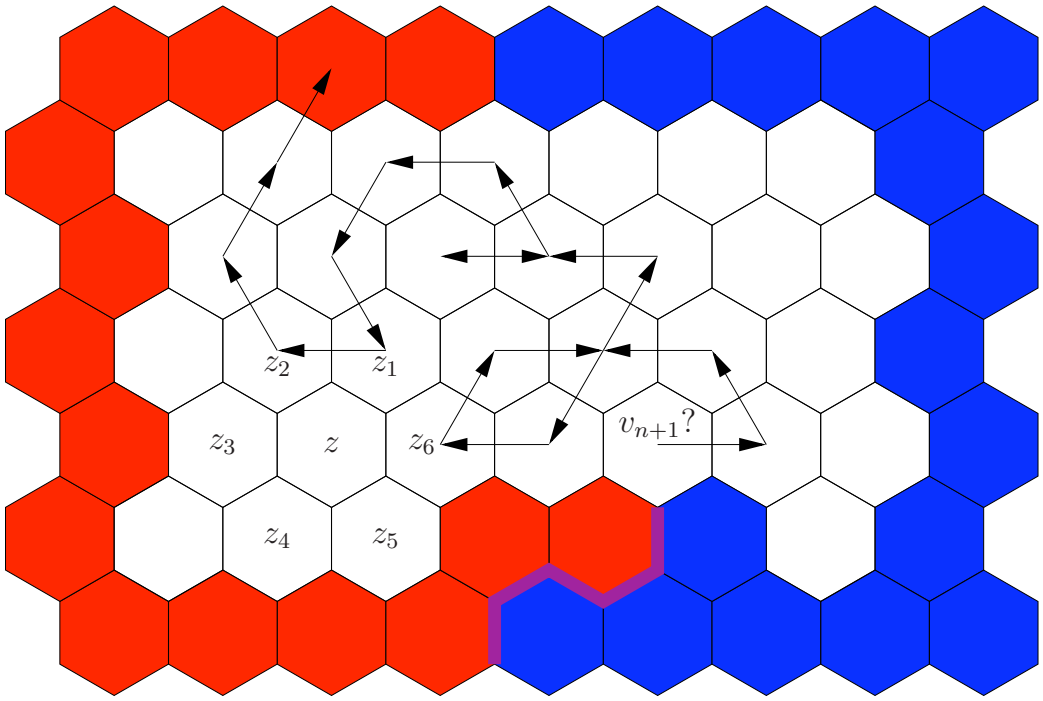

Figure 6.1: The harmonic explorer (magenta) has to know whether the hexagon v_{n+1} is red or blue in order to turn right or left. This colour is the same of the boundary hit by a random walker on hexagons starting from v_{n+1} and it is red with probability $H_n(v_{n+1})$, where H_n is the unique harmonic function at step n with the given boundary conditions (1 on red, 0 on blue). Here $n = 4$.

the second order,

$$H_n(z_j) = H_n(z) + H_n(z)a\mathrm{e}^{\mathrm{i}j\frac{2\pi}{m}} + H_n(z)a^2\mathrm{e}^{\mathrm{i}j\frac{4\pi}{m}} + O(a^2)$$

into (6.1), we obtain

$$\begin{aligned} H_n(z) &= \frac{1}{m}\sum_{j=1}^{m}\left(H_n(z) + H_n(z)a\mathrm{e}^{\mathrm{i}j\frac{2\pi}{m}} + H_n(z)a^2\mathrm{e}^{\mathrm{i}j\frac{4\pi}{m}} + O(a^2)\right) = \\ &= H_n(z) + \frac{1}{m}H_n(z)a\sum_{j=1}^{m}\mathrm{e}^{\mathrm{i}j\frac{2\pi}{m}} + \frac{1}{m}H_n(z)a^2\sum_{j=1}^{m}\mathrm{e}^{\mathrm{i}j\frac{4\pi}{m}} + O(a^2) = \\ &= H_n(z) + \frac{1}{m}H_n(z)a\cdot 0 + \frac{1}{m}H_n(z)a^2\sum_{j=1}^{m}\mathrm{e}^{\mathrm{i}j\frac{4\pi}{m}} + O(a^2) = \\ &= H_n(z) + a^2\triangle H_n(z) + O(a^2) \end{aligned} \quad (6.2)$$

the last equalities being due to the definition itself of the discrete Laplacian.

In other words, first order term is simply proportional to the mean displacement from z after the first step of the random walker and therefore vanishes, whereas the second order term is related to the mean square displacement and, generally speaking, is not expected to vanish. However, here the diffusive term has to be zero in order to ensure that (6.2) holds up to the second order. Thus, H_n is the unique harmonic function in the lattice domain with boundary conditions 1 on the red boundary and 0 on the blue one.

6.1.2 Random walk and conformal invariance

Now we want to highlight the crucial role of an exploration ruled based on the random walk in order to ensure the convergence of the harmonic exploration process to a SLE. Indeed, as we will see soon, two properties, Markovianity and conformal invariance, are guaranteed by this simple rule. It is worth noticing that both are fundamental in order to obtain an SLE in the continuous limit. In this section the conformal invariance (apart from a time dilation) of the random walk will be shown, the Markovianity being ensured by the definition of the random walk. As a consequence, the harmonic explorer itself inherits the two properties.

A random walk is described by the following equations:

$$\begin{cases} \mathrm{d}x = \mathrm{d}W_x(t) & (6.3\mathrm{a}) \\ \mathrm{d}y = \mathrm{d}W_y(t) & (6.3\mathrm{b}) \end{cases}$$

where $W_x(t)$ and $W_y(t)$ are two independent one-dimensional Brownian motions.

Let us consider a conformal transformation

$$\begin{cases} u = u(x,y) \\ v = v(x,y) \end{cases} \quad \text{such that} \quad \begin{cases} \partial_x u = \quad \partial_y v \\ \partial_y u = -\partial_x v \end{cases} \tag{6.4}$$

i.e. a map from $\mathcal{D} \subset \mathbb{C}$ to $\mathcal{D}' \subset \mathbb{C}$ respecting the Cauchy–Riemann equations, from which it is straightforward to extract the following relations

$$\begin{cases} \partial_x^2 u = \quad \partial_x \partial_y v = -\partial_y^2 u & (6.5\mathrm{a}) \\ \partial_x^2 v = -\partial_x \partial_y u = -\partial_y^2 v & (6.5\mathrm{b}) \end{cases}$$

Thus, under the conformal map the random walk (6.3) becomes

$$\begin{cases} \mathrm{d}u = \partial_x u \,\mathrm{d}x + \partial_y u \,\mathrm{d}y + \frac{1}{2}\partial_x^2 u \,\mathrm{d}t + \frac{1}{2}\partial_y^2 u \,\mathrm{d}t = \partial_x u \,\mathrm{d}x + \partial_y u \,\mathrm{d}y \\ \mathrm{d}v = \partial_x v \,\mathrm{d}x + \partial_y v \,\mathrm{d}y + \frac{1}{2}\partial_x^2 v \,\mathrm{d}t + \frac{1}{2}\partial_y^2 v \,\mathrm{d}t = \partial_x v \,\mathrm{d}x + \partial_y v \,\mathrm{d}y \end{cases}$$

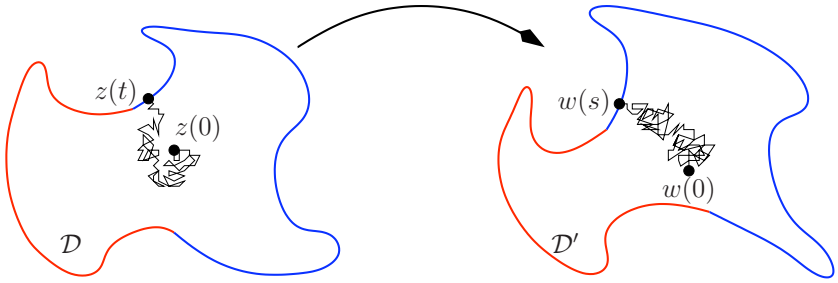

Figure 6.2: A random walker starting from the bulk point $z(0) \in \mathcal{D}$ reaches the boundary in $z(t)$, t being the first hit time (left). How does a conformal map act on a random walk? Its trace still describes a random walk in the new domain $\mathcal{D}'$ as shown by (6.8), but with a different first hit time s (right). However, the exit points $z(t)$ and $w(s)$ share the same boundary conditions (indicated by different colours, red or blue, from now on).

where the terms proportional to $\mathrm{d}t$ cancel each other thanks to (6.5). Finally, (6.3) allow us to express the conformally mapped random walk in terms of the two independent Brownian motions:

$$\begin{cases} \mathrm{d}u = \partial_x u \, \mathrm{d}W_x + \partial_y u \, \mathrm{d}W_y & (6.6a) \\ \mathrm{d}v = \partial_x v \, \mathrm{d}W_x + \partial_y v \, \mathrm{d}W_y & (6.6b) \end{cases}$$

The latter expression is a *martingale*, i.e. a stochastic process X_t in the growing parameter t with the property

$$\forall s \leqslant t \quad \mathscr{E}[X_t | X_r, r \leqslant s] = X_s \tag{6.7}$$

In other words, if X_t is the total gain after t fair-coin tosses, the martingale property states that the expected value of X_t, conditioned to a total gain of X_s after $s \leqslant t$ tosses, is X_s. I.e. the mean gain after t tosses is the gain after s, if you know the latter.

The martingale (6.6) can be reformulated in terms of a new time $s(t)$ such that

$$\begin{cases} \mathrm{d}u = \mathrm{d}W_u(s) & (6.8a) \\ \mathrm{d}v = \mathrm{d}W_v(s) & (6.8b) \end{cases}$$

Thus, the random walk is conformally invariant, provided that a rescaled time is used. However, here we are interested in the conformal invariance of the harmonic explorer and for this exploration process it is not important how long the random walker takes to reach the boundary (but only the colour of that boundary). Indeed, at every step, one has to know only *where* the random walker hits the boundary for the first time, not *how long* its wander is, in order to determine

the new direction of the explorer. Since the imposed boundary condition on the hit point does not change under a conformal map, the harmonic explorer turns to the same direction too, thus proving its conformal invariance (as sketched in figure 6.2).

6.2 The harmonic function as a martingale

In section 6.1.2 it has been shown that, by construction, the harmonic explorer turns out to be both Markovian and conformally invariant. In particular, this follows from an exploration process intrinsically based on the random walk. Since an $\mathrm{SLE}_\varkappa$ is defined on the same two properties, it is straightforward to guess the convergence of the harmonic explorer to an $\mathrm{SLE}_\varkappa$ in the continuous limit.

Before this convergence can be proved, the question to be addressed is on which $\varkappa$ could be compatible with the specific features of the harmonic explorer. Thus, we have to identify one particular property $\mathrm{p}_\varkappa$ shared both by the harmonic explorer and by an $\mathrm{SLE}_\varkappa$ at a fixed $\varkappa$. Here the involved $\mathrm{p}_\varkappa$ concerns the harmonic function $H_n(z)$:

Property 6.1 (The harmonic function is a martingale)**.**

$$\mathrm{p}_\varkappa \quad : \quad \forall m \leqslant n, z \in \mathcal{D} \quad \mathscr{E}[H_n(z)|H_l(z), l \leqslant m] = H_m(z)$$

Here, z is a point in the complex domain $\mathcal{D}$ and the centre of a face in the corresponding lattice domain $\mathcal{D}^\#$; l, m and n are either step numbers of the exploration process, in the discrete case, or times spent by the SLE, in the continuous case.

In the lattice domain $H_n(z)$ is the probability that the face z is red after n explorer steps. Therefore $H_n(z)$ has value 1 on the red boundary and 0 on the blue one, once the boundary conditions are fixed. Moreover, $H_n(z)$ is discretely harmonic in the domain bulk. Notice that z indicates both the face and its centre, as usual; therefore, we can write $z \in \mathcal{D}$ or $z \in \mathcal{D}^\#$ according to the actual meaning.

6.2.1 The discrete case

Let us show how property 6.1 works in the discrete case. We have to demonstrate that

$$\langle H_{n+1}(z) \rangle = H_0(z) \quad \forall z \in \mathcal{D}^\#$$

If that is true for $n+1$, it is clearly true for n too (i.e. $\langle H_n(z) \rangle = H_0(z)$), because n is a generic natural number here. Thus, it is enough to only prove

that the martingale property holds for the last step:

$$\langle H_{n+1}(z)\rangle = H_n(z) \quad \forall z \in \mathcal{D} \tag{6.9}$$

By definition $H_n(z)$ satisfies the discrete Laplace equation with given boundary conditions. Therefore if property 6.1 holds on the domain boundary, it has to be valid also in the domain bulk. Indeed, once the boundary conditions are kept fixed, the Laplace equation has a unique solution. As the harmonic explorer performs a new step, the only change in the domain is in the face v_{n+1} in front of the tip, which is coloured, becoming part of the boundary. So, from step n to step $n+1$ the boundary remains the same and, as a consequence, the boundary conditions themselves do not change. Finally, the martingale property (6.9) has to be tested only in the face $z = v_{n+1}$ (whose colour is chosen at step $n+1$) in order to prove the relation in the whole domain:

$$\langle H_{n+1}(v_{n+1})\rangle = H_n(v_{n+1}) \tag{6.10}$$

Since $H_n(v_{n+1})$ is the probability that v_{n+1} becomes red, we can simply write

$$\langle H_{n+1}(v_{n+1})\rangle = 1 \cdot H_n(v_{n+1}) + 0 \cdot \big(1 - H_n(v_{n+1})\big) = H_n(v_{n+1}) \tag{6.11}$$

This relation is true for each new face added to the boundary. Thence, it is true in the whole domain for analytic continuation.

More rigorously, calling $\mathcal{B}_n^{\#}$ and $\mathcal{B}_{n+1}^{\#} = \mathcal{B}_n^{\#} \cup v_{n+1}$ the domain boundaries at step n and $n+1$, respectively, and $\mathscr{P}\big[z \xrightarrow[n]{\text{rw}} z'\big]$ the probability that, in the domain at step n, a random walker starting from the face z reaches the face z' before hitting the boundary, we can compute H_{n+1} in a bulk face $z \notin \mathcal{B}_n^{\#}$

$$\begin{aligned}
H_{n+1}(z) &= \sum_{b\in\mathcal{B}_{n+1}^{\#}} \mathscr{P}\Big[z \xrightarrow[n+1]{\text{rw}} b\Big] H_{n+1}(b) = \\
&= \sum_{b\in\mathcal{B}_n^{\#}} \mathscr{P}\Big[z \xrightarrow[n+1]{\text{rw}} b\Big] H_{n+1}(b) + \mathscr{P}\Big[z \xrightarrow[n+1]{\text{rw}} v_{n+1}\Big] H_{n+1}(v_{n+1}) = \\
&= \sum_{b\in\mathcal{B}_n^{\#}} \Big(\mathscr{P}\Big[z \xrightarrow[n]{\text{rw}} b\Big] - \mathscr{P}\Big[z \xrightarrow[n]{\text{rw}} v_{n+1}\Big]\mathscr{P}\Big[v_{n+1} \xrightarrow[n]{\text{rw}} b\Big]\Big) H_n(b) + \\
&\qquad + \mathscr{P}\Big[z \xrightarrow[n]{\text{rw}} v_{n+1}\Big] H_{n+1}(v_{n+1}) = \\
&= \sum_{b\in\mathcal{B}_n^{\#}} \mathscr{P}\Big[z \xrightarrow[n]{\text{rw}} b\Big] H_n(b) - \sum_{b\in\mathcal{B}_n^{\#}} \mathscr{P}\Big[z \xrightarrow[n]{\text{rw}} v_{n+1}\Big]\mathscr{P}\Big[v_{n+1} \xrightarrow[n]{\text{rw}} b\Big] H_n(b) + \\
&\qquad + \mathscr{P}\Big[z \xrightarrow[n]{\text{rw}} v_{n+1}\Big] H_{n+1}(v_{n+1}) = \\
&= H_n(z) - \mathscr{P}\Big[z \xrightarrow[n]{\text{rw}} v_{n+1}\Big] H_n(v_{n+1}) + \mathscr{P}\Big[z \xrightarrow[n]{\text{rw}} v_{n+1}\Big] H_{n+1}(v_{n+1})
\end{aligned} \tag{6.12}$$

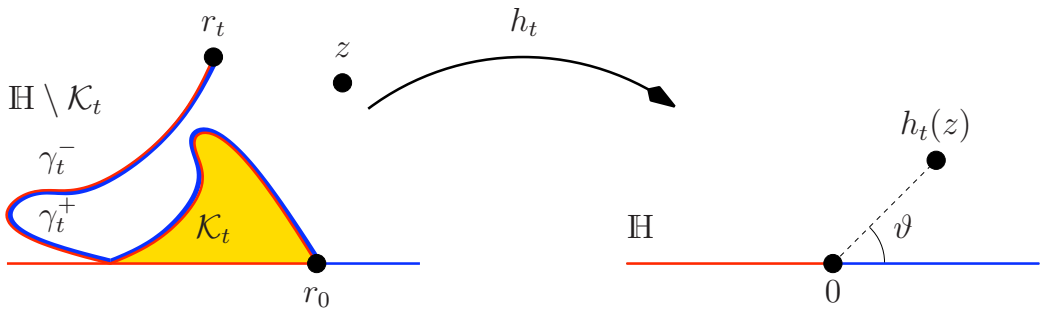

Figure 6.3: The uniformizing map h_t in the upper half-plane maps the tip r_t of a generic SLE$_\varkappa$ curve into the origin. Boundary conditions of the harmonic function $H_t(z)$ are fixed to 1 (red) on the left boundary and to 0 (blue) on the right one. Left and right are considered with respect to either the tip, in the cut domain, or the origin, in the uniformized domain. Here, the harmonic function in a bulk point z is simply proportional to the argument ϑ of its image $h_t(z)$.

Therefore, from step n to step $n+1$ the harmonic function is subjected to the increase

$$H_{n+1}(z) - H_n(z) = \mathscr{P}\Big[z \xrightarrow[n]{\text{rw}} v_{n+1}\Big]\big(H_{n+1}(v_{n+1}) - H_n(v_{n+1})\big) \tag{6.13}$$

Finally, averaging (6.13) leads to

$$\begin{aligned}\langle H_{n+1}(z)\rangle - H_n(z) &= \\ &= \mathscr{P}\Big[z \xrightarrow[n]{\text{rw}} v_{n+1}\Big]\Big(1 \cdot H_n(v_{n+1}) + 0 \cdot \big(1 - H_n(v_{n+1})\big) - H_n(v_{n+1})\Big) = 0\end{aligned} \tag{6.14}$$

6.2.2 The continuous case

Now we want to find an SLE$_\varkappa$, i.e. a special $\varkappa$, where the same martingale property is present; speaking more formally, we are looking for a

$$\varkappa \quad \text{such that} \quad \langle H_t(z)\rangle = H_0(z)$$

If we consider an SLE$_\varkappa$ evolving in the upper half-plane $\mathbb{H}$, H_t is defined in the cut domain $\mathbb{H} \setminus \mathcal{K}_t$ and follows the Laplace equation

$$\partial^2 H_t(z) = 0 \tag{6.15a}$$

which ensures harmonicity. In addition, boundary conditions have to be given; here we choose

$$H_t(z) = \begin{cases} 1 & z \in (-\infty, a_0) \cup \gamma_t^- \\ 0 & z \in \gamma_t^+ \cup (a_0, +\infty) \end{cases} \tag{6.15b}$$

as represented in figure 6.3.

The meaning of the harmonic function is still the same in this different framework: if at any time t a random walker is launched from the point z, $H_t(z)$ is the probability that this random walker hits the 1-boundary first. However, the trace γ_t of the $\mathrm{SLE}_\varkappa$ curve could be very winding, so much that extracting the analytic expression of H_t could result very difficult. Nevertheless, in section 6.1.2 it is shown that the boundary condition of the point hit by the random walker does not change under conformal transformations, so proving the conformal invariance of the harmonic function. Thus, it is more convenient to search H_t in a simpler (conformally mapped) domain rather than in the cut one $\mathbb{H} \setminus \mathcal{K}_t$. Obviously, the best choice is the upper half-plane $\mathbb{H}$ itself, obtained via the uniformizing function

$$h_t : \mathbb{H} \setminus \mathcal{K}_t \mapsto \mathbb{H} \tag{6.16a}$$

$$h_t = g_t - \sqrt{\varkappa} B_t \tag{6.16b}$$

which maps the tip r_t into the origin, following the stochastic equation

$$\mathrm{d}h_t = \frac{2\,\mathrm{d}t}{h_t} - \sqrt{\varkappa}\,\mathrm{d}B_t \tag{6.17}$$

In the uniformized domain H_t, φ will be the solution of the Laplace equation

$$\begin{cases} \partial^2 \varphi(z) = 0 & \text{(6.18a)} \\ \varphi(z) = \begin{cases} 1 & z \in \mathbb{R}^- \\ 0 & \mathbb{R}^+ \end{cases} & \text{(6.18b)} \end{cases}$$

and can be expressed in polar coordinates as the phase function

$$\varphi = \frac{\vartheta}{\pi}$$

Indeed, in these coordinates the Laplace equation $(6.18\mathrm{a})$ becomes

$$\begin{aligned} &\frac{1}{r}\partial_r(r\partial_r\varphi) + \frac{1}{r^2}\partial_\vartheta^2\varphi = 0 \\ \Longrightarrow \qquad &0 + \frac{1}{r^2}\partial_\vartheta^2\frac{\vartheta}{\pi} = 0 \end{aligned}$$

In terms of the conformal map h_t the harmonic function is

$$H_t(z) = \frac{1}{\pi}\arg h_t(z) \tag{6.19}$$

Now we need to extract a dependence on the SLE parameter $\varkappa$ from this expression, in order to identify the special $\mathrm{SLE}_\varkappa$ where the martingale property for the harmonic function is valid. Let us remember that $\arg z = \operatorname{Im} \log z$ and that a function $\psi(x_t)$ of a stochastic variable x_t obeys to the Itô formula

$$\mathrm{d}\psi(x_t) = \frac{\mathrm{d}}{\mathrm{d}x_t}\psi(x_t)\,\mathrm{d}x_t + \frac{1}{2}\frac{\mathrm{d}^2}{\mathrm{d}x_t^2}\psi(x_t)\varkappa\,\mathrm{d}t \tag{6.20}$$

Here the harmonic function is a stochastic function of the uniformizing map h_t; hence, plugging (6.19) into (6.20) and exploiting (6.17), we can write

$$\begin{aligned}\mathrm{d}H_t(z) = \frac{1}{\pi}\operatorname{Im}\mathrm{d}\big(\log h_t(z)\big) = \frac{1}{\pi}\operatorname{Im}\left(\frac{\mathrm{d}h_t(z)}{h_t(z)} - \frac{1}{2}\frac{\varkappa\,\mathrm{d}t}{h_t^2(z)}\right) = \\ = \frac{1}{\pi}\operatorname{Im}\left(\frac{(4-\varkappa)\,\mathrm{d}t}{2h_t^2(z)} - \frac{\sqrt{\varkappa}\,\mathrm{d}B_t}{h_t(z)}\right)\end{aligned} \tag{6.21}$$

Since the Brownian term has zero mean by definition, the martingale property can be guaranteed if and only if the $\mathrm{d}t$-term in (6.21) vanishes, i.e. when $4-\varkappa = 0$:

$$\langle \mathrm{d}H_t(z)\rangle = 0 \quad \Longleftrightarrow \quad \varkappa = 4 \tag{6.22}$$

Here we did not show a complete demonstration that the harmonic explorer has a continuous limit in the SLE_4 (you can find it in [SS05]), but only that the unique SLE compatible (i.e. sharing the same identifying property) with the harmonic exploration must have $\varkappa = 4$.

6.3 Generalized harmonic explorers

Although the convergence of an exploration process to an $\mathrm{SLE}_\varkappa$ is proved rigorously only for few values of $\varkappa$ (namely, $\varkappa = 4, 6$ for the time being), it is well known, thanks to both theoretical and numerical results, that each $\mathrm{SLE}_\varkappa$ is in correspondence with a spin model in the discrete case. However, simulating an $\mathrm{O}(n)$ model at every step is still too expensive from a computational point of view, because it requires solving the entire domain. On the contrary, the harmonic explorer offers a cheaper alternative, basically due to its convenient exploration rule: at every step only a random walker has to run, with a computational cost proportional to the total number of grid points N, whereas $\mathrm{O}(n)$ models have a cost increasing with N^2.

Moreover, only few and isolate examples of discrete growth processes are known to converge to an $\mathrm{SLE}_\varkappa$. This represents an (aesthetically) inconvenient truth: on the one hand, the $\mathrm{SLE}_\varkappa$ are a family of stochastic curves in the continuous parameter $\varkappa$, on the other hand no continuous family of exploration processes is known.

The basic idea of the present work emerges from these two needs: building a one-parameter family of computationally cheap exploration processes in correspondence one to one with $\mathrm{SLE}_\varkappa$ (obviously, this correspondence should be proved for every $\varkappa$). Let us consider the harmonic explorer again: by construction it contains the discrete version of the two SLE defining properties — Markovianity and conformal invariance — thanks to the random walk. Furthermore, the same random walk guarantees a fast advance in the domain. So, it is interesting to think to a generalization of the harmonic explorer.

6.3.1 The stretched harmonic explorers

The harmonic explorer advances from step n to $n+1$ by colouring — say, in the honeycomb lattice — the hexagon v_{n+1} red with probability $H_n(v_{n+1})$. Now the idea for generalized harmonic explorers is: colour v_{n+1} red with probability $f\big(H_n(v_{n+1})\big)$, where f is a function which stretches the original probability given by $H_n(v_{n+1})$. We could call this new class of explorers as *stretched harmonic explorers* (or, in short, f-HE). Here f should not be an arbitrary function, but should obey some constraints in order to give a right probability and to allow a continuous limit. More precisely,

$$\begin{aligned}\mathscr{P}[v_{n+1}\text{ red}] = P_-\big(v_{n+1}\big) = f\big(H_n(v_{n+1})\big)\\ \iff \quad f(x) \quad \text{such that} \quad x, f \in [0,1];\ f\left(x-\tfrac{1}{2}\right) \text{ odd}\end{aligned} \tag{6.23}$$

The first requirement is straightforward: f has to be a function of a probability ($0 \leqslant H_n \leqslant 1$) and a probability itself ($0 \leqslant f \leqslant 1$). The second requirement implies that f has a fixed point in $\left(\frac{1}{2}, \frac{1}{2}\right)$ and is an odd function around it. To see that, let us call P_+ and P_- the probability that the hexagon is coloured blue (or marked with spin $+1$) and red (spin -1), respectively. Thus, f has to be such that

$$\begin{cases} P_-(v_{n+1}) = f\big(H_n(v_{n+1})\big) & \text{(6.24a)}\\ P_+(v_{n+1}) = 1 - f\big(H_n(v_{n+1})\big) & \text{(6.24b)}\\ P_+(v_{n+1}) = f\big(1 - H_n(v_{n+1})\big) & \text{(6.24c)}\end{cases}$$

Indeed, P_+ can be computed either as $1-P_+$ (from $(6.24\mathrm{b})$) or as the function of the probability to colour v_{n+1} blue from (from $(6.24\mathrm{c})$). If we call $x_0 = 1 - H_n(v_{n+1})$ and $x_1 = H_n(v_{n+1})$ the harmonic probabilities of hitting the blue and red boundary, respectively, for the first time, equations $(6.24\mathrm{b})$ and $(6.24\mathrm{c})$ can be combined, giving

$$\begin{cases} P_+ = 1 - P_- = 1 - f(x_1) \\ P_+ = f(x_0) = f(1-x_1)\end{cases} \implies 1 - f(x_1) = f(1-x_1) \implies f\left(\tfrac{1}{2}\right) = \tfrac{1}{2}$$

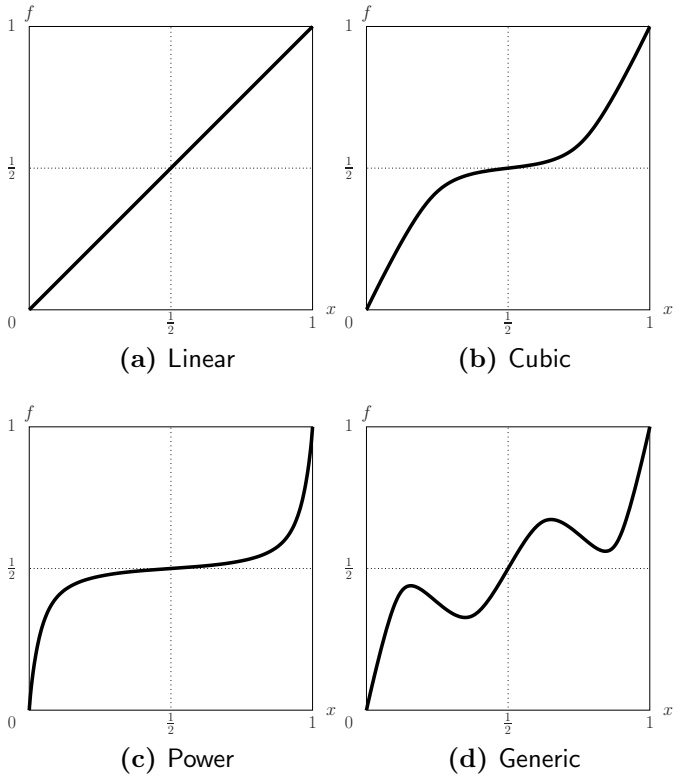

(a) Linear (b) Cubic

(c) Power (d) Generic

Figure 6.4: Sketches in the unitary square of some acceptable stretching functions; notice that f is odd around the fixed point $\frac{1}{2}$ and that also 0 and 1 are fixed points. In figures (a)–(c) power lwas with equation $f(x) = \alpha(x - \frac{1}{2})^{2q+1} + \frac{1}{2}$ are plotted ($q = 0$ in (a), $q = 1$ in (b) and $q > 1$ in (c); in all three cases $\alpha = 2^{2q}$). In figure (d) a generic function is sketched.

Notice that other two fixed points are present in order to ensure the preservation of the boundary conditions. Indeed, if v_{n+1} is on the blue or red boundary, $H_n(v_{n+1})$ has value 0 or 1, respectively, as a reminiscence that it cannot change its fixed colour. Consequently, f can deform the probability given by the harmonic function only outside of 0 and 1. At last, three fixed points are present:

$$\begin{cases} f(0) = 0 \\ f\left(\frac{1}{2}\right) = \frac{1}{2} \\ f(1) = 1 \end{cases}$$

Once a function $f(x)$ is selected, the stochastic behaviour of the explorer is given, but we still have to evaluate the probability. In the linear case, the probability is proportional to the harmonic function, so that only a run of one random walk is needed, as for the harmonic explorer. Analogously, with a cubic

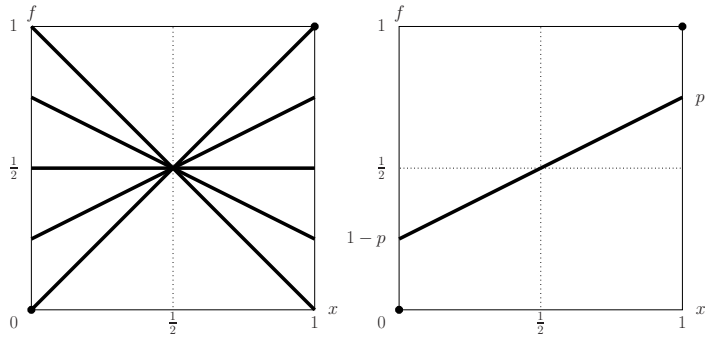

(a) The family of p-HE **(b)** A generic p-HE

Figure 6.5: A particular subclass of stretched harmonic explorer is identified by a linear stretching function, with at most two discontinuities in 0 and 1, and labelled by the slope $2p-1$. Varying the real parameter p from 1 to 0, a family of new explorers (the overruled harmonic explorers) is obtained, as represented in figure (a). A generic p is picked out in figure (b).

function ($f \sim H_n^3$) three random walks are needed, with a computational cost proportional to $3N$. Speaking more generally, for a power law of degree $2q+1$ ($f \sim H_n^{2q+1}$), the number of random walks should be $2q+1$ with cost $(2q+1)N$. Finally, a generic odd function could require up to an infinite number of random walks, resulting in an infinite computational cost.

To have a clearer picture, it is useful to plot $f(x)$ in a square $[0,1] \times [0,1]$, as sketched in figure 6.4.

6.3.2 The overruled harmonic explorers

What just explained about the stretched harmonic explorers highlights that the advantage to use a probability based on the random walk gets lost with a nonlinear stretching function. Moreover, the f-HE class of explorers is too wide to be eventually compared in the continuous limit with the $\mathrm{SLE}_\varkappa$ class of curves; maybe it should be subdivided into subclasses of special symmetries of f. This is an interesting research field and also another challenge for the future. For the time being, we want both to preserve computational advantages and to treat a narrower class of functions. Hence, from now on we will only consider linear functions with some discontinuities at most: this is the simplest generalization of the harmonic explorer.

The simplest choice for the discontinuities is to localize them in 0 and 1, varying the slope of the linear function in $\frac{1}{2}$. Since the slope $2p-1$ is labelled by the real parameter p, the obtained explorers constitute a one-parameter class of stochastic curves in the lattice, just like $\varkappa$ labels a one-parameter class of

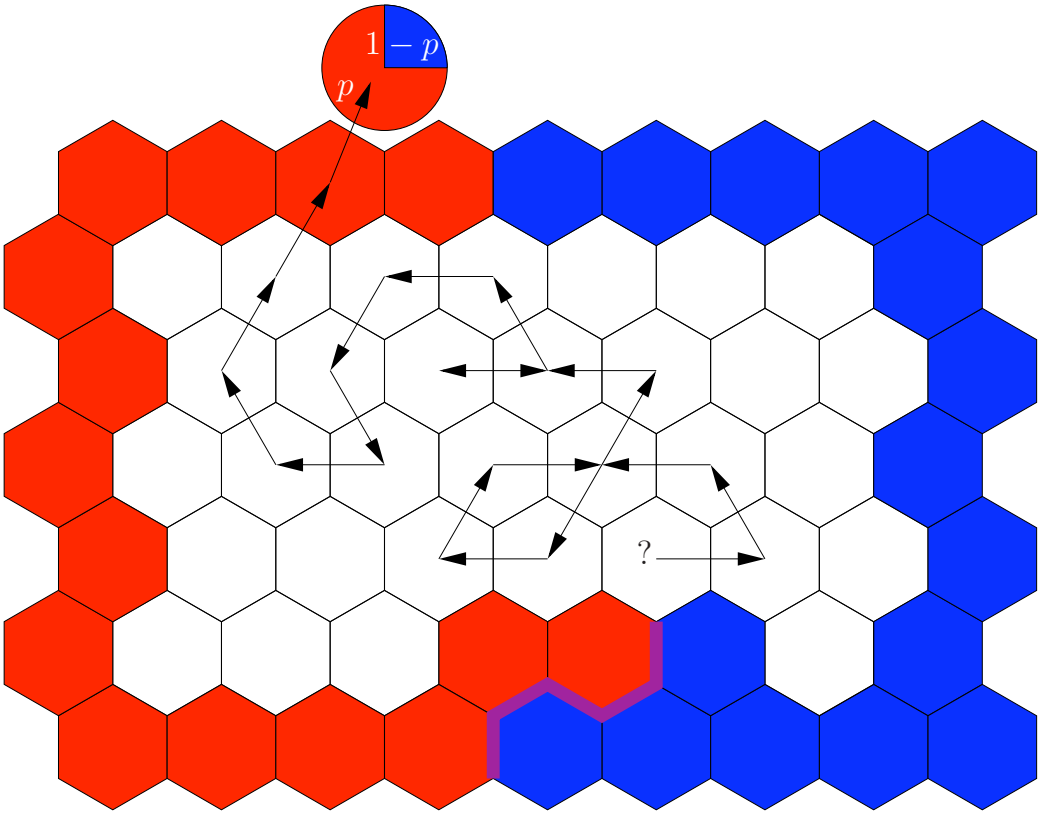

Figure 6.6: An overruled harmonic explorer advancing in a box domain. The explorer (magenta) has to know the colour of the hexagon in front of its tip in order to decide the new direction: it will turn right if that hexagon is coloured red, left if blue. Like the harmonic explorer, a random walker is launched from that hexagon and stopped once an already coloured hexagon is reached. Unlike the harmonic explorer, the colour of the final hexagon is accepted only if confirmed by an unfair-coin toss, i.e. with probability p; on the contrary, the result of the random walk is overruled and overturned with probability $1 - p$.

stochastic curves in the continuum. Figure 6.5a schematizes the kind of functions we are thinking to.

To have a more precise idea of this new class of generalized harmonic explorers, let us take a particular value of p. We want to understand how the explorer goes on in this process operatively. From the hexagon v_{n+1} in front of the tip of the explorer, a random walker on the hexagons is launched and, as soon as it hits the boundary for the first time, it is stopped. Until this point the procedure is the same of the harmonic explorer, so that the probability that the hit boundary hexagon is red is $H_n(v_{n+1})$. Now, instead of colouring the hexagon v_{n+1} red if the hit boundary is red, we colour it red with probability p. In other words, it

happens something similar to a tennis match: the rally between the two players is our random walk; when player A wins the rally, the random walker hits the red boundary; but the point has to be awarded by the umpire, who could overrule it; in our case, the umpire upholds the outcome of the random walk with probability p and overturns it with probability $1-p$ (see figure 6.6). For this reason we call this class of explorers *overruled harmonic explorers* (or, in short, p-HE) and the parameter p the *uphold probability*. At every step, only two stochastic operations are needed: a random walk which selects a boundary colour (cost proportional to N) and an unfair-coin toss which does or does not accept this colour (cost of order 0). Clearly, if v_{n+1} is already on the boundary neither the random walk nor the unfair-coin toss is required, because the colour is already fixed there.

More rigorously, the overruled harmonic explorers are a subclass of the stretched harmonic explorers, with a linear stretching function defined as:

$$f(x) = \begin{cases} 0 & x = 0 \\ 1 - p + (2p-1)x & 0 < x < 1 \\ 1 & x = 1 \end{cases} \tag{6.25}$$

as plotted in figure 6.5b. Notice that outside 0 and 1 the function has value $px + (1-p)(1-x) = 1 - p + (2p-1)x$, since v_{n+1} is coloured red with probability p when the hit boundary is red, but also with probability $1-p$ when the hit boundary is blue. Hence, the probability P_- that the hexagon in front of the tip is coloured red (or has spin -1) is

$$P_-(v_{n+1}) = \begin{cases} 0 & H_n(v_{n+1}) = 0 \\ 1 - p + (2p-1)H_n(v_{n+1}) & 0 < H_n(v_{n+1}) < 1 \\ 1 & H_n(v_{n+1}) = 1 \end{cases} \tag{6.26}$$

6.4 Generalized harmonic explorers and SLE

In section 6.3 a new class of explorers has been introduced generalizing the harmonic exploration process. The basic idea was to build discrete growth processes starting from the same elements which ensure Markovianity and conformal invariance to the continuous limit of the harmonic explorer. However, the case of the unfair percolation, which is the simplest generalization of the critical percolation and is still Markovian but not conformally invariant (as mentioned in 4.1.3), warns us about the risks of generalized explorers: indeed, they might involve elements which break symmetries (e.g., the unfair coin introduces a drift). Here this is not the case, but this is far from a rigorous demonstration! Proving that both properties hold for every generalized harmonic explorer in the continuous

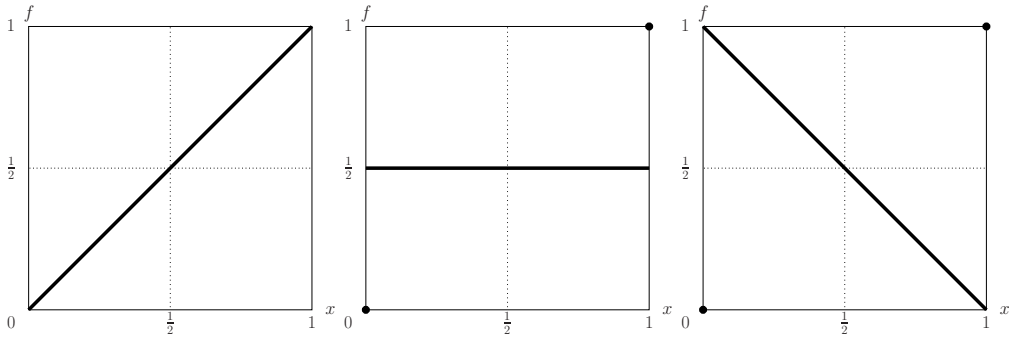

(a) Harmonic explorer (b) Critical percolation (c) Antiharmonic explorer

Figure 6.7: Three extreme cases of overruled harmonic explorers: the 1-HE (a) is nothing but the harmonic explorer itself, whose convergence to SLE_4 in the scaling limit is proved ($p = 1 \to \varkappa = 4$); the $\frac{1}{2}$-HE (b) is a cumbersome way to obtain a simple critical-percolation growth, whose convergence to SLE_6 is also proved ($p = \frac{1}{2} \to \varkappa = 6$); the 0-HE (c) is the opposite case of the harmonic explorer, i.e. the antiharmonic explorer, where the outcome of the random walk is always overturned, resulting in a self-attractive and space-filling tendency ($p = 0 \overset{?}{\to} \varkappa = 8$).

limit is a demanding challenge, a complete demonstration being needed not only for every lattice, but also for every stretching function f (or symmetry class of it).

This section provides a brief review of some special examples of generalized harmonic explorers and their — proved or guessed — relation with SLE.

6.4.1 Special overruled harmonic explorers

Three extreme cases of overruled harmonic explorers recover well-known exploration processes at $p = 1, \frac{1}{2}, 0$ (see figure 6.7 for the sketches of the respective stretching functions).

- $p = 1 \longrightarrow P_-(v_{n+1}) = H_n(v_{n+1})$: harmonic explorer (figure 6.7a)
  This is the trivial version of an overruled harmonic explorer: if $p = 1$, the outcome of the random walk is always accepted, so that the growth process is simply the harmonic explorer itself. More formally, since in this case $f(x) = x$, the probability of colouring the (not yet coloured) hexagon v_{n+1} red is $f\big(H_n(v_{n+1})\big) = H_n(v_{n+1})$, i.e. the harmonic function itself.

- $p = \frac{1}{2} \longrightarrow P_-(v_{n+1}) = \frac{1}{2}$: critical percolation (figure 6.7b)
  This is the other extreme case. By definition, an overruled harmonic explorer is composed by two stages: a random walk and an unfair-coin toss.

When $p = 1$, the second stage is avoided and the probability is simply due to the first one. When $p = \frac{1}{2}$, as in this case, the opposite occurs: indeed, the outcome of the random walk is upheld or overturned with the same probability, meaning that the colour is actually determined only by the final coin toss. If the random walker had not be launched, the probability of colouring v_{n+1} red would be the same, i.e. $\frac{1}{2}$, recovering the critical-percolation process. The same value can also be obtained by putting $p = \frac{1}{2}$ into (6.26): the terms in H_n cancel each other, removing any role of the random walk, resulting in the probability $f\big(H_n(v_{n+1})\big) = \frac{1}{2}$.

- $p = 0 \longrightarrow P_-(v_{n+1}) = 1 - H_n(v_{n+1})$: antiharmonic explorer (figure 6.7c) Again, there is actually no coin toss here and the outcome of the random walk is always overturned: if it hits a red boundary first, blue is assigned to v_{n+1} (and vice versa). Such an explorer is presented in [BB06], where its tendency of being attracted by boundaries, and thus of being space filling, is conjectured and numerically observed. The explorer measure is complementary to that of the harmonic explorer, i.e. $f\big(H_n(v_{n+1})\big) = 1 - H_n(v_{n+1})$.

Since p is a probability, it is clear that its value can only run from 0 to 1. Hence, the special explorers listed above exhaust all the extreme cases, the other ones being limited by these. This is an important point in order to establish a relation between the uphold probability p and the diffusion coefficient $\varkappa$, and will be tackled in section 6.4.3.

6.4.2 Nonlinear stretched harmonic explorers

Every linear-harmonic explorer (i.e. with a measure which is a linear function of the harmonic function) is recovered varying the real parameter p in the range $[0, 1]$. However, also nonlinear-harmonic explorers are involved by our generalization of the harmonic explorer. From an operative point of view, the simplest example is the cubic-harmonic explorer sketched in figure 6.4b, which requires the launch of three random walks at every step. In this case, f is a cubic function of H_n with three free real parameters (with some range constraints in order to obtain a probability function), the fourth being fixed by the odd character of f. Like the linear case, f is a continuous function, except in the extreme fixed points 0 and 1, where discontinuities can be localized. With this spirit, one can build more and more complex stretched harmonic explorers by increasing the (odd) degree of the power function. At degree $2q + 1$ (see figure 6.4c), $2q + 1$ random walks are needed at every step and $2q + 1$ free real parameters are available. It is clear that the class of stretched harmonic explorers becomes larger and larger

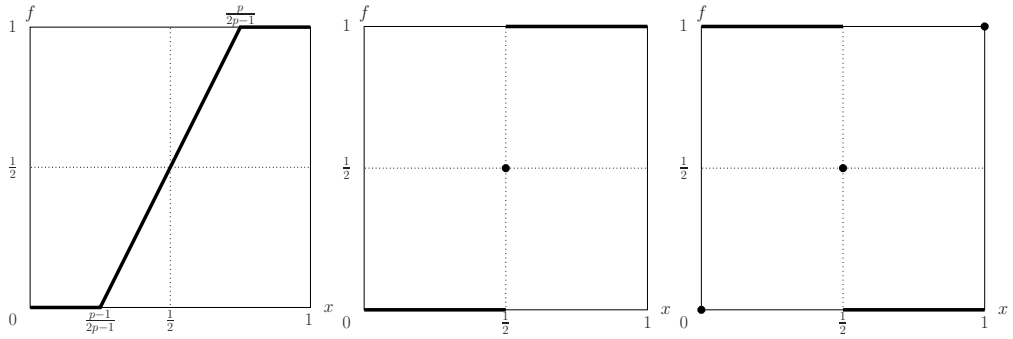

(a) Piecewise linear **(b)** Step up **(c)** Step down

Figure 6.8: Nonlinear stretched harmonic explorers can be defined involving continuous piecewise-linear functions of H_n. A linear range of slope $2p-1$ is present between the two points $\frac{p-1}{2p-1}$ and $\frac{p}{2p-1}$, where the derivative is discontinuous; outside the function is constant with values 0 or 1 (a). Now $p \in (-\infty, 0) \cup (1, +\infty)$. Two extreme cases can be obtained in the infinite limit: if $p \to +\infty$, $f = \vartheta(x - \frac{1}{2})$ (b); if $p \to -\infty$, $f = \vartheta(\frac{1}{2} - x)$ (c).

and a possible parallelism with SLE, which is a one-parameter family, more and more difficult to find.

A different way of thinking about nonlinear-harmonic explorers is taking continuous piecewise-linear stretching functions, as sketched in figure 6.8a. In terms of the same parameter p appearing in the linear case, the oblique line has slope $2p-1$, with either $p < 0$ or $p > 1$ now, depending on whether f is increasing or decreasing, respectively. More formally, if $p < 0$

$$f(x) = \begin{cases} 1 & 0 \leqslant x < \frac{p}{2p-1} \\ 1 - p + (2p-1)x & \frac{p}{2p-1} \leqslant x \leqslant \frac{p-1}{2p-1} \\ 0 & \frac{p-1}{2p-1} < x \leqslant 1 \end{cases} \tag{6.27}$$

and if $p > 1$

$$f(x) = \begin{cases} 0 & 0 \leqslant x < \frac{p-1}{2p-1} \\ 1 - p + (2p-1)x & \frac{p-1}{2p-1} \leqslant x \leqslant \frac{p}{2p-1} \\ 1 & \frac{p}{2p-1} < x \leqslant 1 \end{cases} \tag{6.28}$$

Here p is no more a probability and there is no analogous operative way to build such an explorer. Indeed, this kind of nonlinearity implies the exploitation of an infinite number of random walks (or, alternatively, the exact evaluation of the harmonic function in the whole domain at every step), whereas the cubic nonlinearity only of three of them. In other words, we can generalize overruled

harmonic explorers on two different sides: by increasing the degree of the power function, from an operative point of view; by extrapolating p out of the range $[0, 1]$, from a more formal approach. In the latter case, it is worth to consider two extreme situations (see figure 6.8)

- $p \to +\infty \longrightarrow P_-(v_{n+1}) = \vartheta\big(H_n(v_{n+1}) - \frac{1}{2}\big)$: *step-harmonic explorer* (figure 6.8b)
  Let us guess what kind of trace could be generated by such an explorer. In the upper half-plane, where hexagons on the positive real axis are coloured blue, as soon as the random walker tends to the right (i.e. to the blue boundary) v_{n+1} is coloured blue and the explorer turns left. Thus, as soon as the explorer moves a little closer to the blue boundary, it is forced back to the red one (and vice versa), resulting in a straight-line trace.

- $p \to -\infty \longrightarrow P_-(v_{n+1}) = \vartheta\big(\frac{1}{2} - H_n(v_{n+1})\big)$: *step-antiharmonic explorer* (figure 6.8c)
  This is the opposite case. As soon as the explorer moves a little closer to the blue boundary, the random walker is more likely expected to reach it, v_{n+1} will be coloured red and the explorer will still turn right. Thus, this explorer is extremely attracted by boundaries and continues to coil itself. It is the extreme space-filling path.

6.4.3 Guessed convergence to $\mathrm{SLE}_\varkappa$

Generalizing the harmonic exploration process, in the present chapter we have introduced a large number of new explorers, which we can be collected in some families. The scope was to build a class of discrete stochastic explorers as the counterpart of the $\mathrm{SLE}_\varkappa$ class of continuous stochastic curves. Provided that the generalized harmonic explorers are really Markovian and conformally invariant, some guesses about their convergence to $\mathrm{SLE}_\varkappa$ are proposed in this section. However, it is not our aim to provide complete proofs here, but, if anything, only some clues and sketches.

First, let us tackle the simplest case, i.e. the overruled harmonic explorers. We are looking for a relation between the two real parameters p and $\varkappa$. As a first step this could be assumed linear. Since the harmonic explorer and the critical percolation are proved to converge to SLE_4 and SLE_6, respectively, two constraints are kept fixed: $p = 1 \longleftrightarrow \varkappa = 4$ and $p = \frac{1}{2} \longleftrightarrow \varkappa = 6$. So, if p and $\varkappa$ are bound by a linear relation, the unique possibility (by straightforward computation) is given by the following

Conjecture 6.1 (The relation between p and $\varkappa$ is linear)**.**

$$p = 2 - \frac{\varkappa}{4} \quad \Longleftrightarrow \quad \varkappa = 4(2-p)$$
$$p \in [0,1] \quad \Longleftrightarrow \quad \varkappa \in [4,8]$$

Another way to be led to conjecture 6.1 is offered by the comparison between the evolutions of the harmonic functions in the discrete and in the continuous case, respectively. Rewriting (6.14) for a generic p-HE, i.e. averaging (6.13) according to the measure associated to that specific overruled harmonic explorer, leads to

$$\begin{aligned}\langle H_{n+1}(z)\rangle - H_n(z) &= \mathscr{P}\Big[z \xrightarrow[n]{\text{rw}} v_{n+1}\Big]\big(1-p+(2p-1)H_n(v_{n+1}) - H_n(v_{n+1})\big) \\ &= (1-p)\mathscr{P}\Big[z \xrightarrow[n]{\text{rw}} v_{n+1}\Big]\big(1-2H_n(v_{n+1})\big) \quad (6.29\text{a})\end{aligned}$$

whereas averaging (6.21) for a generic $\mathsf{SLE}_\varkappa$ returns

$$\mathrm{d}\,\langle H_t(z)\rangle = \frac{4-\varkappa}{2}\frac{1}{\pi}\,\mathrm{Im}\,\frac{1}{h_t^2(z)}\,\mathrm{d}t \qquad (6.29\text{b})$$

The comparison between (6.29a) and (6.29b) suggests that the ratio of the prefactors where p and $\varkappa$ are involved is constant, i.e. that p and $\varkappa$ are supposed to show the linear relation stated in conjecture 6.1. Let us notice that under this p-$\varkappa$ conjecture, the antiharmonic explorer is guessed to converge to SLE_8 and, hence, to present a trace with fractal dimension 2, which is compatible with its observed space-filling tendency.

If conjecture 6.1 holds, the whole class of the overruled harmonic explorers is associated to the whole second phase of SLE, i.e. the phase where $\varkappa \in [4,8]$. It is worth noticing that the critical percolation is the central divide of this class: before it ($p < \frac{1}{2}$), the stretching functions are increasing; after it ($p > \frac{1}{2}$), they are decreasing.

Now, a question naturally arise: is it possible to sort out two subclasses of generalized harmonic explorers which are expected to recover the first ($\varkappa \in [0,4)$) and the third ($\varkappa \in (8,\infty)$) phase of SLE in the continuous limit, respectively? By analogy with the linear case — but, of course, with less clues — we can guess that, if all the admissible linear stretching functions describe the whole second phase of SLE in the scaling limit, nonlinear stretching functions would describe the other two phases. Moreover, if below or above $\varkappa = 6$ increasing or decreasing linear functions are needed, respectively, the first phase would be associated to increasing nonlinear functions, whereas the third one to decreasing linear functions.

We can summarize these guessed relations between $\mathsf{SLE}_\varkappa$ and stretching functions f (neglecting discontinuities in the fixed points 0 and 1) as follows:

- ∘ $\varkappa = 0 \longleftrightarrow f = \vartheta\left(x - \frac{1}{2}\right)$
- • $0 < \varkappa < 4 \longleftrightarrow$ increasing nonlinear f
- $*$ $\varkappa = 4 \longleftrightarrow f = x$
- • $4 \leqslant \varkappa < 6 \longleftrightarrow$ increasing linear f
- $*$ $\varkappa = 6 \longleftrightarrow f = \frac{1}{2}$
- • $6 < \varkappa \leqslant 8 \longleftrightarrow$ decreasing linear f
- • $\varkappa = 8 \longleftrightarrow f = 1 - x$
- ∘ $8 < \varkappa < \infty \longleftrightarrow$ decreasing nonlinear f
- ∘ $\varkappa \to \infty \longleftrightarrow f = \vartheta\left(\frac{1}{2} - x\right)$

where proved relations are identified by asterisks, conjecture 6.1 by bullets and simple guesses by circles. Finally, if we only consider linear or continuous piecewise-linear functions, both sharing the oblique line labelled by the slope $2p - 1$ as sketched in figures 6.5b and 6.8a, respectively, we can identify the three phases:

- ∘ $0 < \varkappa < 4 \longleftrightarrow +\infty > p > 1$
- • $4 \leqslant \varkappa \leqslant 8 \overset{\varkappa=4(2-p)}{\longleftrightarrow} 1 \geqslant p \geqslant 0$
- ∘ $8 < \varkappa < \infty \longleftrightarrow 0 > p > -\infty$

6.4.4 Alternative guesses

In section 6.4.3 it is assumed that the uphold probability p is a linear function of the diffusivity $\varkappa$. This is a first-order conjecture, based on both symmetry and simplicity arguments. However, as one tries to extrapolate conjecture 6.1 outside the probability range of p, i.e. involving continuous piecewise-linear stretching functions, he can find that $\varkappa = 0$ is linked to $p = 2$ instead of $p \to +\infty$, as imagined. Hence, we can try to draw an alternative conjecture where the extrapolation also works well both in that and in the opposite limits. More clearly, not only $p = 1 \longleftrightarrow \varkappa = 4$ and $p = \frac{1}{2} \longleftrightarrow \varkappa = 6$ are to be kept fixed, but also the limit cases $p \to +\infty \longleftrightarrow \varkappa = 0$ and $p \to -\infty \longleftrightarrow \varkappa \to \infty$.

The first limit requires that, at least, p is proportional to $1/\varkappa$ as $\varkappa \to 0$, whereas the second one that, at least, p is proportional to $\varkappa$ as $\varkappa \to \infty$. These two minimal constraints are compatible with the following kind of relation

$$p = \frac{a_{-1}}{\varkappa} + a_0 - a_1\varkappa$$

The other two constraints come out of the harmonic explorer and the critical percolation, leaving, though, a free parameter, say a_0. Therefore, if linear and continuous piecewise-linear functions can be joined in a common family labelled by $p \in \mathbb{R}$ and if the explorers they describe are Markovian and conformally invariant in the scaling limit, p should have the form

$$p = \frac{12(2-a_0)}{5\varkappa} + a_0 - \left(\tfrac{1}{2} + a_0\right)\frac{\varkappa}{10} \tag{6.30}$$

Conjecture 6.1 is restored at $a_0 = 2$.

6.5 In the search of martingales

So far no proof of our guesses has been given. Besides, giving a complete demonstration of the convergence of a specific explorer to a specific $\mathrm{SLE}_\varkappa$ is a very hard challenge, involving, e.g., the convergence in every kind of lattice. Here we only want to sketch what is the basic idea a demonstration has to start from. As explained for the harmonic explorer, the crucial key is finding a martingale process shared by both the discrete and the continuous processes. In section 6.2 it is shown that the harmonic function is the searched martingale in that case. The main way to establish an analytic relation between p and $\varkappa$ (in addition to a starting point for a demonstration) is to find a common martingale for every couple p-$\varkappa$.

6.5.1 Functions of the harmonic function

Since the overruled harmonic explorers are based on a linear function of the harmonic function, the first idea which arises is to investigate the properties a function $F(H_n)$ should have in order to be a martingale at a certain p. By definition, martingale property states that

$$\begin{aligned}&\big\langle F\big(H_{n+1}(z)\big)\big\rangle = \\ &= \left\langle F\left(H_n(z) + \mathscr{P}\Big[z \xrightarrow[n]{\mathrm{rw}} v_{n+1}\Big]\big(H_{n+1}(v_{n+1}) - H_n(v_{n+1})\big)\right)\right\rangle = F\big(H_n(z)\big)\end{aligned} \tag{6.31}$$

where (6.13) is used. Since $H_{n+1}(v)$ equals either 1 with probability $P_-(v_{n+1})$ or 0 with probability $P_+(v_{n+1})$, (6.31) can be rewritten as

$$\begin{aligned} F\big(H_n(z)\big) &= F\left(H_n(z) + \mathscr{P}\Big[z \xrightarrow[n]{\text{rw}} v_{n+1}\Big]\big(1 - H_n(v_{n+1})\big)\right) P_-(v_{n+1}) + \\ &\quad + F\left(H_n(z) - \mathscr{P}\Big[z \xrightarrow[n]{\text{rw}} v_{n+1}\Big] H_n(v_{n+1})\right) P_+(v_{n+1}) = \\ &= F\left(H_n(z) + \mathscr{P}\Big[z \xrightarrow[n]{\text{rw}} v_{n+1}\Big]\big(1 - H_n(v_{n+1})\big)\right)\big(1 - p + (2p-1)H_n(v_{n+1})\big) + \\ &\quad + F\left(H_n(z) - \mathscr{P}\Big[z \xrightarrow[n]{\text{rw}} v_{n+1}\Big] H_n(v_{n+1})\right)\big(p - (2p-1)H_n(v_{n+1})\big) \end{aligned} \tag{6.32}$$

The simplest desirable situation occurs when $F(x)$ is a polynomial in the form $\sum_{i=0}^{q} \alpha_i x^i$. In this case one would like to find the relations $\alpha_i(p)$ which satisfy (6.32) up to order q, thus ensuring that the stochastic process $\sum_{i=0}^{q} \alpha_i H_n^i(z)$ is a martingale. The same procedure has to be followed in the continuous case, where one would like to find the analogous relations $\alpha_i(\varkappa)$. Finally, the constraint $\alpha_i(p) = \alpha_i(\varkappa)$ would give the searched relation between p and $\varkappa$. Unfortunately, computation on (6.32) returns $\alpha_i = 0$ for every $i > 0$. This way does not seem to be very profitable.

6.5.2 Building a martingale process

A different approach can be represented by building a martingale process by hand for every p and $\varkappa$. Once such a process is found, clearly it still remains to show that the discrete process converges to the continuous one. Let us start from SLE case this time and consider the following stochastic processes:

$$H_t(z) = \frac{1}{\pi} \arg h_t(z) \tag{6.33a}$$

$$F_t(z) = \frac{1}{\pi} \frac{\varkappa - 4}{4} \arg \tilde{f}_t'\big(h_t(z)\big) \tag{6.33b}$$

$$M_t(z) = H_t(z) + F_t(z) \tag{6.33c}$$

where $\tilde{f}_t$ is the inverse of the uniformizing map (6.16a), H_t the common harmonic function, F_t a new stochastic process depending on $\varkappa$ and M_t a martingale for every $\varkappa$, as we are going to show. From now on, the derivative with respect to the complex variable will be indicated with a prime.

In the Löwner equation for the uniformizing map, the stochastic term does not depend on z. Thus, differentiating (6.17) with respect to z returns

$$\mathrm{d}(h_t') = (\mathrm{d}h_t)' = -\frac{2h_t'}{h_t^2}\,\mathrm{d}t$$

and, hence,

$$\mathrm{d}(\log h'_t) = \frac{1}{h'_t}\,\mathrm{d}h'_t = -\frac{2}{h_t^2}\,\mathrm{d}t \tag{6.34}$$

Since

$$\tilde{f}'_t\big(h_t(z)\big) = \frac{1}{h'_t(z)}$$

the stochastic process M_t can be rewritten as

$$M_t(z) = \frac{1}{\pi}\left(\arg h_t(z) + \frac{\varkappa - 4}{4}\arg \tilde{f}'_t\big(h_t(z)\big)\right) = \\ = \frac{1}{\pi}\left(\arg h_t(z) + \frac{4-\varkappa}{4}\arg h'_t(z)\right) \tag{6.35}$$

Finally, averaging (6.35) and exploiting (6.21) and (6.34) gives

$$\langle \mathrm{d}M_t(z)\rangle = \frac{1}{\pi}\operatorname{Im}\left\langle \mathrm{d}\big(\log h_t(z)\big) + \frac{4-\varkappa}{4}\,\mathrm{d}\big(\log h'_t(z)\big)\right\rangle = \\ = \frac{1}{\pi}\operatorname{Im}\left\langle \frac{(4-\varkappa)\,\mathrm{d}t}{2h_t^2(z)} - \frac{\sqrt{\varkappa}\,\mathrm{d}B_t}{h_t(z)} - \frac{(4-\varkappa)\,\mathrm{d}t}{2h_t^2(z)}\right\rangle = -\operatorname{Im}\left\langle \frac{\sqrt{\varkappa}\,\mathrm{d}B_t}{\pi h_t(z)}\right\rangle = 0 \tag{6.36}$$

Thus, M_t is a martingale for every $\varkappa \geqslant 0$.

Then, we should define a corresponding discrete process M_n for every overruled harmonic explorer, verify whether it is a martingale for every p, show its convergence to M_t, if possible, and, finally, identify the relation between p and $\varkappa$. However, before tackling these issues (which will not be done here), it is important to understand the meaning of the process M_t, or rather of F_t, which at every $\varkappa \neq 4$ balances and cancels out the drift generated by the harmonic function H_t. Indeed, once the geometrical interpretation of F_t is cleared in the continuous case, it will be easier to mimic it in the discrete one.

Let us start from the simple case where γ_t is a polygonal chain and, hence, $\tilde{f}_t = h_t^{-1} = f_{\mathrm{SC}}$ is the Schwarz–Christoffel mapping defined in section 5.1.5. In figure 6.9 the case with l lines is considered (the chain being closed at infinity). There, the $2l+1$ prevertices u_i on the real axis are mapped by h_t into the vertices of the $2l+1$ angles α_i. In particular, the origin $u_{l+1} = 0$ is mapped into the tip of γ_t. Moreover, the point at infinity $u_{2(l+1)} = \infty$, with corresponding angle $\alpha_{2(l+1)} = -\pi$, is mapped into itself; however, since its contribution can be absorbed by the scaling factor C, we will neglect it. Left-hand $(i < l+1)$ and right-hand $(i > l+1)$ points and angles are in correspondence as follows

$$\begin{cases} \alpha_{2l+1} = \pi - \alpha_1 \\ \alpha_{2l+1-i} = 2\pi - \alpha_i \quad 0 < i \leqslant l \\ \alpha_{l+1} = 2\pi \end{cases} \longleftrightarrow \begin{cases} u_{2l+1} = -u_1 \\ u_{2l+1-i} = -u_i \quad 0 < i \leqslant l \\ u_{l+1} = 0 \end{cases} \tag{6.37}$$

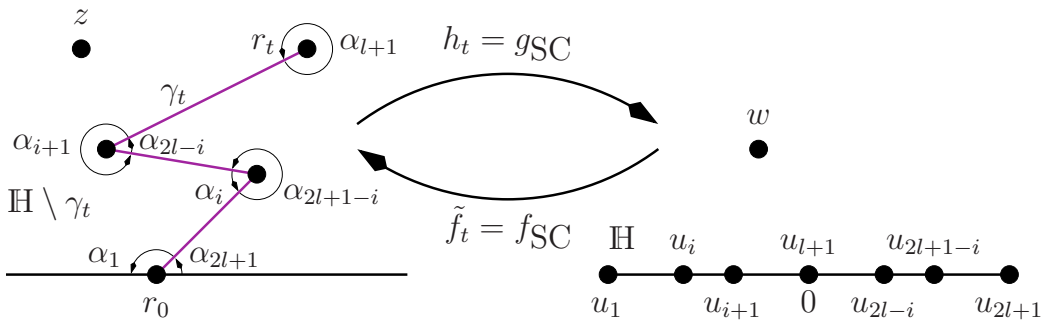

Figure 6.9: The curve γ_t is composed by l straight lines and grows from $r_0 \in \mathbb{R}$ to $r_t \in \mathbb{H}$. We can also regard $\mathbb{R}^- \cup \gamma_t \cup \mathbb{R}^+$ as the boundary of a $2(l+1)$-sided polygon with one point at infinity and its corresponding angle $\alpha_{2(l+1)} = -\pi$. Thus, the uniformizing map is a Schwarz–Christoffel transformation mapping the curve left side into negative reals, the tip r_t into the origin and the right side into positive reals.

From (5.9), a bulk point $z \in \mathbb{H} \setminus \gamma_t$ is the Schwarz–Christoffel image of the point $w \in \mathbb{H}$ according to

$$\tilde{f}_t(w) = C \int^w \prod_{i=1}^{2l+1} (\omega - u_i)^{\alpha_i/\pi - 1} \, \mathrm{d}\omega + c \tag{6.38}$$

$$\implies \tilde{f}_t'(w) = C \prod_{i=1}^{2l+1} (w - u_i)^{\alpha_i/\pi - 1} \tag{6.39}$$

Without loss of generality, the scaling factor C can be fixed to 1 by choosing a particular map. Computing the argument of (6.39) leads to the value of F_t in

$w = h_t(z)$ for this polygonal chain:

$$\begin{aligned}
\frac{1}{\pi}\arg \tilde{f}_t'\big(h_t(z)\big) &= \frac{1}{\pi}\operatorname{Im}\sum_{i=1}^{2l+1}\Big(\frac{\alpha_i}{\pi}-1\Big)\log\big(h_t(z)-u_i\big) = \\
&= \frac{1}{\pi}\sum_{i=1}^{2l+1}\Big(\frac{\alpha_i}{\pi}-1\Big)\arg\big(h_t(z)-u_i\big) = \sum_{i=1}^{2l+1}\frac{\alpha_i-\pi}{\pi}\frac{\arg\big(h_t(z)-u_i\big)}{\pi} = \\
&= \frac{\alpha_1-\pi}{\pi}\frac{\arg\big(h_t(z)-u_1\big)}{\pi} + \sum_{i=2}^{l}\frac{\alpha_i-\pi}{\pi}\frac{\arg\big(h_t(z)-u_i\big)}{\pi} + \\
&\quad + \frac{\alpha_{l+1}-\pi}{\pi}\frac{\arg\big(h_t(z)-u_l\big)}{\pi} + \\
&+ \sum_{i=2}^{l}\frac{2\pi-\alpha_i-\pi}{\pi}\frac{\arg\big(h_t(z)+u_i\big)}{\pi} + \frac{\pi-\alpha_1-\pi}{\pi}\frac{\arg\big(h_t(z)+u_1\big)}{\pi} = \\
&= \frac{\alpha_1-\pi}{\pi}\frac{\arg\big(h_t(z)-u_1\big)}{\pi} - \frac{\alpha_1}{\pi}\frac{\arg\big(h_t(z)+u_1\big)}{\pi} + \frac{\arg\big(h_t(z)\big)}{\pi} + \\
&\quad + \sum_{i=2}^{l}\frac{\alpha_i-\pi}{\pi}\left(\frac{\arg\big(h_t(z)-u_i\big)}{\pi} - \frac{\arg\big(h_t(z)+u_i\big)}{\pi}\right) \qquad (6.40)
\end{aligned}$$

where (6.37) has been exploited.

Since F_t is also harmonic, it is sufficient to determine its value on the boundary in order to obtain the unique harmonic function in $\mathbb{H}\setminus\gamma_t$ with that boundary conditions:

$$f(z)\in\mathbb{R} \quad\Longrightarrow\quad \frac{\arg\big(h_t(z)-u_i\big)}{\pi} = \begin{cases} 0 & h_t(z) > u_i \\ 1 & h_t(z) < u_i \end{cases} \qquad (6.41)$$

If z is on the right branch of the real axis, every point u_i lies on the left of $h_t(z)$ and all the arguments in (6.40) are zero. The same result occurs if z is on the left branch of $\mathbb{R}$, when every u_i lies on the right of $h_t(z)$ and all the arguments in (6.40) are one; now F_t is the sum of the angles encountered along the boundary coming from $+\infty$ and vanishes because every angle is balanced by its conjugate:

$$\frac{1}{\pi}\arg \tilde{f}_t'\big(h_t(z)\big) = \frac{\alpha_1-\pi}{\pi} - \frac{\alpha_1}{\pi} + 1 + \sum_{i=2}^{l}\frac{\alpha_i-\pi}{\pi}(1-1) = 0$$

It remains to estimate F_t both on the right and on the left side of the polygonal chain, i.e. when $u_i < h_t(z) < u_{i+1}$ for a certain $1 < i < 2l$. In this case (6.41)

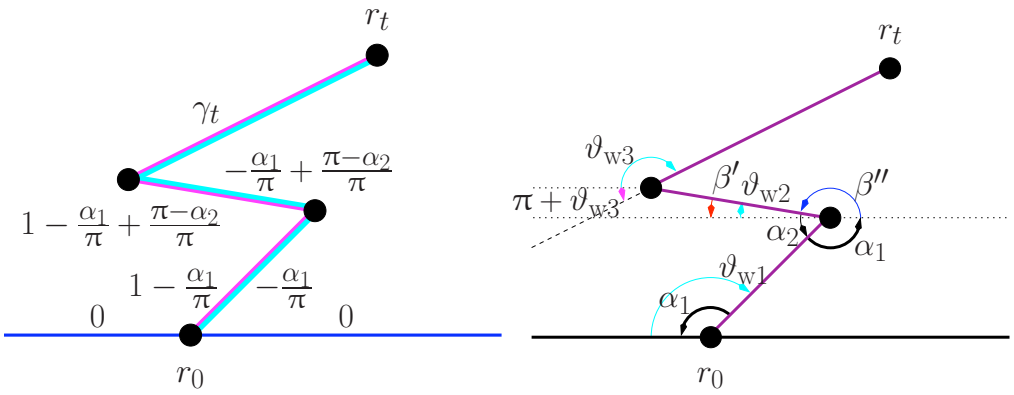

(a) Boundary conditions of F_t **(b)** Angular relations

Figure 6.10: In figure (a) the boundary conditions of the stochastic process F_t are shown as functions of the angles between two successive lines (on blue boundaries $F_t = 0$; cyan and magenta boundaries have right-side and left-side conditions, respectively). However, they can be simplified by simple angular relations, as figure (b) sketches. Let us call ϑ_{wi} the oriented angle between $\mathbb{R}^-$ and the i-th line, β' the angle between the second line and the horizontal line and β'' its supplementary. It is easy to verify that $-\alpha_i = \vartheta_{w1}$ and $\pi - \alpha_1 - \alpha_2 = 2\pi - \pi - \alpha_1 - \alpha_2 = \beta'' - \pi = -(\pi - \beta'') = -\beta' = \vartheta_{w2}$, so showing that F_t has boundary conditions given by the winding angle ϑ_{wi}.

returns the sum of the turning angles encountered from $+\infty$ to z_+ or z_- ($+$ and $-$ referring to the sign of $h_t(z_+)$ and $h_t(z_-)$) along the polygonal chain, as sketched in 6.10. These cumbersome boundary conditions can be expressed in a simpler way as a function of the current winding angle ϑ_{wi} of z_+ or z_-, counter-clockwise oriented with respect to $\mathbb{R}^-$ (figure 6.10 provides a complete explanation). Now it is easy to believe that the same result holds when the polygonal chain is substituted by a smooth curve. One can be persuaded by substituting the sum in (6.40) with an integral directly. Here, $\vartheta_w(s_+)$ is a function of the parametrisation of γ_t and gives the oriented angle between $\mathbb{R}^-$ and the tangent to γ_t in r_s coming from r_0 (all windings included), whereas for $\vartheta_w(s_-) = \pi + \vartheta_w(s_+)$ the tangent is oriented coming from r_t (see figure 6.11). Thus, the stochastic process $F_t(z)$ has boundary conditions

$$F_t(z) = \begin{cases} 0 & z \in \mathbb{R} \\ \dfrac{\varkappa - 4}{4}\dfrac{\vartheta_w(s_\pm)}{\pi} & z = r_{s_\pm} \in \gamma_t \end{cases} \tag{6.42}$$

The unanswered question — until now — is whether such a F_t has a discrete counterpart and, if yes, whether the discrete stochastic process $M_n = H_n + F_n$ is a martingale and converges to M_t.

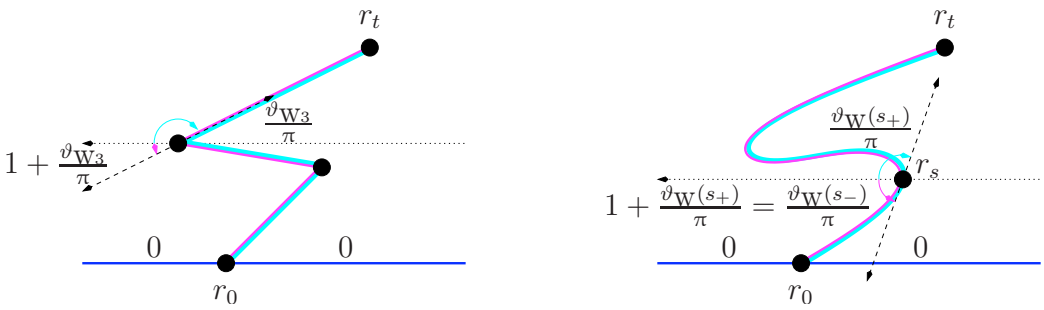

Figure 6.11: The boundary conditions of F_t are the same for both a polygonal chain and a standard SLE curve, being proportional to the winding angle. Conditions on the two sides of the curve differ by 1, which corresponds to the sudden change of direction of π encountered in r_t.

Chapter 7

Numerical analysis

A new class of discrete stochastic explorers, the overruled harmonic explorers, has been defined in chapter 6. Since they are built on the harmonic measure, by construction they inherit promising properties in order to ensure Markovianity and conformal invariance in the scaling limit. However, no rigorous proof of this limit is still available until now. Moreover, the relation between the two parameters p and $\varkappa$ has not been determined by our efforts into searching a general martingale both for the discrete family of p-HE and for the continuous family of SLE$_\varkappa$. On the other hand, the assumption of a linear relation leads to conjecture 6.1, which states that $p = 2 - \varkappa/4$. Now, it is convenient to leave the analytic approach and switch to a numerical analysis of the overruled harmonic explorers. Here, the main aim is to verify whether these explorers are conformally invariant in the continuous limit or not, the Markovianity being guaranteed from the beginning. If the conformal invariance holds too, each p-HE converges to a SLE$_\varkappa$. Hence, the second aim is to find which $\varkappa$ corresponds to each considered p and to compare the results with the given conjecture.

We considered five values of p, viz. $p = 0$, $\frac{1}{4}$, $\frac{1}{2}$, $\frac{3}{4}$ and 1 ($\frac{1}{2}$ and 1 only for control purposes) in two kinds of domain, i.e. the upper half-plane and the rectangle of aspect ratio R. In section 7.1 we give some details on the implementation in both domains. Section 7.2 offers some samples of overruled harmonic explorers and a brief discussion about their features. Then, a deeper analysis of their properties follows. In section 7.3 the crossing probabilities in four different rectangular domains show the conformal invariance of p-HE paths. Afterwards, we deal with the fractal dimensions of some sets of points in the upper half-plane in order to determine the values of $\varkappa(p)$. In particular, we consider the fractal dimensions of exploration trace (section 7.4), of trace points on the real axis (section 7.5) and of trace double points (section 7.6).

We can announce in advance here that numerical results show an evident conformal invariance of the overruled harmonic explorers, whereas no conclusive

statement can be given about the relation between p and $\varkappa$.

7.1 Lattices and domains

An exploration process is defined once a measure on its path is assigned. In the case of the overruled harmonic explorer the measure is a linear function of the harmonic measure, more precisely $1-p+(2p-1)H_n$ (n being the number of steps). Although this definition holds independently of the kind of lattice, the operative definition of section 6.3.2 specially makes sense in the honeycomb lattice, where explorer implementation results the simplest. Therefore, we adopted such a lattice in our numerical analysis.

We can imagine the lattice as embedded into the complex plane and, thus, identify the face z with the position of its centre in $\mathbb{C}$. At the same time, hexagon centres are also the vertices of the dual triangular lattice. Exploration paths lie on the triangular lattice, whereas the random walks required to determine new explorer directions run in the hexagonal one. The lattice spacing (i.e. the distance between the centres of two adjacent faces) corresponds to side length of the faces in the dual lattice. If we call l_3 and $l_6 = l_3/\sqrt{3}$ the lengths of triangle and hexagon sides, i.e. the lattice spacing in the hexagonal and in the triangular lattice, respectively, each face has centre in

$$\begin{aligned} z_{\mathrm{ex}} &= x_{\mathrm{ex}} + \mathrm{i}y_{\mathrm{ex}} = \tfrac{1}{2}l_3 i_{\mathrm{ex}} + \mathrm{i}\tfrac{1}{2}l_6\left(3j_{\mathrm{ex}} + \tfrac{1}{2} - \tfrac{1}{2}(-1)^{i_{\mathrm{ex}}+j_{\mathrm{ex}}}\right) && i_{\mathrm{ex}}, j_{\mathrm{ex}} \in \mathbb{Z} \\ z_{\mathrm{rw}} &= x_{\mathrm{rw}} + \mathrm{i}y_{\mathrm{rw}} = \tfrac{1}{2}l_3\left(2i_{\mathrm{rw}} + \tfrac{1}{2} + \tfrac{1}{2}(-1)^{j_{\mathrm{rw}}}\right) + \mathrm{i}\tfrac{1}{2}l_6\left(3j_{\mathrm{rw}} - 1\right) && i_{\mathrm{rw}}, j_{\mathrm{rw}} \in \mathbb{Z} \end{aligned}$$

where subscripts 'ex' and 'rw' refer to the position of the explorer on the triangular lattice and that of the random walker on the hexagonal one, respectively. As clarified in figure 7.1, the lattice is centred with respect to the triangle $(i_{\mathrm{ex}}, j_{\mathrm{ex}}) = (0,0)$, whose centre is the origin of the complex plane. The range spanned by the integer coordinates depends on the selected domain.

Since we want to compare exploration paths with chordal-SLE traces, the exploration final point r_* has to be a boundary point. Thus, two choices are available in order to select the discrete domain: it can be either compact with finite r_*, such as a rectangle, or non-compact with $r_* = \infty$, such as the upper half-plane. In the following both cases are considered, allowing us to test whether properties known to be conformally invariant in the scaling limit transform in different domains. If they are preserved, one has a first clue of p-HE conformal invariance. Moreover, while in the continuous case no substantial difference exists between the two domains, which are in correspondence with a simple Schwarz–Christoffel mapping, from a numerical point of view the situation is not the same. Indeed, on the one hand the exploration process in the upper half-plane

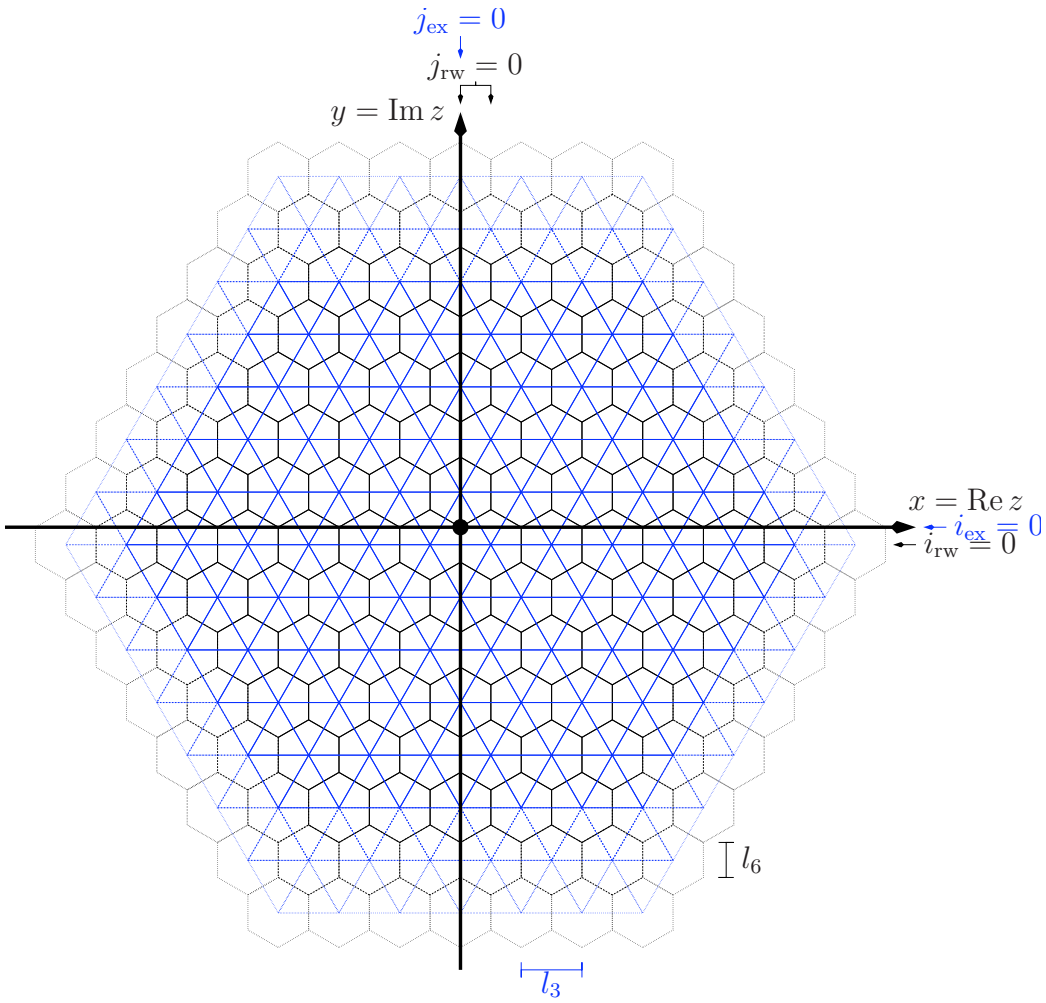

Figure 7.1: Regular hexagons of side l_6 (black) and equilateral triangles of side l_3 (blue) form the honeycomb lattice and its dual, respectively. There, hexagon vertices are triangle centres and vice versa. Integer coordinates i_{rw} and j_{rw} label hexagon rows and columns, respectively, whereas i_{ex} and j_{ex} label triangle rows and columns. The meaning of subscripts 'ex' and 'rw' is related to the processes which take place in the two lattices: the explorer follows hexagon edges and, hence, lies on triangle centres; moreover, at each step it needs a random walk on hexagons in order to determine its new direction. The origin of the complex plane is the centre of triangle $(0, 0)$ and leaves hexagon $(0, 0)$ below on its right.

cannot be completed in a finite number of steps. Therefore, crossing probabilities can be computed only in the rectangle. On the other hand determining fractal dimensions requires an infinite domain like the upper half-plane. Let us deal with some computational details about the code implementation in both domains.

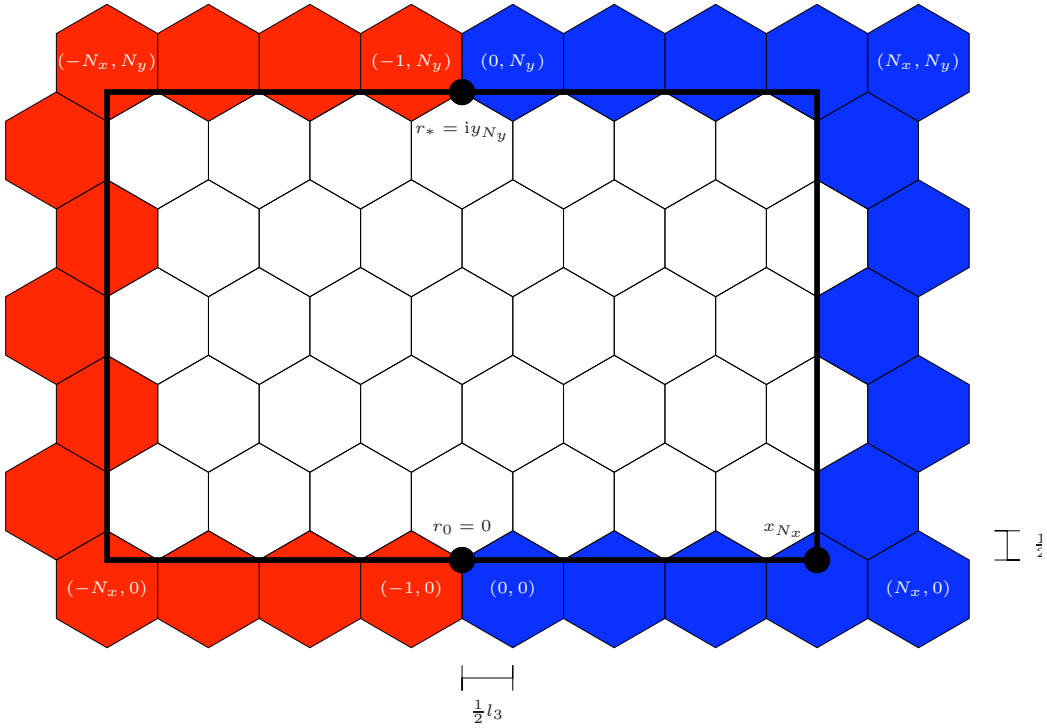

Figure 7.2: Lattice rectangular domain $\mathcal{R}^{\#}_{\mathrm{rw}}$ is bounded by hexagon columns $i_{\mathrm{rw}} = -N_x$ and N_x and by hexagon rows $j_{\mathrm{rw}} = 0$ and N_y. Boundary conditions for the harmonic function are fixed by colouring boundary hexagons either red $(H_0 = 1)$ or blue $(H_0 = 0)$ according to whether the integer abscissa is negative or not. If the exploration process starts from the origin, i.e. from triangle $(0, 0)$, it can exit the domain only from triangle $(0, N_y - 1)$, whose centre is $r_* = \mathrm{i}y_{N_y} = \mathrm{i}\frac{1}{2}l_6(3N_y - 2)$. The thick black line delimits the complex rectangular region $\mathcal{R}_{\mathrm{ev}} = \mathcal{R}_{2x_{N_x} \times y_{N_y}}$ where the corresponding evolution in the continuous limit takes place. Although left-boundary points at $i_{\mathrm{ex}} = 2N_x$ are not enclosed in $\mathcal{R}_{\mathrm{ev}}$, the statistical properties of the path are not affected. Indeed, if the explorer reaches position $(2N_x, j_{\mathrm{ex}})$, necessarily it will also reach $(2N_x, j_{\mathrm{ex}} + 1)$ and $(2N_x - 1, j_{\mathrm{ex}} + 1)$, without any randomness. However, in section 7.3 it will be cleared that path statistics is not sensitive to boundary setting.

7.1.1 Rectangular domains

The simplest domain one can use is a rectangle of aspect ratio R. Indeed, in this case the exploration process is always well defined, whereas some problems arise in non-compact domains, as we will see in section 7.1.2. Here, once the number of hexagons is set and the boundary conditions are assigned, an overruled harmonic explorer can span the domain according to the operative rules given in section 6.3.2.

As shown in figure 7.2, the row at $j_{\rm rw} = 0$ is chosen as lower boundary in the hexagonal lattice (and the corresponding row at $j_{\rm ex} = 0$ in the triangular lattice). If we label the right-boundary column and the upper-boundary row of the hexagonal lattice with $i_{\rm rw} = N_x$ and $j_{\rm rw} = N_y$, respectively, the integer coordinates run in the ranges $-N_x \leqslant i_{\rm rw} \leqslant N_x$ and $0 \leqslant j_{\rm rw} \leqslant N_y$. Thus the lattice consists of $N_6 = (2N_x + 1)(N_y + 1) \sim 2N_xN_y$ hexagons. Notice that in this rectangle of hexagons, $\mathcal{R}^{\#}_{\rm rw}$, there is an offset of $\frac{1}{2}l_3$ between odd and even rows. For this reason the domain is almost symmetric with respect to the imaginary axis.

With regard to the boundary conditions, we colour all boundary hexagons red ($H_0 = 1$) if $i_{\rm rw}$ is negative, otherwise blue ($H_0 = 0$). Thus, the explorer starts from $(i_{\rm ex}, j_{\rm ex}) = (0, 0)$ (i.e. from the point $r_0 = 0$) and ends its path in $(i_{\rm ex}, j_{\rm ex}) = (0, N_y - 1)$ (i.e. in the point $r_* = {\rm i}y_{N_y} = {\rm i}\frac{1}{2}l_6(3N_y - 2)$, if N_y is even, as in our cases). The triangular-lattice region $\mathcal{R}^{\#}_{\rm ex}$ available to the explorer is $-2N_x + 1 \leqslant i_{\rm ex} \leqslant 2N_x$ and $0 \leqslant j_{\rm ex} \leqslant N_y - 1$. Therefore, triangular lattice consists of $N_3 = 4N_xN_y \sim 2N_6$ faces.

Because of the short offset between rows, this domain approximates a classic rectangle only if N_x and N_y are very large. However, they must be very large in order to minimize finite-size effects in the comparison with SLE$_\varkappa$. For this comparison a Schwarz–Christoffel mapping of the domain is required. The rectangle $\mathcal{R}_{\rm ev}$ to be mapped is the smallest symmetric with respect to the imaginary axis and enclosing all the points available to the explorer (and significant for the statistics, as better specified in figure 7.2). Let us summarize domain extents:

$$\mathcal{R}^{\#}_{\rm rw} = \{i_{\rm rw}, j_{\rm rw} \in \mathbb{Z} \mid -N_x \leqslant i_{\rm rw} \leqslant N_x \ , \ 0 \leqslant j_{\rm rw} \leqslant N_y\}$$
$$\mathcal{R}^{\#}_{\rm ex} = \{i_{\rm ex}, j_{\rm ex} \in \mathbb{Z} \mid -2N_x + 1 \leqslant i_{\rm ex} \leqslant 2N_x \ , \ 0 \leqslant j_{\rm ex} \leqslant N_y - 1\}$$
$$\mathcal{R}_{\rm ev} = \{x, y \in \mathbb{R} \mid -l_3(N_x - \tfrac{1}{2}) \leqslant x \leqslant l_3(N_x - \tfrac{1}{2}) \ , \ 0 \leqslant y \leqslant l_6(\tfrac{3}{2}N_y - 1)\}$$

Thus, the aspect ratio of $\mathcal{R}_{\rm ev}$ is

$$R = \frac{2x_{N_x}}{y_{N_y}} = \frac{4}{\sqrt{3}}\frac{N_x - \frac{1}{2}}{N_y - \frac{2}{3}} \simeq \frac{4}{\sqrt{3}}\frac{N_x}{N_y}$$

At $p = 0$, $\frac{1}{4}$ and $\frac{3}{4}$ we investigated four different values of R corresponding to $(N_x, N_y) = (250, 1000)$, $(250, 500)$, $(500, 500)$ and $(750, 500)$, i.e. to $R \simeq 0.58$, 1.2, 2.3 and 3.5, respectively. For each of these cases we performed $N_{\rm r} = 10^4$ realizations. Table 7.1a offers a list of significant simulation parameters.

7.1.2 Upper half-plane

Defining the lattice version of the upper half-plane is simple. Indeed, it suffices to give the integer coordinates of the lower boundary, which, not surprisingly, are

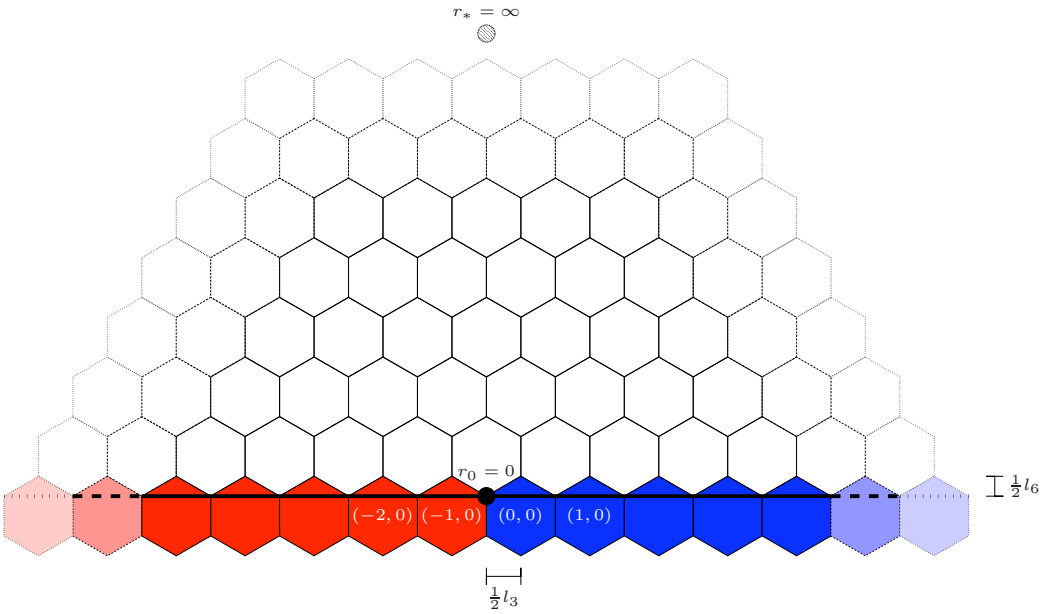

Figure 7.3: The lattice counterpart $\mathbb{H}^{\#}$ of the complex upper half-plane $\mathbb{H}$ has hexagon row $i_{\mathrm{rw}} = 0$ as lower boundary. Boundary conditions for the harmonic function are fixed by colouring boundary hexagons either red ($H_0 = 1$) or blue ($H_0 = 0$) according to whether the integer abscissa is negative or not. The exploration process starts from the origin, i.e. from triangle $(0, 0)$, and heads for the point at infinite.

set to $j_{\mathrm{rw}} = 0$ and $j_{\mathrm{ex}} = 0$ (see figure 7.3). Again, all boundary hexagons with negative i_{rw} are coloured red, remaining boundary hexagons blue. Here, the exploration process still starts from $r_0 = 0$, but the destination point r_* is placed at infinity.

On the other hand, because of the infinite size of the domain, some problems arise with the operative definition of the overruled harmonic explorer. Indeed, at every step a random walker on hexagons has to be launched, but its expected exit time is not finite. In other words, although short random walks are the most probable events, especially when the path is very winding (i.e. when its fractal dimension is closer to 2), the probability of infinite random walks is not zero, especially when the path proceeds straight ahead (i.e. when its fractal dimension is closer to 1). An algorithm which prevents us from waiting for the outcome indefinitely is needed. Clearly, it is an approximating algorithm. Moreover, computational costs force us to limit the exploration process in a small region of the upper half-plane, whereas random walks can span a larger region, because they have not to be stored.

These two problems can be overcome by considering four regions in the do-

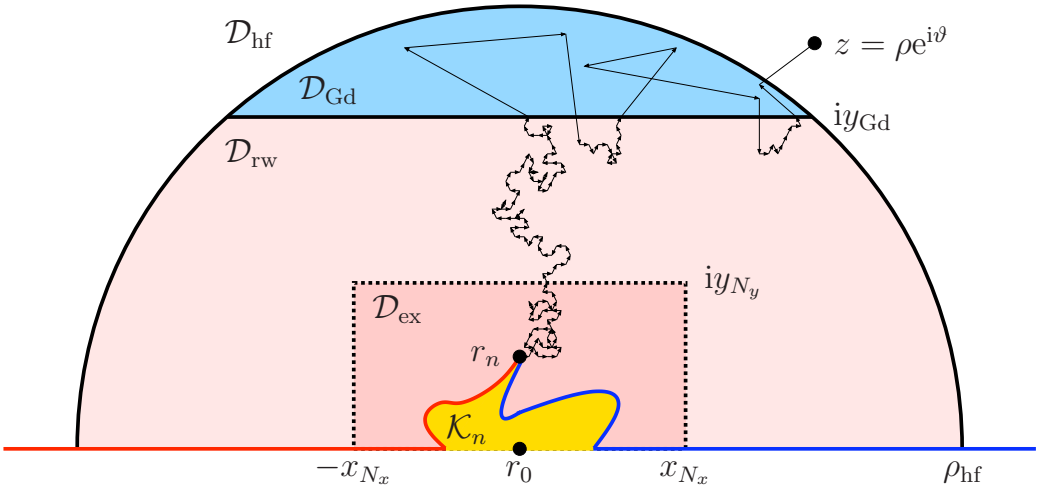

Figure 7.4: Starting from the point r_0, the explorer reaches the point r_n after n steps. Its path encloses a hexagon hull $\mathcal{K}_n^{\#}$ (yellow), whose external boundary is coloured red on the left of r_n and blue on the right (in this large-scale sketch the lattice cannot be drawn and lattice domains are represented via their complex counterpart). The new direction of the explorer is selected by a random walk (black arrows) starting from the hexagon v_{n+1} in front of r_n. Since $\mathbb{H}^{\#}$ is non-compact, this random walk can take an infinite time. To avoid it, the domain is split into three regions: in $\mathcal{D}_{\rm rw}^{\#}$ (pink) a usual random walk on hexagons takes place; in $\mathcal{D}_{\rm Gd}$ (light blue) the random walker is sped up by converting it in a Gaussian diffusion with large standard deviation; in $\mathcal{D}_{\rm hf}$ (white) the random walker is stopped and v_{n+1} is coloured red with probability $H_n(\rho e^{i\vartheta}) = \vartheta/\pi$. The exploration process is followed as far as it stays inside $\mathcal{D}_{\rm ex}^{\#} \subset \mathcal{D}_{\rm rw}^{\#}$.

main: let us call them $\mathcal{D}_{\rm ex}$, $\mathcal{D}_{\rm rw}$, $\mathcal{D}_{\rm Gd}$ and $\mathcal{D}_{\rm hf}$. They are defined as follows:

$$\begin{aligned}
\mathcal{D}_{\rm ex} &= \{z \in \mathbb{H} \mid -x_{N_x} \leqslant \mathrm{Re}\, z \leqslant +x_{N_x}\ ,\ \mathrm{Im}\, z \leqslant y_{N_y}\} \\
\mathcal{D}_{\rm rw} &= \{z \in \mathbb{H} \mid \mathrm{Im}\, z < y_{\rm Gd}\ ,\ |z| < \rho_{\rm hf}\} \\
\mathcal{D}_{\rm Gd} &= \{z \in \mathbb{H} \mid \mathrm{Im}\, z \geqslant y_{\rm Gd}\ ,\ |z| < \rho_{\rm hf}\} \\
\mathcal{D}_{\rm hf} &= \{z \in \mathbb{H} \mid |z| \geqslant \rho_{\rm hf}\}
\end{aligned}$$

$\mathcal{D}_{\rm ex}$ is the rectangular region available to the explorer: since only a finite number of steps can be performed, it is always possible to determine a box which will contain it wholly: the explorer is stopped either after $N_{\rm st}$ steps or when it crosses rectangle sides, which are delimited by hexagon row N_y and by hexagon columns $-N_x$ and N_x. In this way, the exploration path to be stored is finite and under control. Besides, the random walk needed at each step can often escape from $\mathcal{D}_{\rm ex}$, without any computational cost as far as it does not escape too much upwards. Hence, we limit it into $\mathcal{D}_{\rm rw}$. If a random walk crosses the upper

boundary of $\mathcal{D}_{\rm rw}$ placed at $\mathrm{i}y_{\rm Gd}$, it is converted into a faster Gaussian diffusive process on the complex plane: from point $z \in \mathcal{D}_{\rm Gd}$ a step toward $z' = z + \sigma(z)\eta_z$ is taken with standard deviation σ proportional to the distance between z and explorer hull ($\eta_z = \eta_z + \mathrm{i}\eta_y$ being a normal white noise). If this process comes below $\mathrm{i}y_{\rm Gd}$ again, the random walk restarts on hexagons. If either the discrete or the Gaussian diffusive processes cross the radius $\rho_{\rm hf}$ reaching $z = \rho \mathrm{e}^{\mathrm{i}\vartheta}$, they are stopped and the hexagon in front of the tip is coloured red according to the harmonic function in the upper half-plane, i.e with probability ϑ/π. Figure 7.4 gives a clearer idea of these four regions.

In short, the actual lattice is $\mathcal{D}^{\#}_{\rm rw}$. The two complex domains outside have no lattice counterpart. Problems in the diffusive process do not arise when the random walk moves too much away horizontally, but upwards. $\mathcal{D}_{\rm Gd}$ serves as a buffer, in order to speed up this (zero-mean) process and wait for a shorter time before it either comes back to $\mathcal{D}^{\#}_{\rm rw}$ or escapes far away to $\mathcal{D}_{\rm hf}$. The latter domain serves as a cut-off region.

Some points have to be discussed more deeply about the approximations involved. First, the Gaussian diffusion is subjected to two constraints: its step must be both large enough to approximate a series of random-walk steps and short enough not to approach domain boundary. Namely, it must be much larger than lattice spacing, but with zero probability of approaching a point $z_{\rm b}$ of either the real axis or path hull. Since this probability is of order 10^{-42} within 10σ, we can safely require that

$$l_3 \ll 100 l_3 \lesssim \sigma(z) \lesssim \tfrac{1}{10}\left(y - y_{N_y}\right) \leqslant \tfrac{1}{10}\min|z - z_{\rm b}| \qquad z = x + \mathrm{i}y \in \mathcal{D}_{\rm Gd}$$

In terms of hexagons this amounts to take steps of the order of 100 faces at least and, therefore, to place $y_{\rm Gd} = \min y$ about 1000 hexagons above row N_y at least (i.e. at row $j_{\rm Gd} = 1000 + N_y$).

We still have to estimate a reasonable radius $\rho_{\rm hf}$ for the harmonic cut-off. If $z = \rho \mathrm{e}^{\mathrm{i}\vartheta}$ is a point far from the origin, the uniformizing map can be expanded according to (5.2). Thus, the probability that a random walk starting from z hits the red boundary first can be approximated by that in the continuous limit and, hence, regarded as a multipole expansion with respect to the capacity C_n of the hull $\mathcal{K}_n$ at step n. The monopole term, i.e. the harmonic measure in $\mathbb{H}$, has to be much larger than any other beyond the cut-off radius, so that there the hull is viewed as squashed to the origin. Calling ρ_n the radius enclosing $\mathcal{K}_n$, first-order capacity is ρ_n^2 and multipole expansion up to the first order gives

$$H_n(z) = \frac{1}{\pi}\arg h_t(z) = \frac{1}{\pi}\arg\left(z + \frac{\rho_n^2}{z} + O(z^{-2})\right) = \\ = \frac{1}{\pi}\arg\left(\mathrm{e}^{\mathrm{i}\vartheta} + \frac{\rho_n^2}{\rho^2}\mathrm{e}^{-\mathrm{i}\vartheta} + O(\rho^{-3})\right) \approx \frac{\vartheta}{\pi} \qquad \rho \gg \rho_n$$

R	N_x	N_y	0	$\frac{1}{4}$	$\frac{1}{2}$	$\frac{3}{4}$	1	p
0.58	250	1000	10000	10000	10000	10000	-	
1.15	250	500	10000	10000	-	10000	-	
2.31	250	250	10000	-	-	-	-	N_{r}
2.31	500	500	10000	10000	10000	10000	-	
3.47	750	500	10000	10000	-	10000	-	

(a) $\mathcal{R}^{\#}_{\mathrm{ex}}$

p	0	$\frac{1}{4}$	$\frac{1}{2}$	$\frac{3}{4}$	1
N_x	4000	3700	3000	2000	1600
N_y	1300	1700	2000	2000	2000
N_{st}	275000	135000	135000	66000	33000
N_{r}	20000	27404	10000	20000	10000
j_{Gd}	$1000+N_y$	$1000+N_y$	$1000+N_y$	$1000+N_y$	$1000+N_y$
ρ_{hf}	$1000y_{N_y}$	$1000y_{N_y}$	$1000y_{N_y}$	$1000y_{N_y}$	$1000y_{N_y}$

(b) $\mathbb{H}^{\#}$

Table 7.1: Significant parameters of the performed realizations are listed in table (a) for box domains and in table (b) for the upper half-plane. Notice the N_x and N_y have different meanings in the two cases: they set the boundaries of $\mathcal{R}^{\#}_{\mathrm{ex}}$ and $\mathcal{D}^{\#}_{\mathrm{ex}}$, but the latter is only the small portion of $\mathbb{H}^{\#}$ where the explorer takes its N_{st} steps.

Therefore, the constraint is simply $\rho_{\mathrm{hf}} \gg \rho_n$. In our numerical analysis we considered $\rho_{\mathrm{hf}} = 1000y_{N_y}$. On average, the evaluation via harmonic function occurred less than 10^{-6} times per step.

We performed $N_{\mathrm{r}} = 2\ 10^4$ realizations at $p = 0$, $\frac{1}{4}$ and $\frac{3}{4}$ and 10^4 realizations at $p = \frac{1}{2}$ and 1. N_x, N_y and N_{st} depend on the value of p as a compromise between computational costs and explorer behaviours. Indeed, as we will see in section 7.2, p-HE explore the half-plane with very different tendencies. In table 7.1b a list of significant simulation parameters can be found.

7.2 Samples of exploration paths

Before dealing with a deeper analysis of some numerical results, it can be useful to show several snapshots of exploration processes in order to have a first idea on the behaviour of the overruled harmonic explorer at different p and in different domains (main realization parameters are summarized in table 7.1).

7.2.1 Upper half-plane

Let us start with the upper half-plane, where the exploration process is free to advance indefinitely (of course, until we decide to stop it, after N_{st}). Since this is the canonic domain for chordal SLE, after a very high number of steps,

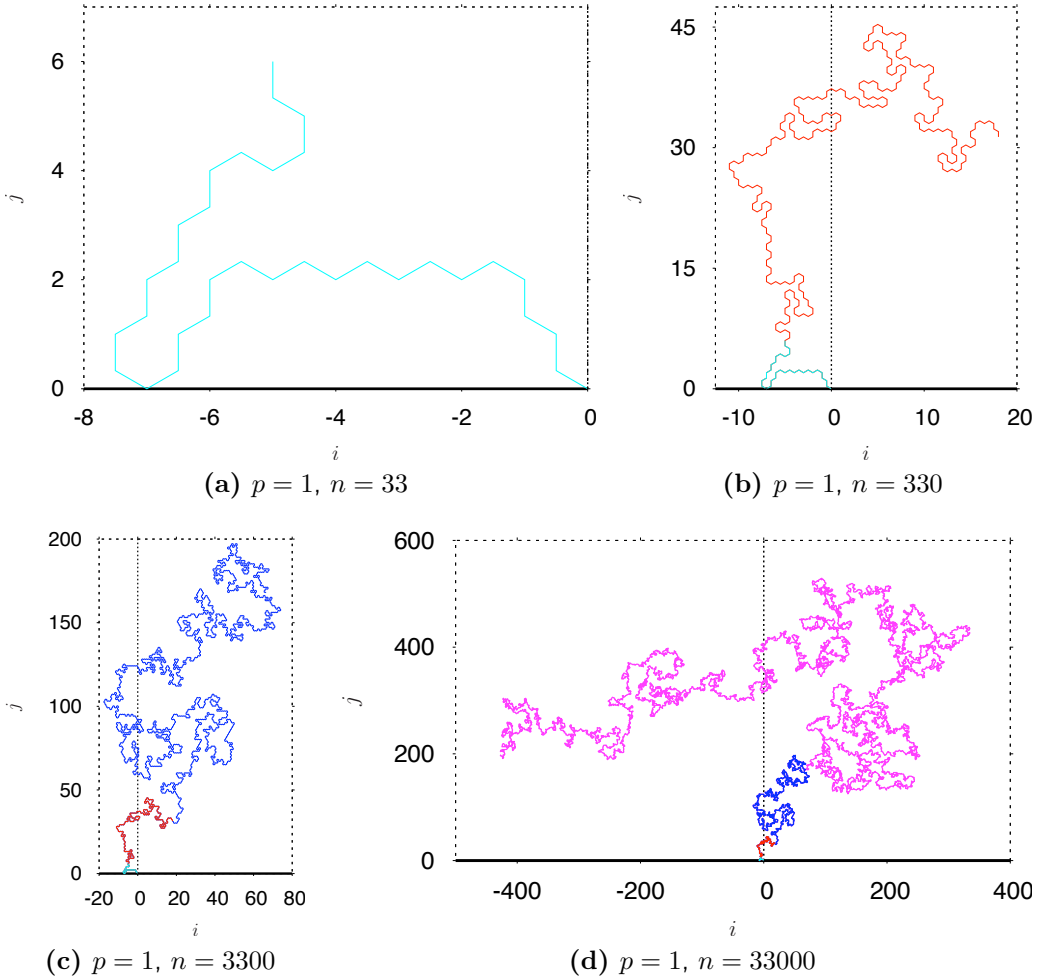

(a) $p = 1$, $n = 33$ **(b)** $p = 1$, $n = 330$

(c) $p = 1$, $n = 3300$ **(d)** $p = 1$, $n = 33000$

Figure 7.5: A harmonic explorer wandering around the upper half-plane. Four exploration paths are presented: γ_{33} (cyan), γ_{330} (red), γ_{3300} (blue) and γ_{33000} (magenta). Here and in the other figures of this section, $i = x/l_3$ and $j = y/\frac{3}{2}l_6$ label either the i-th hexagon column and the j-th hexagon row or the $2i$-th triangle column and the j-th triangle row. However, path aspect ratios are preserved.

n, exploration paths observed here would approximate SLE traces, provided that the scaling limit holds. Thus, explorer tendencies are supposed to mimic those of the SLE counterpart. In figures 7.5-7.9 samples of overruled harmonic explorers in $\mathbb{H}^{\#}$ are presented at decreasing values of p. For the sake of completeness and comparison, we include the well-known cases of the harmonic explorer and the critical percolation too.

To follow explorer progression in the domain, four snapshots at increasing n are given for each p-HE. Step numbers are chosen from four different orders of

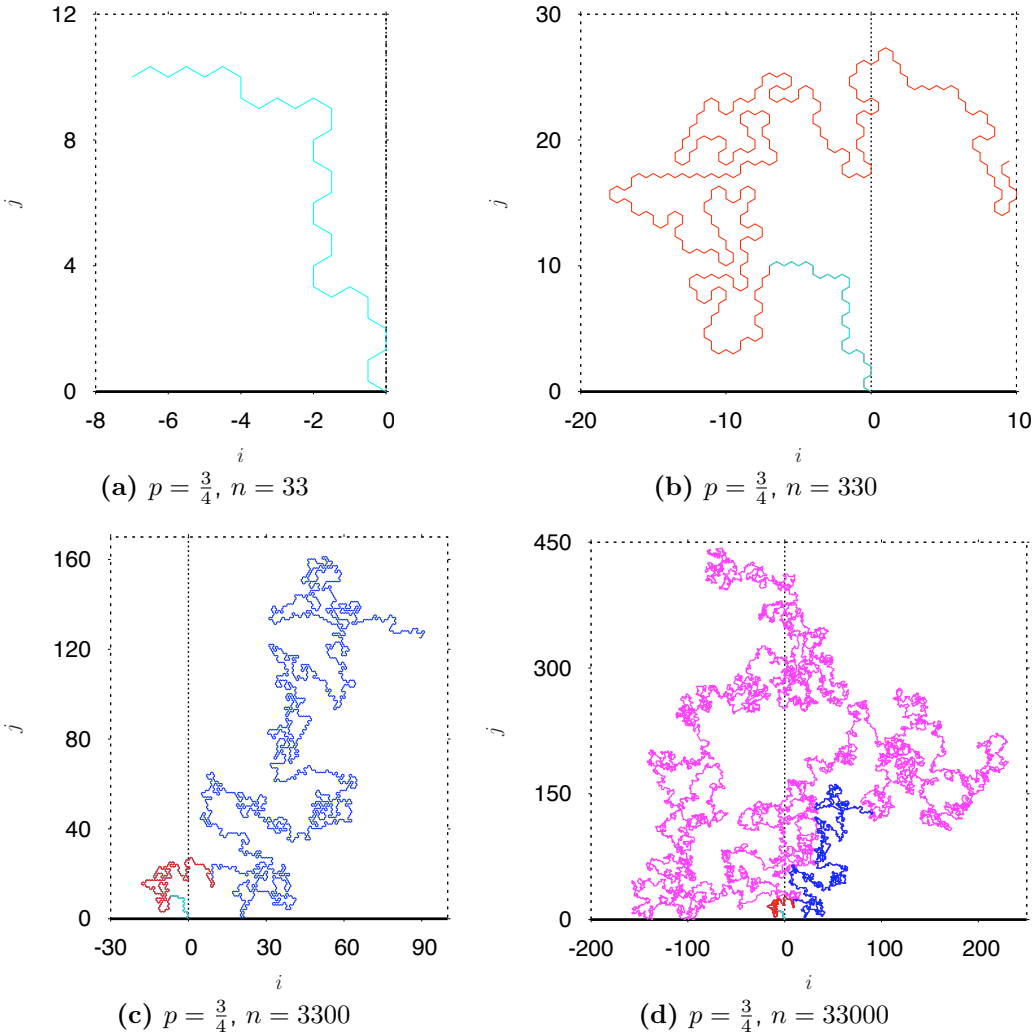

(a) $p = \frac{3}{4}$, $n = 33$ **(b)** $p = \frac{3}{4}$, $n = 330$

(c) $p = \frac{3}{4}$, $n = 3300$ **(d)** $p = \frac{3}{4}$, $n = 33000$

Figure 7.6: A $\frac{3}{4}$-harmonic explorer wandering around the upper half-plane.

magnitude, so that it is possible to have a first look at path fractal dimensions. Indeed, if the path is enclosed by a half circle of radius ρ_t, the fractal dimension can be extracted by the relation $\rho_n \sim n^{d_f}$, as we will see in section 7.4 with more details.

From direct observation of figures 7.5-7.9 we can pick out two evident features, from which it results clear that conjecture 6.1 moves in the right direction.

First, exploration paths become more and more winding and space-filling (corresponding to larger and larger values of $\varkappa$) as p decreases. The extreme case is that of the antiharmonic explorer, which seems to have a fractal dimension of order 2 and, hence, to tend to a $\mathrm{SLE}_\varkappa$ with $\varkappa$ of order 8 or larger than 8.

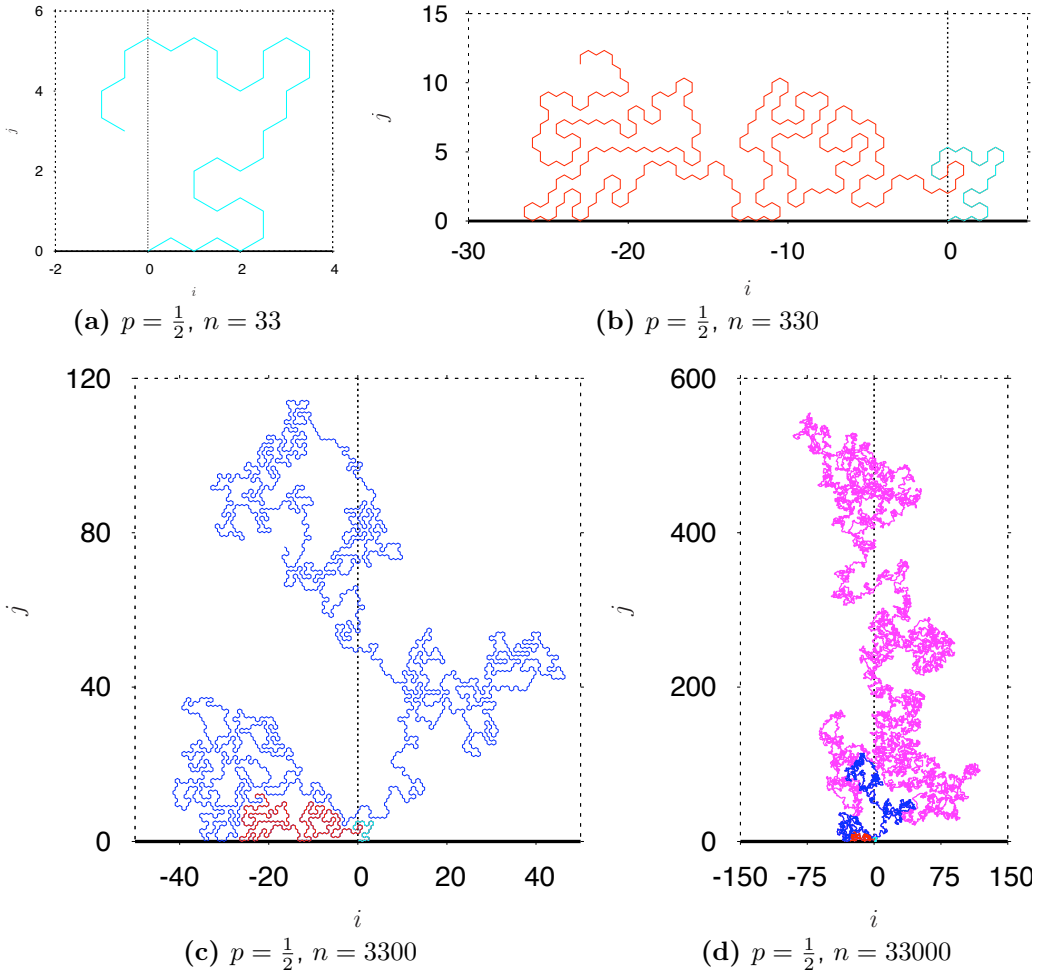

(a) $p = \frac{1}{2}$, $n = 33$ **(b)** $p = \frac{1}{2}$, $n = 330$

(c) $p = \frac{1}{2}$, $n = 3300$ **(d)** $p = \frac{1}{2}$, $n = 33000$

Figure 7.7: A critical-percolation explorer wandering around the upper half-plane.

Thus, as p runs from 1 to 0, it recovers the range $\varkappa \geqslant 4$. However, for the moment we cannot give an upper bound for $\varkappa$. Indeed, $d_{\mathrm{f}} = 2$ tells us nothing about the actual value of the diffusivity, because any $\mathrm{SLE}_{\varkappa \geqslant 8}$ shares this fractal dimension.

A second clue comes from path development in the horizontal direction with respect to the vertical one. It is well known from theory that SLE hulls broaden and get higher and higher with different time rates: the larger is $\varkappa$, the broader the hull. This property has an easy explanation: indeed, increasing $\varkappa$ implies increasing $\mathrm{SLE}_{\varkappa}$ tendencies of touching boundaries, i.e. of touching both itself and the real axis. The same feature seems to be shared by overruled harmonic explorers as p decreases.

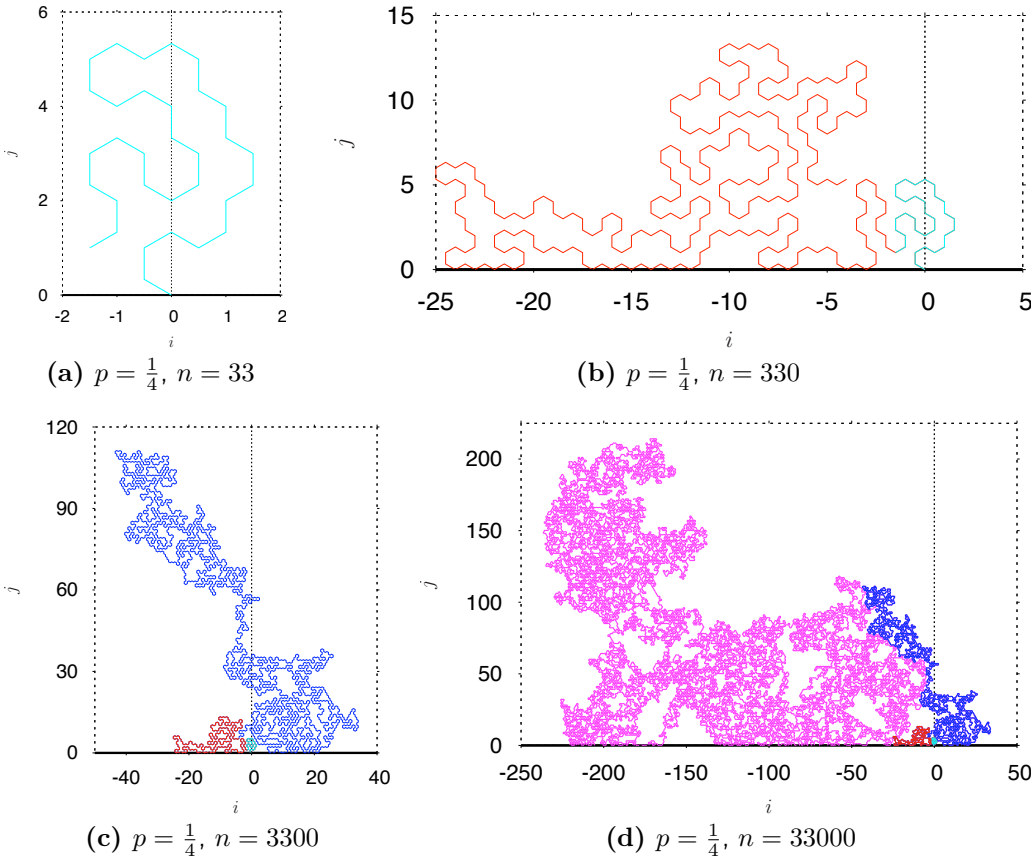

(a) $p = \frac{1}{4}$, $n = 33$ **(b)** $p = \frac{1}{4}$, $n = 330$

(c) $p = \frac{1}{4}$, $n = 3300$ **(d)** $p = \frac{1}{4}$, $n = 33000$

Figure 7.8: A $\frac{1}{4}$-harmonic explorer wandering around the upper half-plane.

7.2.2 Rectangular domains

In box domains exploration paths are not stopped after a certain number of steps, but followed until they end in the exit point r_*. Thus, the total number of steps depends on both the particular realization and, mainly, the kind of explorer. From a computational point of view, generating overruled harmonic explorers in a compact domain is faster than in a non-compact one, because random walks take shorter times, but it requires the storage of a large amount of data.

This section provides only a tracking shot of complete exploration processes in rectangular domains at decreasing values of the uphold probability p and increasing values of rectangle aspect ratio R. Let us only remark that figures 7.10-7.12 confirm what observed about p-HE spatial properties in the upper half-plane: at any R, as p decreases, the path becomes more winding and space-filling.

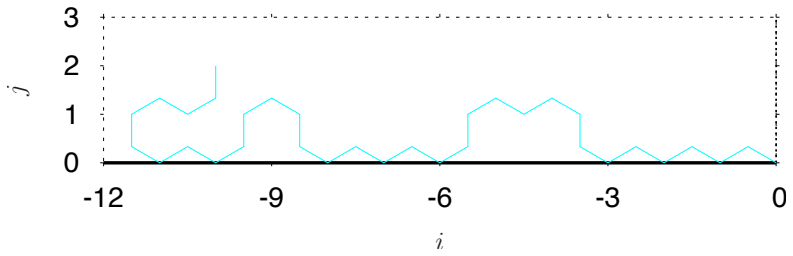

(a) $p = 0$, $n = 33$

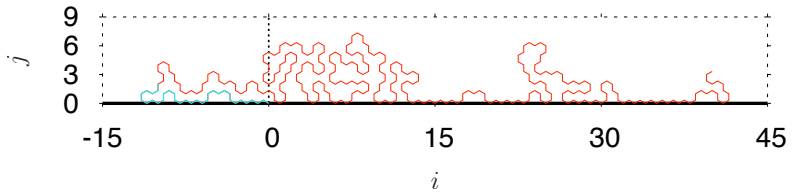

(b) $p = 0$, $n = 330$

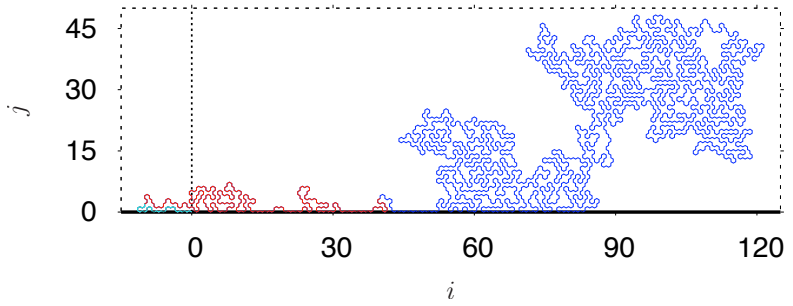

(c) $p = 0$, $n = 3300$

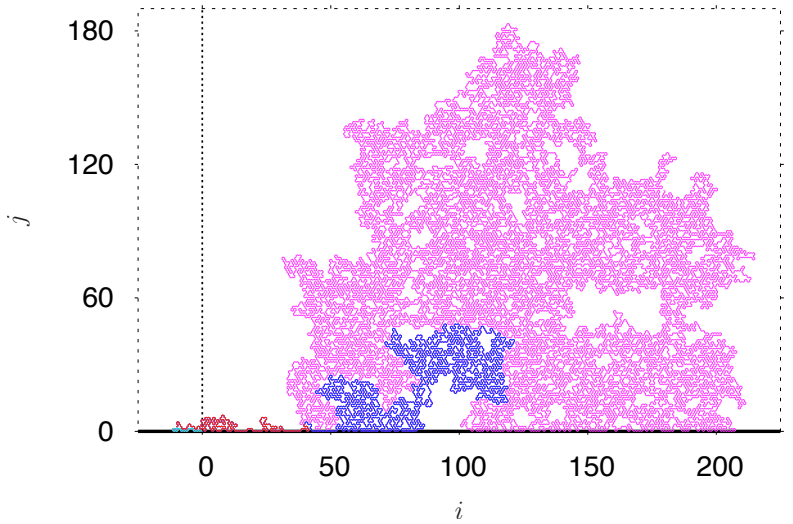

(d) $p = 0$, $n = 33000$

Figure 7.9: An antiharmonic explorer wandering around the upper half-plane.

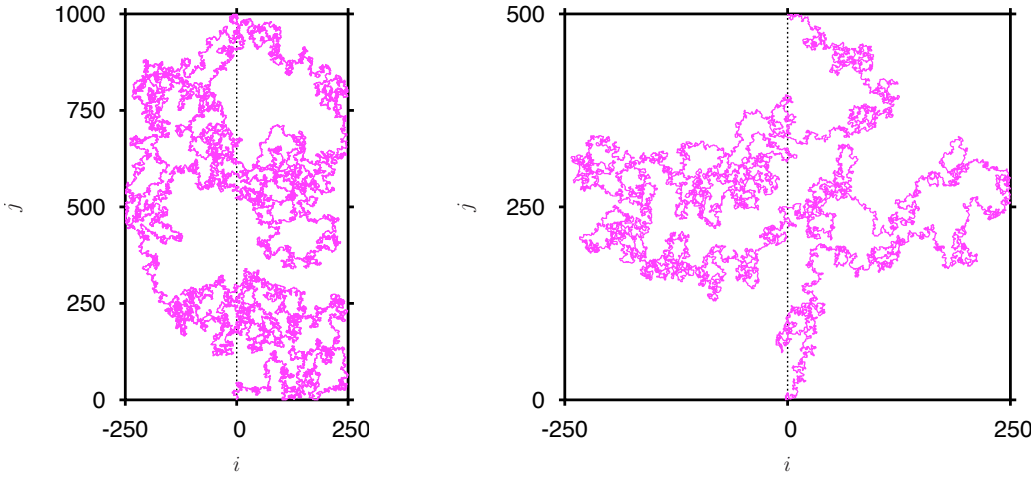

(a) $p = \frac{3}{4}$, $R = 0.58$

(b) $p = \frac{3}{4}$, $R = 1.15$

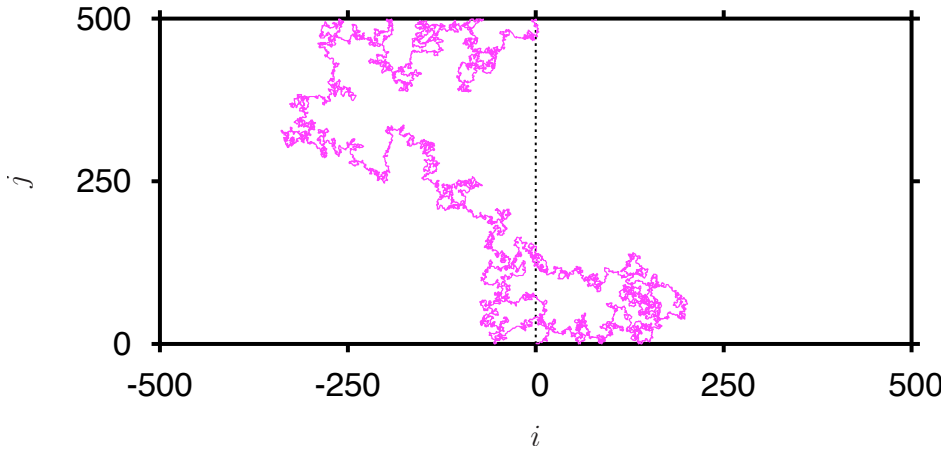

(c) $p = \frac{3}{4}$, $R = 2.31$

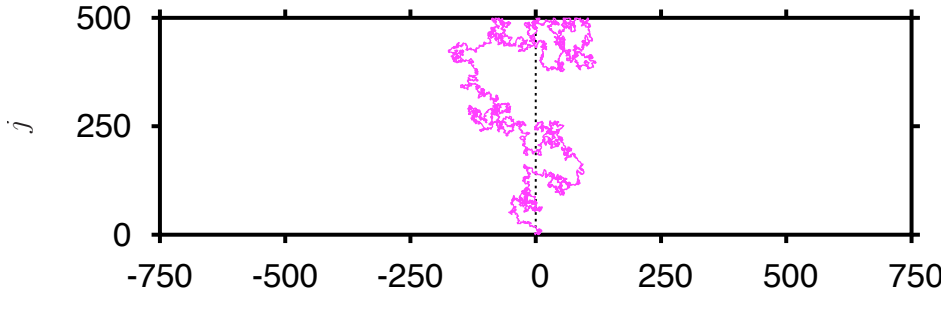

(d) $p = \frac{3}{4}$, $R = 3.47$

Figure 7.10: A complete $\frac{3}{4}$-harmonic exploration in different rectangular domains of aspect ratio R.

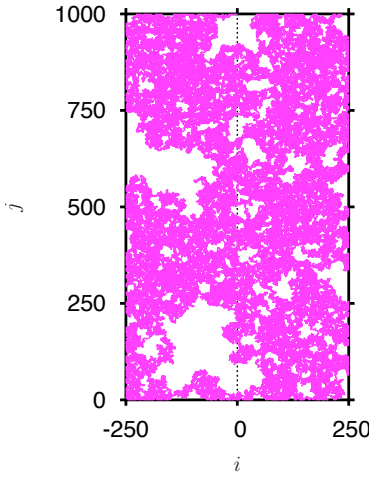

(a) $p = \frac{1}{4}$, $R = 0.58$

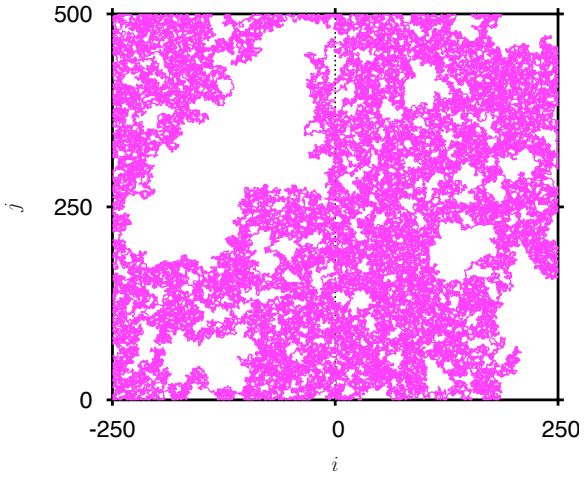

(b) $p = \frac{1}{4}$, $R = 1.15$

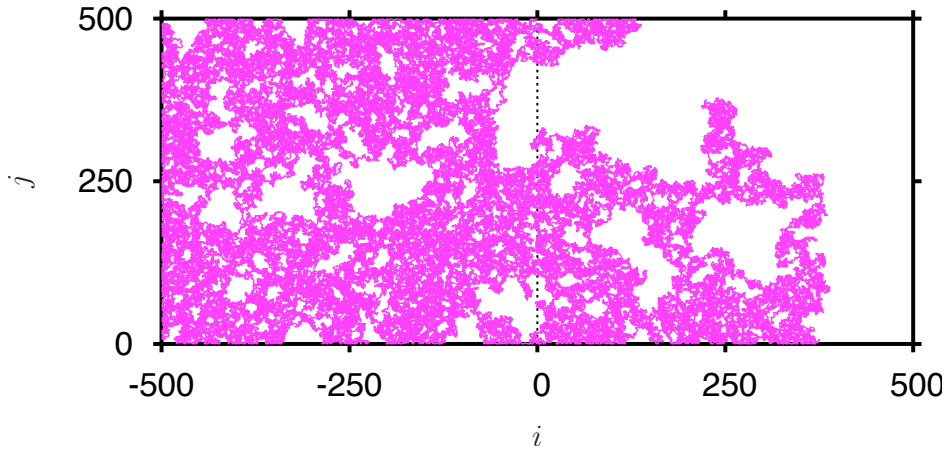

(c) $p = \frac{1}{4}$, $R = 2.31$

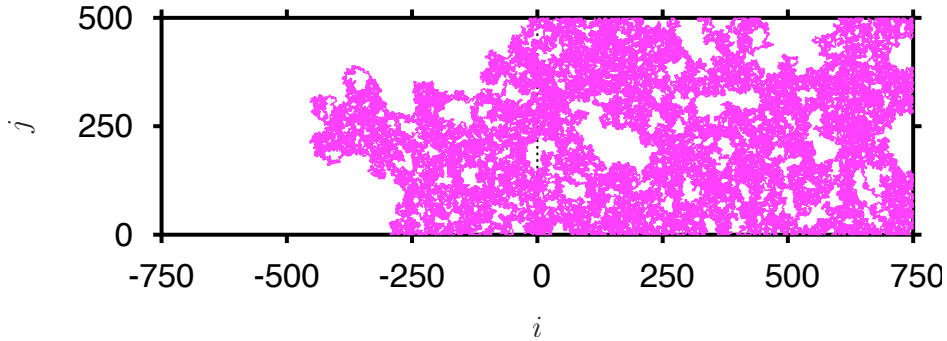

(d) $p = \frac{1}{4}$, $R = 3.47$

Figure 7.11: A complete $\frac{1}{4}$-harmonic exploration in different rectangular domains of aspect ratio R.

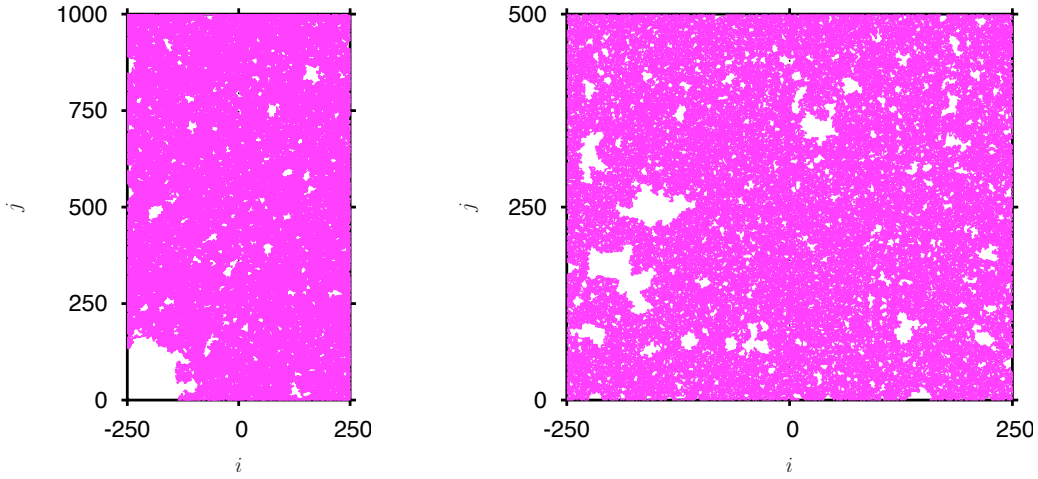

(a) $p = 0$, $R = 0.58$

(b) $p = 0$, $R = 1.15$

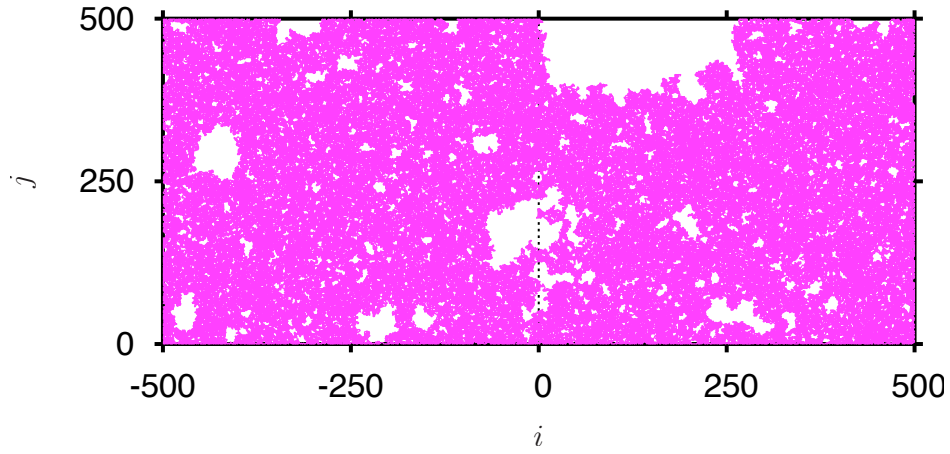

(c) $p = 0$, $R = 2.31$

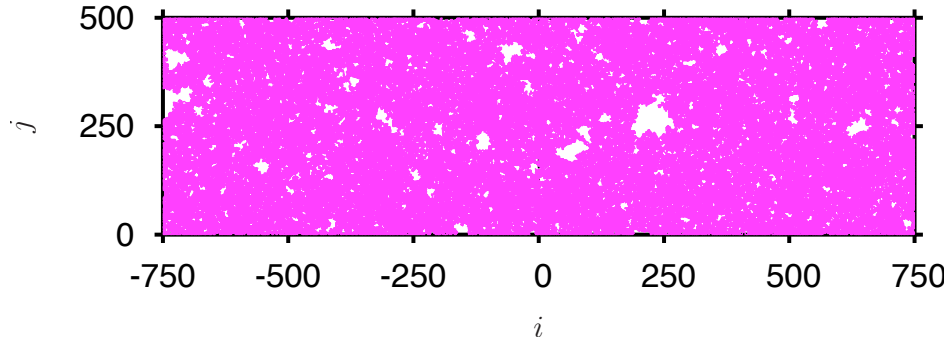

(d) $p = 0$, $R = 3.47$

Figure 7.12: A complete antiharmonic exploration in different rectangular domains of aspect ratio R.

7.3 Crossing probability

The general behaviour of the overruled harmonic explorers has been highlighted by samples of them in different domains and in a qualitative way in section 7.2. Now, a more detailed analysis is needed. The aim is to verify whether p-HE really converge to SLE$_\varkappa$ and, if yes, to determine the relation between p and $\varkappa$ numerically. Therefore, the first property to be examined is the conformal invariance. Indeed, the other definition property of SLE, the domain Markov property, is still guaranteed by construction. Conformal invariance can be tested by computing some well-known probabilities in different domains: if exploration paths are conformally invariant, such a probability has to be the same in both domains. More rigorously, if two complete exploration paths $\gamma_* \in \mathcal{D}$ and $\gamma'_* \in \mathcal{D}'$ are conformally invariant, the probabilities $P(z \in \mathcal{D})$ and $P(z' \in \mathcal{D}')$ must be equal if $\gamma'_* = g(\gamma_*)$ and $z' = g(z)$ are the images of γ_* and z under the conformal map $g : \mathcal{D} \to \mathcal{D}'$, respectively.

Here, for this purpose we consider the crossing probability P_{cr} computed in section 5.2.5 and four different rectangular domains. Since the crossing probability between two real points $u_- < 0$ and $u_+ > 0$ in $\mathbb{H}$ only depends on their ratio $r = -u_-/u_+ > 0$, we are free to fix one of them. The simplest choice is to keep fixed one of the lower rectangle corners located in $-x_{N_x}$ and $+x_{N_x}$. Indeed, the Schwarz–Christoffel transformation (5.12) from the rectangular domain to the upper half-plane maps them to -1 and 1, respectively.

Let us define the right crossing probability P_{cr}^+ of an overruled harmonic explorer inside a rectangle $\mathcal{R}_R$ as the probability of swallowing the left lower corner $-x_{N_x}$ into the hull before a point z_+ on the right boundary $\mathcal{B}_{0+}^{\#}$ of the rectangle (and vice versa for the left crossing probability P_{cr}^-). For an easier comparison between different domains, we directly define both in terms of the ratio r. If g_R is the Schwarz–Christoffel transformation (5.12) mapping $\mathcal{R}_R = \mathcal{R}_{\mathrm{ev}}$ in $\mathbb{H}$ (and f_R its inverse), in the right case we simply have

$$r = -\frac{g_R(-x_{N_x})}{g_R(z_+)} = \frac{1}{u_+}$$

For the left probability, we can consider it as a right probability in the reflected domain $\pi(\mathcal{R}_R)$, where $\pi(x + \mathrm{i}y) = -x + \mathrm{i}y$:

$$r = -\frac{g_R\big(\pi(+x_{N_x})\big)}{g_R\big(\pi(z_-)\big)} = -\frac{g_R(-x_{N_x})}{g_R(-z_-)} = \frac{1}{-u_-}$$

Then, we define the two crossing probabilities as

$$\begin{aligned} P_{\mathrm{cr}}^{+}(p,R;r) &\coloneqq \mathscr{P}[\gamma_* \text{ swallows } -x_{N_x} = f_R(-1) \text{ before } z_+ = f_R\left(\tfrac{1}{r}\right) \in \mathcal{B}_{0+}^{\#}] \\ P_{\mathrm{cr}}^{-}(p,R;r) &\coloneqq \\ &= \mathscr{P}[\gamma_* \text{ swallows } +x_{N_x} = \pi\big(f_R(-1)\big) \text{ before } z_- = \pi\left(f_R\left(\tfrac{1}{r}\right)\right) \in \mathcal{B}_{0-}^{\#}] = \\ &= \mathscr{P}[\pi(\gamma_*) \text{ swallows } -x_{N_x} = f_R(-1) \text{ before } z_+ = f_R\left(\tfrac{1}{r}\right) \in \mathcal{B}_{0-}^{\#}] \end{aligned}$$

The conformal invariance of the overruled harmonic explorer is signalled when both probabilities are independent of the aspect ratio R, i.e. equal for every rectangle ($P_{\mathrm{cr}}^{+}(p,R;r) = P_{\mathrm{cr}}^{+}(p,R';r),\ \forall R \neq R'$). Moreover, if $P_{\mathrm{cr}}^{+}(p,R;r) = P_{\mathrm{cr}}^{-}(p,R;r)$, the crossing probability is invariant under horizontal reflections. This should be the case in our domain symmetric with respect to the imaginary axis (except for a short offset). From a computational point of view, taking their arithmetic mean corresponds to doubling the number of realizations with a reflected version for each one. For this purpose, let us define

$$\begin{aligned} P_{\mathrm{cr}}^{\pm}(p,R;r) &= \tfrac{1}{2}P_{\mathrm{cr}}^{+}(p,R;r) + \tfrac{1}{2}P_{\mathrm{cr}}^{-}(p,R;r) \\ \Delta_{\mathrm{cr}}^{\pm}(p,R;r) &= \tfrac{1}{2}P_{\mathrm{cr}}^{+}(p,R;r) - \tfrac{1}{2}P_{\mathrm{cr}}^{-}(p,R;r) \end{aligned}$$

In the following, we will consider the former as the crossing probability and the latter, the *left-right gap*, as a symmetry control.

Figure 7.13 shows both p-HE crossing probabilities and the corresponding left-right gaps at four different R for each considered p. Each probability arises from 10000 realizations plus 10000 reflected ones. The evident result is that all the probabilities are superimposed for each p; they are independent of the aspect ratio. Moreover, the distance between right and left probabilities has a noisy behaviour and $\Delta_{\mathrm{cr}}^{\pm}/P_{\mathrm{cr}}^{\pm} \sim 10^{-2}$, a clear fingerprint of statistical fluctuations. In short, p-HE crossing probabilities are invariant under horizontal reflections and, more important, conformally invariant.

The further step is the comparison between p-HE and SLE$_\varkappa$ crossing probabilities. Indeed, once the conformal invariance is attested, it remains to investigate whether $P_{\mathrm{cr}}^{\pm}(p,R;r)$ reproduces SLE crossing formula (5.25) for some value of $\varkappa$. As a first approach, we compare each probability with its SLE counterpart according to conjecture 6.1. From figure 7.14 it is evident that conjecture 6.1 works in the right direction: increasing p corresponds to decreasing $\varkappa$ and both the order of magnitude and the shapes of the probabilities are got right.

Nevertheless, the conjectured prediction is not accurate at the smallest r, i.e. at the largest scales corresponding to boundary points close to the exit point r_*. Several effects can be responsible for this. First, it is possible that a diffusivity different from the conjectured one is involved. Otherwise, we should consider

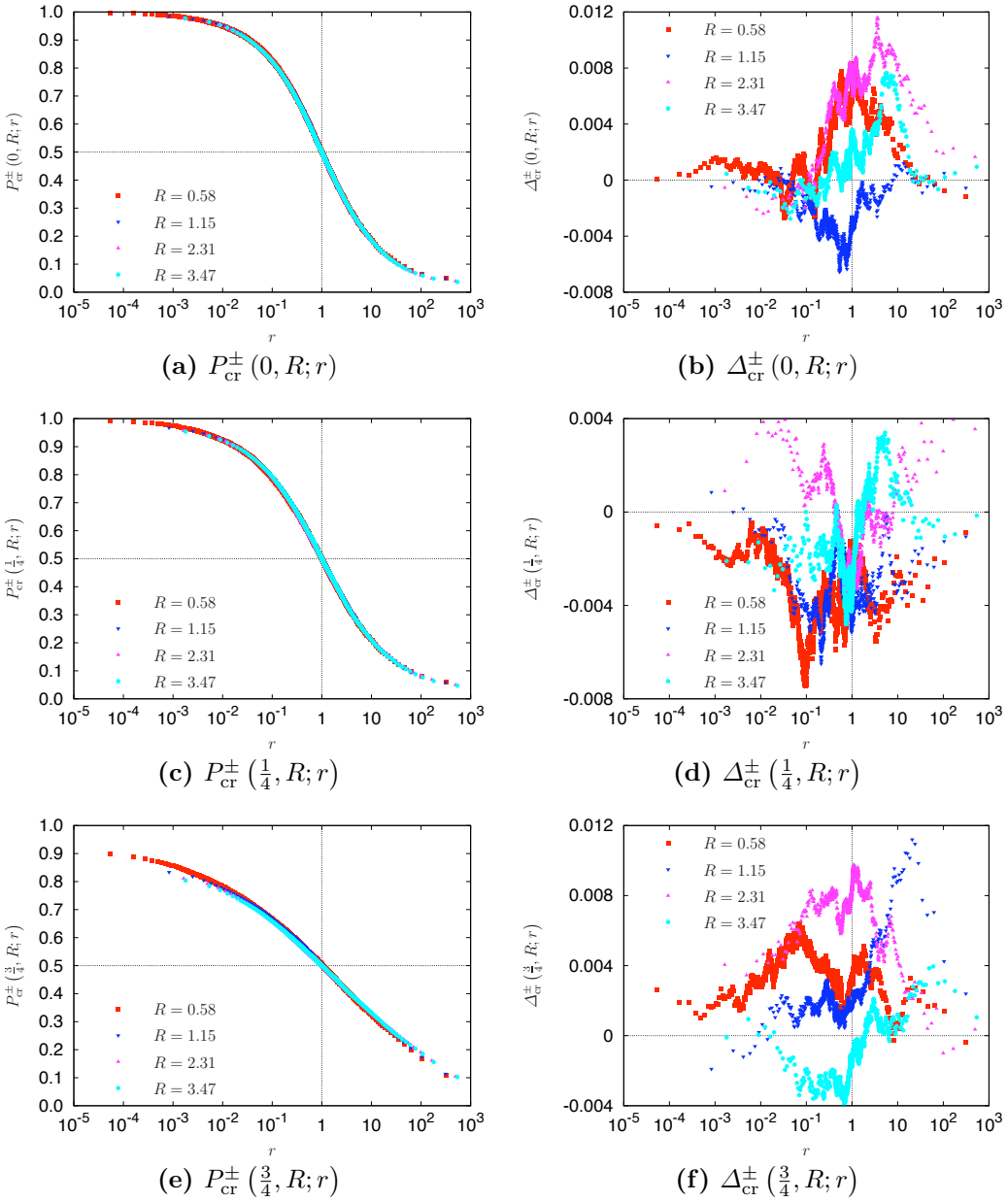

(a) $P^{\pm}_{\rm cr}\,(0,R;r)$ **(b)** $\Delta^{\pm}_{\rm cr}\,(0,R;r)$

(c) $P^{\pm}_{\rm cr}\,(\frac{1}{4},R;r)$ **(d)** $\Delta^{\pm}_{\rm cr}\,(\frac{1}{4},R;r)$

(e) $P^{\pm}_{\rm cr}\,(\frac{3}{4},R;r)$ **(f)** $\Delta^{\pm}_{\rm cr}\,(\frac{3}{4},R;r)$

Figure 7.13: The crossing probabilities $P^{\pm}_{\rm cr}(p,R;r)$ of the overruled harmonic explorers are conformally invariant at each considered p (left, figures (a), (c) and (e)). Indeed, exploration paths in rectangular domains of different aspect ratios R share the same $P^{\pm}_{\rm cr}$, once each domain is conformally mapped to the upper half-plane. There is only a noisy slight gap $\Delta^{\pm}_{\rm cr}\,(p,R;r)$ between left and right crossing probabilities (right, figures (b), (d) and (f)). Since it is due to the statistical variability rather than to any asymmetry of the exploration process, we are allowed to average on $P^{+}_{\rm cr}$ and $P^{-}_{\rm cr}$ in order to improve the statistics.

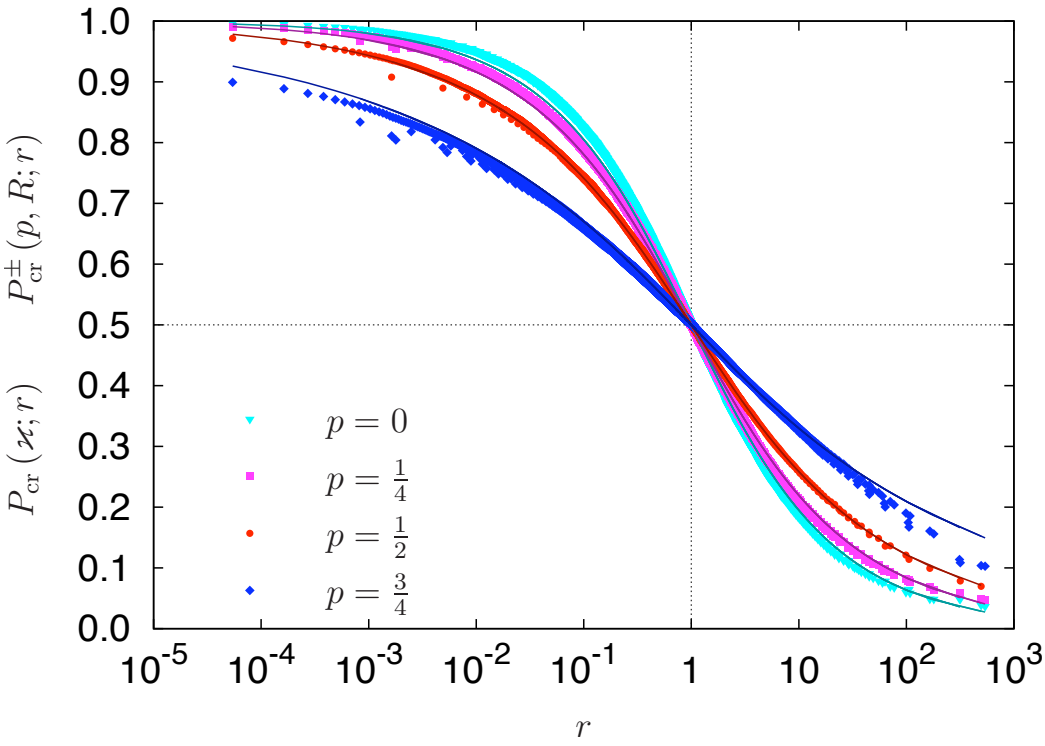

Figure 7.14: The p-HE crossing probabilities $P_{\rm cr}^{\pm}(p,R;r)$ (symbols) are compared with their conjectured SLE$_\varkappa$ limits $P_{\rm cr}(\varkappa;r)$ (darker lines). All the aspect ratios are plotted together. Conjecture 6.1 clearly works in the right direction and each p seems to be compatible with its corresponding conjectured $\varkappa$. However, the largest scales (i.e. the smallest r) are not well described by the conjectured curve. This can be blamed on the Schwarz–Christoffel map acting on points close to the exit point r_*, which is mapped to infinity, where the lattice spacing is enlarged more and more.

finite-size effects. In particular, since r_* is mapped to infinity by the Schwarz–Christoffel transformation, the lattice spacing in the region close to r_* is blown up consequently, so that the continuous limit of the grid is not well defined there. Therefore, the mapped probability may result very sensitive. Finally, also statistical fluctuations could affect the probabilities. However, this seems not to be the case, because figure 7.14 shows a continuous behaviour of $P_{\rm cr}^{\pm}$ in its whole range and a clear trend for each p-HE at the smallest r: e.g. $P_{\rm cr}^{\pm}(0,R;r)$ lies above $P_{\rm cr}(8;r)$ there, whereas $P_{\rm cr}^{\pm}(\frac{3}{4},R;r)$ below $P_{\rm cr}(5;r)$.

Let us deal with a deeper analysis in order to identify which effect predominates. It is useful to observe the behaviour of the p-$\varkappa$ *gap*

$$\Delta_{\rm cr}^{\varkappa}(p,R;r) = P_{\rm cr}^{\pm}(p,R;r) - P_{\rm cr}(\varkappa;r)$$

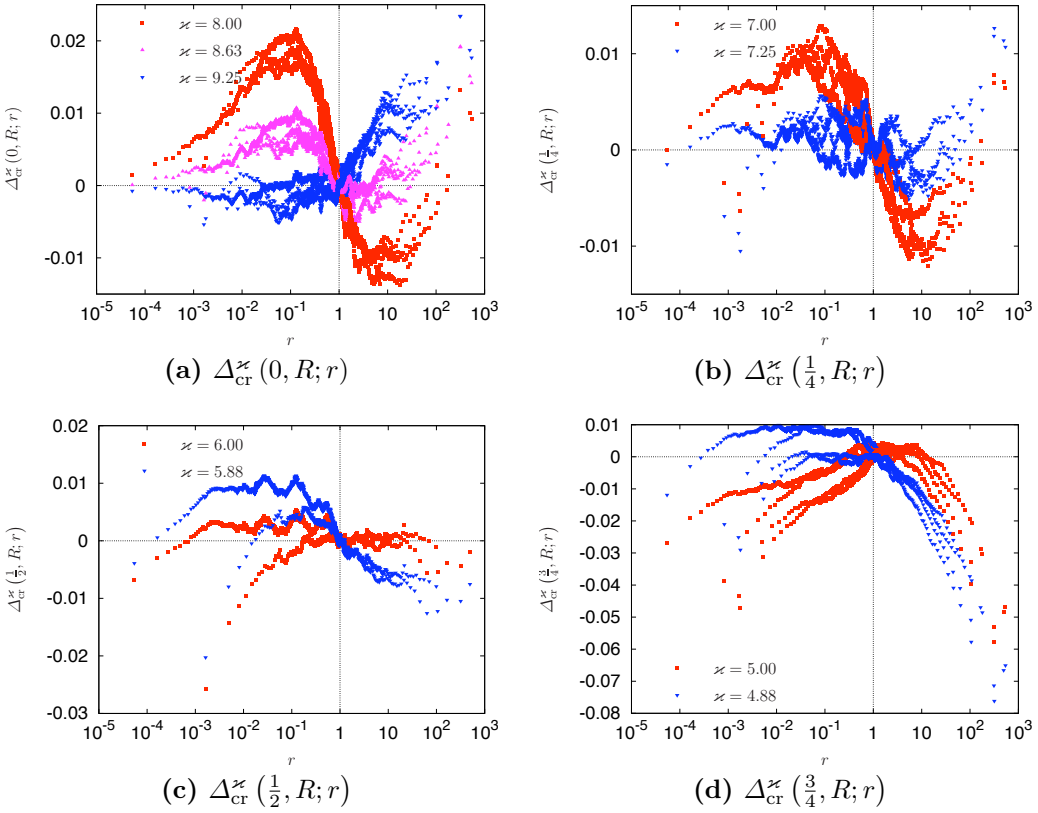

(a) $\Delta^{\varkappa}_{\mathrm{cr}}(0, R; r)$ **(b)** $\Delta^{\varkappa}_{\mathrm{cr}}\left(\frac{1}{4}, R; r\right)$

(c) $\Delta^{\varkappa}_{\mathrm{cr}}\left(\frac{1}{2}, R; r\right)$ **(d)** $\Delta^{\varkappa}_{\mathrm{cr}}\left(\frac{3}{4}, R; r\right)$

Figure 7.15: The distances $\Delta^{\varkappa}_{\mathrm{cr}}(p, R; r)$ between p-HE and $\mathrm{SLE}_{\varkappa}$ crossing probabilities are plotted for all the aspect ratios together. The gap for the conjectured $\varkappa$ (red squares) approximate 0 well only for the critical percolation (figure (c)). In the other cases the distance for different $\varkappa$ (blue downwards triangles and magenta upwards triangle) approximates 0 better, suggesting a different relation between p and $\varkappa$ with respect to the conjectured one. However, improving the description of the left tail causes a worsening in the right one. At this point, we cannot decide whether conjecture 6.1 fails or it holds and we are only observing finite-size effects.

Clearly, if this gap approximates 0, $\varkappa$ should be the diffusivity parameter of the searched limit $\mathrm{SLE}_{\varkappa}$. In figure 7.15 $\Delta^{\varkappa}_{\mathrm{cr}}$ is plotted for some values of $\varkappa$ for each p. All the aspect ratios are reported. Indeed, thanks to the conformal invariance, we can improve the statistics by considering all the realizations in the four different domains as a unique series of exploration processes in the upper half-plane. The qualitative trends showed in figure 7.15 can be studied in a more quantitative way by averaging data over all the available both r and R, as reported in table 7.2. The result which emerges is that conjecture 6.1 is not so accurate. In particular, for $p = 0$ and $p = \frac{3}{4}$ a larger $\varkappa$ is observed (viz. $\varkappa \approx 9$

$\varkappa$	$\langle \Delta_{\rm cr}^{\varkappa} \rangle$	$\langle (\Delta_{\rm cr}^{\varkappa})^2 \rangle$
8.00	$4.6\ 10^{-3}$	$8.9\ 10^{-5}$
8.63	$2.2\ 10^{-3}$	$1.6\ 10^{-5}$
8.75	$1.8\ 10^{-3}$	$1.0\ 10^{-5}$
9.00	$1.1\ 10^{-3}$	$0.5\ 10^{-5}$
9.25	$0.6\ 10^{-3}$	$0.6\ 10^{-5}$

(a) $p = 0$

$\varkappa$	$\langle \Delta_{\rm cr}^{\varkappa} \rangle$	$\langle (\Delta_{\rm cr}^{\varkappa})^2 \rangle$
7.00	$2.1\ 10^{-3}$	$2.3\ 10^{-5}$
7.12	$1.3\ 10^{-3}$	$1.0\ 10^{-5}$
7.25	$0.6\ 10^{-3}$	$0.3\ 10^{-5}$
7.50	$-0.8\ 10^{-3}$	$0.9\ 10^{-5}$

(b) $p = \frac{1}{4}$

$\varkappa$	$\langle \Delta_{\rm cr}^{\varkappa} \rangle$	$\langle (\Delta_{\rm cr}^{\varkappa})^2 \rangle$
5.88	$3.2\ 10^{-3}$	$3.1\ 10^{-5}$
6.00	$1.1\ 10^{-3}$	$0.4\ 10^{-5}$
6.25	$2.9\ 10^{-3}$	$4.2\ 10^{-5}$

(c) $p = \frac{1}{2}$

$\varkappa$	$\langle \Delta_{\rm cr}^{\varkappa} \rangle$	$\langle (\Delta_{\rm cr}^{\varkappa})^2 \rangle$
4.75	$5.2\ 10^{-3}$	$20.4\ 10^{-5}$
4.88	$1.4\ 10^{-3}$	$3.4\ 10^{-5}$
5.00	$-1.7\ 10^{-3}$	$2.3\ 10^{-5}$
5.25	$-7.2\ 10^{-3}$	$28.1\ 10^{-5}$

(d) $p = \frac{3}{4}$

Table 7.2: The gaps $\Delta_{\rm cr}^{\varkappa}(p, R; r)$ between p-HE and $\mathrm{SLE}_{\varkappa}$ crossing probabilities have been averaged over r and R, in order to extract their mean $\langle \Delta_{\rm cr}^{\varkappa} \rangle$ and mean square departure $\langle (\Delta_{\rm cr}^{\varkappa})^2 \rangle$ for each p-$\varkappa$ pair. The smallest $\langle (\Delta_{\rm cr}^{\varkappa})^2 \rangle$ identifies the most likely $\varkappa$, which is compatible with the conjectured one only for $p = \frac{3}{4}$ (table (d)). For both $p = \frac{1}{4}$ (table (b)) and $p = 0$ (table (a)) a larger $\varkappa$ is observed. Notice that we cannot invoke finite-size effects here, because SLE_6 probability is well recovered at $p = \frac{1}{2}$ (table (c)), as we know it must be.

and $\varkappa \approx 7.25$, respectively).

If the gap were due to lattice effects, we should find it for the critical percolator too. However, both figure 7.15c and table 7.2c show that this does not occur at $p = \frac{1}{2}$. Since in this case the relation between p and $\varkappa$ is proved and data are in good agreement with it, we are led to believe that in the other cases the problem may be conjecture 6.1.

To test the possible importance of lattice effects, one can compare the crossing probability in two similar domains, e.g. the rectangle $(N_x, N_y) = (500, 500)$ and its reduced version $(250, 250)$. We did it for $p = 0$, but no difference is observed between the two cases. A further test is the comparison between the crossing probability $P_{\rm cr}^{\pm}(p, R; r)$ and its inverse $1 - P_{\rm cr}^{\pm}\left(p, R; \frac{1}{r}\right)$, reported in figure 7.16. By definition, the former is the probability that the left lower corner is swallowed before a right-boundary point $z_+ = x_+ + \mathrm{i}y_+$. If scaling invariance holds (i.e. the crossing probability only depends on r), the latter is the probability that the symmetric left-boundary point $z_- = -x_+ + \mathrm{i}y_+$ is swallowed before the right lower corner. When both the reflection symmetry and the scaling invariance are present, the two probabilities should be equal. However, their overlapping is not complete on their tails, so attesting that the probability is not well described at scales close to both the starting and the final point.

In conclusion, the analysis of crossing probabilities shows that overruled harmonic explorers are conformally invariant growth processes, whose continuous

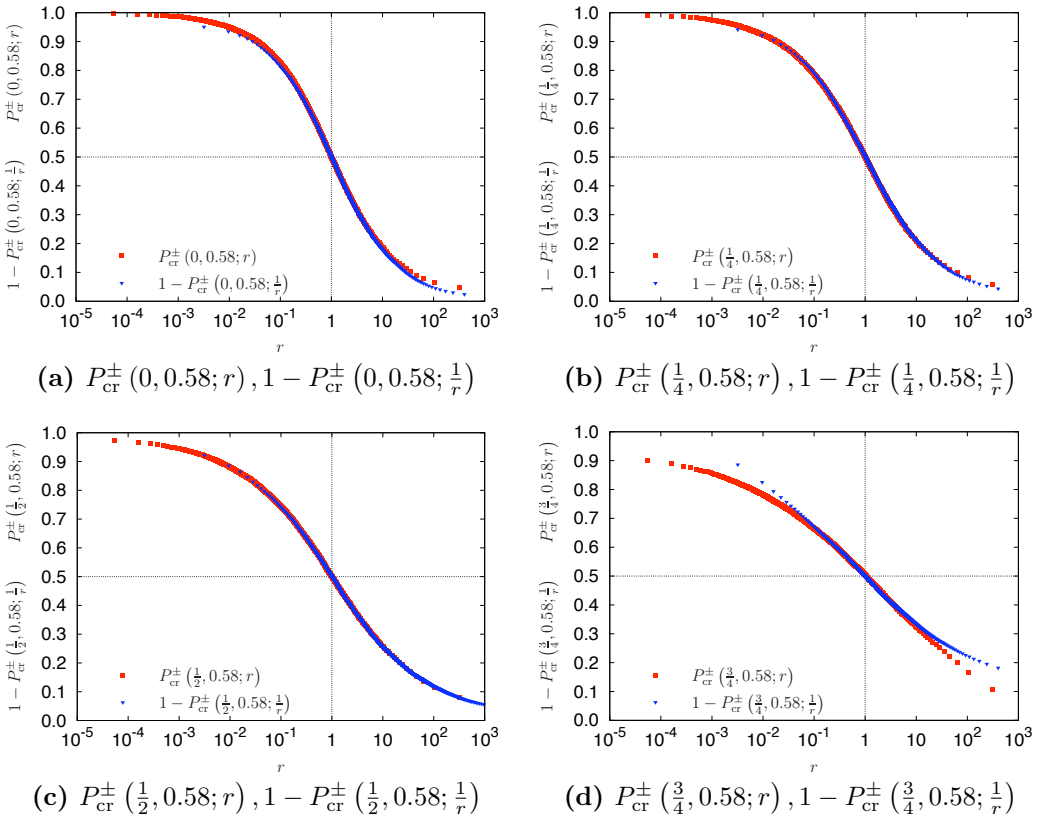

(a) $P^{\pm}_{\rm cr}\left(0,0.58;r\right),1-P^{\pm}_{\rm cr}\left(0,0.58;\frac{1}{r}\right)$ **(b)** $P^{\pm}_{\rm cr}\left(\frac{1}{4},0.58;r\right),1-P^{\pm}_{\rm cr}\left(\frac{1}{4},0.58;\frac{1}{r}\right)$

(c) $P^{\pm}_{\rm cr}\left(\frac{1}{2},0.58;r\right),1-P^{\pm}_{\rm cr}\left(\frac{1}{2},0.58;\frac{1}{r}\right)$ **(d)** $P^{\pm}_{\rm cr}\left(\frac{3}{4},0.58;r\right),1-P^{\pm}_{\rm cr}\left(\frac{3}{4},0.58;\frac{1}{r}\right)$

Figure 7.16: The crossing probabilities $P^{\pm}_{\rm cr}\left(p,0.58;r\right)$ (red squares) and their inverse $1-P^{\pm}_{\rm cr}\left(p,0.58;\frac{1}{r}\right)$ (blue triangles) are compared at each considered p in the domain $(N_x,N_y)=(250,1000)$. Although by reflection and scaling symmetries they should be equal, we observe a slight difference between their tails, probably due to finite-size effects, which are enlarged close to the exit point.

limit seems to be an $\mathrm{SLE}_\varkappa$. The general trend of the correspondence between p and $\varkappa$ is well described by conjecture 6.1, but the actual values of $\varkappa$ seems to be slightly different. The latter statement could be influenced by finite-size effects at large scales.

7.4 Path fractal dimension

The observation of overruled harmonic explorers in different rectangular domains highlights their clear conformal invariance. Besides, determining the $\mathrm{SLE}_\varkappa$ they tend to by exploiting the crossing probability, which is a hypergeometric function with $\varkappa$ as an argument, is not a straightforward task. An easier ap-

proach deals with the investigation of the geometrical properties of p-HE paths. In particular, it is quite simple to compute the fractal dimension of some set of points related with the path, because it generally involves only a linear fitting. Here, we consider the path γ_n itself. The following two sections will consider the set of points of γ_n lying on the real axis (*real points*, section 7.5) and the set of points where γ_n touch itself (*double points*, section 7.6).

As explained in section 5.2, SLE$_\varkappa$ traces are unifractal objects, i.e. their Renyi dimensions d_α, defined by (5.13), are all equal. This property allows us to determine the fractal dimension by exploiting the most convenient one. Of course, a rigorous approach should still investigate p-HE unifractality. However, because of computational convenience, we studied one fractal dimension for different fractal objects rather than more than one.

Since fitting needs a scaling range whose lower bound is lattice spacing, a non-compact domain is more useful. Thus, from now on we will consider overruled harmonic explorer in the upper half-plane. Let us start from the fractal dimension d_γ of the path. Applying conjecture 6.1 to prediction (5.18) computed for an SLE$_\varkappa$ leads to the conjectured value

$$d_\gamma^{\mathrm{con}} = 2 - \frac{p}{2}$$

which spans the range $[1.5, 2]$, as p runs from 1 to 0. In particular, the antiharmonic explorer is guessed to fill the half-plane. It is worth to notice that from the observation of $d_\gamma = 2$ at $p = 0$ we cannot infer that the antiharmonic explorer converges to SLE$_8$ in the continuous limit, but only that $\varkappa = 8$ is a lower bound. Indeed, all SLE$_{\varkappa \geqslant 8}$ share the same fractal dimension, i.e. the dimension of the space where they evolve.

To extract the scaling exponent d_γ, we computed the mean distance from the origin, $\langle |r_n| \rangle$, reached by the explorer after n steps. This distance gives a measure of the mean hull radius. Averages are intended over realizations. Then, we plotted the path length $L_n = n l_6$ with respect to $\langle |r_n| \rangle$, exploiting the capacity dimension d_0 defined by $(5.14\mathrm{a})$, where $\varepsilon = 1/\langle |r_n| \rangle$ now. In other words, we counted the number n of l_6-long lines needed to cover the fractal object contained in the region of radius $\langle |r_n| \rangle$. The mean radius was stored in two ways: both by a logarithmic sampling, i.e. at each step 2^i, and by a linear sampling, i.e. every m steps, where i runs over positive integers and m is a fixed integer. In the former case, the fractal dimension emerges from the linear fitting

$$\log n = a + d_\gamma^{\log} \log \langle |r_n| \rangle$$

whereas in the latter from the power-law fitting

$$n = \alpha \langle |r_n| \rangle^{d_\gamma^{\mathrm{lin}}}$$

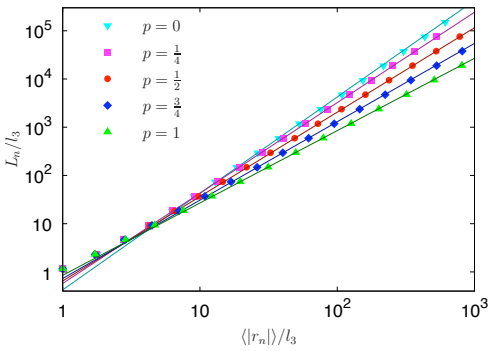

(a) $\langle|r_n|\rangle$ (logarithmic sampling)

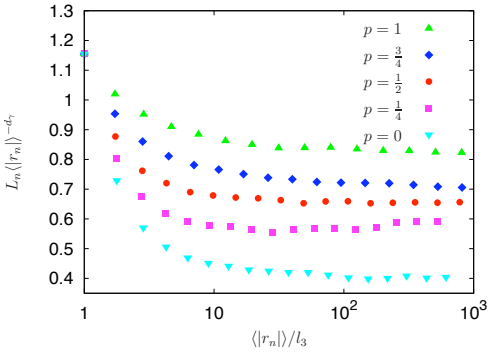

(b) $L_n \langle|r_n|\rangle^{-d_\gamma^{\mathrm{con}}}$ (logarithmic sampling)

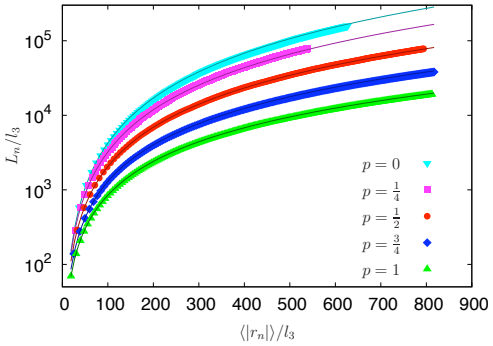

(c) $\langle|r_n|\rangle$ (linear sampling)

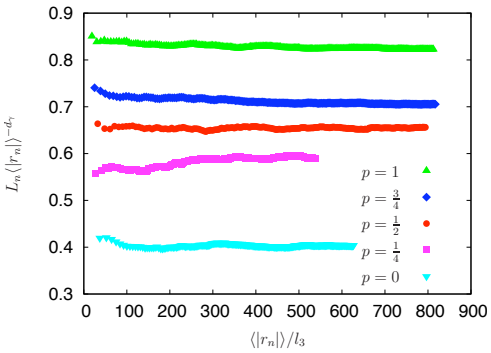

(d) $L_n \langle|r_n|\rangle^{-d_\gamma^{\mathrm{con}}}$ (linear sampling)

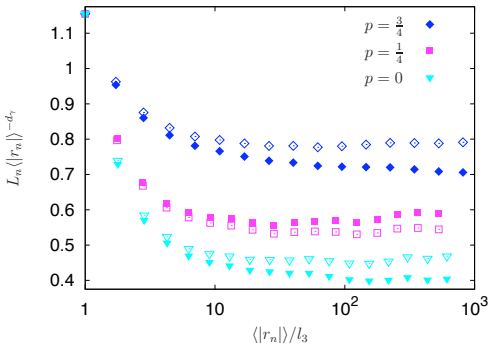

(e) $L_n \langle|r_n|\rangle^{-d_\gamma^{\mathrm{con}}}$ and $L_n \langle|r_n|\rangle^{-d_\gamma^{\log 10}}$

Figure 7.17: The length L_n of the exploration path and the mean distance $\langle r_n \rangle$ reached by the explorer after n steps scale with the power d_γ, which is the capacity dimension of the exploration path. In figures (a) and (c) data are plotted via a logarithmic sampling at steps 2^i and via a linear sampling every m steps, respectively. Darker lines indicate the conjectured scaling. In figures (b) and (d) L_n is compensated by $\langle r_n \rangle^{d_\gamma^{\mathrm{con}}}$: if conjecture 6.1 holds, we should observe a constant trend. However, figure (e) shows that compensating with a fitted d_γ (open symbols) results in a more horizontal behaviour.

p	0	$\frac{1}{4}$	$\frac{1}{2}$	$\frac{3}{4}$	1
d_γ^{con}	2	$\frac{15}{8} = 1.875$	$\frac{7}{4} = 1.75$	$\frac{13}{8} = 1.625$	$\frac{3}{2} = 1.5$
d_γ^{lin}	2.002 ± 0.001	1.892 ± 0.001	1.7523 ± 0.0006	1.6138 ± 0.0003	1.4921 ± 0.0003
$d_\gamma^{\mathrm{log10}}$	1.977 ± 0.004	1.888 ± 0.004	1.744 ± 0.002	1.608 ± 0.002	1.490 ± 0.001
$d_\gamma^{\mathrm{log30}}$	1.985 ± 0.006	1.896 ± 0.004	1.748 ± 0.002	1.614 ± 0.001	1.493 ± 0.001

(a) $d_\gamma(p)$

p	0	$\frac{1}{4}$	$\frac{1}{2}$	$\frac{3}{4}$	1
$\varkappa_{\mathrm{con}}$	8	7	6	5	4
$\varkappa(d_\gamma^{\mathrm{lin}})$	8.016 ± 0.008	7.136 ± 0.008	6.018 ± 0.005	4.910 ± 0.002	3.937 ± 0.002
$\varkappa(d_\gamma^{\mathrm{log10}})$	7.82 ± 0.03	7.10 ± 0.03	5.95 ± 0.02	4.86 ± 0.02	3.92 ± 0.01
$\varkappa(d_\gamma^{\mathrm{log30}})$	7.88 ± 0.05	7.17 ± 0.03	5.98 ± 0.02	4.91 ± 0.01	3.94 ± 0.01

(b) $\varkappa\left(d_\gamma(p)\right)$

Table 7.3: Fitting results for the fractal dimensions d_γ of p-HE paths (table (a)) and for the corresponding extracted $\varkappa$ (table (b)) are listed. We considered a power-law fitting on linearly-sampled data ($\alpha x^{d_\gamma^{\mathrm{lin}}}$) and linear fitting on logarithmically-sampled data ($a + d_\gamma^{\mathrm{log10}} x$ and $a + d_\gamma^{\mathrm{log30}} x$, where 10 and 30 stand for the minimum radius of the fitted ranges). Diffusivities at $p = 0$ are to be intended as lower bounds. The errors refer to fitting errors, not to realization statistics.

Figure 7.17 shows that, after a small region where finite-size effects are important, a scaling range is present over three orders of magnitude. Moreover, at first glance data are in good agreement with the conjectured behaviour. However, plotting the compensated quantities $n \langle |r_n| \rangle^{-d_\gamma^{\mathrm{con}}}$, which should be constant, reveals that the conjectured values d_γ^{con} are slight different from those observed. This qualitative observation is confirmed by fitting results, which are listed in table 7.3 for different scaling ranges.

7.5 Real-point fractal dimension

The second fractal object we considered is the subset of p-HE paths formed by points lying on the real axis. In section 5.2.3 the density of real points was studied. Again, combining conjecture 6.1 with SLE prediction (5.19) leads to a conjectured fractal dimension

$$d_{\mathrm{rp}}^{\mathrm{con}} = 2 - \frac{2}{2-p}$$

Here the whole available range $[0, 1]$ is covered, as p runs from 1 to 0.

Also in this case the extracted dimension is the capacity dimension. Here $\varepsilon = 1/|x|$, where $|x|$ identifies an increasing interval of the real axis. Then, we looked at how the mean number $\langle n_{\mathrm{rp}} \rangle$ of real points present in the interval

p	0	$\frac{1}{4}$	$\frac{1}{2}$	$\frac{3}{4}$	1
$d_{\mathrm{rp}}^{\mathrm{con}}$	1	$\frac{6}{7} \simeq 0.8571$	$\frac{2}{3} \simeq 0.6667$	$\frac{2}{5} = 0.4$	0
$d_{\mathrm{rp}}^{\mathrm{lin}}$	0.888 ± 0.006	0.803 ± 0.006	0.630 ± 0.004	0.414 ± 0.004	0.169 ± 0.002
$d_{\mathrm{rp}}^{\mathrm{log}}$	0.921 ± 0.004	0.838 ± 0.006	0.669 ± 0.005	0.445 ± 0.006	0.180 ± 0.005

(a) $d_{\mathrm{rp}}(p)$

p	0	$\frac{1}{4}$	$\frac{1}{2}$	$\frac{3}{4}$	1
$\varkappa_{\mathrm{con}}$	8	7	6	5	4
$\varkappa(d_{\mathrm{rp}}^{\mathrm{lin}})$	$\geqslant 7.19 \pm 0.05$	6.68 ± 0.05	5.84 ± 0.04	5.05 ± 0.05	4.37 ± 0.06
$\varkappa(d_{\mathrm{rp}}^{\mathrm{log}})$	$\geqslant 7.41 \pm 0.04$	6.88 ± 0.05	6.01 ± 0.04	5.14 ± 0.07	4.4 ± 0.1

(b) $\varkappa\left(d_{\mathrm{rp}}(p)\right)$

Table 7.4: Fitting results for the fractal dimension d_{rp} of the set of p-HE points lying on the real axis (table (a)) and for the corresponding extracted $\varkappa$ (table (b)) are listed. We considered a power-law fitting on linearly-sampled data ($\alpha x^{d_{\mathrm{rp}}^{\mathrm{lin}}}$) and a linear fitting on logarithmically-sampled data ($a + d_{\mathrm{rp}}^{\mathrm{log}} x$). As for path fractal dimension, $\varkappa(p = 0)$ are to be intended as lower bounds. The errors refer to fitting errors, not to realization statistics.

$[-|x|, |x|]$ scales with $|x|$. Again, data are stored both by a logarithmic sampling (i.e. increasing the radius as α^i) and by a liner sampling (i.e. increasing the radius as ai). In the former case, the fractal dimension emerges from the linear fitting

$$\log \langle n_{\mathrm{rp}} \rangle = a + d_{\mathrm{rp}}^{\mathrm{log}} \log|x|$$

whereas in the latter from the power-law fitting

$$\langle n_{\mathrm{rp}} \rangle = \alpha |x|^{d_{\mathrm{rp}}^{\mathrm{lin}}}$$

In figure 7.18 we can observe that a scaling range is present over two orders of magnitudes between a region at smaller scales where finite-size effects are relevant and a region at larger scales where the number of real points saturates because of hull finiteness. Although slopes are less clear here, it is evident that conjecture 6.1 moves in the right direction. Conjectured and fitted values, listed in table 7.4, are in a worse agreement. A low statistics and finite-size effects are probably responsible for this. Indeed the agreement worsens as p increases, i.e. as real points become rarer events. The case of the harmonic explorer confirms our interpretation: although real points are proved to be absent, some of them are observed. The explanation is that in the continuum the curve can get closer and closer to the boundary without touching it, whereas on the lattice there is always a non-zero hitting probability (e.g. $\frac{1}{2}$ at the second step). Therefore, the analysis on real points results more qualitative than that on p-HE paths.

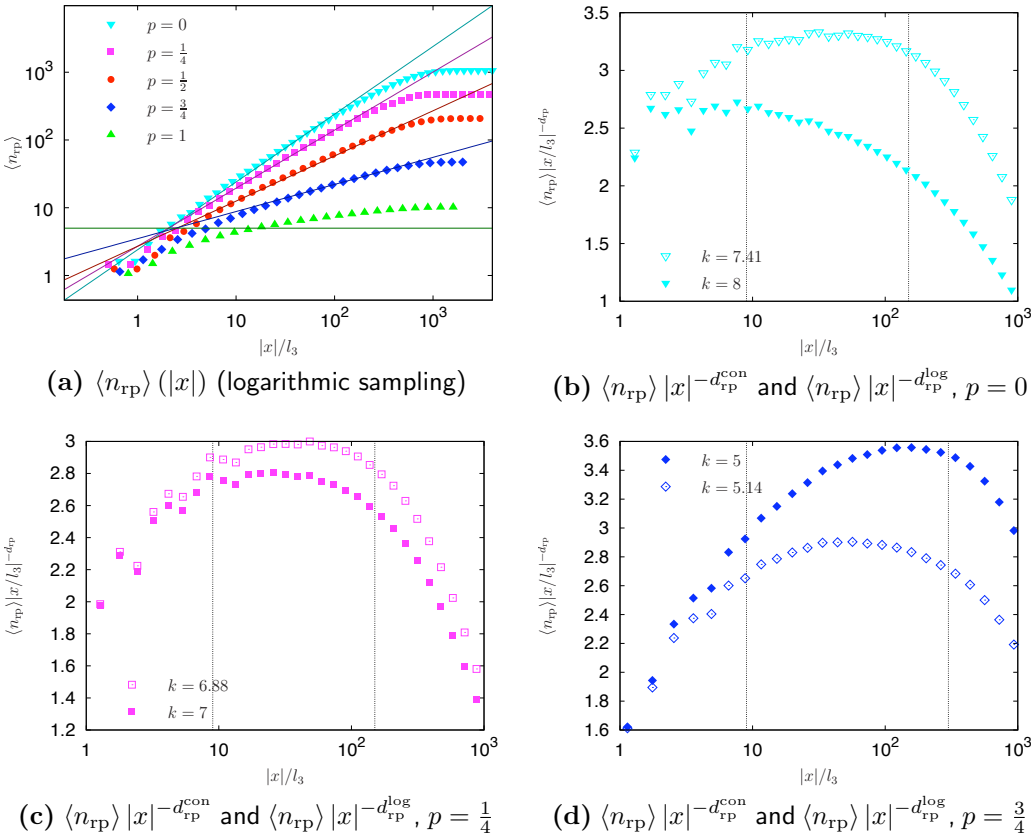

(a) $\langle n_{\rm rp}\rangle$ ($|x|$) (logarithmic sampling)

(b) $\langle n_{\rm rp}\rangle\,|x|^{-d_{\rm rp}^{\rm con}}$ and $\langle n_{\rm rp}\rangle\,|x|^{-d_{\rm rp}^{\rm log}}$, $p = 0$

(c) $\langle n_{\rm rp}\rangle\,|x|^{-d_{\rm rp}^{\rm con}}$ and $\langle n_{\rm rp}\rangle\,|x|^{-d_{\rm rp}^{\rm log}}$, $p = \frac{1}{4}$

(d) $\langle n_{\rm rp}\rangle\,|x|^{-d_{\rm rp}^{\rm con}}$ and $\langle n_{\rm rp}\rangle\,|x|^{-d_{\rm rp}^{\rm log}}$, $p = \frac{3}{4}$

Figure 7.18: The mean number $\langle n_{\rm rp}\rangle$ of points lying on the real axis in the interval $[-|x|, |x|]$ scales with $|x|$ to the power $d_{\rm rp}$, which is the capacity dimension of the set of path real points. In figures (a) logarithmically-sampled data are reported together with the corresponding conjectured laws (darker lines). In figures (b)-(d) $\langle n_{\rm rp}\rangle$ is compensated by both $|x|^{d_{\rm rp}^{\rm con}}$ (filled symbols) and $|x|^{d_{\rm rp}^{\rm log}}$ (open symbols), where superscript 'log' stands for fit results on logarithmically-sampled data. In the latter case, the constant behaviour is better approximated in the fitting range between the vertical lines.

7.6 Double-point fractal dimension

Finally, we considered a second subset of p-HE paths, viz. that formed by points where the path hits itself. Its conjectured fractal dimension arises from conjecture 6.1 combined with SLE value (5.20):

$$d_{\rm dp}^{\rm con} = \frac{(p-1)(p-5)}{2(2-p)} \tag{7.1}$$

As p runs from 1 to 0, the range $[0, \frac{5}{4}]$ is covered. It is worth to notice that the study of this fractal object is important for the antiharmonic explorer especially. Indeed, here $\mathrm{SLE}_{\varkappa \geqslant 8}$ are distinguishable.

Unfortunately, in lattice domain some problems arise together with the question on which points of the path can be considered double points. By construction, exploration paths are not self-intersecting: when the explorer hits path boundaries, it is forced to turn away; hence, the smallest accessible distance is hexagon side l_6 and no double points exist. Nevertheless, we are interested in double points emerging in the continuous limit, i.e. as $l_6 \to 0$ and $n \to \infty$ such that path length $L_n = nl_6 \to L_t$ is preserved. We are induced to consider points on adjacent hexagon vertices as double points, but more care is needed. First, every path point r_m has distance l_6 from points r_{m-1} and r_{m+1}, without tending to any double point. The explorer has to wander somewhere before hitting its boundary (itself in the continuous limit) in a double point. Let us give the simplest example: if the explorer turns four times left from point r_m, the new tip r_{m+4} will be l_6 away from point r_{m-1}; will the pair (r_{m-1}, r_{m+4}) converge to a double point in the scaling limit? No, because the whole path between the two points encloses a single hexagon and will collapse in a single point. The collapse does not occur if the path between them is long enough, say n_{cl} steps. In this case, after a long excursion the explorer finds the hull again and double points are the border of cluster regions (i.e. neighbouring regions which are distant with respect to exploration time n). In conclusion, we define two path points r_m and $r_{m'}$ a double point if $|r_m - r_{m'}| = l_6$ and $|m - m'| \geqslant n_{\mathrm{cl}}$.

Clearly, threshold parameter n_{cl} introduces a bit of arbitrariness in the analysis. On the one hand, the shorter n_{cl}, the larger the number n_{dp} of double points and the better the statistics. On the other hand, a too short n_{cl} causes the inclusion of spurious points, raising up the observed dimension to d_γ. On the contrary, if n_{cl} is too large, double points are rare, the statistics is not well described and their dimension tends to decrease (the scaling slope decreases because distant points are unlikely). Sensitivity to n_{cl} was tested. Figure 7.19 provides one sample of double-point distribution for each value of p and for different thresholds n_{cl}. The result is that double-point density decreases by increasing p, as indicated by (7.1). Especially for $p = 0$, the distribution follows filaments, which are cluster borders.

Here, to extract the fractal dimension we exploited the correlation dimension d_2 defined by $(5.14\mathrm{c})$: we counted the number m_{dp} of double-point pairs closer than radius ρ_{dp}, then averaged over realizations. Different n_{cl} were considered. We performed the linear fitting

$$\log \langle m_{\mathrm{dp}} \rangle = a + d_{\mathrm{dp}}^{\log} \log \rho_{\mathrm{dp}}$$

from logarithmically-sampled data.

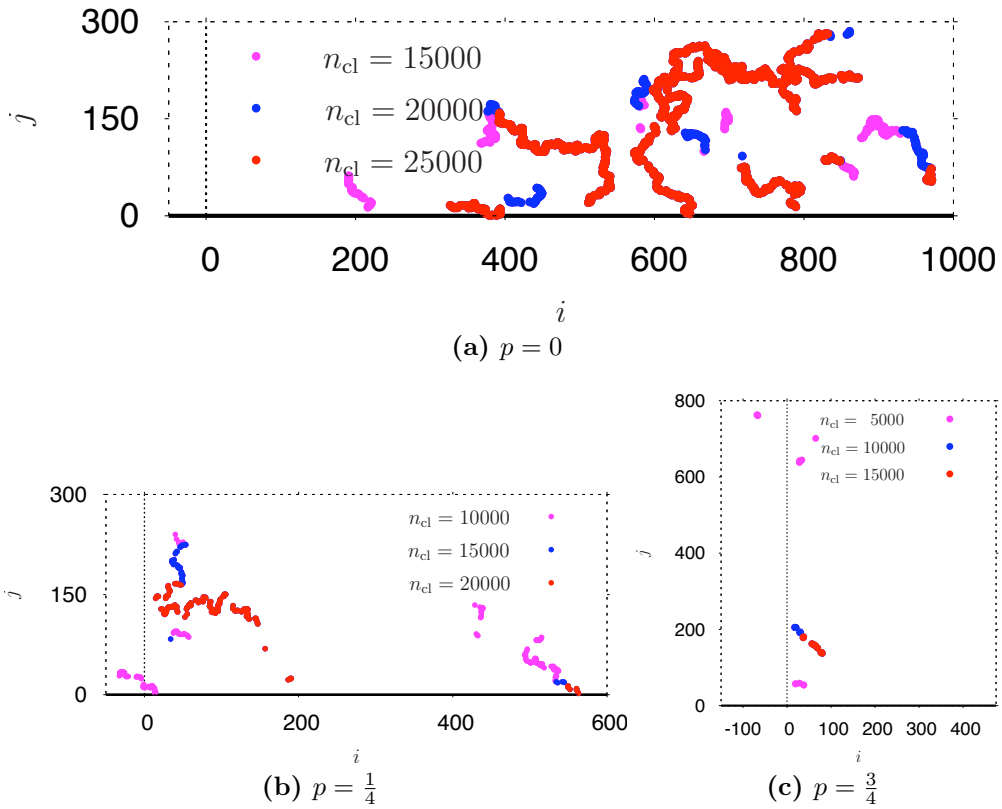

(a) $p = 0$

(b) $p = \frac{1}{4}$

(c) $p = \frac{3}{4}$

Figure 7.19: Double points of an SLE are points where the curve touches itself (without intersections) and can be regarded as the limit of two adjacent vertices on the lattice when the lattice spacing tends to 0. However, if two adjacent points r_m and $r_{m'}$ are not separated enough in terms of the number of steps, e.g. $|m - m'| < n_{\rm cl}$, in the scaling limit the whole trace between them is swallowed into a unique point, which is no more a double point. Double points appear when the path comes back from a long wander to a previously visited region. In other words, they describe the boundaries of well separated clusters. In the three samples provided here double points are separated by three different thresholds $n_{\rm cl}$.

Figure 7.20 shows how the mean number of pairs inside a semicircle scales with its radius. Like for real points, a clear scaling range is present over two orders of magnitude. At smaller scales finite-size effects prevail; since exploration paths are finite, at larger scales a saturation occurs. Plotted and fitted data only refer to thresholds $n_{\rm cl}$ for which a reasonable scaling range was observed. Scaling slopes result in good agreement with the conjectured values for each p and for different $n_{\rm cl}$. Table 7.5 summarizes fitting results. The most important of them is that the antiharmonic explorer is compatible with SLE_8, whereas from the analysis on crossing probabilities we were induced to think to larger values of $\varkappa$.

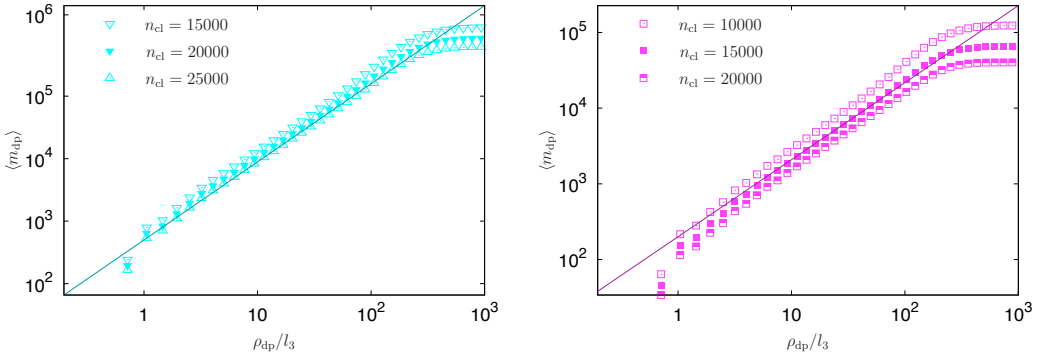

(a) $\langle m_{\rm dp} \rangle (\rho_{\rm dp})$, $p = 0$ **(b)** $\langle m_{\rm dp} \rangle (\rho_{\rm dp})$, $p = \frac{1}{4}$

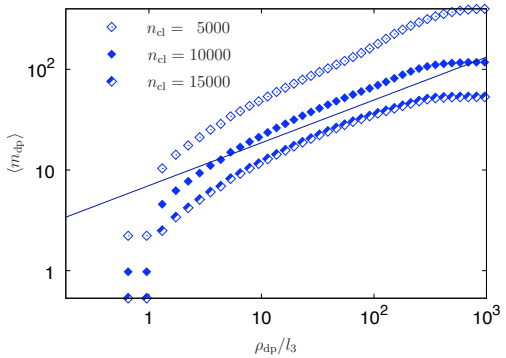

(c) $\langle m_{\rm dp} \rangle (\rho_{\rm dp})$, $p = \frac{3}{4}$

Figure 7.20: The mean number $\langle m_{\rm dp} \rangle$ of couples of double points closer than $\rho_{\rm dp}$ scales with $\rho_{\rm dp}$ to the power $d_{\rm dp}$, which is the correlation dimension of the set of double points. The scaling behaviour is close to the conjectured one (darker lines). The choice of the threshold should take into account two effects: if $n_{\rm cl}$ is too small, adjacent points cover the lattice; if it is too large, there is not enough statistics. However, since $d_{\rm dp}$ slightly depends on the selected threshold, there is some arbitrariness in that choice.

7.7 Results summary

This chapter provided a first review of the results of our numerical analysis on the overruled harmonic explorers. It is not exhaustive and many properties are still to be investigated. The aim of our first analysis was to determine whether p-HE are good candidates as SLE$_\varkappa$ continuous limits and whether the conjectured relation between p and $\varkappa$ is correct. Since the overruled harmonic explorers exhibit conformally invariant properties, the former question finds a clear positive answer. The answer to the latter question is more delicate. Indeed, on the one hand we observe that conjecture 6.1 gets the right trend and gives

p	0	$\frac{1}{4}$	$\frac{3}{4}$
$d_{\rm dp}^{\rm con}$	$\frac{5}{4} = 1.25$	$\frac{57}{56} \simeq 1.018$	$\frac{17}{40} = 0.425$
$d_{\rm dp}^{\log 5000}$	-	-	0.553 ± 0.008
$d_{\rm dp}^{\log 10000}$	-	1.101 ± 0.006	0.54 ± 0.01
$d_{\rm dp}^{\log 15000}$	1.285 ± 0.009	1.063 ± 0.004	0.53 ± 0.01
$d_{\rm dp}^{\log 20000}$	1.245 ± 0.007	1.041 ± 0.005	-
$d_{\rm dp}^{\log 25000}$	1.214 ± 0.005	-	-

(a) $d_{\rm rp}(p)$

p	0	$\frac{1}{4}$	$\frac{3}{4}$
$\varkappa_{\rm con}$	8	7	5
$\varkappa(d_{\rm dp}^{\log 5000})$	-	-	5.37 ± 0.03
$\varkappa(d_{\rm dp}^{\log 10000})$	-	7.35 ± 0.02	5.31 ± 0.04
$\varkappa(d_{\rm dp}^{\log 15000})$	8.16 ± 0.02	7.18 ± 0.02	5.30 ± 0.04
$\varkappa(d_{\rm dp}^{\log 20000})$	7.98 ± 0.02	7.10 ± 0.02	-
$\varkappa(d_{\rm dp}^{\log 25000})$	7.84 ± 0.02	-	-

(b) $\varkappa\,(d_{\rm dp}(p))$

Table 7.5: Fitting results for the fractal dimension $d_{\rm dp}$ of the set of p-HE double points (table (a)) and for the corresponding extracted $\varkappa$ (table (b)) are listed. We considered linear fittings on logarithmically-sampled data ($a + d_{\rm dp}^{\log n_{\rm cl}} x$, where $n_{\rm cl}$ stands for the minimum number of steps between the two points). The errors refer to fitting errors, not to realization statistics.

a good approximation of real data; on the other hand, some discrepancies are evident. Figure 7.21 provides a summary of every $\varkappa$ determined for each p. Indications coming from crossing probabilities are not confirmed by the other considered properties. Combining all results does not highlight a trend different from the conjectured one. We also compared them with alternative guesses, such as (6.30), but fixing the free parameter a_0 at, say, $p = 0$, resulted in a worse description than the one conjectured at $p = \frac{1}{4}$ and $\frac{3}{4}$. Therefore, we can conclude that conjecture 6.1 is a first-order approximation of the function $\varkappa(p)$. Since data are affected by the finite size of the lattice, at this point we cannot deduce that all the other orders are 0. A deeper analysis is required, both on other properties and on much longer exploration paths.

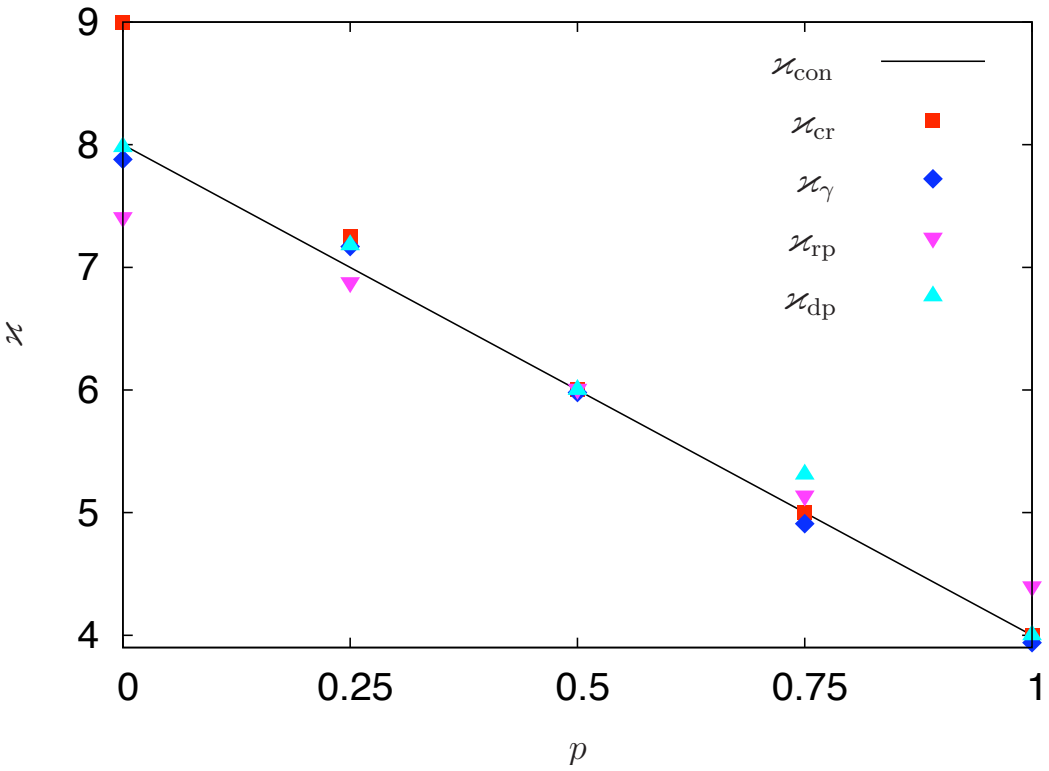

Figure 7.21: SLE diffusivities $\varkappa(p)$, as extracted by different p-HE properties, are plotted with respect to each considered p. The diffusivities $\varkappa_{\mathrm{cr}}$ extracted by the crossing probabilities (red squares) are only qualitatively approximated, whereas $\varkappa_{\gamma}$ (blue diamonds), $\varkappa_{\mathrm{rp}}$ (magenta downwards triangles) and $\varkappa_{\mathrm{dp}}$ (cyan upwards triangles) come from the fitted fractal dimensions of paths, real points and double points, respectively. It is worth noticing that $\varkappa_{\gamma}(0)$ and $\varkappa_{\mathrm{rp}}(0)$ are to be intended as lower bounds. The conjectured relation (black line) gets the right behaviour. However, several values do not lie close to the conjectured curve, although a general trend cannot be extracted. A deeper research is needed in order to determine whether conjecture 6.1 is true.

Conclusions

Since the formulation and the development of the conformal-field theory and, more recently, the stochastic Löwner evolution, the study of stochastic growth processes on planar lattices has been an issue of paramount interest. Indeed, some special families of them can be regarded as the discrete counterparts of the conformal processes involved in these theories. Such a parallelism between discrete and continuous models turns out to be a fruitful tool, e.g. offering the opportunity of a deep numerical analysis of the continuous models and the exploitation of the more convenient framework in order to carry out computations or, most of all, allowing a classification of many different physical systems in universality classes. Thanks to this last feature, researchers from many different fields, such as mathematics, statistical mechanics, quantum gravity, turbulence or fracture physics, are devoting themselves to the study of discrete growth processes and their relation with continuous models.

The exploration process, i.e. a growing self-avoiding polygonal chain on lattice edges, is the simplest growth process on a planar lattice. Given some boundary conditions and a stochastic exploration rule, in general depending on them, a growing tip describes a non-intersecting path, whose left and right sides, step by step, become part of the boundary of a cut domain, so restricting the available initial domain. Among the several properties displayed by explorers, two particular properties are interesting and very powerful if present together: the domain Markov property and the conformal invariance. The former ensures that the probability of an exploration path, the first n steps being given, is the same of an exploration path in the cut domain emerging from the tip after n steps. The latter property holds when the continuous limit of the exploration path is conformally invariant. While building a Markovian explorer is easy by imposing that the advancing rule only depends on the boundary conditions of the cut domain, proving its conformal invariance is a demanding challenge, which has been completed only for few cases. However, the numerical evidence of conformal invariance is attested for a higher number of explorers.

A crucial feature of many growing paths is that they share the same measure as the critical interfaces of equilibrium clusters in a statistical-mechanics model.

Thus, studying the dynamical properties of a physical system at equilibrium would correspond to investigate the geometrical properties of growing curves. Such an approach convinced Oded Schramm to define a continuous version of the discrete explorers, the stochastic Löwner evolutions. SLE are stochastic growing curves on a bounded complex domain displaying both Markovianity and conformal invariance. Here, instead of giving a differential advancing rule, the curve is described by the evolution of the conformal map mapping the cut domain in the original one. Since such an evolution follows a stochastic law, SLE paths are controlled by the only diffusive coefficient $\varkappa \in \mathbb{R}^+$ and, therefore, constitute a one-parameter family. An alternative way for generating SLE curves is their definition by conformal field operators, whose central charge c is a function of $\varkappa$. Analogously to the discrete case between exploration processes and statistical-mechanics models, stochastic Löwner evolution and conformal field theory result as dual theories, the former being the geometrical face, the latter the dynamical one.

An important and fascinating skill of SLE is the possibility of classifying two-dimensional physical systems in universality classes, labelled by $\varkappa$. Very different systems have revealed to share the same $\varkappa$, i.e. the same symmetries. As a surprising example, the isolines of the vorticity and temperature fields in two-dimensional turbulence (in the inverse cascade regime) share the same universality class of critical percolation and the harmonic explorer, respectively. However, while $\mathrm{SLE}_\varkappa$ are a one-parameter family, a discrete analogue does not exist for the time being. Discrete one-parameter families of spin models could be exploited for this scope, but defining an exploration process from these models is a very cumbersome (and computationally costly) way, because it would require the simulation of an equilibrium system at each step.

Our work aimed to the definition of a new class of explorers by a simple generalization of the harmonic explorer, whose advancing rule is given by the outcome of a random walk from the explorer tip to the domain boundary. Indeed, if the random walk hits the boundary labelled as red (or left boundary) first, the explorer turns right. Thus, the probability of turning right is the discrete harmonic function with the specified boundary conditions. In our generalization the probability of a right turn is a real function of the harmonic measure, which is stretched by such a function. Therefore, we called this huge class of growth processes stretched harmonic explorers. If the stretching function is a power law of degree q, the corresponding explorer can be implemented by the launch of q random walks from its tip at each step, whereas in general an infinite number is required.

The simplest subfamily of stretched harmonic explorers is obtained for linear stretching functions, whose slope $2p - 1$ allows their classification via the real continuous parameter $p \in [0, 1]$. Here, the interpretation is simpler: at each step

a random walk is launched from the explorer tip and stopped once a boundary point is hit; now its outcome (the colour of the hit boundary) is upheld with probability p and overturned with probability $1-p$. For this reason we named p the uphold probability and the resulting explorers the overruled harmonic explorers. Some well-known growth processes are recovered at special values of p, viz. the harmonic explorer itself at $p = 1$, the critical percolator at $p = \frac{1}{2}$ and the antiharmonic explorer at $p = 0$.

The overruled harmonic explorers are Markovian by construction and their measure based on random walks is a promising basis for their conformal invariance, because the random walk is conformally invariant (apart from a time dilation). Therefore, they are good candidates to converge to an $\mathrm{SLE}_\varkappa$ in the continuous limit. In this case, the natural question arising is on which p corresponds to which $\varkappa$, i.e. whether there is an analytic relation between the two parameters. If this is the case, the continuous one-parameter family would result as the scaling limit of the discrete one. Such a correspondence would have important implications on both a theoretical and a computational side, the latter being due to the very simple and cheap exploration rule. Proving this limit is a very difficult challenge, involving the proof for every lattice and every explorer. Indeed, a lot of ingenuity has been necessary in order to prove the scaling limit of the few cases completed until now.

In this work we have conjectured that the relation between p and $\varkappa$ is linear. Since the continuous limit of two special cases is known (the harmonic explorer, $p = 1$, is proved to converge to SLE_4 and critical percolation, $p = \frac{1}{2}$, to SLE_6), the conjectured relation is fixed to $\varkappa = 4(2 - p)$ for $\varkappa \in [4, 8]$. This range describes the so-called second phase of SLE, where curves hit the boundary and themselves without being space filling. The other SLE phases could be recovered by stretching harmonic explorers whose stretching function is nonlinear. A promising class is defined by a continuous piecewise-linear function (of the kind constant-oblique-constant), which can be labelled by the same parameter p out of the range $[0, 1]$. They can be viewed as an extension of the overruled harmonic explorers, although their advancing rule is less simple. In particular, $p = -\infty$ would correspond to $\varkappa = 0$ and $p = +\infty$ to $\varkappa = \infty$.

We have tried to carry out a schematic proof of our conjecture, for the time being without success. However, we provided a sketch of how a proof should work. The idea is to define a family of martingale processes with the same geometrical properties in the discrete as in the continuous case, to study their evolution law and to take the scaling limit of the discrete incremental law. We suggested to sum the harmonic probability to another harmonic function with different boundary conditions, given by the winding angle of the boundary with respect to the real axis, the prefactor of the latter addend being linear in p (in the discrete case) or $\varkappa$ (in the continuous one). Indeed, such a process is a martingale

for any $\varkappa$. The implementation on the lattice has resulted more problematic.

To test the conformal invariance of the overruled harmonic explorers and the validity of our conjecture, we performed a series of numerical realizations of these explorers on a honeycomb lattice for three values of p, viz. $p = 0$, $p = \frac{1}{4}$ and $p = \frac{3}{4}$ (plus $p = \frac{1}{2}$ and $p = 0$ as control references). At first sight, it is evident how the exploration path becomes more and more space-filling as the outcome probability decreases (in qualitative agreement with our conjecture).

First, we had to test the conformal invariance. For this purpose we chose rectangular domains of different aspect ratios. Indeed, a compact domain allows the explorer to complete its path, thus allowing us to compute well-known probabilities of the complete trace, such as the crossing probability (i.e. the probability that the trace hits a specific point on the left boundary before one on the right). Since this probabilities are conformally invariant for SLE curves, their equality in different domains is a decisive clue for the conformal invariance of the explorer. The most important result of our work is that for each explorer the crossing probability is independent of the considered domain.

The overruled harmonic explorers are Markovian by construction and observed to be conformally invariant. Thus, they should converge to an $\mathrm{SLE}_{\varkappa}$. According to the crossing probabilities, our conjecture works in the right direction, but the conjectured values are not so accurate as the conformal property. Since the crossing probabilities involve the fitting parameter as an argument of hypergeometric functions, it is easier to extract the value of $\varkappa$ from the fractal dimensions of some subsets of the exploration path. Thus, a non-compact domain, such as the standard upper half-plane, is needed. There we studied the fractal dimensions of the trace itself, of real points (the set of trace points lying on the real axis) and of double points (the set of points where the trace hit itself). Again, our conjecture is able to capture the right trend, but some values are not well predicted. However, an alternative relation could not be extracted from our data and, for the moment, our conjecture can be regarded as a first-order approximation of the relation between the discrete class of the overruled harmonic explorers and the stochastic Löwner evolutions. Finite-size effects can be blamed for the discrepancies from the prediction.

A deeper analysis is needed in order to determine the relation between p and $\varkappa$. As a first step, more interesting properties can be extracted from our data, especially from those in the rectangular domains. While our statistics seems to be good, to avoid finite-size effects a higher resolution with more grid points is needed for a new series of realizations. Moreover, different domains and geometries could be tested, such as a disc and a strip domain for the comparison with radial and dipolar SLE, respectively. Fortunately, SLE provides a huge amount of analytic results to which numerical ones can be compared.

Of course, a more interesting way would be proving our conjecture for any p.

The further step could be the study of the piecewise-linear harmonic explorers, trying to extend the p-$\varkappa$ relation to the first and the third SLE phases. A further development could be the identification of symmetry classes of stretched harmonic functions whose corresponding explorers have the same convergence to an $\mathrm{SLE}_{\varkappa}$.

Finally, as a bridge between growth processes in the atmosphere and in critical systems, the study of the diffusion-limited aggregation could help us to properly include ice particles and snowflake formation in our cloud model.

Bibliography

[Akh90] N. I. Akhiezer. *Elements of the theory of elliptic functions*. Vol. 79. Translations of Mathematical Monographs. Translated from the second Russian edition by H. H. McFaden. Providence, RI: American Mathematical Society, 1990, pp. viii+237. ISBN: 0-8218-4532-2. See p. 119.

[BB06] Michel Bauer and Denis Bernard. "2D growth processes: SLE and Loewner chains". In: *Phys. Rep.-Rev. Sec. Phys. Lett.* 432.3-4 (2006), pp. 115–221. ISSN: 0370-1573. See pp. 92, 106, 107, 145.

[BKW76] R. J. Baxter, S. B. Kelland, and F. Y. Wu. "Equivalence of the Potts model or Whitney polynomial with an ice-type model". In: *J. Phys. A: Math. Gen.* 9 (Mar. 1976), pp. 397–406. DOI: 10.1088/0305-4470/9/3/009. See p. 102.

[Ber70] V. L. Berezinskiĭ. "Destruction of long-range order in one-dimensional and two-dimensional systems having a continuous symmetry group. I. Classical systems". In: *Ž. Èksper. Teoret. Fiz.* 59 (1970), pp. 907–920. See p. 101.

[Car03] John Cardy. "Conformal invariance in percolation, self-avoiding walks, and related problems". In: *Ann. Henri Poincaré* 4.suppl. 1 (2003), S371–S384. ISSN: 1424-0637. See p. 108.

[Car05] John Cardy. "SLE for theoretical physicists". In: *Ann. Phys.* 318.1 (2005), pp. 81–118. ISSN: 0003-4916. See p. 92.

[Car92] John L. Cardy. "Critical percolation in finite geometries". In: *J. Phys. A Math. Gen.* 25.4 (1992), pp. L201–L206. ISSN: 0305-4470. See p. 124.

[DS88] Bertrand Duplantier and Hubert Saleur. "Winding-angle distributions of two-dimensional self-avoiding walks from conformal invariance". In: *Phys. Rev. Lett.* 60.23 (1988), pp. 2343–2346. ISSN: 0031-9007. See p. 108.

[DT02] Tobin A. Driscoll and Lloyd N. Trefethen. *Schwarz-Christoffel mapping*. Vol. 8. Cambridge Monographs on Applied and Computational Mathematics. Cambridge: Cambridge University Press, 2002, pp. xvi+132. ISBN: 0-521-80726-3. See p. 117.

[ER85] J.-P. Eckmann and D. Ruelle. "Ergodic theory of chaos and strange attractors". In: *Rev. Modern Phys.* 57.3, part 1 (1985), pp. 617–656. ISSN: 0034-6861. See p. 119.

[FK72] C. M. Fortuin and P. W. Kasteleyn. "On the random-cluster model. I. Introduction and relation to other models". In: *Physica* 57 (1972), pp. 536–564. See p. 102.

[KNK04] Wouter Kager, Bernard Nienhuis, and Leo P. Kadanoff. "Exact solutions for Loewner evolutions". In: *J. Statist. Phys.* 115.3-4 (2004), pp. 805–822. ISSN: 0022-4715. See p. 114.

[KT73] J. M. Kosterlitz and D. J. Thouless. "Ordering, metastability and phase transitions in two-dimensional systems". In: *J. Phys. C: Solid State Phys.* 6 (Apr. 1973), pp. 1181–1203. DOI: 10.1088/0022-3719/6/7/010. See p. 101.

[LSW04a] Gregory F. Lawler, Oded Schramm, and Wendelin Werner. "Conformal invariance of planar loop-erased random walks and uniform spanning trees". In: *Ann. Probab.* 32.1B (2004), pp. 939–995. ISSN: 0091-1798. See pp. 101, 126, 127.

[LSW04b] Gregory F. Lawler, Oded Schramm, and Wendelin Werner. "On the scaling limit of planar self-avoiding walk". In: *Fractal geometry and applications: a jubilee of Benoît Mandelbrot, Part 2*. Vol. 72. Proc. Sympos. Pure Math. Providence, RI: Amer. Math. Soc., 2004, pp. 339–364. See pp. 108, 126.

[Löw23] Karl Löwner. "Untersuchungen über schlichte konforme Abbildungen des Einheitskreises. I". In: *Math. Ann.* 89.1-2 (1923), pp. 103–121. ISSN: 0025-5831. See pp. 114, 116.

[Nie82] Bernard Nienhuis. "Exact critical point and critical exponents of O(n) models in two dimensions". In: *Phys. Rev. Lett.* 49.15 (1982), pp. 1062–1065. ISSN: 0031-9007. See p. 101.

[PV87] Giovanni Paladin and Angelo Vulpiani. "Anomalous scaling laws in multifractal objects". In: *Phys. Rep.* 156.4 (1987), pp. 147–225. ISSN: 0370-1573. See p. 119.

[SK66] H. E. Stanley and T. A. Kaplan. "High-temperature expansions—the classical Heisenberg model". In: *Phys. Rev. Lett.* 16 (1966), pp. 981–983. ISSN: 0031-9007. See p. 101.

[SS05] Oded Schramm and Scott Sheffield. "Harmonic explorer and its convergence to SLE_4". In: *Ann. Probab.* 33.6 (2005), pp. 2127–2148. ISSN: 0091-1798. See pp. 105, 127, 138.

[Sch00] Oded Schramm. "Scaling limits of loop-erased random walks and uniform spanning trees". In: *Isr. J. Math.* 118 (2000), pp. 221–288. ISSN: 0021-2172. See pp. 101, 114, 124.

[Smi01] Stanislav Smirnov. "Critical percolation in the plane: conformal invariance, Cardy's formula, scaling limits". In: *C. R. Acad. Sci. Paris Sér. I Math.* 333.3 (2001), pp. 239–244. ISSN: 0764-4442. See pp. 96, 124, 127.

[Smi05] Stanislav Smirnov. "Critical percolation and conformal invariance". In: *XIVth International Congress on Mathematical Physics*. World Sci. Publ., Hackensack, NJ, 2005, pp. 99–112. See p. 96.

[Tri79] S. Trimper. "Two-dimensional Heisenberg model and pseudoparticle solutions". In: *Phys. Lett. A* 70.2 (1979), pp. 114–116. ISSN: 0031-9163. See p. 101.

[WS81] T. A. Witten and L. M. Sander. "Diffusion-Limited Aggregation, a kinetic critical phenomenon". In: *Phys. Rev. Lett.* 47.19 (Nov. 1981), pp. 1400–1403. DOI: 10.1103/PhysRevLett.47.1400. See p. 109.

[WS83] T. A. Witten and L. M. Sander. "Diffusion-limited aggregation". In: *Phys. Rev. B (3)* 27.9 (1983), pp. 5686–5697. ISSN: 0163-1829. See p. 109.